Università degli Studi di Palermo

AREA RICERCA E TRASFERIMENTO TECNOLOGICO
SETTORE DOTTORATI E CONTRATTI PER LA RICERCA
U. O. DOTTORATI DI RICERCA

Dottorato di Ricerca in Scienze Fisiche e Chimiche
Dipartimento di Fisica e Chimica - Emilio Segrè
Settore Scientifico Disciplinare PHYS-03/A

PHOTOPHYSICS AND PHOTONICS OF SELF-ASSEMBLED SUPERSTRUCTURES

IL DOTTORE
PIETRO CASTRONOVO

IL COORDINATORE
PROF. MARCO CANNAS

TUTOR
PROF. FABRIZIO MESSINA

CO TUTOR
DOTT.SSA ALICE SCIORTINO

CICLO XXXVIII

ANNO CONSEGUIMENTO TITOLO 2026

To my late Grandfathers,
Biagio and Pietro

Contents

Summary

Nanomaterials represent a cornerstone of modern materials science, as their diverse properties enable functionalities unattainable in bulk form. In recent years, assembling nanoparticles into mesoscopic structures has emerged as a powerful route to unlock an even wider range of collective and emergent behaviours. When nanocrystals are brought into close proximity, their interactions reshape the electronic and optical responses in ways that transcend those of isolated particles. Progress in colloidal synthesis, purification, and assembly now enables near monodisperse nanoparticles to be organised into three dimensional superstructures with crystalline, quasi crystalline, or amorphous symmetry, often referred to as superparticles. Virtually any colloidal nanoparticle can serve as a building block for these artificial solids, including chalcogenide and perovskite quantum dots or nanorods, plasmonic nanoparticles, magnetite nanocrystals, and ultrasmall noble metal nanoclusters. Their assemblies display a plethora of intriguing behaviours including exciton delocalisation and band like transport, collective plasmonic resonances, ultra efficient surface enhanced Raman scattering, superfluorescence, long range charge or energy migration, and coupled photonic or excitonic modes, as well as aggregation induced photoluminescence. While the mechanisms underpinning self assembly and the technological promise of these materials have both been intensely studied, the systematic connection between structure and collective response remains far from fully established. Addressing these open questions requires approaches that combine high spatial and temporal resolution, capable of isolating the behaviour of individual superstructures while tracking interparticle cross-talk effects that evolve on sub nanosecond timescales.

Within this framework, the aim of this thesis is to elucidate the photophysics and photonics of three-dimensional superstructures assembled from different classes of semiconductor- and metal-based nanosystems. To this end, we combine diverse assembly strategies with structural characterisation, first-principles simulations, and spectroscopic techniques spanning different spatial and temporal scales. Leveraging a broad palette of building blocks enables us to

probe a correspondingly broad range of collective behaviours, while the synergy between complementary experimental approaches provides a more complete understanding of their responses. Among the characterisation techniques we employ, a prominent role is played by ultrafast transient absorption microscopy, which combines high spatial and temporal resolution thereby allowing to unravel the photoinitiated dynamics of single superstructures at the subnanosecond timescales. The results presented in this thesis advance the fundamental understanding of the collective behaviour of artificial solids, thereby informing future efforts to rationally design self-assembled materials with tailored functionalities.

The thesis is organised into four parts.

Part I establishes the theoretical and experimental foundation for the work presented here.

- chapter 1 introduces the concept of self-assembly and outlines its implications for the behaviour of nanoscale systems.
- chapter 2 examines the physical properties of quantum-confined semiconductor nanocrystals and the ways in which self-organisation modifies their response.
- chapter 3 discusses the optical and electronic behaviour of metals at the nanoscale, from localized plasmon resonances to the molecule-like features of ultrasmall clusters, with emphasis on how collective effects emerge upon assembly.
- chapter 4 provides an overview of the main experimental techniques employed throughout the thesis.

Part II focuses on semiconductor-based superstructures:

- chapter 5 investigates the ultrafast modulation of optical resonances in spherical superstructures assembled from core–shell quantum dots.
- chapter 6 compares the exciton dynamics in such architectures with those of the isolated building blocks, highlighting how cross-talk impacts their photocycle.

- chapter 7 explores the slow-evaporation assembly dynamics of crystalline perovskite supercubes, pinpointing how cross-talk gradually modifies their response.

Part III turns to superstructures composed of metallic nanomaterials:

- chapter 8 addresses supracrystalline assemblies of plasmonic gold nanoparticles and how interparticle distance governes their collective plasmonic response.
- chapter 9 presents fibre-like superstructures assembled from ultrasmall gold nanoclusters, where carrier diffusion following photoexcitation shapes the collective photocycle.

Finally, **Part IV** summarises the key findings presented in the thesis and lists the scientific contributions produced during the PhD.

Sommario

I nanomateriali rappresentano oggi un pilastro fondamentale della moderna scienza dei materiali: l'ampio ventaglio di proprietà che essi manifestano consente infatti di accedere a funzionalità altrimenti precluse ai materiali in forma bulk. Negli ultimi anni, l'auto-organizzazione (self-assembly) di nanoparticelle in strutture mesoscopiche si è rivelata una strategia di eccezionale efficacia per esplorare comportamenti collettivi ed emergenti. Quando i nanocristalli vengono portati a stretto contatto, la loro mutua interazione ne rimodella le risposte elettroniche e ottiche, permettendo di andare ben oltre le caratteristiche tipiche delle unità isolate.

Grazie ai significativi progressi compiuti nella sintesi colloidale, nei processi di purificazione e nelle tecniche di assemblaggio, è oggi possibile organizzare nanoparticelle quasi monodisperse in superstrutture (o superparticelle) tridimensionali dotate di simmetria cristallina, quasi-cristallina o amorfa. I nanomateriali colloidali più disparati possono infatti fungere da unità fondamentali per questi solidi artificiali: dai quantum dots ai nanorods semiconduttori, dalle nanoparticelle plasmoniche ai nanocristalli magnetici e ai nanocluster di metalli nobili. Le superstrutture così ottenute manifestano una pletora di fenomeni affascinanti, che spaziano dalla delocalizzazione eccitonica alla migrazione di carica, dalle risonanze plasmoniche collettive alla superfluorescenza, fino alla comparsa di modi ottici accoppiati e alla fotoluminescenza indotta da aggregazione (AIE).

Sebbene i meccanismi di self-assembly e il potenziale tecnologico di tali sistemi siano stati ampiamente investigati, il legame sistematico tra l'architettura strutturale e la risposta collettiva non è ancora stato pienamente elucidato. Lo studio di tali correlazioni struttura-proprietà richiede approcci d'indagine capaci di coniugare elevate risoluzioni spaziali e temporali, così da isolare il comportamento delle singole superstrutture e, simultaneamente, tracciare gli effetti di cross-talk tra le particelle, i quali evolvono tipicamente su scale temporali inferiori al nanosecondo.

In questo quadro, l'obiettivo della presente tesi è chiarire le proprietà fotofisiche

e fotoniche di superstrutture tridimensionali assemblate a partire da diverse classi di nanosistemi semiconduttori e metallici. A tal fine, differenti strategie di assemblaggio sono state coniugate con un protocollo di analisi multidisciplinare che combina caratterizzazione strutturale, simulazioni numeriche da principi primi e, in particolare, tecniche spettroscopiche avanzate. L'impiego di una vasta gamma di unità costitutive ha permesso di esplorare un altrettanto ampio spettro di fenomeni collettivi, mentre la sinergia tra approcci sperimentali complementari ha garantito una comprensione esaustiva della loro risposta ottica. Tra le metodologie adottate, spicca la microscopia di assorbimento transiente ultraveloce (ultrafast transient absorption microscopy): grazie alla sua alta risoluzione spazio-temporale, tale tecnica ha consentito di distinguere le dinamiche fotoindotte all'interno delle singole superstrutture su scale sub-nanosecondo. I risultati presentati in questo lavoro gettano nuova luce sulla fisica fondamentale dei solidi artificiali e contribuiscono a stabilire criteri guida generali per la progettazione razionale di materiali auto-assemblati con proprietà e funzionalità fisico-chimiche predeterminate.

Il presente lavoro di tesi è organizzato in quattro parti.

La **Parte I** delinea il quadro concettuale e gli strumenti sperimentali su cui si basa il lavoro di ricerca:

- Il *capitolo 1* introduce il paradigma del self-assembly, illustrandone le implicazioni fondamentali sulle proprietà della materia alla nanoscala.

- Il *capitolo 2* esamina le proprietà fisiche dei nanocristalli semiconduttori in regime di confinamento quantico, analizzando come il self-assembly ne moduli la risposta intrinseca.

- Il *capitolo 3* discute il comportamento ottico ed elettronico dei metalli alla nanoscala, dalla risonanza plasmonica alle proprietà molecolari dei nanoclusters, con particolare attenzione all'emergere di effetti collettivi a seguito dell'assemblaggio.

- Il *capitolo 4* offre una panoramica delle tecniche sperimentali e dei protocolli di caratterizzazione impiegati nel corso del lavoro.

La **Parte II** è dedicata allo studio di sistemi assemblati a partire da nanomateriali semiconduttori:

- Il *capitolo 5* indaga la modulazione ultraveloce delle risonanze ottiche in superstrutture sferiche composte da quantum dots *core-shell*.
- Il *capitolo 6* presenta un confronto sistematico tra le dinamiche eccitoniche di tali architetture e quelle delle singole unità isolate, evidenziando l'impatto del cross-talk sul fotociclo globale.
- Il *capitolo 7* esplora il processo di assemblaggio per evaporazione controllata di supercubi cristallini di perovskite, tracciando l'evoluzione della loro risposta ottica.

La **Parte III** verte sullo studio di superstrutture composte da nanomateriali metallici:

- Il *capitolo 8* analizza supercristalli di nanoparticelle d'oro, studiando come la distanza interparticellare governi in modo critico la risposta plasmonica collettiva.
- Il *capitolo 9* presenta superstrutture fibrillari ottenute da nanoclusters d'oro, il cui fotociclo è dominato dai processi di diffusione dei portatori di carica lungo l'asse della struttura.

Infine, la **Parte IV** sintetizza i principali traguardi raggiunti, delineando le prospettive future aperte da questo lavoro e riportando l'elenco dei contributi scientifici pubblicati durante il percorso di dottorato.

List of Abbreviations

Samples & Chemicals

AuNP(s)	Gold Nanoparticle(s)
AuSP(s)	Gold Superparticle(s)
DCM	Dichloromethane
FA	Formic Acid
GNC(s)	Gold Nanocluster(s)
IpA	Isopropanol
MeCN	Acetonitrile
MHP(s)	Metal Halide Perovskite(s)
NC(s)	Nanocrystal(s) *or* Nanocluster(s)
NP(s)	Nanoparticle(s)
NR(s)	Nanoribbon(s)
NW(s)	Nanowire(s)
OA	Oleic Acid
OAm	Oleylamine
ODE	Octadecene
QD(s)	Quantum Dot(s)
SC(s)	Supercube(s)
SDS	Sodium Dodecyl Sulfate
SP(s)	Superparticle(s)
TRZ	6-(dibutylamino)-1,3,5-triazine-2,4-dithiol

Experimental Techniques

Cryo-TEM	Cryogenic Transmission Electron Microscopy
DLS	Dynamic Light Scattering
EDX	Energy-Dispersive X-ray spectroscopy
HI	Hot Injection
HRTEM	High-Resolution Transmission Electron Microscopy
LARP	Ligand-Assisted Reprecipitation
PL(E)	Photoluminescence (Excitation) spectroscopy
SAXS	Small-Angle X-ray Scattering
S(T)EM	Scanning (Transmission) Electron Microscopy
SERS	Surface-Enhanced Raman Scattering
TA(M)	Transient Absorption (Microscopy)
TEM	Transmission Electron Microscopy
TCSPC	Time-Correlated Single Photon Counting
(μ)-UV-Vis	Ultraviolet-Visible absorption spectroscopy (/ microscopy)
XPS	X-ray Photoelectron Spectroscopy
μ(TR)PL	(Time-Resolved) Photoluminescence Microscopy

Miscellaneous

BEM	Boundary-Elements Method
DAS	Decay-Associated Spectra
ehp	Electron-hole pair
ExT	Excitation Transfer
FCC	Face-Centered Cubic
FFT	Fast Fourier Transform
FWHM	Full Width at Half-Maximum
HWHM	Half-Width at Half-Maximum
IRF	Instrumental Response Function
LMCT	Ligand-to-Metal Charge Transfer
LSPR	Localized Surface Plasmon Resonance
PA	Photoinduced Absorption
PB	Photoinduced Bleaching
SE	Stimulated Emission
SHG	Second-Harmonic Generation
SPP	Surface Plasmon-Polariton
SVD	Singular Value Decomposition
THG	Third-Harmonic Generation
TE	Transverse Electric
TM	Transverse Magnetic
WGM(s)	Whispering Gallery Mode(s)
XPM	Cross-Phase Modulation

Part I

Theoretical and Experimental Background

1

General Introduction

On the twenty-fifth of September, twelve hundred and sixty-four, at break of day, the Duke of Auge appeared at the summit of the keep of his castle, there to consider, be it ever so little, the historical situation. It was somewhat confused.

— Raymond Queneau

This chapter provides a general overview on the concept of self-assembly, and on the opportunities provided by employing nanoparticles as building blocks for mesoscale assemblies. We will discuss the two main consequences of self-assembly on the response of the nanosystems, namely the onset of cross-talk effects and the emergence of novel properties not reconducible to those of the constituents. Our discussion will focus particularly on the photophysical and photonic properties of superstructures, which consitute the core of this thesis. Finally, we will discuss the synergy between this work and the current research in this lively and multidisciplinary field.

1

1.1 Self-assembly: an ever-recurring pattern

The spontaneous organisation of matter into ordered forms is one of the most pervasive motifs in nature [1]. From the arrangement of lipids into membranes [2], to the crystallisation of minerals [3] and the folding of proteins [4], ensembles of simple interacting units routinely give rise to structures of remarkable complexity. This phenomenon, broadly referred to as *self-assembly*, often reshapes the behaviour and functionalities of the constituent *building blocks*, and enables collective behaviour that is inaccessible to the isolated constituents [1].

A simple yet poignant example of how assembly can transform matter, concerns the electrical behaviour of solids [5], as schematised in Figure 1.1.

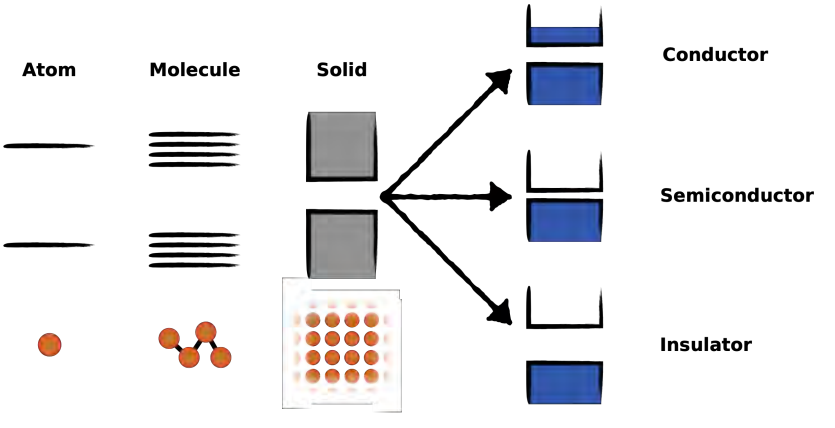

Figure 1.1: The conductivity of solids depends on the occupation and relative positions of the valence and conduction bands, making it a collective property of the solid as a whole, rather than a mere sum of the behaviour of its constituent atoms.

Individual atoms possess discrete, quantised electronic energy levels; taken one by one, they cannot be labelled as conductors, semiconductors, or insulators. Yet when brought together in a crystal, the overlap of their electronic wavefunctions gives rise to continuous *energy bands*. The relative filling of these bands, the presence of an energy gap between them, and its entity, determine whether charge carriers can move freely under an applied field. It is only at this collective level that the characteristic classifications of solid-state physics emerge. The conductivity of a solid is therefore not a simple sum of

the properties of its constituent atoms, but rather a manifestation of their co-operative organisation. In other words, a new material function arises purely from the act of assembling microscopic units into a larger whole, an essential hallmark of self-assembly throughout the natural world.

1.2 Nanoparticles as building blocks

As mentioned in the preface, this thesis revolves around the collective responses of superstructures self-assembled from *nanoparticles* of diverse nature. In contrast with the simple atom-to-solid picture discussed above, it must be emphasised that nanoparticles are themselves complex objects, which can be composed of thousands to millions of atoms, and whose behaviour depends critically on chemical composition, crystallinity, shape, and surface chemistry [6]. In other words, *nanoparticles are not merely scaled-up atoms*.

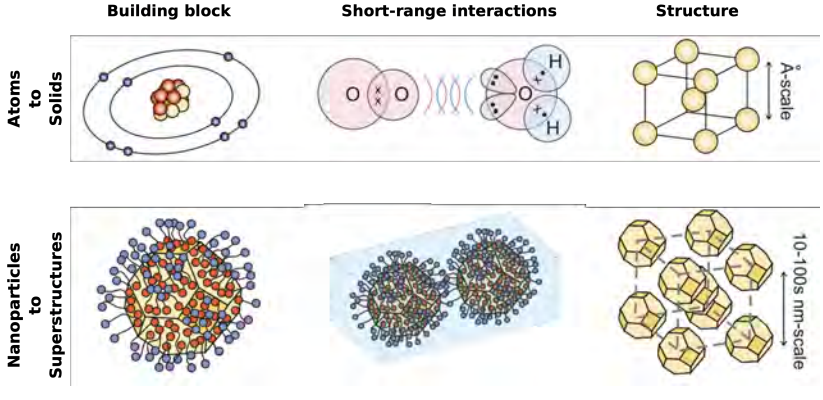

Figure 1.2: Conceptual comparison between the self-assembly of atoms into solids, and that of nanoparticles into superstructures. Adapted from [7]

Broadly speaking, the behaviour of nanoparticles emerges from a combination of *finite size effects* and *surface effects*. The finite, nanometric size of nanoparticles strongly influences their electronic structure and optical response. In semiconductor nanocrystals, for instance, quantum confinement leads to discrete energy levels and size-tunable absorption and emission. In atomically precise noble metal nanoclusters, the familiar free electron response characterising bulk metals gives way to discrete, molecule-like energy states and strong size dependent optical transitions. At the same time, the large surface-

to-volume ratio characteristic of nanoparticles amplifies surface-related phenomena. Atoms at the surface constitute a significant fraction of the total, in stark contrast with bulk materials where surface effects are negligible. This has multiple consequences: conduction electrons at the surface of noble metal nanoparticles can collectively oscillate, giving rise to localized surface plasmon resonances; surface defects or dangling bonds in semiconductor nanocrystals can impair their optical performance unless appropriately passivated; chemical functionalisation of the nanoparticle surface can be exploited to control both their colloidal stability and their interactions with the surrounding environment.

Thus, nanoparticles already possess rich and tunable physical properties arising from their finite size and their highly active surface. Consequently, self-assembled architectures composed of such complex building blocks [1] manifest a plethora of intriguing properties, unlocking numerous applications and revealing precious insight into the interactions between their constituents. Such diverse behaviours can, in general, be rationalised according to two main categories: *cross-talk effects* enabled by the interaction between constituent nanoparticles, and *emergent properties* linked to the superstructure as a whole. In the following sections we will explore these two aspects.

1.3 Cross-talk effects

When nanoparticles are brought into close proximity, their interaction means they can no longer be considered fully independent. The nature and outcome of these interactions, collectively termed *cross-talk effects* [7], depend on the characteristics of the constituents. For instance (see panel (a) of Figure 1.3), in semiconductor-based superstructures the electronic wavefunctions of the confined carriers can hybridise across neighbouring nanoparticles, enabling charge carriers to delocalise over multiple units when surface chemistry, energy alignment, and spacing are favourable. Such coupling reshapes both the energy spectrum and the carrier kinetics of the assembly. In metallic nanostructures, near-field electromagnetic coupling between collective electron oscillations leads to plasmonic hybridisation, where the resulting modes depend sensitively on geometry, spacing, and dielectric environment. In both cases, cross-talk significantly alters the behaviour of isolated nanoparticles.

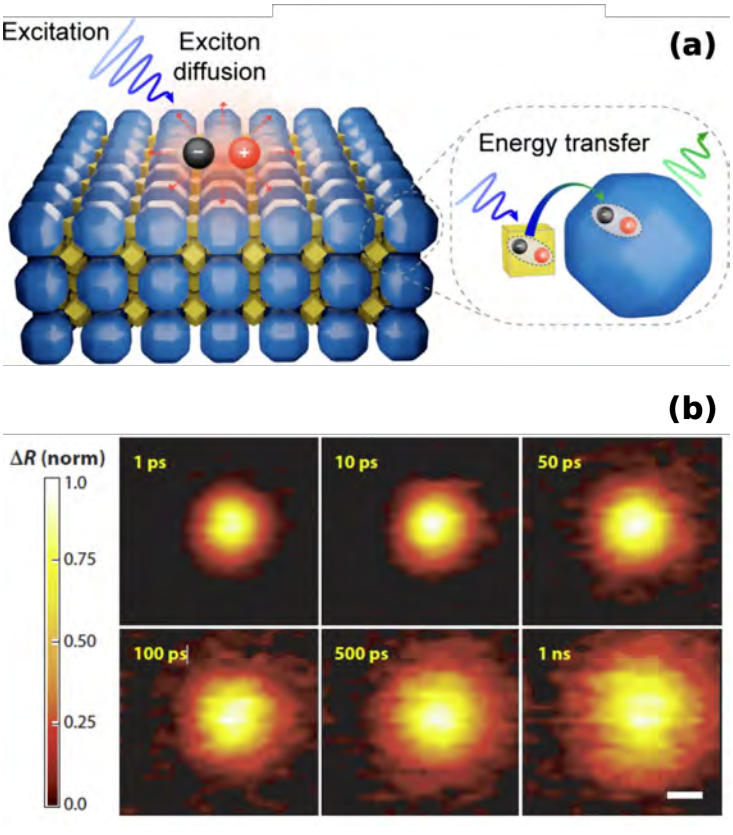

Figure 1.3: (a) schematic representation of the main cross-talk effects in a semiconductor-based superstructure; (b) excitation transfer over micrometric distances (scale bar is 300 nm) in a semiconductor thin-film imaged by ultrafast microscopy. Adapted from [8, 9]

A second important mechanism enabled by cross-talk is *excitation transfer* (ExT) [9, 10], where excitation, whether energy or charge, migrates from the initially excited nanoparticle to its surroundings. ExT pathways include Förster-type dipole–dipole coupling between excitons in semiconductor-based nanocrystals, plasmon–plasmon and plasmon–exciton coupling in metallic and hybrid architectures, as well as photon-mediated transfer via resonant optical modes. These processes act over distances exceeding those accessible by direct wavefunction overlap (see panel (b) of Figure 1.3), extending the spatial range of interaction within the assembly and enabling long-range control of light and energy flow, a crucial pathway towards efficient energy harvesting.

1

1.4 Emergent properties

Besides cross–talk effects which, while profoundly reshaping the response of superstructures, still build upon the properties of the constituent nanoparticles, self-assembly can also give rise to *emergent properties*. These are features of the superstructure as a whole, that do not exist at the level of a single nanoparticle and cannot be predicted by a simple extrapolation of isolated behaviour. Two eloquent examples are found in nature, where precise structural organisation [11] shapes light-matter interaction in awe-inspiring ways (Figure 1.4). The vivid blue of *Morpho rhetenor* butterflies originates not from pigments but from a lamellar nanostructure on the wing scales, whose periodicity is comparable to visible wavelengths. Similarly, natural opals are composed of close-packed silica nanoparticles arranged in a three-dimensional lattice that causes *iridescence* (that is, vivid colourations changing with the view angle) through Bragg diffraction. In both cases, the emergent optical response is inseparable from the mesoscopic order of the material.

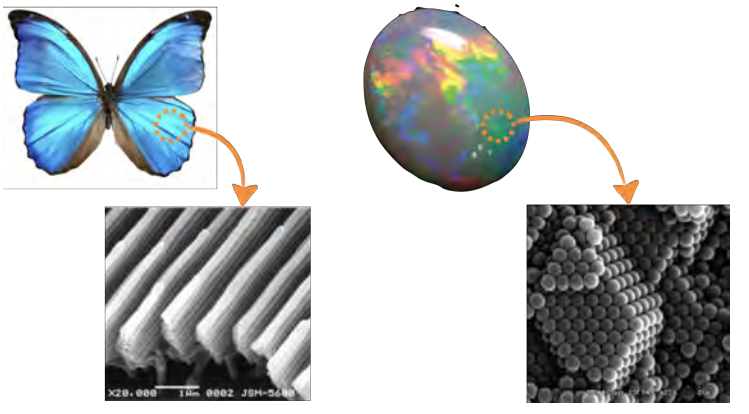

Figure 1.4: Ordered self-assembly shapes the interaction between the superstructure and light. Left: the bright coloring of the wings of *Morpho rhetenor* butterflies results from a lamellar microstructure whose periodicity is comparable to the wavelengths of visible light; right: opals composed of ordered silicon nanoparticles display *iridescence*. Adapted from [11]

In artificial nanoparticle superstructures, similar principles apply. Micrometric superparticles with well-crafted geometries and appropriate optical transmittance can display microresonator behaviour such as whispering gallery modes (WGMs), enabling light trapping and low threshold lasing, whereas the regular

packing of metal nanoparticles results in the appearance of field enhancement hot spots in the inter-nanoparticle regions. In essence, self-assembly does not merely scale up the physics of single nanoparticles, it creates new regimes of material behaviour that only exist through collective organisation.

1.5 Dynamically tracking cross-talk and collective responses

While the existence of cross-talk effects and emergent properties is conceptually well established, experimentally accessing them is all but trivial. Collective phenomena in nanoparticle superstructures are inherently dynamic, span multiple length scales, and often involve intertwined electronic, optical, and thermal processes unfolding throughout the whole superstructure. As a consequence, their investigation requires experimental tools capable of resolving both the relevant time scales, typically ranging from femtoseconds to microseconds, and the spatial scales over which interactions unfold.

Spectroscopic techniques provide a natural entry point to probe collective responses. In particular, ultrafast spectroscopies grant access to the early-time dynamics following photoexcitation, where effects like carrier delocalisation, excitation transfer, and plasmonic hybridisation first emerge. By tracking the temporal evolution of the relevant optical signatures, it becomes possible to study the relaxation pathways, gaining precious insight into the processes governing the collective response. However, ensemble-averaged measurements inevitably obscure heterogeneity. Nanoparticle superstructures often display variations in size, morphology, or packing order, all of which can strongly influence collective behaviour. Microscopy-based approaches overcome this limitation by enabling the investigation of individual superstructures, thereby preserving the direct link between structure and response. Indeed, combining spectroscopy and optical microscopy makes it possible to visualise the generation, migration, and eventual relaxation of excited state species.

In this context, transient absorption microscopy (TAM) emerges as a particularly powerful tool. By combining ultrafast pump–probe spectroscopy with optical microscopy, TAM simultaneously delivers femtosecond temporal resolution and micrometric spatial resolution. This unique capability allows to directly observe cross-talk phenomena as they unfold in space and time within

single superstructures, providing an unmatched platform to interrogate excitation transfer, collective relaxation pathways, and global responses in self-assembled nanoparticle materials.

1.6 Scope and Aim of this Thesis

The field of nanoparticle superstructures is as multifaceted as the materials it investigates, poised at the intersection of chemistry, physics, and materials science. In recent years, significant progress has been made on two fronts. On one side, extensive studies have elucidated how interparticle forces and entropic contributions dictate assembly pathways, governing the emergence of long-range order and complex morphologies. On the other, rapidly growing application-driven research has exploited the remarkable optical, catalytic, and electronic properties of nanoparticle assemblies to push the boundaries of photonics, sensing, and energy conversion. Between these two fronts lies a fertile territory, wherein this thesis is positioned: systematically understanding how structural order translates into new optical and electronic behaviours, and how these behaviours can be observed and controlled at the relevant space and time scales. Fully grasping such structure-property relationships would ultimately lead to virtually endless opportunities for the bottom-up design of superstructures with precisely engineered functionalities.

Two leitmotifs define the approach taken here. First, the systems investigated are intentionally diverse: different classes of semiconductor and metal nanoparticles with fundamentally distinct microscopic responses serve as complementary building blocks to expose different aspects of collective behaviour. Second, the experimental techniques employed (chief among which, transient absorption microscopy) combine high spatial and temporal resolution, enabling direct access to how excitations propagate, interact, and evolve *within* the superstructure. Together, these two guiding principles allow us to interrogate, and ultimately rationalise, the emergence of both cross-talk effects and novel optical and photonic properties in self-assembled nanoparticle materials.

2

Semiconductor Nanocrystals and Superstructures

One should not work on semiconductors. They are a mess. Who knows whether semiconductors exist at all.

— Wolfgang Pauli

The aim of this chapter is to provide the theoretical framework and a broad overview of the current literature on semiconductor nanocrystals and their self-assembled superparticles, in order to contextualise the results presented in chapter 5, chapter 6, and chapter 7. We begin by introducing the key concept of quantum confinement, which underlies the optical and electronic behaviour of semiconductor nanosystems, and then examine strongly confined chalcogenide quantum dots, metal halide perovskite nanocrystals, and the architectures they form upon self-assembly. Particular emphasis is placed on their characteristic optical and photonic responses and on the mechanisms through which collective effects, interparticle coupling, and mesoscale organisation give rise to new properties that are not accessible at the single-nanocrystal level.

2.1 Semiconductors: from bulk to nano

2

Semiconductors represent the backbone of modern technologies, from solar cells and LEDs to transistors and integrated circuits [12]. In a bulk semiconductor, the electronic structure is described by two closely spaced, quasi-continuous manifolds of states known as *bands* [5]. The lower band, the *valence band*, is fully occupied at zero temperature, while the upper *conduction band* is empty. The energetic separation between them (the *bandgap*) is typically on the order of $(1 \div 3)\,\mathrm{eV}$. Absorption of a photon with energy greater than the bandgap can promote an electron from the valence band to the conduction band, leaving behind a positively charged vacancy, or *hole*. Due to Coulomb attraction, the electron–hole pair can form a hydrogen-like bound quasiparticle called an *exciton* [13], whose total energy lies slightly below the free electron–hole continuum. The difference between the bandgap energy and the excitonic transition energy is known as the *exciton binding energy*, a key quantity governing optical absorption, emission efficiency, and charge-carrier dynamics in semiconductors. In the bulk regime, the bandgap and exciton binding energy are size-independent, determined primarily by the chemical composition and crystal structure of the material. As a result, tuning the bandgap in bulk semiconductors typically relies on alloying (for example, in ternary III–V alloys like $\mathrm{In}_x\mathrm{Ga}_{1-x}\mathrm{As}$) [14].

This bulk description breaks down when the spatial dimensions of the material are reduced to the nanoscale, where discrete quantized states emerge and both the bandgap and the exciton binding energy become highly size-dependent. This regime is described as *quantum confinement*, and it is at the core of the unique optical and electronic properties of semiconductor nanocrystals (NCs). In the next section, we will explore this intriguing regime, pinpointing the main consequences it has on the response of semiconductor NCs.

2.1.1 Quantum Confinement

Quantum confinement can be heuristically understood using a simple top–down argument. Consider an otherwise infinite semiconductor crystal in which one of the spatial dimensions (for simplicity, the x-direction) is reduced to a finite size d. Electrons promoted to the conduction band can no longer move freely and indefinitely in that direction; instead, their wavefunctions are re-

stricted within a region of extent approximately equal to d. By Heisenberg's uncertainty principle [15], spatially confining a particle imposes a minimum uncertainty on its momentum:

$$\Delta p_x \sim \frac{\hbar}{\Delta x} = \frac{\hbar}{d} \tag{2.1}$$

This in turn entails an increase in energy according to:

$$\Delta E_{c,x} = \frac{(\Delta p_x)^2}{2m_e} \sim \frac{\hbar^2}{2m_e d^2} \tag{2.2}$$

where m_e is the effective electron mass. Thus, spatial confinement increases the lowest available energy state in the conduction band, effectively widening the bandgap, and the magnitude of this contribution scales as $1/d^2$ (a key insight towards bandgap tuning, as discussed later). A simple way to estimate when confinement becomes relevant is to compare this energy with the thermal energy per degree of freedom:

$$E_{th} = \frac{1}{2} K_B T \tag{2.3}$$

where K_B is the Boltzmann constant. Confinement becomes significant when $\Delta E_{c,x} \gtrsim E_{th}$, that is, when the confinement size satisfies:

$$d \lesssim \frac{\hbar}{\sqrt{m_e K_B T}} \tag{2.4}$$

At room temperature, and considering that $m_e \leq m_o$, where m_o is the free electron mass, one obtains an upper limit for the confinement length:

$$d \lesssim 20\,\mathrm{nm} \tag{2.5}$$

As a concrete example, for cadmium selenide (CdSe), a paradigmatic quantum-dot material discussed later in this work, the electron effective mass is $m_e = 0.13\, m_o$ [16], leading to a confinement length at room temperature of approximately $d \simeq 5.7\,\mathrm{nm}$.

Despite its simplicity, this heuristic approach captures two key points: (i) quantum size effects emerge only when at least one dimension of a semiconductor approaches the nanometre scale, and (ii) bandgap widening scales inversely with the square of the confinement length.

2.1.2 Discretisation of energy states

In order to get a more complete picture of how quantum confinement impacts the energy spectrum of a semiconductor, we must solve the Schrödinger equation for an electron of effective mass m_e that is free to move along y and z ($V(y) = V(z) = 0$), but confined along x by an infinitely tall potential well:

$$V(x) = \begin{cases} 0\,, & 0 < x < d \\ +\infty\,, & x < 0 \ \vee \ x > d \end{cases} \tag{2.6}$$

(note that the lattice potential is accounted for by using the effective mass instead of the free electron mass). Because the motion along y and z is unconfined, we can separate the wavefunction into a confined and a free component:

$$\Psi(x, y, z) = \phi(x)\psi(y, z) \tag{2.7}$$

where the free (plane–wave) solution is

$$\psi(y, z) = A\, e^{\,i(\boldsymbol{k}\cdot\boldsymbol{r})}, \qquad \boldsymbol{r} = (y, z) \tag{2.8}$$

with a continuous energy spectrum given by:

$$E_{free}(\boldsymbol{k}) = \frac{\hbar^2|\boldsymbol{k}|^2}{2m_e} \ , \ \ \boldsymbol{k} = (k_y, k_z) \tag{2.9}$$

and $\phi(x)$ satisfies the one–dimensional time–independent Schrödinger equation with the potential given by (2.6) and the boundary conditions:

$$\phi(0) = \phi(d) = 0 \tag{2.10}$$

The solution is well known [15]: only standing–wave states are allowed inside the well,

$$\phi_n(x) = \sqrt{\frac{2}{d}} \sin\left(\frac{n\pi x}{d}\right), \qquad n = 1, 2, 3, \ldots \tag{2.11}$$

with discrete, quantised energies:

$$E_{x,n} = \frac{\hbar^2\pi^2 n^2}{2m_e d^2} \tag{2.12}$$

Notably, for the lowest excited state ($n = 1$), this yields:

$$E_{x,1} = \frac{\hbar^2\pi^2}{2m_e d^2} \tag{2.13}$$

which is extremely similar to the confinement energy found by our initial heuristic approach (see (2.2)). The total electron energy is given by:

$$E_{tot}(n, \boldsymbol{k}) = E_{x,n} + E_{free}(\boldsymbol{k}) = \frac{\hbar^2 \pi^2 n^2}{2 m_e d^2} + \frac{\hbar^2 |\boldsymbol{k}|^2}{2 m_e} \tag{2.14}$$

The number of non-confined dimensions defines the *dimensionality* of the system [17]. The scenario described above, with one confined and two non-confined dimensions, corresponds to a two-dimensional (2D) system, commonly referred to as a *quantum well*. The same argument generalises to systems with confinement along multiple directions: one-dimensional (1D) *quantum wires*, in which two of the three spatial dimensions satisfy (2.4), and zero-dimensional (0D) *quantum dots* (QDs), where all three spatial dimensions are confined.

The dimensionality of a semiconductor nanostructure directly impacts both its density of states (DOS) and the bandgap shift, as schematised in Figure 2.1.

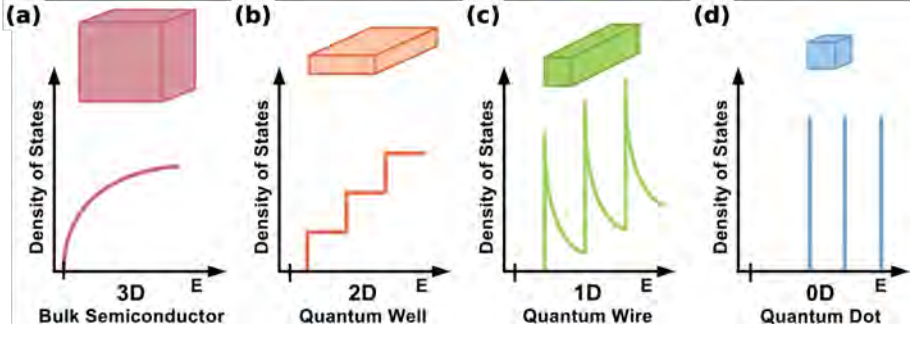

Figure 2.1: Qualitative representation of the density of states in 3D, 2D, 1D, and 0D semiconductors. Adapted from [17]

As the dimensionality is progressively reduced, the continuous bulk density of states is transformed into increasingly discrete energy spectra. In particular, two-dimensional quantum wells exhibit a step-like DOS associated with *sub-band* formation. Further confinement in one-dimensional quantum wires leads to a series of sharp features known as *van Hove singularities* [18]. In the zero-dimensional quantum dot limit, as we will thoroughly discuss in the next section, the DOS collapses into a set of discrete, atom-like energy levels. Additionally, because each confined degree of freedom introduces an increase

in energy given by (2.2), the bandgap shift increases as the dimensionality of the system decreases.

2.1.3 Excitons and quantum confinement

As mentioned at the beginning of this chapter, the promotion of an electron from the valence to the conduction band leaves behind a vacancy, or *hole*, that can interact with the electron via Coulomb attraction, forming a bound, hydrogen-like quasiparticle known as an *exciton*. To understand how excitons behave under quantum confinement, we must compare the confinement length with their *natural length scale*, the *exciton Bohr radius* [19], defined as:

$$a_X = \frac{4\pi\varepsilon_o\varepsilon\hbar^2}{\mu e^2} \tag{2.15}$$

where ε is the relative dielectric constant of the material and μ is the *reduced effective mass* of the electron-hole pair:

$$\mu = \frac{m_e m_h}{m_e + m_h} \tag{2.16}$$

We can therefore identify two limiting confinement regimes [20]:

- *Strong confinement*, when $d < 2a_X$: the confinement energy dominates over the Coulomb interaction between the electron and hole. The carriers behave essentially as independent particles in a potential well, and the bandgap shift follows the $1/d^2$ trend derived above;

- *Weak confinement*, when $d \gtrsim 2a_X$: the Coulomb attraction dominates over quantum confinement, and the electron and hole form a correlated exciton. Confinement still perturbs the energy levels, but the bandgap shift is much smaller, much less sensitive upon the confinement length, and does *not* follow a simple $1/d^2$ scaling.

In the extreme limit $d \gg 2a_X$, confinement becomes negligible, the semiconductor approaches its bulk electronic structure, and size-dependent changes in the bandgap vanish.

2.2 Quantum Dots

2.2.1 Colloidal quantum dots

We now restrict our focus to zero-dimensional, strongly confined semiconductor nanoparticles, commonly known as *quantum dots* (QDs). From now on, the term quantum dot will be used exclusively for nanoparticles in the *strong confinement regime*, while weakly confined zero-dimensional semiconductors such as the metal halide perovskites discussed later in this chapter will be referred to by the more generic term *nanocrystals*.

Quantum dots were independently discovered in the early 1980s, first by Ekimov [21] in a glass matrix, and shortly after by Henglein [22] in colloidal solution. Within a few years, Ekimov [23] and Brus [24] demonstrated for the first time that their optoelectronic properties depend on particle size, while Efros [25] established the first theoretical framework. A major breakthrough came in 1993, when Murray, Norris and Bawendi [26] developed a synthesis protocol yielding colloidal QDs with low size polydispersity ($< 10\%$) and dispersibility in nonpolar organic solvents. This method is widely regarded as a landmark in the field and, despite numerous advances leading to increasingly monodisperse materials with diverse compositions and improved optical performance, modern syntheses largely build upon that foundation. The immense impact of QDs in all fields of nanoscience was recognised in 2023, when the Nobel Prize in Chemistry was awarded to Bawendi, Brus and Ekimov *for the discovery and synthesis of quantum dots* [27].

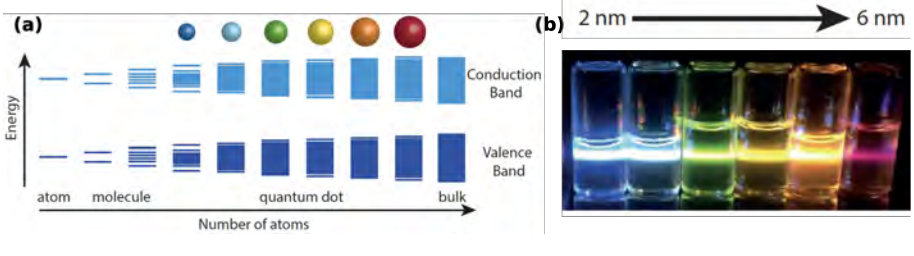

Figure 2.2: The size-dependent bandgap (a) of quantum dots regulates their photoluminescence emission (b) across the visible spectrum. Adapted from [28, 29]

The defining feature of quantum dots is their bright, size-tunable photoluminescence, which arises directly from strong quantum confinement. This prop-

erty underpins a wide range of applications, from bioimaging [30] and lasing [31] to commercial devices such as QLED televisions [32], where QDs serve as precisely engineered emitters that enable vivid, high-efficiency color displays.

2.2.2 The particle-in-a-sphere model

The simplest starting point for understanding the energy spectrum of quantum dots is the *particle-in-a-sphere* model, which extends the reasoning followed for quantum wells by (i) confining the particle in all three spatial dimensions and (ii) assuming spherical symmetry, an idealisation that reflects the roughly isotropic geometry of many colloidal QDs. Introducing spherical coordinates allows us to express the potential solely as a function of the radial coordinate:

$$V(r) = \begin{cases} 0\,, & r < a \\ +\infty\,, & r > a \end{cases} \tag{2.17}$$

where a is the radius of the QD. Owing to this spherical symmetry, the angular part of the wavefunction is described by spherical harmonics, while the radial part is expressed in terms of spherical Bessel functions [15]. Consequently, the eigenstates can be labelled by the familiar hydrogen atom quantum numbers $\{n, l, m_l\}$. Solving the Schrödinger equation with appropriate boundary conditions ($\Psi(r = a) = 0$) then yields:

$$\Psi_{n,l,m_l}(r, \vartheta, \varphi) = \frac{C}{r} j_l(k_{n,l}\, r)\, Y_l^{m_l}(\vartheta, \varphi) \tag{2.18}$$

where C is a normalisation constant, j_l is the spherical Bessel function of order l, $k_{n,l} = \alpha_{n,l}/a$ with $\alpha_{n,l}$ the n-th zero of j_l, and $Y_l^{m_l}$ are the spherical harmonics. The corresponding eigenenergies follow directly from the free-particle dispersion, evaluated at the quantised wavevectors:

$$E_{n,l} = \frac{\hbar^2 \alpha_{n,l}^2}{2 m_e a^2} \tag{2.19}$$

Introducing confinement along all spatial directions therefore leads to a fully discrete energy spectrum (see also panel (d) of Figure 2.1); for this reason, QDs are often referred to as *artificial atoms* [33–35].

As noted earlier, in the strong-confinement regime the Coulomb attraction between electron and hole is small compared to their respective confinement energies, which allows us to treat the two carriers as independent particles. With a

slight abuse of terminology, we will still refer to them collectively as an *exciton* or *electron–hole pair* (ehp). Within this approximation, the ehp wavefunctions can be written as the direct product of the single-particle wavefunctions:

$$\Psi_{ehp}(\boldsymbol{r_e}, \boldsymbol{r_h}) = \Psi^{(e)}_{n_e,l_e,m_{l,e}}(\boldsymbol{r_e})\Psi^{(h)}_{n_h,l_h,m_{l,h}}(\boldsymbol{r_h}) \tag{2.20}$$

while the Coulomb interaction can be accounted for by introducing a first order correction E_c to the eigenenergies:

$$E_{ehp}(n_e, l_e, n_h, l_h) = E_g + \frac{\hbar^2}{2a^2}\left\{\frac{\alpha^2_{n_e,l_e}}{m_e} + \frac{\alpha^2_{n_h,l_h}}{m_h}\right\} - E_c \tag{2.21}$$

where E_g is the bulk bandgap energy, and m_e and m_h indicate the effective masses of electrons and holes, respectively. Thus, according to the particle-in-a-sphere model, the energy levels of QDs are labelled by four quantum numbers (n_e, l_e, n_h, l_h). In real systems, however, the reduced symmetry and finite size lead to strong electron–hole exchange interactions and spin–orbit coupling, such that the appropriate total angular momentum quantum number is not l but $J = l + s$ (where s is the spin). For instance, the lowest-energy state of the CdSe QDs discussed below is typically denoted $1S_{1/2}(e), 1S_{3/2}(h)$.
While highly idealised, the particle-in-a-sphere model captures the key features of quantum confinement in QDs: confining charge carriers in all spatial directions results in a hydrogen-like ladder of discrete energy levels, and leads to an increase of the effective bandgap that scales as $1/d^2$ (in the effective-mass limit). Over the years, a number of more sophisticated theoretical approaches have been developed to describe real quantum dots with greater accuracy. These include $k \cdot p$ perturbation theory [36], as well as models based on the Luttinger Hamiltonian [37], the Kane model [38], and the Pidgeon–Brown model [39].

2.2.3 Exciton dynamics in quantum dots

To build an intuitive picture of carrier dynamics following photoexcitation in semiconductor quantum dots (QDs), consider a QD absorbing a photon with energy well above the bandgap (panel (a) of Figure 2.3), a common scenario in optical spectroscopy. This creates an electron and a hole in a highly excited (so-called hot) excitonic state. Following an extremely quick (few fs) dephasing [40], both carriers begin to relax toward their respective band edges,

losing excess energy predominantly through intraband phonon-mediated scattering [41, 42]. In bulk semiconductors, this thermalisation process typically completes within a few hundred femtoseconds owing to the quasi-continuous electronic density of states and the large phase space for carrier–phonon interactions [43]. In QDs, by contrast, the electronic spectrum is discretised by quantum confinement, and transitions between quantised levels must satisfy energy and symmetry selection rules [15, 41]. When the energy spacing between confined levels exceeds the optical phonon energy, single-phonon relaxation becomes inefficient, potentially leading to a phonon bottleneck [44] in which cooling is slowed to the picosecond regime. Whether the bottleneck is fully realised depends on the availability of multiphonon processes, carrier–carrier scattering, and surface-mediated channels, which can mitigate the slowdown.

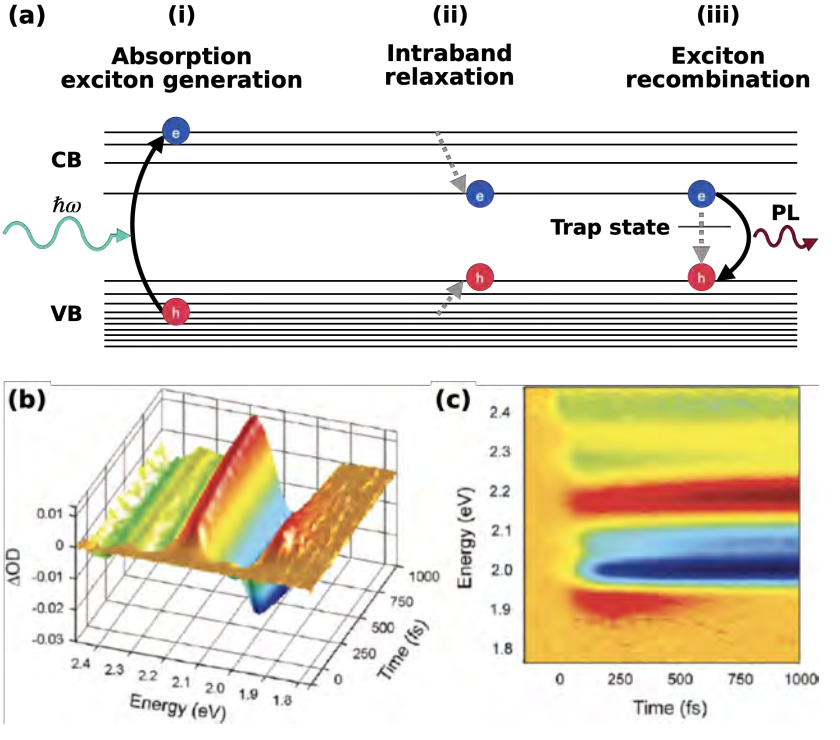

Figure 2.3: (a) schematic representation of exciton dynamics in QDs following photoexcitation; (b-c) transient absorption (TA) signal of colloidal QDs, evidencing PA and PB signals reconducible to state filling dynamics. Adapted from [41]

Because these dynamics occur on ultrafast timescales, techniques with femtosecond to picosecond resolution are required for direct observation. Ultrafast transient absorption (TA) spectroscopy [45], in which a pump pulse excites the system and a time-delayed probe pulse monitors spectral changes (see chapter 4), provides access to the evolving population across energy levels. As excited carriers occupy specific states, they block ground-state optical transitions into those states, giving rise to negative photoinduced bleaching (PB) signals at the corresponding transition energies, as shown in panels (b–c) of Figure 2.3 for strongly confined CdSe QDs. In parallel, positive photoinduced absorption (PA) signals arise from excited-state absorption pathways, yielding further signatures of population redistribution. The joint temporal evolution of PB and PA thus enables quantitative analysis of intraband relaxation (also referred to as *state filling*) as well as competing processes such as trapping and Auger recombination.

Once carriers reach the lowest-energy exciton manifold, several relaxation pathways compete. Ideally, recombination proceeds radiatively from optically allowed ("bright") states on nanosecond timescales, producing efficient photoluminescence [42]. However, nonradiative trapping at surface or interface defect states, and relaxation to optically forbidden ("dark") exciton states via exchange and spin–orbit interactions, can strongly modify emission dynamics [46–48].

2.2.4 Beyond single excitons

The discussion above is strictly valid for the dynamics of a single electron–hole pair. At higher excitation densities, multiple e–h pairs can be generated within a single nanocrystal. Coulomb interactions between carriers in this regime give rise to additional many-body states and decay channels that deviate substantially from the single-exciton case.

Biexcitons

A biexciton [49] consists of two excitons confined within the same nanocrystal and coupled via Coulomb interactions. Its total energy E_{XX} is not exactly twice the exciton energy E_X; instead, a biexciton binding energy comes into play, defined as:

$$\Delta_{XX} = E_{XX} - 2E_X \tag{2.22}$$

Such energy may be positive (net repulsion) or negative (net attraction), depending on screening, wavefunction overlap, shape anisotropy, and dielectric confinement. In strongly confined QDs, $|\Delta_{XX}|$ is typically on the order of a few to tens of meV. Consequently, biexciton radiative recombination produces photons slightly red- or blue-shifted relative to the single-exciton transition, and this shift gives direct access to the binding energy. As discussed in chapter 6, biexciton signatures can be isolated in TA spectroscopy even at low excitation fluences, because the pump and probe can sequentially populate one exciton each; tracking the biexciton feature over time enables the study of exciton–exciton correlations and relaxation.

trions and (charged) multiexcitons

A trion [50, 51] is a charged exciton comprising either two electrons and one hole (negative trion - X^-) or one electron and two holes (positive trion - X^+). Trions arise when the nanocrystal carries a net charge, which may occur through intentional doping, electrostatic gating, charging via charge-transfer processes, or localised trap states. Because of attractive Coulomb interactions within the three-particle complex, trions generally emit at lower energy than neutral excitons and often display reduced oscillator strength due to altered spatial distributions of carrier wavefunctions. Higher-order (neutral or charged) multiexciton states can be produced under sufficiently high excitation fluence or electrical injection, but are typically short-lived due to efficient nonradiative decay channels.

Nonradiative decay: Auger effect

In multiexcitonic states, the dominant decay pathway in strongly confined nanocrystals is often Auger recombination [52], in which the recombination energy of an e–h pair is transferred to a third carrier rather than emitted as a photon. The resulting hot carrier relaxes back to the band edge by phonon emission. The Auger rate increases strongly as nanocrystal volume decreases, making it highly efficient in the quantum-confined regime. As a result, Auger recombination severely limits multiexciton photoluminescence and presents a key obstacle for optical gain in colloidal nanocrystals. As discussed later in this chapter, an efficient strategy to limit Auger recombination is engineering core-shell quantum dot architectures with carefully crafted band alignment.

2.2.5 Case study: cadmium selenide QDs

We will now restrict our focus to cadmium selenide (CdSe) quantum dots. CdSe is widely regarded as an archetypal system for colloidal chalcogenide nanocrystals [53–56], owing to its well-established hot-injection synthesis [26], which enables the reproducible preparation of highly monodisperse QDs with high photoluminescence quantum yield. By tuning the particle diameter between approximately $1.5\,\mathrm{nm}$ and $7\,\mathrm{nm}$ (the exciton Bohr radius is $\approx 5.7\,\mathrm{nm}$), the effective bandgap can be varied from about $3.0\,\mathrm{eV}$ down to near the bulk value of $1.75\,\mathrm{eV}$, enabling efficient emission across the entire visible spectrum [54].

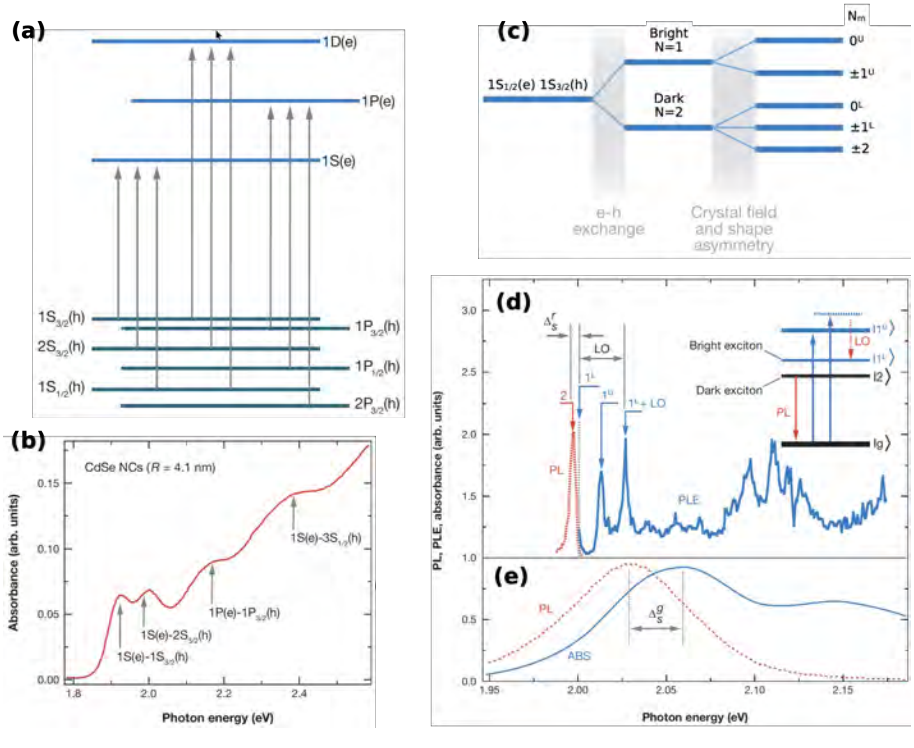

Figure 2.4: Left: (a) energy level diagram and (b) UV-Vis absorption spectrum of CdSe QDs; Right: (c) schematics of the band-edge fine structure splitting, (d) PL and PLE spectra recorded at $T = 10\,\mathrm{K}$, showing the fine structure, and (e) comparison betweeen the UV-Vis and PL spectra, highlighting the stokes shift. Adapted from [49]

Colloidal CdSe QDs typically crystallise in the wurtzite structure [57], a hexagonal lattice characterised by a polar crystallographic axis (the c-axis). In this structure, the conduction band minimum is well described by a single, nearly parabolic band and can be accurately modelled within the particle-in-a-sphere approximation. In contrast, the valence band exhibits a more complex structure arising from the coupling and mixing of three sub-bands, referred to as heavy-hole (hh), light-hole (lh), and split-off (so), induced by crystal-field splitting and spin–orbit interaction [58]. As a result, hole states are strongly mixed and cannot be assigned a single angular-momentum character. The resulting single-particle energy spectrum is schematically shown in panel (a) of Figure 2.4, while panel (b) displays a representative absorption spectrum of CdSe QDs (here with a mean radius of $4.1\,\mathrm{nm}$), featuring pronounced peaks corresponding to transitions between well-defined quantized states.

To fully elucidate the emission properties of CdSe QDs, it is necessary to analyse the fine-structure splitting of the band-edge exciton, conventionally denoted as $1S_{1/2}(e)\,1S_{3/2}(h)$ (see panels (c-e) of Figure 2.4). In the absence of interactions beyond quantum confinement, this excitonic state is eightfold degenerate, reflecting the twofold spin degeneracy of the electron and the fourfold degeneracy of the hole ground state. This degeneracy is first lifted by the electron-hole exchange interaction, which couples the electron and hole angular momenta and splits the band-edge exciton into a lower-energy state with total angular momentum $N = 2$ (five-fold degenerate) and a higher-energy (three-fold degenerate) one with $N = 1$ [59, 60]. Optical selection rules dictate that only exciton states with $N = 1$ carry a non-zero transition dipole moment and are therefore optically active (*bright*), whereas the $N = 2$ states are optically forbidden (*dark*) in the electric-dipole approximation.

In real CdSe QDs, the intrinsic anisotropy of the wurtzite crystal lattice, together with deviations from perfect spherical symmetry, further lifts the degeneracy within each manifold. As a result, the original eight excitonic states are reorganised into five energetically distinct levels, labelled by the projection N_m of the total angular momentum along the crystal c-axis (the states characterised by non-zero values of N_m are twofold degenerate). The lowest-energy level ($N = 2$, $N_m = \pm 2$) is strictly dark,whereas weakly allowed transitions emerge for some of the higher-lying states within the $N = 2$ manifold (notably, $\pm 1^L$), which acquire a finite oscillator strength due to valence-band

mixing and symmetry breaking.

This fine structure has two key consequences for the photophysics of CdSe QDs [49]. First, the energy splitting between the lowest dark exciton state ($|\pm 2\rangle$) and its nearest optically allowed counterpart ($\pm 1^L$) is typically in the range of $1 \div 10\,\mathrm{meV}$, implying that both states are thermally populated at room temperature, while at cryogenic temperatures the exciton population relaxes predominantly into the dark state. This leads to a pronounced slowing down of the photoluminescence decay upon cooling. Second, steady-state absorption at the band edge is dominated by higher-lying bright exciton states, whereas emission occurs from the lowest-energy exciton level. This imbalance gives rise to a substantial Stokes shift between absorption and photoluminescence. Such behaviour stands in sharp contrast to lead-halide perovskite nanocrystals, discussed later in this chapter, in which the absorbing and emitting states are separated by a much smaller energy gap and the resulting Stokes shift is typically almost negligible.

2.2.6 Core-shell quantum dots

Although high-quality synthesis protocols have greatly improved monodispersity and radiative efficiency in colloidal quantum dots, surface-related trap states remain a major limitation for both CdSe and other chalcogenide quantum dots [61]. The large surface-to-volume ratio of strongly confined QDs results in a high density of under-coordinated atoms and dangling bonds, which can introduce mid-gap electronic states. These trap states provide fast non-radiative recombination pathways that compete with radiative exciton decay, reducing photoluminescence quantum yield, shortening emission lifetimes, and in extreme cases even quenching emission entirely. To suppress these deleterious channels, core–shell architectures [62, 63] were developed. The basic idea is simple: passivate the core with an epitaxial inorganic shell whose lattice constant and band alignment are chosen to minimise strain, eliminate surface traps, and protect the exciton from the environment. When the shell is grown with good crystallographic matching and sufficient thickness, both trapping and blinking can be dramatically reduced, and photoluminescence quantum yields can approach unity [64]. Core–shell structures also provide a toolbox to deliberately engineer exciton localisation, separation, and recombination dynamics [29].

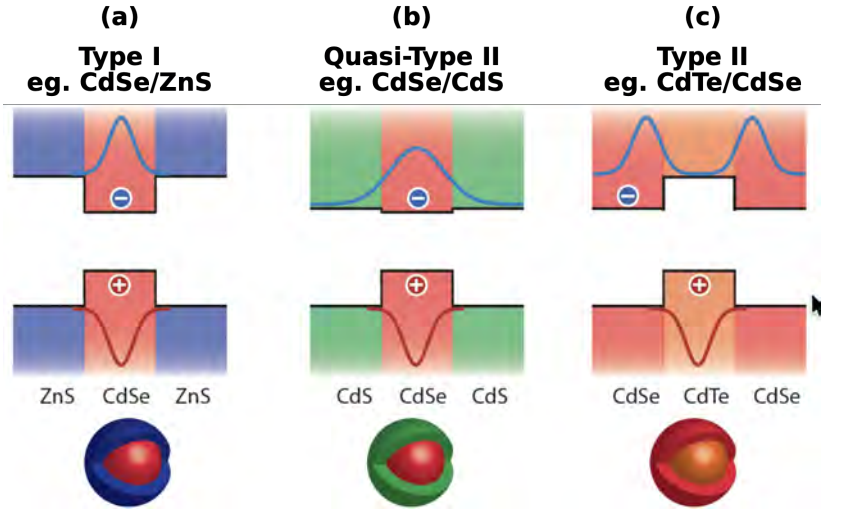

Figure 2.5: Relative bandgap positions and carrier localisation in type I, quasi-type II, and type II core-shell quantum dots. Adapted from [29]

Core-shell quantum dots (CSQDs) are commonly classified based on the relative positions of the core and shell band edges, as summarised in Figure 2.5. In particular, we distinguish [29, 63]:

- **Type I CSQDs**: the core bandgap lies completely within the shell one, resulting in both carriers being essentially confined to the core alone. This configuration minimises trap states and carrier delocalisation, resulting in near-unity quantum yields, and is commonly found in CdSe/ZnS and giant-shell CdSe/CdS QDs;
- **Quasi-Type II CSQDs**: here, the top of the core valence band lies well above the shell one, whereas the bottom of the two conduction bands virtually coincide. As a consequence, the hole stays confined within the core, while the electron delocalises over the whole QD. This partial delocalisation reduces electron-hole overlap, leading to longer exciton lifetimes and reduced Auger recombination. The CdSe/CdS CSQDs presented in chapter 5 and chapter 6 belong to this category.
- **Type II CSQDs**: here, the bandgaps are vertically shifted, so that the hole localises in the core and the electron in the shell. This band configuration strongly reduces the wavefunction overlap of the two charges,

further reducing the probability of recombination and extending the exciton lifetime, while also resulting in a drastic reduction of the radiative recombination rates.

It is also worth mentioning *Inverse Type I* and *Inverse Type II* configurations, which correspond to the same band-alignment principles but with the carrier localisation reversed with respect to the Type I and Type II structures. Albeit less common, these structures offer additional degrees of freedom for engineering charge separation, exciton diffusion, and interfacial recombination dynamics.

2.3 Quantum dot superparticles

2.3.1 From discrete states to minibands

Because quantum dots are frequently described as *artificial atoms*, their controlled assembly into mesoscopic superparticles (SPs) can be seen as the logical route to creating *artificial solids*. This picture is less naive than it seems: The cross-talk between neighbouring QDs within densely packed SPs results in a mixing of their discrete electronic states. This can ultimately lead to the formation of quasi-continuous bands (panels (a-b) of Figure 2.6), denoted as *minibands* [65, 66] to distinguish them from those resulting from the electronic coupling of atomic levels in natural solids. In principle, the formation of minibands allows charge carriers generated within a given QD to delocalise over the whole superparticle, leading to highly efficient charge transport properties and a profoundly different photocycle compared to that of the isolated QDs. In practice, however, the emergence of fully delocalised states is strongly constrained by the intrinsic polydispersity of the constituent QDs, which introduces two main sources of disorder. First, the bandgap dependence upon particle diameter in strongly confined QDs implies that size polydispersity generates energetic disorder (Figure 2.6(c)), producing energy offsets that carriers must overcome to *hop* between neighbouring QDs. It can be shown [67] that for a polydispersity of $\sim 6\%$, the resulting energetic disorder is already on the order of the thermal energy at room temperature. Secondly, polydispersity hampers optimal packing within the SP, increasing the average interparticle distance. This further suppresses electronic coupling, as carriers must tunnel through deeper potential barriers when transitioning between QDs. In addition

to these structural sources of disorder, surface trap states, whether arising from imperfect passivation or from ligand rearrangement during assembly, introduce nonradiative pathways that further localise carriers and quench delocalisation.

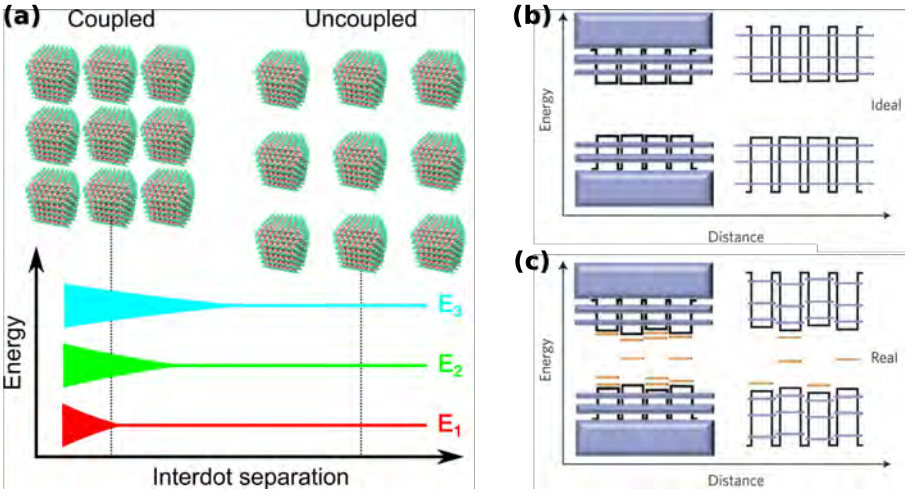

Figure 2.6: Miniband formation in ideal QD superstructures. (a) schematics of the energy spectrum of uncoupled and coupled QDs, highlighting the emergence of minibands; (b-c) electron and hole states in coupled and uncoupled ideal (b) and (c) real QD systems. Adapted from [66, 68]

These limitations notwithstanding, SPs undoubtedly represent a powerful platform for engineering collective behaviour. Even when full miniband formation is suppressed, partial electronic coupling, controlled interparticle distances, and the dielectric environment resulting from close-packing, can profoundly reshape exciton dynamics, carrier relaxation pathways, and optical and photonic responses. Moreover, advances in ligand exchange protocols, narrow-size syntheses, and directed self-assembly continue to push SPs closer to the regime where extended states and miniband-like features become experimentally accessible. As a result, QD superparticles provide a uniquely tunable mesoscale system in which the transition from discrete, molecule-like behaviour to collective, solid-like phenomena can be systematically explored. In the following sections, we will present the main assembly protocols employed to obtain QD superparticles, as well as some notable results regarding their photophysical and photonic properties.

2.3.2 QD superparticles: fabrication methods

QD thin films

Early efforts to organise colloidal QDs into ordered structures focused predominantly on quasi-two-dimensional (2D) thin films. These assemblies offered the first practical platform for probing collective effects emerging from controlled QD packing. Their fabrication typically relied on solution deposition methods in which solvent evaporation drives self-assembly. Among these, simple drop-casting [69] provided a convenient entry point, as it requires minimal control over processing conditions. More refined techniques such as dip-coating [70], spin-coating [71, 72], and doctor blading [73], introduced greater reproducibility and tunability, allowing precise control over film thickness, drying kinetics, and the degree of in-plane ordering. Together, these approaches established the foundational principles governing QD self-organisation in the solid state.

Three-dimensional QD superparticles

Building on these 2D paradigms, attention progressively shifted toward three-dimensional (3D) architectures, where electronic and optical coupling can develop throughout an entire volume. The most widespread and versatile route to such structures is *emulsion-templated assembly*, schematised in Figure 2.7. In this method, two immiscible liquid phases are combined: one containing the QDs and the other containing a suitable surfactant. Because QDs are typically dispersed in nonpolar organic solvents such as toluene, the second phase is most often aqueous, and the assembly method is referred to as *oil-in-water*. Vigorously mixing the two phases results in the formation of an *emulsion*, consisting of tiny droplets of the QD-rich organic phase, dispersed within the continuous aqueous phase and stabilised by surfactant molecules at the interface. As the solvent gradually evaporates or diffuses out of these droplets, their volume decreases and the QDs are forced into closer proximity. This controlled confinement drives them to pack into dense, spherical superparticles, whose final size reflects the initial droplet dimensions. The surrounding surfactant layer stabilises the resulting structures and prevents their coalescence or uncontrolled aggregation.

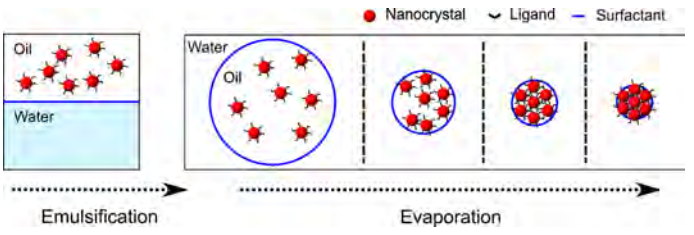

Figure 2.7: Working principle of oil-in-water emulsion-templated assembly. Adapted from [74]

While reliable and relatively straightforward, emulsion-templated assembly presents one notable limitation: the mean size and polydispersity of the resulting SPs are dictated by those of the initial emulsion droplets, whose formation is inherently stochastic. This randomness constrains the attainable monodispersity and limits reproducibility across batches. In addition, control over solvent removal is restricted, as evaporation or diffusion proceeds through the entire droplet population in an uncontrolled manner. As a result, tuning the internal packing density or crystallinity of the SPs is challenging, and subtle variations in temperature, mixing intensity, or surfactant concentration can lead to significant variations in the final structures.

The size and polydispersity issues can be overcome by employing a *microfluidic* setup [75, 76], which guarantees monodisperse droplets of controllable size. On the other hand, the densification kinetics can be steered by introducing a third phase, whose presence influences the pace at which the solvent exits the droplets. These two complementary approaches can be found in the *source-sink emulsion* method recently reported by Marino *et al.* [77] and depicted in Figure 2.8. Notably, this is the technique employed to prepare the SPs reported in chapter 5 and chapter 6.

First, a monodisperse toluene-in-water emulsion is generated using a microfluidic cross-junction. Each droplet contains a dispersion of QDs at a defined initial volume fraction and is stabilised in the aqueous continuous phase by a suitable surfactant (in this case, sodium dodecyl sulfate - SDS). These droplets constitute the *source* emulsion. Downstream, a second oil-in-water emulsion, formed by extended ultrasonication of hexadecane in an aqueous SDS solution, is introduced. This *sink* emulsion consists of droplets three orders of magnitude smaller than those of the source emulsion, and this imbalance drives the unidirectional transfer of toluene from the source droplets to the sink droplets.

Because toluene has a significantly higher aqueous solubility than hexadecane, solvent exchange proceeds efficiently: the sink droplets swell while the toluene droplets shrink, progressively densifying the QDs. Within minutes, the toluene phase is completely depleted and the contracted droplets solidify into dense, spherical QD superparticles.

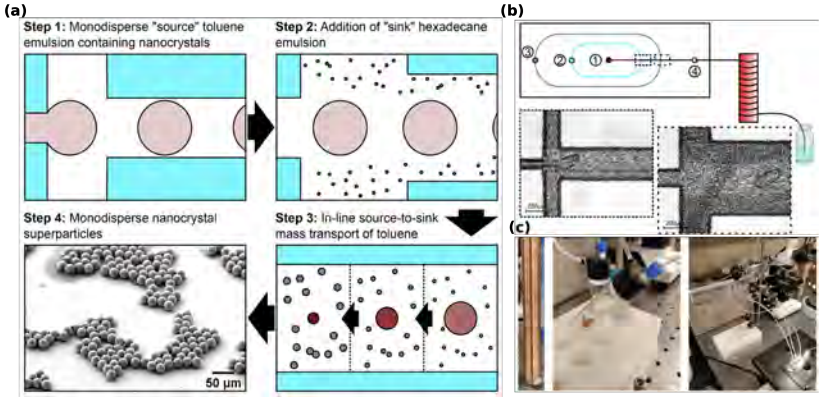

Figure 2.8: Source-sink emulsion assembly of monodisperse QD superparticles. (a) cartoon depicting the assembly protocol; (b) scheme of the microfluidics setup, the micrographs in the insets highlight the controlled droplet formation; (c) pictures of the assembly setup. Adapted from [77]

By controlling the relative flow rates of the two emulsions, their co-residence time in the heated tubing, the temperature (which accelerates toluene transport), and the initial QD volume fraction, the method yields high-quality micrometric superparticles with polydispersities as low as $1-2\,\%$ and tunable diameters, as summarised in Figure 2.9.

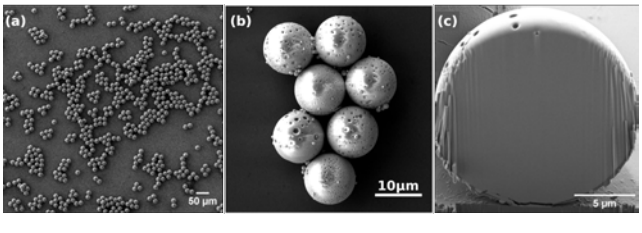

Figure 2.9: (a-b) SEM images of QD superparticles assembled via source-sink emulsion; (c) Cross-sectional SEM micrograph of a single SP obtained by focused ion beam (FIB) milling. Adapted from [77]

2.3.3 QD superparticles: collective optical response

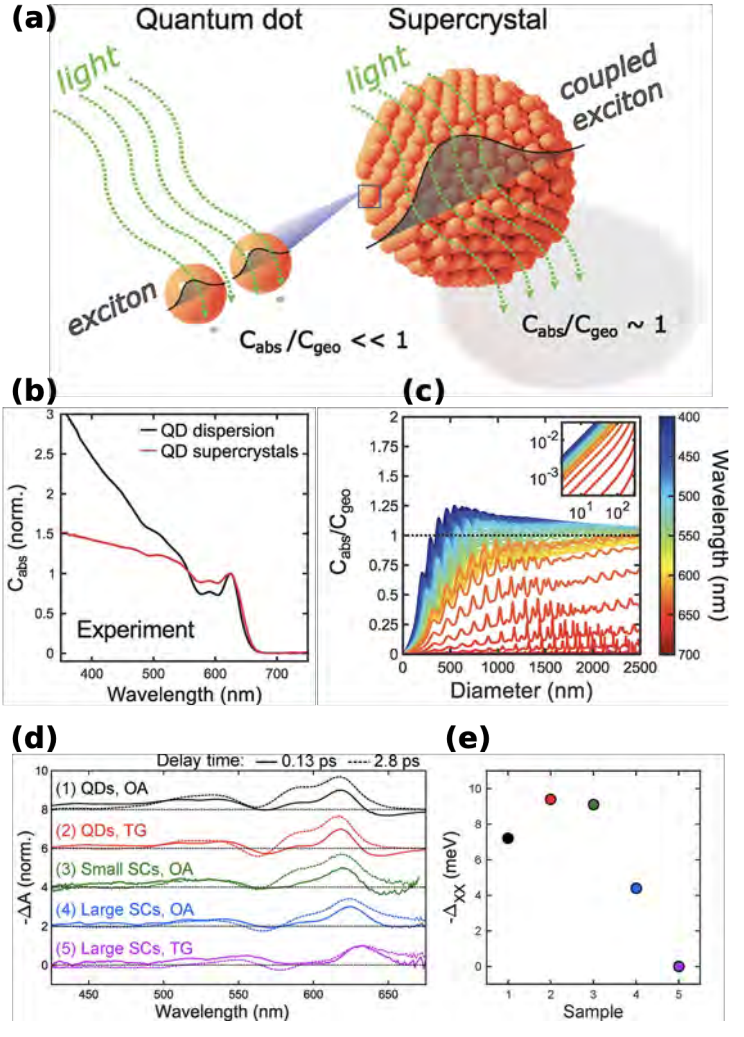

Figure 2.10: Exciton coupling in QD superparticles. (a) schematic representation of the interaction of light with dispersed QDs (left) and a QD superparticle (right); (b) experimentally measured absorption cross-sections of well-dispersed QDs and QD superparticles; (c) simulated ratio between the absorption (C_{abs}) and geometrical (C_{geo}) cross-sections, as a function of the particle diameter and of the incident wavelength; (d) transient absorption signals at two pump-probe delays for QDs and (small and large) SPs with two distinct ligands; (e) biexciton binding energies calculated from the TA spectra in panel (d). Adapted from [78]

As mentioned above, self-assembly often reshapes the photocycle of QDs, owing in general to a combination of cross-talk phenomena between the constituents and long-range effects enabled by the overall geometry of the superparticle [71, 79–83]. This is well exemplified in the study reported by Marino et al. [78], who investigated supraparticles (SPs) obtained by oil-in-water assembly of CdSe QDs. Their findings reveal two primary consequences of self-assembly, summarised in panel (a) of Figure 2.10. First, comparing the optical absorption spectra of isolated QDs and SPs (panel (b)) shows that SPs display a pronounced saturation of the absorbance at $\lambda < 500\,\mathrm{nm}$, whereas dispersed QDs exhibit a much more marked high-energy shoulder. This behaviour is clarified by first-principles modelling based on Mie theory [84] (panel (c)), which treats each SP as a dielectric sphere of QD-defined refractive index. The calculations demonstrate that, once the SP diameter exceeds the threshold for supporting higher-order Mie modes, its absorption cross-section approaches the geometrical cross-section of the entire supraparticle. In practice, this means that virtually every photon impinging on the SP is absorbed: a collective, emergent light-trapping capability inaccessible to individual QDs. The second major consequence of self-assembly concerns the excitonic dynamics within the SPs. Transient absorption measurements on size-selected SPs with two different ligands (panels (d-e)) reveal that, once QDs are densely packed into ordered supracrystals, their biexciton binding energy undergoes a marked reduction compared to isolated QDs, eventually approaching zero upon ligand shortening. This indicates that the pump-generated exciton can delocalise onto neighbouring dots on sub-picosecond timescales, thereby reducing its interaction with the probe-generated one. Such behaviour is absent in small aggregates, and cannot be attributed to differences in dielectric screening or intraband cooling rates. Instead, it emerges only when structural order and reduced interdot spacing jointly promote strong electronic coupling. In chapter 6 we will present a thorough comparison between the optical response of core-shell CdSe/CdS QDs and their superparticles. In comparison with the results discussed above, these SPs present a more complex photophysics by virtue of the core-shell nature of their consituents, enriching their cross-talk and influencing their photocycle.

2.3.4 QD superparticles as microresonators

Besides its influence on the photocycle of QDs, their assembly into spherical superparticles also opens an opportunity to exploit their geometry as *mesoscale optical resonators*. When the diameter of an SP reaches the micrometre range and the packing of the constituent QDs ensures a sufficiently high effective refractive index, the structure can sustain *whispering–gallery modes* (WGMs). The name "whispering gallery" originates from the celebrated acoustic effect in the dome of St. Paul's Cathedral in London, where a faint whisper spoken at one point of the circular gallery can be clearly heard at a distant point along the wall (panel (a) of Figure 2.11).

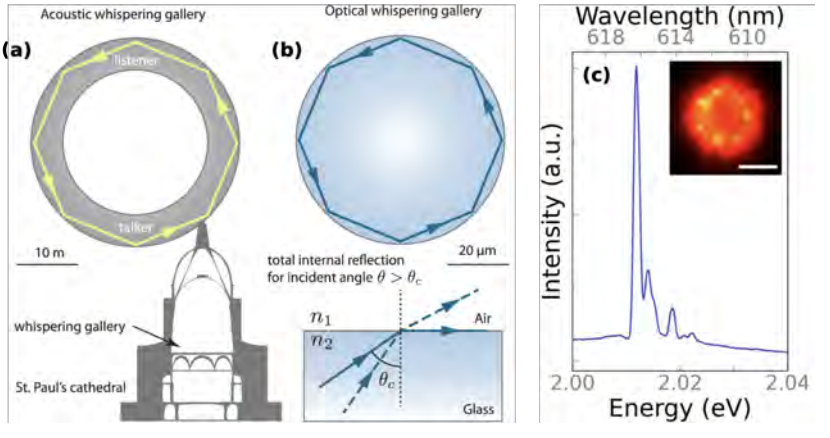

Figure 2.11: Quantum dot superparticles as active microresonators. (a-b) schematic representation of acoustic (a) and optical (b) whispering gallery mode resonances; (c) lasing spectrum of a single SP, shown in the inset (scale bar: 5 µm). Adapted from [85, 86]

In optical resonators (panel (b)), the same principle manifests as total internal reflection supported by the curvature and refractive-index contrast of the dielectric sphere, which traps light and produces standing electromagnetic waves near its surface. When such dielectric spheres are coupled to fluorophores whose emission overlaps spectrally with the WGM resonances, the resulting hybrids can lase efficiently because the resonator provides optical feedback while the fluorophore acts as the gain medium. In contrast with these hybrid systems, QD superparticles behave simultaneously as microresonators *and* gain media, making them *active microresonators*. The high emission effi-

ciency of the constituent QDs, together with the smooth, quasi-perfect spherical geometry enabled by advanced self-assembly techniques, make SPs particularly well suited for supporting cavity-enhanced emission and, under sufficient excitation, microlasing. This behaviour was recently demonstrated by Neuhaus *et al.* [86] for micrometre-sized CdSe/CdS SPs obtained through oil-in-water assembly (panel (c) of Figure 2.11). The inset, showing a micrograph of a single SP in the lasing regime, clearly reveals that the optical emission is concentrated near the particle's perimeter, consistent with its WGM origin. In chapter 5, we will investigate how photoexcitation modifies these WGM resonances, revealing new insight into their ultrafast dynamics. We will further show that optical coupling between the WGMs of neighbouring SPs enables efficient excitation transfer in dimer architectures.

2.4 Metal halide perovskite nanocrystals

Besides chalcogenide QDs, another class of semiconductor nanocrystals that has attracted considerable attention in recent years is that of metal halide perovskites (MHPs). The term *perovskite* originally referred to the naturally occurring mineral calcium titanate ($CaTiO_3$), discovered in the Ural Mountains by Gustav Rose in 1839 and named in honour of the Russian mineralogist Lev Perovski. In modern materials science, this term denotes a broad family of compounds adopting the same underlying crystal structure as $CaTiO_3$. This archetype, shown in panel (a) of Figure 2.12, can be described by the general formula ABX_3, where A is a monovalent cation (such as Cs^+, MA^+, or FA^+), B is a divalent metal cation (typically Pb^{2+} or Sn^{2+}), and X is a monovalent anion, most commonly a halide. Structurally, perovskites consist of a cubic or orthorhombic lattice of corner-sharing BX_6 octahedra (highlighted in pink in the scheme), with the A-site cations occupying the larger cavities at the centre of each octahedral cage.

All-inorganic caesium lead halides ($CsPbX_3$, where X = Cl, Br, or I) represent a particularly promising and widely studied class of MHPs, especially at the nanoscale, where they typically crystallise into *nanocubes*. $CsPbX_3$ nanocrystals have indeed attracted significative attention owing to their facile synthesis and advantageous optical and electronic properties. However, they are highly sensitive to moisture, which can rapidly compromise their structural integrity.

Figure 2.12 summarises the main properties of this class of NCs, which will be discussed in the following sections.

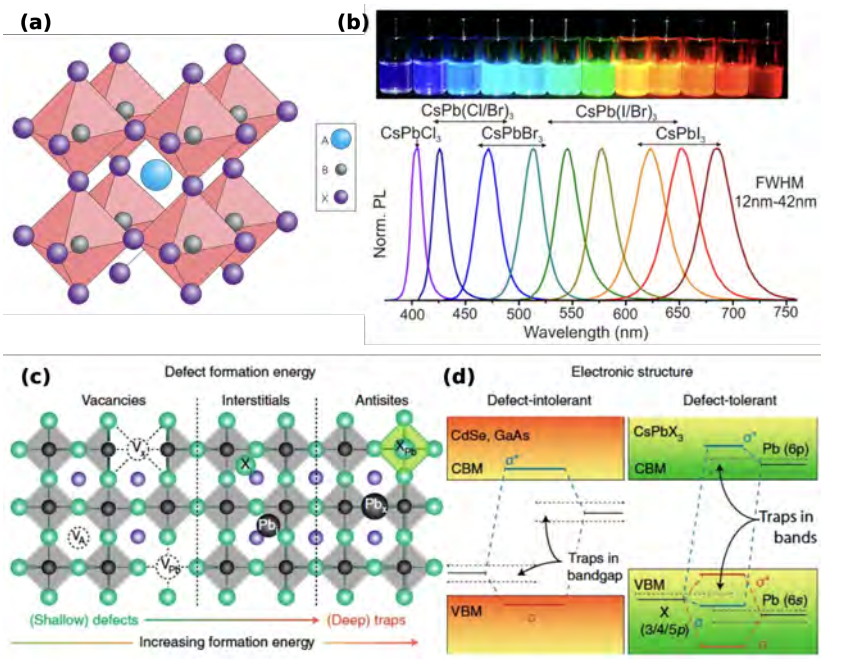

Figure 2.12: (a) crystal structure of metal halide perovskites; (b) luminescence under UV exposure (upper panel) and PL spectra (lower panel) of caesium lead perovskite nanocrystals with various halide compositions; (c) schematic representation of the various possible defects in perovskite NCs, ordered according to their formation energies; (d) qualitative comparison between the defect-intolerant chalcogenide QDs and the defect-tolerant MHPs. Adapted from [87–89]

2.4.1 Caesium lead halide NCs: synthesis

Colloidal $CsPbX_3$ nanocrystals can be prepared by several routes, both bottom-up and top-down, the most established being hot-injection [88] and ligand-assisted reprecipitation (LARP) [90]. In the hot-injection method, a caesium precursor is swiftly injected into a hot solution of lead halide and coordinating ligands, prompting rapid nucleation followed by controlled growth. This approach generally yields highly monodisperse nanocrystals with narrow emission linewidths and good batch-to-batch reproducibility, but it requires elevated temperatures, an inert atmosphere, and relatively strict control over precursor chemistry, impairing large-scale production. In contrast, LARP is car-

ried out at room temperature by mixing precursor solutions in polar and nonpolar solvents in the presence of surface ligands. It is operationally simple, scalable, and tolerant to ambient conditions, making it attractive for large-area or high-throughput processing. However, LARP often produces broader size distributions and nanocrystals that contain more ionic residues or loosely bound ligands, which can compromise stability and photoluminescence compared to hot-injection products.

2.4.2 $CsPbX_3$ NCs: optical properties

A key feature of $CsPbX_3$ NCs is that their bandgap (and, consequently, their optical absorption and emission properties) depends primarily on the nature of the halide anions. As illustrated in panel (b) of Figure 2.12, $CsPbCl_3$, $CsPbBr_3$, and $CsPbI_3$ nanocrystals emit in the blue, green, and red regions of the spectrum, respectively. Mixed-halide compositions obtained via partial halide exchange show intermediate emission wavelengths [88, 91]. This behavior reflects the intermediate-to-weak quantum confinement regime typical for these NCs: their exciton Bohr radius is comparable to or smaller than the NC size, so size-dependent shifts in the electronic levels are modest, and the bandgap is predominantly dictated by the halide-dependent orbital energies. Furthermore, and in stark contrast with conventional chalcogenide QDs, $CsPbX_3$ NCs exhibit a bright band-edge exciton. This behaviour arises from a combination of factors. First, the intermediate-to-weak quantum confinement regime limits the splitting of the band-edge exciton fine structure. Second, and more fundamentally, the electronic structure of metal halide perovskites plays a decisive role: the conduction band minimum is primarily derived from Pb $6p$ orbitals, while the valence band maximum originates from antibonding hybridised Pb $6s$–halide p states. This strong spin–orbit coupling, together with the orbital composition of the band edges, results in optically allowed interband transitions and suppresses the formation of a dark exciton state [91, 92]. As a consequence, absorption and emission both originate from the same bright excitonic transition, leading to a very small Stokes shift (often $< 10\,\mathrm{nm}$). The intrinsically bright nature of the lowest-energy exciton underpins the high photoluminescence quantum yields typically observed in colloidal perovskite NCs and enables strong resonant dipole–dipole interactions, which are central to many collective optical phenomena in closely packed assemblies, as discussed

in the next section.
Another important aspect distinguishing $CsPbX_3$ NCs from conventional chalcogenide QDs is their unusually high defect tolerance [89]. As shown in panel (c) of Figure 2.12, common point defects such as vacancies, interstitials, and antisites tend to introduce electronic states lying within the bands or very close to their edges. These so-called shallow traps do not efficiently capture charge carriers at room temperature and therefore have a limited impact on radiative recombination. This defect tolerance extends to the NC surface, where undercoordinated ions and ligand-induced imperfections rarely generate deep midgap states. As a result, surface defects do not typically introduce long-lived non-radiative pathways or dark emissive states, in sharp contrast to chalcogenide QDs, where surface traps often dominate the recombination dynamics. This intrinsic resilience against defect-induced quenching is a key factor behind the robust optical performance of $CsPbX_3$ NCs, even in the presence of relatively weakly coupled ligand shells.

2.5 Perovskite nanocrystal superstructures

2.5.1 Assembly strategies and superstructure morphology

Akin to their chalcogenide counterparts, the electronic and optical properties of colloidal $CsPbX_3$ NCs make them promising building blocks for functional assemblies. However, unlike quasi-spherical QDs, their sharp-edged cubic morphology introduces additional complexity in the short-range interactions that drive self-assembly, strongly influencing the geometry and ordering of the resulting superstructures, as illustrated in Figure 2.13.
Emulsion-based assembly techniques typically yield spheroidal superparticles, which often exhibit suboptimal packing due to the isotropic nature of the emulsion environment [93]. In contrast, controlled solvent evaporation on a substrate allows the NCs to pack more efficiently, maximizing NC–NC contacts and promoting the formation of well-defined *supercubes* [94]. This method has gained prominence in recent years, as many collective properties of perovskite superstructures, such as enhanced exciton coupling and coherent light emission, benefit from the strong interparticle interactions enabled by optimal packing.

Indeed, perovskite supercubes (SCs) with lateral dimensions reaching several tens of micrometers have been successfully assembled in various studies [95–98].

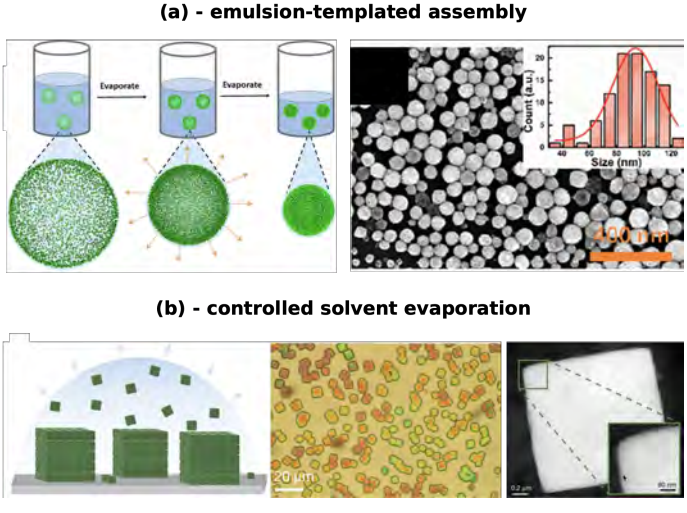

Figure 2.13: Assembly schematics and micrograph of $CsPbBr_3$ superstructures assembled by emulsion-based (a) and slow solvent evaporation (b) protocols. Adapted from [93, 94]

The geometry and packing of NCs within these superstructures critically determine their collective properties. Sharp-cornered cubes favor face-to-face alignment, enhancing orbital overlap and facilitating exciton delocalization, while the high degree of structural order suppresses defects that could otherwise act as nonradiative recombination centers. In the following section, we discuss some of the most prominent collective electronic and optical behaviors exhibited by $CsPbX_3$ SCs, which have attracted considerable interest in recent literature.

2.5.2 Collective electronic and optical behaviour

Excitonic coupling and carrier mobility

As already discussed for chalcogenide QD superparticles, reducing the interparticle spacing strengthens electronic coupling by allowing partial overlap of carrier wavefunctions. In $CsPbX_3$ SCs this effect is more pronounced, because their defect-tolerant electronic structure and the weak size-dependence of the bandgap minimise energetic disorder, which is often the main limitation in

conventional QD solids. When the assembly protocol yields highly ordered supercubes, the resulting translational symmetry increases the coherence of inter-NC interactions, enabling collective electronic states that extend beyond individual NCs. Indeed, it has been reported [99] that perovskite superstructures exhibit red-shifted absorption and emission peaks with respect to those of the constituent NCs, coherently with miniband formation (panel (a) of Figure 2.14), and that ordered SCs present impressive exciton diffusion lengths compared with randomly packed NCs [100, 101], indicating that structural order directly improves electronic performance. This property is particularly relevant for optoelectronic applications such as photodetectors, solar cells, and light-emitting devices, where efficient exciton or carrier transport is essential for device functionality.

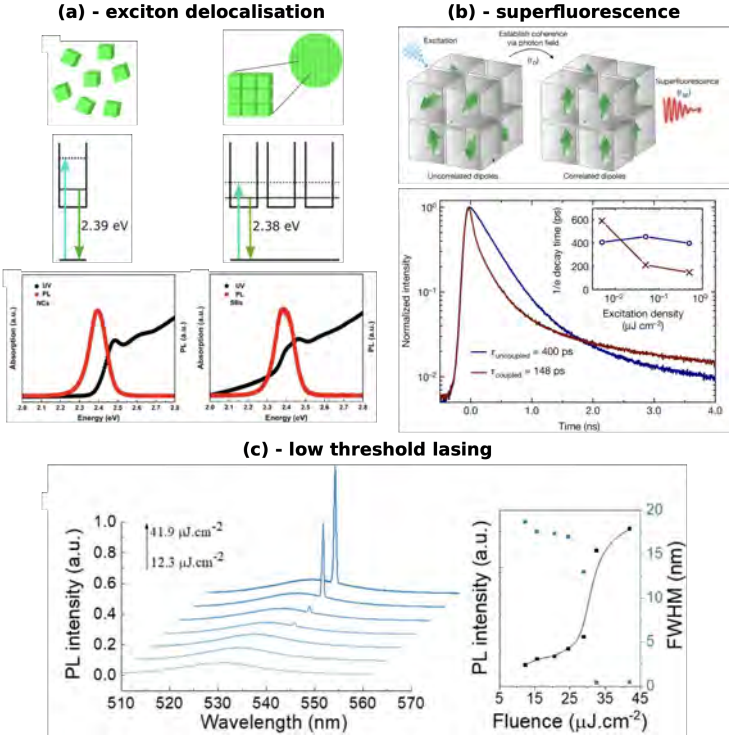

Figure 2.14: Collective behaviour of perovskite SCs: (a) exciton delocalisation, (b) superfluorescence, and (c) low threshold lasing. Adapted from [94, 99, 102]

Cooperative emission: superfluorescence

The strong inter-NC coupling discussed in the previous subsection does not only enhance transport; under suitable conditions, it also allows the optical dipoles of many NCs to interact coherently. A prominent example is the observation of superfluorescence (SF) in $CsPbX_3$ superlattices, reported in detail by Rainò *et al.* [94] and summarised in panel (b) of Figure 2.14. In SF, an ensemble of emitters that is initially incoherent undergoes spontaneous phase synchronization through dipole–dipole interactions and releases a delayed, intense optical burst whose characteristics reflect collective, rather than single-particle, dynamics: neighbouring NCs emit as a single, *giant* dipole. The requirements for SF mirror those enabling strong excitonic coupling in ordered SCs: narrow inhomogeneous linewidths, uniform NC transition energies, and precise translational ordering that supports long-range dipole coupling. These conditions are naturally met in perovskite supercubes assembled with tight face-to-face alignment. However, low temperatures remain necessary to limit phonon-driven dephasing, which would strongly impair SF.

Low-threshold lasing

Beyond exciton delocalisation and cooperative emission, the strong electronic cross talk and high structural order of perovskite SCs also enable low threshold lasing [102]: $CsPbX_3$ NCs possess an optically bright lowest exciton with large oscillator strength, and when assembled into ordered supercubes the reduced energetic disorder and partial inter NC coupling suppress nonradiative relaxation pathways, allowing a dense population of bright excitons to accumulate and favouring amplified spontaneous emission at comparatively low pump fluences. Additionally, it has been demonstrated [103] that single $CsPbX_3$ NCs act as Fabry-Perot resonating cavities by virtue of their sharp cubic shape. This effect could be enhanced in ordered supercubes, further lowering the lasing threshold.

In chapter 7, we will employ a recently proposed refinement on the slow evaporation protocol to produce high quality, micrometric $CsPbBr_3$ SCs, unravelling the kinetics of the assembly process by a combination of structural and optical characterisation techniques.

2

3

Metal Nanocrystals and Superstructures

Nanoparticles are everywhere. You eat them, drink them, breathe them, pay to have them, and pay even more to get rid of them.

— Alexandra Navrotsky

This chapter delves into the intriguing properties of metals at the nanoscale, ranging from plasmonic nanoparticles to ultrasmall nanoclusters. The fundamental properties of these two distinct classes of nanometals will be discussed, along with their most common applications. Additionally, we will explore the possibilities offered by self-assembly in expanding those properties and enabling the emergence of novel behaviors. The final aim of this chapter is to provide the theoretical framework and an overview of the state of the art for the contextualization of the specific results presented in chapter 8 and chapter 9.

3.1 Metals at the Nanoscale

The significant attention drawn by metal-based nanomaterials in the last few decades can be largely attributed to the plethora of different behaviors they manifest. Indeed, while bulk metals are characterized by high reflectivity and excellent electrical and thermal conduction properties, metals at the nanoscale deviate fundamentally from bulk behavior and display a variety of size-dependent optical and electronic responses, as schematized in Figure 3.1.

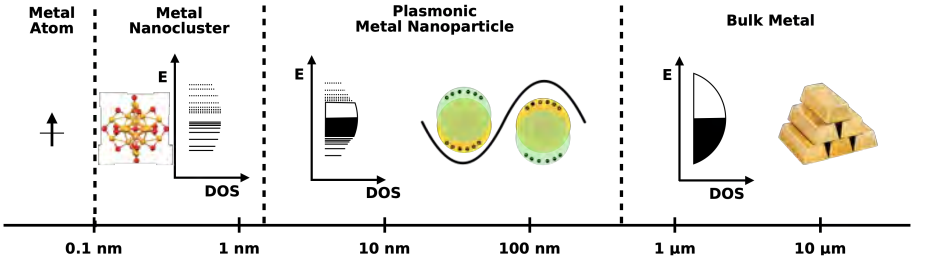

Figure 3.1: Outline of the properties of metals at varying length scales, ranging from single atoms to bulk metals. Image adapted from [104]

These interesting properties emerge when metals are reduced to sub-micrometre dimensions. In the larger-nanoparticle regime (tens to thousands of nanometers), the high surface-to-volume ratio dictates the emergence of Localized Surface Plasmon Resonance (LSPR). LSPR dominates the interaction between the nanoparticle and the electromagnetic field, leading to intense absorption, scattering, and field-enhancement capabilities. As the size decreases below a few nanometers, plasmonic resonance gives way to the quantum confinement-dominated, molecule-like behavior characterizing metal nanoclusters. These atomically precise arrangements constituted by up to a few hundred atoms, often protected by a ligand shell, display pronounced photoluminescence emission. In the following sections, these two primary regimes - plasmonic nanoparticles and atomically precise nanoclusters - will be examined in detail, followed by an exploration of the possibilities offered by their self-assembly into functional superstructures.

3.2 Plasmonic Metal Nanoparticles

3.2.1 Plasmon resonance

In order to understand plasmon resonance in metal nanoparticles, we must start by considering the Drude-Lorentz free electron model [5], according to which the equation of motion for conduction electrons within a bulk metal under an oscillating electric field reads:

$$m^*\ddot{\mathbf{x}} + m^*\gamma\dot{\mathbf{x}} = -e\mathbf{E}(t) = -e\mathbf{E_o}e^{-i\omega t} \tag{3.1}$$

where m^* is the material-dependent effective electron mass, ω is the frequency of the oscillating field, and γ is a damping factor accounting for the presence of the metal lattice. Solving this equation, we obtain:

$$\mathbf{x}(t) = \frac{e}{m^*\left(\omega^2 + i\gamma\omega\right)}\mathbf{E}(t) \tag{3.2}$$

From (3.2) we can calculate the relative dielectric function $\varepsilon_r(\omega)$ as:

$$\varepsilon_r(\omega) = 1 - \frac{Nex}{\varepsilon_o E} = 1 - \frac{Ne^2}{\varepsilon_o m^*}\frac{1}{\omega^2 + i\gamma\omega} \tag{3.3}$$

where N represents the concentration of conduction electrons. By introducing the *plasma frequency*, ω_p, defined as:

$$\omega_p = \sqrt{\frac{Ne^2}{\varepsilon_o m^*}} \tag{3.4}$$

we can rewrite (3.3) in the form:

$$\varepsilon_r(\omega) = 1 - \frac{\omega_p^2}{\omega^2 + i\gamma\omega} \tag{3.5}$$

In the low damping limit, $\gamma \ll \omega$, (3.5) becomes:

$$\varepsilon_r(\omega) = 1 - \frac{\omega_p^2}{\omega^2} \tag{3.6}$$

The plasma frequency represents the natural frequency of collective oscillations of the electron gas against the positively charged ionic background. This can be illustrated by considering a metallic slab of thickness d and assuming

that the conduction electrons are rigidly displaced by a distance x perpendicular to the slab. Such a displacement produces surface charge densities $\pm\sigma$, with

$$\sigma = Nex. \tag{3.7}$$

The resulting internal electric field is $E = \sigma/\varepsilon_0$, which exerts a restoring force on the electrons. Their equation of motion then reads

$$m^*\ddot{x} = -eE = -\frac{Ne^2}{\varepsilon_0}x. \tag{3.8}$$

Solving (3.8) shows that the electrons undergo harmonic oscillations with angular frequency ω_p. The quanta associated with these collective charge-density oscillations are known as *plasmons*.
Notably, to fully represent the optical response of metals across the whole spectrum, (3.5) should be modified by also taking into account inter-band absorption features [105], such as the one stemming from the $5d \mapsto 6s$ transition that gives bulk gold its characteristic yellow colour. Therefore, a more complete version of (3.5) should have the form:

$$\varepsilon_r(\omega) = \varepsilon_{ib} + 1 - \frac{\omega_p^2}{\omega^2 + i\gamma\omega} \tag{3.9}$$

Plasmon resonance manifests itself in different ways depending on the dimensionality of the system, as summarised in Figure 3.2.

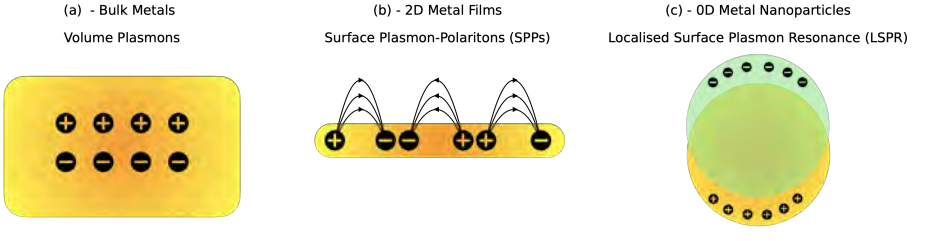

.

Figure 3.2: Schematic representation of plasmon resonance in bulk, 2D, and 0D metals. Image adapted from [106]

Bulk metals support *volume plasmons* (panel (a)), corresponding to longitudinal collective oscillations of the conduction-electron density throughout the

material. As discussed in the previous section, these oscillations occur at the plasma frequency ω_p, which is set by the electronic properties of the metal. Because volume plasmons are purely longitudinal excitations, they cannot be directly excited by light, which carries a transverse electromagnetic field. When electromagnetic retardation is taken into account, longitudinal plasma oscillations can hybridize with transverse electromagnetic waves, giving rise to bulk plasmon–polaritons; however, in metals these hybrid modes occur at frequencies close to ω_p and play only a marginal role in the optical response relevant to the present discussion. The plasma frequency nevertheless leaves a clear fingerprint in the optical properties of bulk metals: since the complex refractive index is related to the dielectric function as $\tilde{n} = n + ik = \sqrt{\varepsilon_r}$, (3.6) shows that metals are highly reflective for $\omega < \omega_p$ (negative ε_r, imaginary $\tilde{n}$), whereas they become transparent for $\omega > \omega_p$ (positive ε_r, real $\tilde{n}$).

In two-dimensional metallic films or at extended metal–dielectric interfaces, plasmonic excitations take the form of *surface plasmon polaritons* (SPPs, panel (b)) [107], hybrid light–matter modes arising from the coupling between surface charge-density oscillations and an electromagnetic field bound to the interface. These modes propagate along the interface and are characterized by an in-plane wavevector that is larger than that of a freely propagating photon at the same frequency. As a result, direct excitation of SPPs by far-field light is not possible in planar, translationally invariant systems, as the required in-plane momentum cannot be supplied by the incident radiation.

Finally, 0D metal nanoparticles (NPs) support localised surface plasmon resonance (LSPR - panel (c)). Akin to SPPs, LSPR is a coherent oscillation of surface electrons; however, because of the reduced dimensionality of NPs, LSPR is unable to propagate, remaining - as its name implies - localised over the surface of the NP. In the following, the characteristics of LSPR will be examined in detail.

3.2.2 Localised surface plasmon resonance (LSPR)

The hallmark of LSPR is that it can be directly excited by light, unlike volume plasmons or SPPs, as it corresponds to a *transverse* oscillation of the conduction electrons on the surface of a nanoparticle. This gives rise to a pronounced resonance peak in the extinction (absorption plus scattering) spectrum of the NP.

To understand the origin of this resonance, let us consider a spherical NP whose diameter is much smaller than the wavelength of the incident light ($d \ll \lambda$). In this regime, the dipole approximation applies: the incident electric field can be considered essentially uniform across the NP, and the NP responds as a single oscillating dipole. The induced dipole moment $\mathbf{p}$ is then proportional to the incident field $\mathbf{E_0}$:

$$\mathbf{p} = \alpha \mathbf{E_0} \tag{3.10}$$

where α is the NP polarizability, which quantifies how easily the electron cloud is displaced relative to the positively charged lattice. For a spherical NP of radius $a = d/2$ and dielectric function $\varepsilon_p(\omega)$, embedded in a medium of permittivity ε_m, it can be demonstrated [108] that:

$$\alpha = 4\pi\varepsilon_p(\omega)\varepsilon_m a^3 \frac{\varepsilon_p(\omega) - \varepsilon_m}{\varepsilon_p(\omega) + 2\varepsilon_m} \tag{3.11}$$

Thus, the maximum induced dipole moment is attained at a frequency ω_r such that:

$$\mathrm{Re}\left[\varepsilon_p(\omega_r)\right] = -2\varepsilon_m \tag{3.12}$$

This is commonly referred to as the *Fröhlich condition* [109], and the corresponding frequency can be computed from (3.6) and (3.12), yielding:

$$\omega_r = \frac{\omega_p}{\sqrt{1 + 2\varepsilon_m}} \tag{3.13}$$

An especially important consequence of LSPR is the phenomenon of *near-field enhancement*: the collective oscillation of conduction electrons at the NP surface leads to a strong enhancement of the incident electromagnetic field, resulting in local field intensities in the immediate vicinity of the NP that can exceed the driving field by orders of magnitude. Indeed, it can be shown that the total electric field (incident plus induced), reaches its maximum value at the surface of the NP, where:

$$\mathbf{E_{max}} = \frac{3\varepsilon_p(\omega)}{\varepsilon_p(\omega) + 2\varepsilon_m}\mathbf{E_o} \tag{3.14}$$

For example, as displayed in panel (c) of Figure 3.3, simulations of a single $5\,\mathrm{nm}$ gold nanoparticle (AuNP) in air, excited at its LSPR wavelength

($521\,\mathrm{nm}$), show that the local field amplitude near the particle is about six times larger than the incident field, corresponding to a 36-fold increase in field intensity. Experimentally, a colloidal suspension of 5 nm gold nanoparticles exhibits a clear absorption peak at $\sim 520\,\mathrm{nm}$, alongside interband absorption at shorter wavelengths (panel (b)), which explains its ruby red colour (panel (a)).

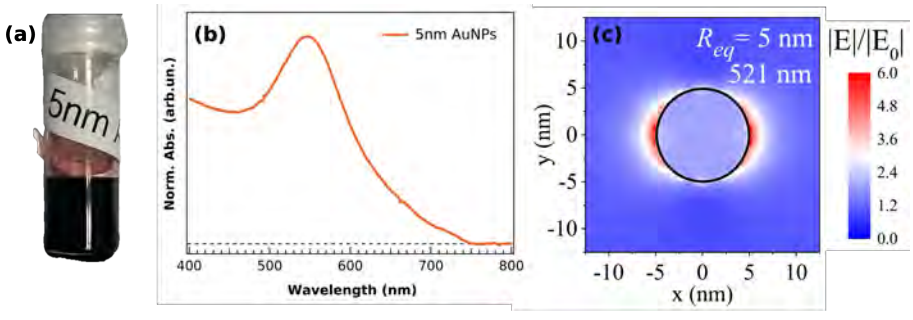

Figure 3.3: (a) concentrated colloidal suspension of 5nm gold nanoparticles; (b) Absorption spectrum of the same nanoparticles; (c) simulated near-field enhancement for a single 5nm gold nanoparticle in air (adapted from [110]).

The key feature of LSPR, underpinning many of its applications, is its sensitive dependence upon a number of parameters, as discussed in detail in the following section.

3.2.3 LSPR: driving factors

NP composition and size

As mentioned earlier, the chemical composition of the NP directly influences its plasmon resonance (see panel (a) of Figure 3.4), as both the effective electron mass, electron density, and damping ratio are material-dependent. For instance, silver NPs (AgNPs - panel (b)) typically showcase LSPR around $400\,\mathrm{nm}$, while the abovementioned AuNPs (panel (c)) are characterized by resonances near $500\,\mathrm{nm}$. The difference in resonance position is clear when observing the colours of colloidal suspensions of AgNPs and AuNPs, as shown in the insets of panels (b-c).

Size also plays an important role in determining the plasmonic response of NPs. For very small NPs ($d \leq 10\,\mathrm{nm}$), quantum confinement and surface scattering broaden the resonance and reduce field enhancement, culminating in

the total disappearance of LSPR in nanoclusters. As the particle size increases, the LSPR profile will change as a consequence of the varying ratio between absorption and scattering cross section. Indeed, it can be shown that the former scales with d^3, while the latter is proportional to d^6. Therefore, the larger the particle the more dominant scattering becomes, as exemplified in panels (d-f) of Figure 3.4. Finally, for even bigger NPs, the dipole approximation is no longer valid, and multipolar oscillation components - or *phase retardation* effects - emerge (see scheme in panel (g)), generally resulting in a broadening and redshift of the LSPR peak.

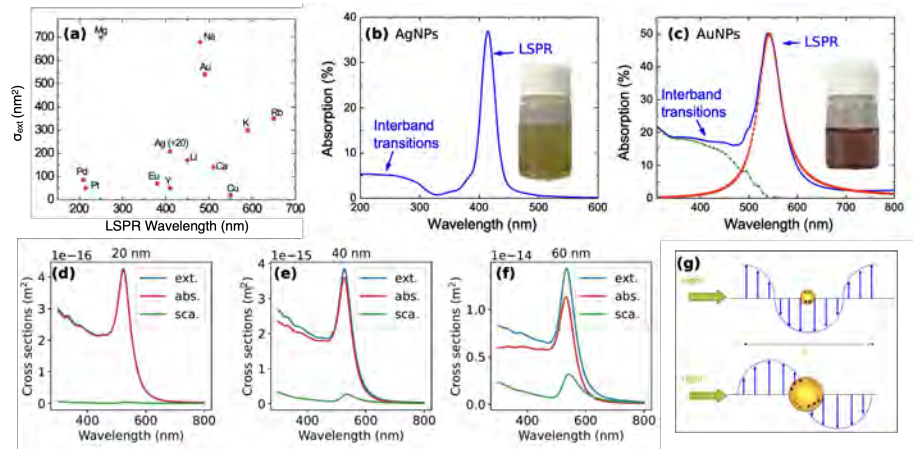

Figure 3.4: Top row - LSPR vs composition: (a) LSPR wavelength and corresponding extinction cross sections for 10 nm NPs of various metals; (b-c) absorption spectra of colloidal suspensions (shown in the insets) of (b) 40 nm AuNPs and (c) 40 nm AgNPs; Bottom row - LSPR vs size: (d-f) simulated absorption, scattering, and extinction spectra for 20 nm (d), 40 nm (e), and 60 nm (f) AuNPs; (g) schematic representation depicting the deviation from the dipole approximation as the NP size increases. Adapted from [106, 111]

NP geometry

Beyond size, the shape of nanoparticles exerts a decisive influence on their plasmonic response. As shown in panels (a–b) of Figure 3.5, deviations from spherical symmetry lift the degeneracy of the dipolar resonance and give rise to multiple plasmon modes, whose spectral positions and relative intensities depend sensitively on the particle's aspect ratio.

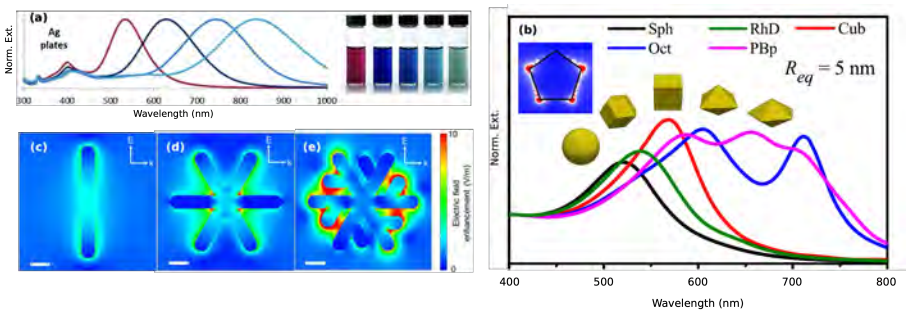

Figure 3.5: (a) normalised extinction spectra of colloidal suspensions of Ag plates of different sizes (shown on the right); (b) normalised extinction spectra of AuNPs of different shapes (sphere, rhombic dodecahedron, cube, octahedron, and pentagonal bipyramid) with an equivalent radius of 5 nm. The inset shows the near-field enhancement of the pentagonal bipyramid along its equatorial plane; (c-e) near-field enhancement of single (c) and branched (d-e) nanorods. Adapted from [110, 112, 113].

Thus, even for nanoparticles of identical equivalent size, the optical response can be tailored by morphology, making shape control a powerful strategy for engineering plasmonic properties. In particular, anisotropic geometries such as cubes, octahedra, and bipyramids feature sharp edges, vertices, and facets that concentrate charge density (*lightning-rod effect*) and act as localized *hot spots* for field enhancement (see inset of panel (b)). The impact of morphology on near-field behaviour is further highlighted in panels (c–e), where complex branched structures exhibit much stronger electric field localization than simple rod-like counterparts. Such enhancements not only broaden the accessible spectral range but also provide unique opportunities for applications in sensing, nonlinear optics, and nanoscale light–matter interactions [110, 112].

Surrounding environment

Since the Fröhlich condition directly involves the dielectric constant of the surrounding medium (ε_m - see equation (3.12)), the LSPR frequency is highly sensitive to changes in the NP environment. As exemplified for aluminum nanoparticles (AlNPs) in panel (a) of Figure 3.6, increasing ε_m results in a red-shift, broadening and damping of the LSPR. This sensitivity originates from the plasmonic near-field enhancement, which is strongly localized at the nanoparticle surface and rapidly decays with distance. As a result, its entity is mainly determined by the dielectric properties of the immediate surroundings

of the NP. Panels (b–c) of Figure 3.6 illustrate this point: even a few molecular layers (hence, only a few Å) of a dielectric shell are sufficient to produce a noticeable red-shift in the LSPR of AgNPs and AuNPs.

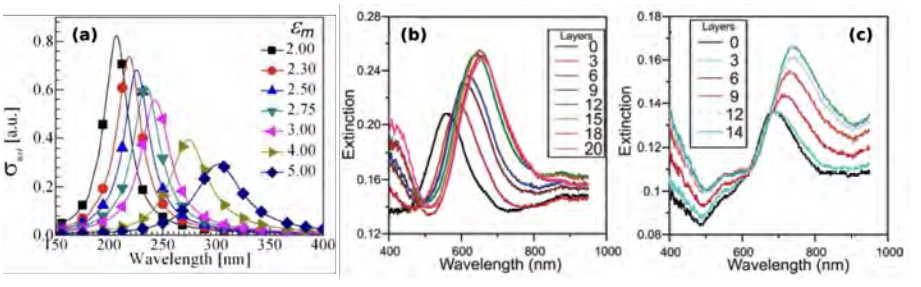

Figure 3.6: (a) Simulated extinction spectra of 5 nm AlNPs as a function of the dielectric constant of the surrounding medium; (b-c) extinction spectra of AgNPs (b) and AuNPs (b) surrounded by monolayers of Cu^{2+}/HS$-(CH_2)_{10}$COOH, as a function of the number of layers. Adapted from [114, 115].

3.2.4 LSPR: plasmon dynamics

Beyond the spectral characteristics of plasmon resonances and their associated near-field enhancement, it is equally important to examine the temporal dynamics of charge carriers following the impulsive photoexcitation of a metallic nanoparticle.

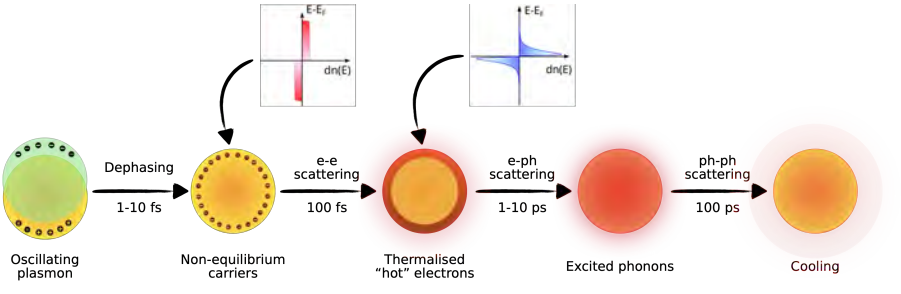

Figure 3.7: Schematic representation of the carrier dynamics in photoexcited plasmonic nanoparticles. Adapted from [106].

These processes, which predominantly unfold on sub-nanosecond timescales, govern how the absorbed energy is redistributed within the nanoparticle and ultimately dissipated into the surrounding environment, thereby determining

both the fundamental mechanisms of plasmon decay and the practical performance of plasmonic nanostructures. A schematic overview of the relevant dynamical stages is provided in Figure 3.7.

Immediately after photoexcitation, the nanoparticle sustains coherent plasmon oscillations, which rapidly lose phase coherence through *Landau damping* [116], typically within $1 - 10\,\mathrm{fs}$. This process converts the collective plasmon mode into a non-thermal distribution of highly energetic electrons. At slightly longer delays, electron–electron (e–e) scattering redistributes the absorbed energy among the electronic degrees of freedom, driving the system toward a thermalised Fermi–Dirac distribution characterised by an elevated electronic temperature. This thermalisation typically occurs on timescales of the order of $\sim 100\,\mathrm{fs}$ [117]. Once this quasi-equilibrium within the electron gas is established, the subsequent energy flow between electrons and the lattice can be described within the framework of the *two-temperature model* (TTM), which treats the electronic and lattice subsystems as two coupled heat reservoirs with distinct temperatures [118]. Within the TTM regime, energy is transferred from the hot electron gas to the lattice via electron–phonon (e–ph) coupling, leading to lattice heating on characteristic timescales of $1 - 10\,\mathrm{ps}$. Finally, phonon–phonon (ph–ph) scattering and heat diffusion into the surrounding medium allow the nanoparticle to cool down and return to thermal equilibrium over hundreds of picoseconds. The characteristic timescales associated with each of these processes are not universal but depend on several factors, including the material composition of the nanoparticle, its size and geometry, and the surrounding dielectric environment. Importantly, they are also influenced by the excitation conditions: increasing the pump fluence enhances the initial electronic temperature, which can modify electron–electron and electron–phonon scattering rates and, at sufficiently high excitation densities, lead to deviations from linear-response behaviour. As a result, time-resolved optical techniques with sub-nanosecond resolution are essential not only to resolve the intrinsic plasmon relaxation pathways, but also to quantify their dependence on the excitation regime.

3.2.5 LSPR: applications

As mentioned earlier, the multitude of factors governing the plasmonic response of metal NPs makes these systems excellent candidates for an equally

diverse range of applications, some notable examples of which are reported in Figure 3.8. Among these, surface-enhanced Raman scattering (SERS) stands out as one of the most powerful and well-established. SERS relies on the intense near-field amplification generated at the surface of plasmonic nanoparticles to boost the inherently weak Raman signal of analyte molecules positioned in their vicinity (panel (a) of Figure 3.8). This effect can increase the Raman scattering cross-section by several orders of magnitude (up to 10^{10}), enabling even single-molecule detection in favourable conditions. In parallel, non-radiative energy transfer from the analyte to the nanoparticle often suppresses competing photoluminescence signals, further improving the detectability of vibrational fingerprints. Furthermore, NP surface functionalization can be exploited to enable the selective binding of a given analyte. This strategy, known as *label-based SERS*, is particularly valuable for detecting trace amounts of target molecules within complex mixtures of multiple Raman-active species, thereby extending the reach of SERS into areas such as biosensing and environmental monitoring. Branched NPs such as gold nano-stars or nano-urchins [119] are particularly suited for SERS, owing to the strong field enhancement near their vertices.

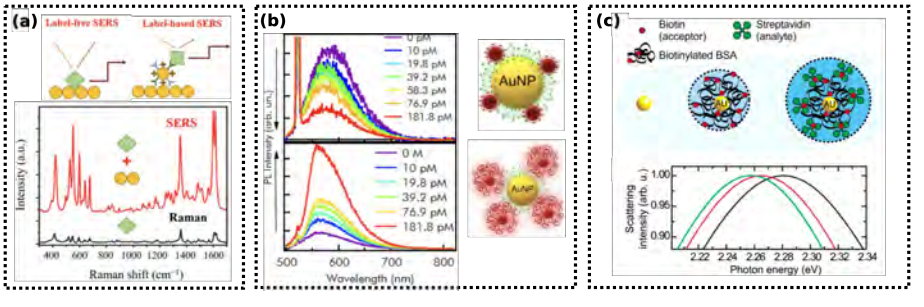

Figure 3.8: Notable examples of applications for plasmonic NPs: (a) surface-enhanced Raman scattering (SERS); (b) quenching (top panel) or enhancement (bottom panel) of photoluminescence; (c) sensing. Adapted from [120–122].

Besides SERS, the coupling of photoluminescent nanosystems such as dyes, quantum dots, or carbon-based nanomaterials with plasmonic NPs also provides a versatile route to control their light-emitting properties [121, 123–126]. Indeed, because of the enhanced field near the NP surface, fluorophors in its vicinity experience an increase in excitation rate and, consequently, enhanced

photoluminescence (PL). Additionally, near-field enhancement can result in an increase in the radiative decay rate of nearby fluorophores, due to the so-called *Purcell effect* [127]. While both these effects produce an enhancement of the PL quantum yield (see chapter 4) of the fluorophore, the former does not impact the PL lifetime, while the latter does. Therefore, time-resolved PL measurements can be used to discriminate between the two contributions. Conversely, as mentioned for SERS, short-range interaction with the plasmonic NP can promote nonradiative decay and energy transfer from the fluorophore to the NP, resulting in PL quenching. The interplay between PL enhancement and quenching is mainly governed by the mutual distance between the NP and the fluorophore, as demonstrated by Sciortino *et al.* [121] for carbon dots (CDs) coupled to AuNPs: As summarised in panel (b) of Figure 3.8, at $\sim 2\,\mathrm{nm}$ separation the increase in excitation rate prevails, yielding enhanced PL, whereas closer spacing ($\lesssim 1\,\mathrm{nm}$) promotes non-radiative energy transfer, quenching the CD photoluminescence. Importantly, even smaller spacing can initiate strong coupling between the NP and emitter, with coherent energy exchange between the two resulting in hybrid states such as the so-called *plasmon-exciton polariton* (or *plexciton*) observed in transition metal dichalcogenide QDs coupled to plasmonic NPs [128].

As a final example, we will consider the use of plasmonic NPs for sensing applications. As discussed in the previous section, the position and profile of LSPR changes when varying the dielectric constant of the surrounding medium, and even a few monolayers of a given species on the surface of the NP can yield a measurable variation of the plasmon resonance (see panels (b-c) of Figure 3.6). Even higher sensitivity and selectivity can be obtained by appropriately functionalising the NP surface [122], as summarised in panel (c) of Figure 3.8, where a few molecules of an analyte (streptavidin) are enough to sensibly shift the LSPR of AuNPs coated by biotinilated bovine serum albumin (BSA). Another mechanism that can be employed for plasmonic sensing is the above-discussed PL enhancement, which allows for the detection of weakly emitting species at low concentrations.

Taken together, these examples represent only a small fraction of the rich landscape of LSPR-enabled applications, which further extends into areas such as photocatalysis [129], nanomedicine [130, 131], and beyond.

3.3 Plasmonic NP Superstructures

The self-assembly of plasmonic nanoparticles of varying shape and size into superstructures (SPs) takes the tuneability of plasmon modes even further. Indeed, the interplay between the LSPR of nanoparticles within densely packed SPs gives rise to so-called *plasmon coupling* phenomena, whereby the individual resonances mix to form collective modes sensitive to particle spacing, arrangement, and orientation, often resulting in stronger near-field enhancements, broader absorption, and the emergence of entirely new resonances.

In general, plasmon coupling can be explained in view of the fact that, when NPs in close proximity to one another are photoexcited, the total electric field perceived by the *i*-th NP will be given by the sum of the incident field $\mathbf{E_o}$ and the near-fields $\mathbf{E_{nf}^{(j)}}$ generated by all the other NPs, that is:

$$\mathbf{E_{tot}^{(i)}} = \mathbf{E_o} + \sum_{j \neq i} \mathbf{E_{nf}^{(j)}} \tag{3.15}$$

It is therefore evident that - as mentioned above - the collective response of a plasmonic superstructure greatly varies with the characteristics of its constituent NPs, as well as its geometry and interparticle spacing. Below, we will explore these variations for increasingly complex SPs.

3.3.1 Plasmon coupling in dimers and metamolecules

Plasmonic NP dimers

The simplest case of plasmonic coupling arises when two nanoparticles are brought in close proximity, forming a *dimer* (Figure 3.9). In this configuration, the individual LSPR modes hybridize through their near-field interaction, akin to molecular orbital formation. Depending on the relative orientation between the interparticle axis and the incident electric field, distinct *bonding* and *antibonding* plasmon modes emerge (panel (b) of Figure 3.9).

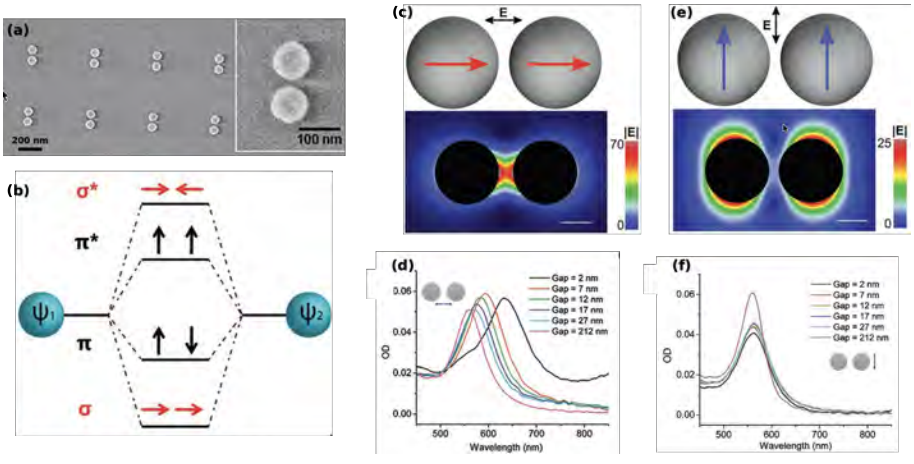

Figure 3.9: Plasmon coupling in NP dimers: (a) electron micrograph of AuNP dimers; (b) qualitative scheme of hybridised plasmon states; (c-f) near-field enhancement and dependence of the LSPR upon interparticle distance with the excitation field polarised along the dimer axis (c-d) and orthogonally (e-f). Adapted from [132].

In particular, when the incident field is polarised along the dimer axis, strong longitudinal coupling leads to the formation of a lower-energy σ-like bonding state and a higher-energy σ^*-like antibonding state, accompanied by intense localisation of the electric field in the interparticle region (the so-called *hot spot* - see panel (c)). On the other hand, excitation polarised orthogonally to the dimer axis produces a (bonding) π-like and a (antibonding) π^*-like state, with significantly weaker coupling and no hot spot formation (panel (e)). The optical activity of the hybridised states depends on their net dipole moment. In particular, for *homodimers* (that is, dimers composed of two identical NPs), in the longitudinal case the σ bonding state carries a finite dipole moment and is therefore optically bright, while the antibonding σ^* state has zero dipole moment and remains dark. Conversely, in the transverse configuration, the π bonding state is dark, whereas the antibonding π^* state is bright. As a consequence, only the σ and π^* modes can be observed in the dimer extinction spectrum, while the other two remain hidden unless symmetry breaking or higher-order multipolar interactions come into play. Importantly, the spectral profile of such resonances is sensitive to the interparticle spacing: for excitation along the axis dimer, the collective LSPR red-shifts as the NPs get closer, whereas for transverse excitation a blue-shift is observed as the interparticle

distance decreases. The entity of the blue-shift is, however, drastically lower when compared with the red-shift seen in the former case, as the coupling in the transverse excitation regime is much weaker than that in the longitudinal excitation case. The sensitive distance-dependence of the LSPR when exciting along the dimer axis is at the base of one of the most well-established applications of plasmonic NP dimers: the so-called *plasmon ruler* [133, 134]. As the red-shift follows an approximately exponential dependence on the gap size, the resonance wavelength serves as a highly sensitive probe for measuring interparticle distances with sub-nanometer precision, well below the diffraction limit of light, making plasmonic dimers a powerful tool for monitoring biomolecular conformational changes and dynamic processes at the single-molecule level. Additionally, the intense hot spot appearing in the interparticle region can be exploited for ultra-efficient enhancement of Raman or fluorescence signals of single molecules [132].

Plasmonic metamolecules

While dimers represent the most elementary example of plasmon coupling, they also set the conceptual foundation for more complex assemblies. Indeed, it is possible to extend the same principle to a larger number of plasmonic NPs (usually up to a few hundred), assembled in ordered (typically planar) nanoscale architectures referred to as *metamolecules* or *oligomers* (Figure 3.10). These systems expand on the coupling effects observed in dimers, as the increased number of constituents gives rise to correspondingly complex interactions, sensitive to the specific number, nature, arrangement and mutual distances of the NPs [135]. Figure 3.10 presents a few examples of plasmonic metamolecules, highlighting their peculiar behavior.

Firstly, constructive and destructive interference among single-particle modes can produce a manifold of bright and dark collective resonances, as reported by Greybush *et al.* [136] for planar metamolecules composed of up to a few tens of gold nanoparticles. In particular, panel (a) of Figure 3.10 shows the extinction spectra of six distinct metamolecules, each comprising 31 nanoparticles, under out-of-plane (p, left) and in-plane (s, right) polarized light. A quick comparison reveals how small geometric variations produce marked spectral differences, especially under s-polarization, where the in-plane electric field excites hybridized collective modes extending across the entire oligomer.

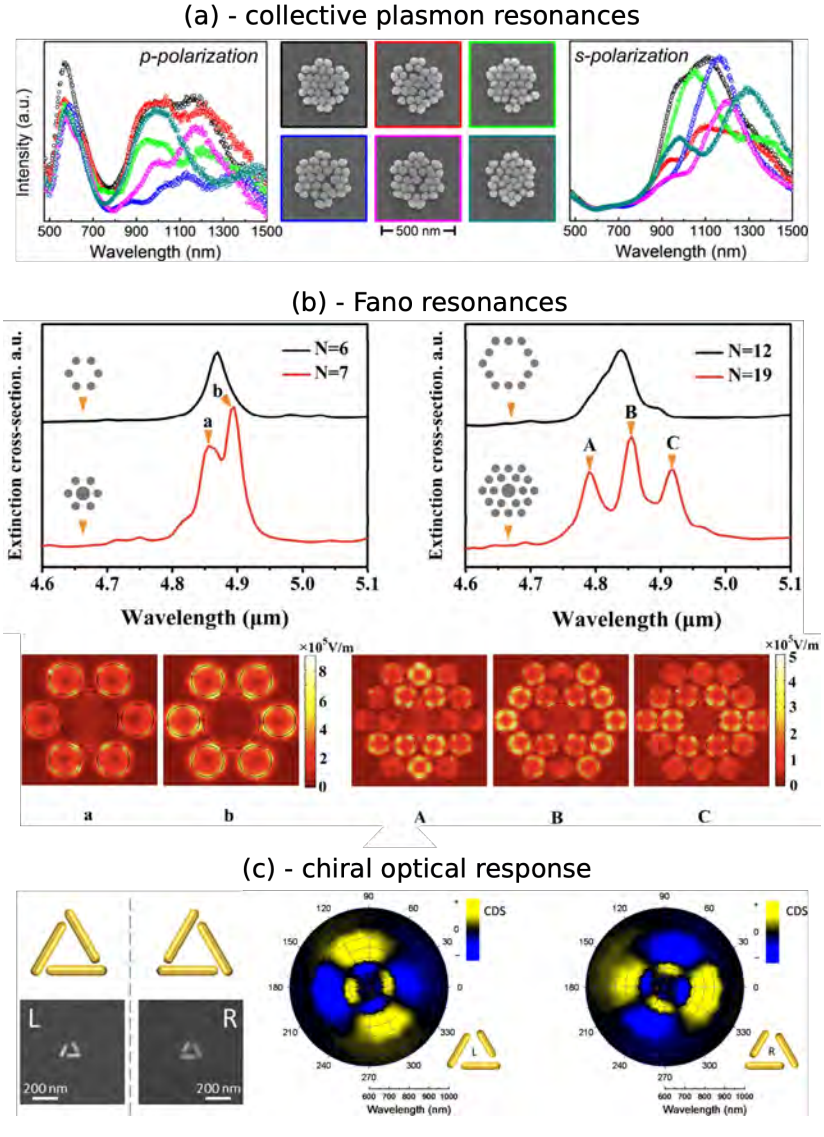

Figure 3.10: Examples of plasmonic metamolecules and their collective behavior: (a) Normalised extinction spectra of planar AuNP metamolecules containing 31 NPs, under p- and s-polarised light (adapted from [136]; (b) fano resonances in single-ring and double-ring nanodisk oligomers, arising from the addition of a central nanodisk (adapted from [137]); (c) Au nanorod trimers with left-handed and right-handed chiral geometries and their simulated circular differential scattering maps (adapted from [138]).

Additionally, plasmonic metamolecules can exhibit *Fano resonances* (FRs), a distinctive class of collective resonances originating from the interference between a narrow, discrete mode and a broad, continuum-like mode [137, 139, 140]. In the context of plasmonics, this interference is often realized through the coupling of a broad, *bright* mode with a narrow, *dark* mode, leading to a characteristically asymmetric line shape in the extinction spectrum. This hallmark profile typically appears as sharp dips superimposed on, or adjacent to, a broader peak (see for instance panel (b) of Figure 3.10). Beyond the bright–dark picture, however, the Fano mechanism more generally describes any interference between discrete resonances and continua, and can also emerge from multipolar plasmon coupling [141] or hybridization of the plasmon resonances with the photonic modes of a waveguide or photonic crystal [142]. Importantly, sharpness and asymmetry of FRs make them extremely sensitive to changes in the dielectric environment, enabling their use in ultrasensitive refractive-index sensing, label-free molecular detection, and other nanophotonic applications.

Finally, plasmonic oligomers possessing chiral geometries also display chirality in their collective resonances. A clear example of this behaviour is provided by the gold nanorod (AuNR) trimers reported in [138] and shown in panel (c) of Figure 3.10. Here, the three AuNRs are arranged in a triangular pattern and slightly shifted to impart left- or right-handed chirality to the oligomer. Optical measurements and simulations reveal that these trimers exhibit strong circular dichroism, arising from the hybridization of longitudinal nanorod dipolar plasmons with collective circulating modes around the trimer. The latter behave as effective magnetic dipoles normal to the trimer plane, and their coupling to the electric dipoles produces a pronounced chiroptical response under circularly polarized illumination. Crucially, this work highlights how chirality in plasmonic metamolecules can be introduced by the appropriate arrangement of otherwise achiral building blocks.

3.3.2 Plasmonic superparticles

When the number of building blocks increases even further, the discrete metamolecule picture gives way to a regime of dense nanoparticle assemblies, or *plasmonic superparticles* (SPs) [143–148]. These are typically $0.1 - 10\ \mu\mathrm{m}$ in diameter and contain several thousand NPs. At this level of complexity, plas-

mon coupling occurs concurrently on multiple length scales, with long-range order effects contributing to the overall response of the superstructure. Typically, this determines wide-band absorption across the visible range, hence the term *black gold* often used for dense gold superparticles (AuSPs).
Plasmonic superparticles are most commonly obtained through emulsion based assembly techniques [143], akin to those discussed in the previous chapter for the assembly of semiconductor QDs. However, different approaches such as *in-situ* spontaneous assembly have also been demonstrated [144]. Two notable examples are reported in Figure 3.11.

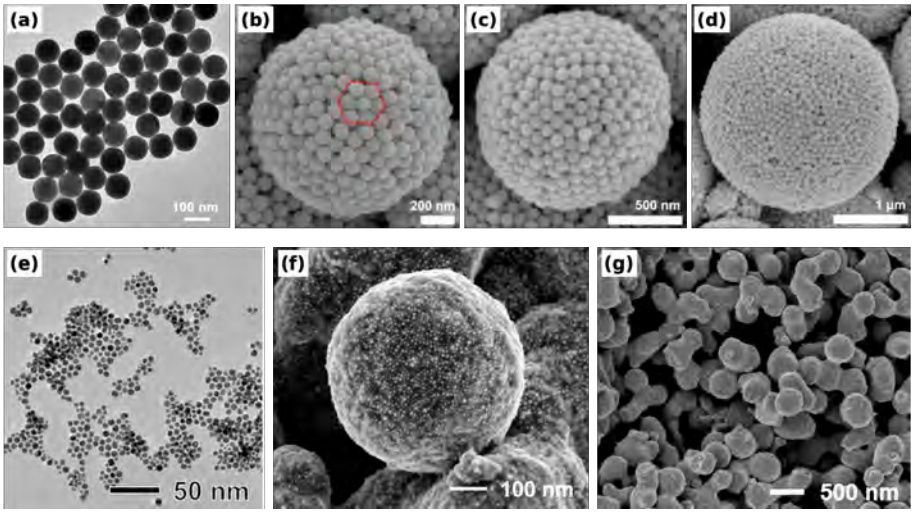

Figure 3.11: Examples of AuSPs. Top row: (a) TEM image of monodisperse AuNPs; (b-d) SEM micrographs of AuSPs of increasing diameter, obtained via emulsion-templated assembly (adapted from [143]). Bottom row: chemical self-assembly of AuSPs (f-g) from in-situ formed AuNPs (e) (adapted from [144]).

Plasmonic SPs: supra-crystalline ordering and structural control

The AuSPs reported by Liu *et al.* [144] and shown in the top row of Figure 3.11 present an interesting property: the constituent AuNPs are not randomly arranged, but rather organized in an hexagonal-close-packed (HCP) supra-crystalline structure (as evidenced by the dotted hexagon in panel (b)). Such crystalline ordering, critically dependent on the starting concentration of the colloidal AuNP dispersion, has a strong impact on the short- and long-range interactions between NPs, ultimately shaping the collective plasmon

resonance of the SP. Crystalline SPs also offer intriguing structural control opportunities: the well-defined nearest-neighbour distance between NPs can be tuned by modifying the ligands that surround them [149–151]. A notable demonstration of this fine-tuning was provided by Wan *et al.* [151],who showed that the interparticle distance in AuSPs can be precisely controlled by varying both the ligand chain length and the solvent environment during assembly. Specifically, ligand exchange with alkanethiols of increasing chain length led to a systematic increase in interparticle distance, which scales linearly with the number of carbon atoms in the chain (black and red squares in panel (a) of Figure 3.12).

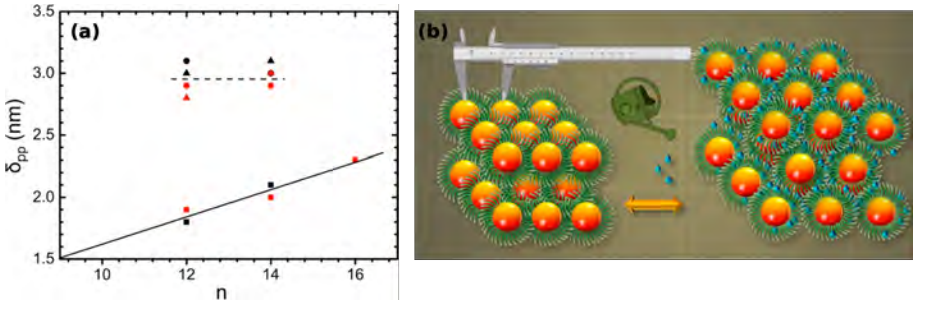

Figure 3.12: Controlling the interparticle distance in AuSPs: (a) surface-to-surface interparticle distance as a function of the number of carbon atoms in the ligand chain for AuSPs assembled from 5 nm AuNPs (black) and 7 nm AuNPs (red), under 0% (squares), 39% (circles), and 75% (triangles) relative toluene vapour pressure; (b) cartoon representing the reversible ligand swelling caused by toluene vapours. Adapted from [151].

Interestingly, they also demonstrate that the interparticle spacing can be *reversibly modulated* by exposing the SPs to solvent vapours (see panel (b) of Figure 3.12): in particular, exposure to toluene vapour causes a swelling of the ligands, increasing the NP–NP separation while maintaining the crystalline order, while subsequent reduction of the toluene vapour pressure restores the original condition. This dynamic structural adaptability highlights how ligand chemistry provides a powerful route to post-synthetically tune plasmonic coupling in superparticles. In the study reported in chapter 8, we employ a similar ligand exchange strategy to tune the nearest-neighbour distance in FCC supracrystalline AuSPs.

The intriguing properties of plasmonic SPs, combined with their relative ease of assembly compared to oligomers, promote them for a wide range of applications, encompassing ultra-efficient, broadband SERS, sensing, catalysis, photonics, drug delivery, and energy conversion [144, 147, 148, 152]. Despite this broad interest, the fundamental properties of plasmonic SPs remain largely underexplored, particularly in contrast to the extensive studies on smaller plasmonic metamolecules. More in detail, very little is known on how cross-talk between neighbouring NPs and long-range order effects impact plasmon dynamics. In chapter 8, we will investigate the ultrafast carrier dynamics in supra-crystalline AuSPs, focusing on their dependence on the interparticle distance.

3.4 Noble Metal Nanoclusters

As briefly mentioned at the beginning of this chapter, noble metal nanoclusters (NCs) [153] are atomically precise aggregates composed of up to a few hundred metal atoms, stabilized by a surrounding shell of organic ligands, with overall sizes generally not exceeding $\sim 2\,\mathrm{nm}$. Their growing appeal arises from their unique role in bridging the gap between plasmonic nanoparticles and molecular systems [154], as illustrated in Figure 3.1. Indeed, when the particle size is reduced below $\sim 3\,\mathrm{nm}$, quantum confinement effects lead to the discretization of energy bands: collective plasmon resonances are quenched, and molecule-like electronic transitions emerge. As a consequence, NCs exhibit properties that sharply distinguish them from larger nanoparticles, most notably their well-defined and size-dependent photoluminescence [155]. In the following, we will focus primarily on gold nanoclusters (AuNCs), which stand as the paradigmatic system in this field due to their well-established synthetic protocols, structural precision, and the breadth of studies devoted to unraveling their electronic, optical, and chemical properties. As AuNCs are typically stabilised by thiolate ligands, it has become commonplace to label them as $\mathrm{Au}_m(\mathrm{SR})_n$, where m and n respectively indicate the number of gold atoms and ligand molecules constituting the NC.

3.4.1 Atomically precise gold nanoclusters

The first atomically precise AuNC, $\mathrm{Au}_{102}(\mathrm{SR})_{44}$, was reported in 2007 by Jadzinsky *et al.* [156]. Since then, over forty atomically precise AuNC struc-

tures have been discovered [157–162]. Typically, AuNCs consist of an Au(0) core surrounded by a shell of Au(I)–thiolate complexes, which stabilize the cluster and define its surface chemistry [153]. This core–shell arrangement underlies the remarkable stability of certain AuNCs and forms the basis for describing their electronic structure in terms of delocalized electrons. A useful framework to rationalize AuNC stability is the *superatom model* [163], in which delocalized electrons in the metallic core occupy quantized orbitals reminiscent of atomic shells. Closed electronic shells (e.g., 2, 8, 18 electrons) correspond to particularly stable clusters. This model explains the stability of archetypal $Au_{25}(SR)_{18}$ clusters [164], which feature 8 delocalized electrons, and guides predictions of their electronic and optical properties. Figure 3.13 shows selected AuNC structures and commonly used water-soluble ligands.

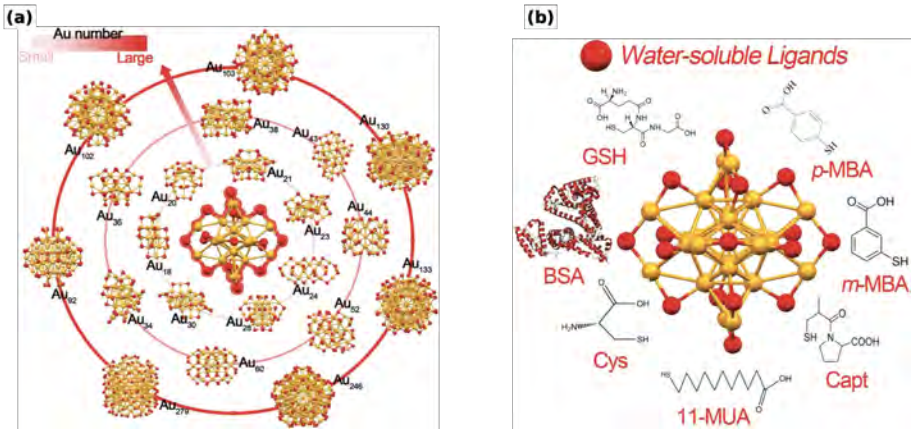

Figure 3.13: (a) Selected $Au_m(SR)_n$ structures determined with atomic precision (yellow: Au, red: S in thiolate ligands); (b) commonly employed water-soluble ligands. Adapted from [164].

The core–shell architecture also governs the photophysical behavior of AuNCs, determined by the interplay of core states, outer shell (*semiring*) states, and ligand-mediated charge transfer. Using $Au_{25}(SR)_{18}$ as a model system, its UV–Vis absorption spectrum (panel (a) of Figure 3.14) exhibits three molecule-like bands. TDDFT calculations [165, 166] assign these to HOMO–LUMO (a), intraband (b), and interband (c) transitions, primarily localized on the Au(0) core.

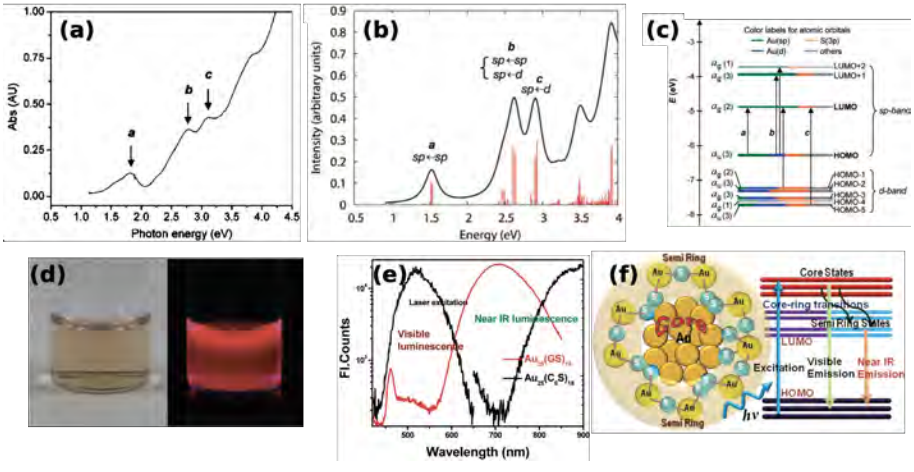

Figure 3.14: Role of core and semiring states in AuNC optical properties. Top row: measured (a) and simulated (b) UV–Vis spectra of $Au_{25}(SR)_{18}$; (c) TDDFT energy spectrum highlighting the three transitions. Bottom row: (d) aqueous dispersion under ambient light and UV; (e) photoluminescence showing weak core (visible) and stronger semiring (NIR) emission; (f) simplified Jablonski diagram summarizing the photocycle. Adapted from [165, 167, 168].

Semiring states associated with the outer Au(I) shell are also important. Devadas *et al.* [168] reconstructed the photocycle of $Au_{25}(SR)_{18}$, showing weak, short-lived visible emission from core HOMO–LUMO transitions and stronger, longer-lived NIR photoluminescence from *core–ring* transitions. Similar results were reported by Green and Knappenberger [169] and Yau *et al.* [170]. This complex photocycle, with long lifetimes, reflects the high delocalization of the involved states and the multiple relaxation pathways.

Ligand-mediated charge-transfer processes, specifically ligand-to-metal (LMCT) and ligand-to-metal-to-metal (LMMCT) transitions, further modulate electronic states, affecting emission wavelength, quantum yield, and excited-state dynamics. Wu *et al.* [171] systematically showed that increasing either ligand electropositivity or core charge enhances emission intensity. Ligand involvement underpins the pronounced environmental sensitivity of AuNCs, which is central to many applications [155].

3.4.2 Ultrasmall Au(I) clusters

A particularly intriguing class of gold-based nanosystems is represented by *ultrasmall* Au(I) clusters, or *nanocomplexes* [172, 173]. Comprising no more

than twelve gold atoms, these clusters lack the well-defined Au(0) core of larger nanoclusters; all gold atoms are in the Au(I) oxidation state and interact directly with ligands. Consequently, their photocycle is dominated by hybrid ligand–metal states and ligand-to-metal charge transfer (LMCT) transitions.

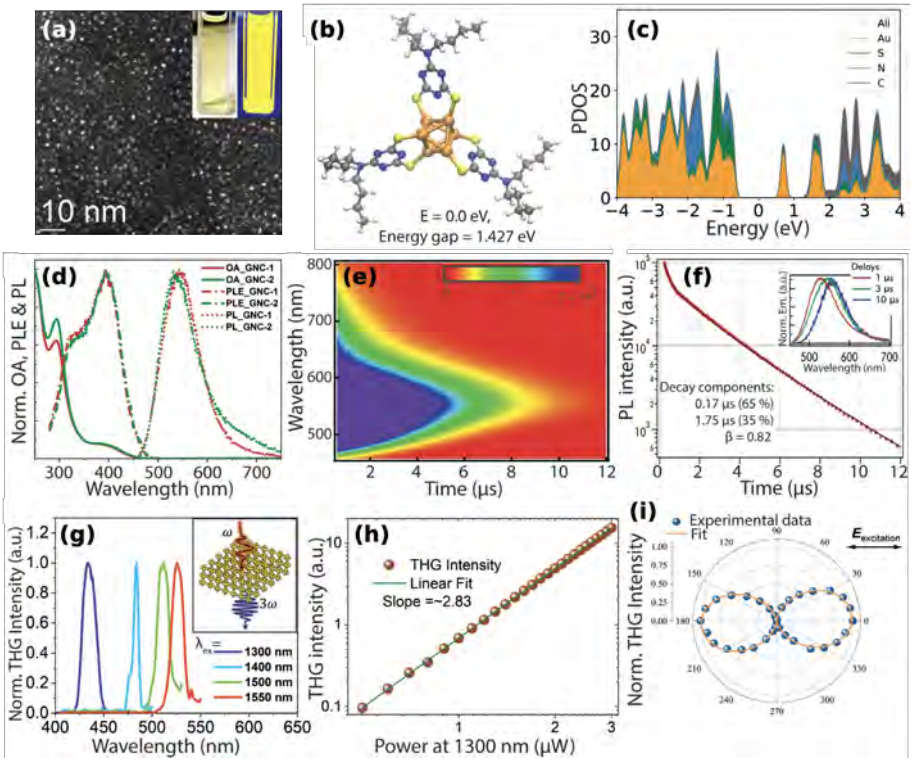

Figure 3.15: Structure and photophysics of triazine-capped Au(I)6 clusters. (a) STEM image of dropcasted clusters (insets: dispersion in DCM under natural and UV light); (b) DFT-optimized structure; (c) density of states; (d) normalized OA, PL, and PLE spectra of clusters obtained via ascorbic acid (GNC-1) and $NaBH_4$ (GNC-2); (e) time–wavelength PL map of GNC-1; (f) kinetic trace at the PL peak (inset: spectra at varying delays); (g) normalized THG spectra at various excitation wavelengths; (h) THG intensity versus excitation power for GNC-1 at $\lambda_{exc} = 1300\,\mathrm{nm}$; (i) polar plot of THG intensity. Adapted from [173].

Chandra *et al.* [173] exemplify these properties with triazine-capped $Au(I)_6$ clusters synthesized via a two-step reduction. Six Au(I) atoms coordinated by three triazine-based ligands (6-(dibutylamino)-1,3,5-triazine-2,4-dithiol) form a compact, nearly octahedral structure (Figure 3.15). The clusters are stabi-

lized by *ligand-derived atomic steric locking*, where ligands physically constrain the Au(I) atoms and prevent aggregation, yielding exceptional chemical and photostability under ambient conditions. DFT-calculated density of states (panel (c)) shows that the HOMO, LUMO, and nearby states have significant contributions from sulfur, nitrogen, and carbon atoms, highlighting the dominant role of the ligands in the cluster's electronic structure.

These Au(I) clusters also exhibit notable nonlinear optical properties (panels g–i of Figure 3.15). In particular, highly efficient third-harmonic generation (THG) is observed under ultrafast laser excitation, reflecting the inversion symmetry of the octahedral cluster structure. Ultrafast transient absorption (TA, Figure 3.16) reveals that quantum coherence contributes to the photocycle. Coherent oscillations are observed in the kinetic traces extracted from TA (panels b–c). By fitting the overall signal with a multiexponential model and analyzing the residuals, two principal frequencies are identified at 90 and $365\,\mathrm{cm}^{-1}$, corresponding to Au–Au core vibrations and Cl–C–Cl solvent modes, respectively. Photoexcitation displaces the Au core from equilibrium, initiating Au–Au vibrations that damp within $(200 - 300\,\mathrm{fs}$, with energy subsequently transferred to the cluster and solvent, producing solvent oscillations.

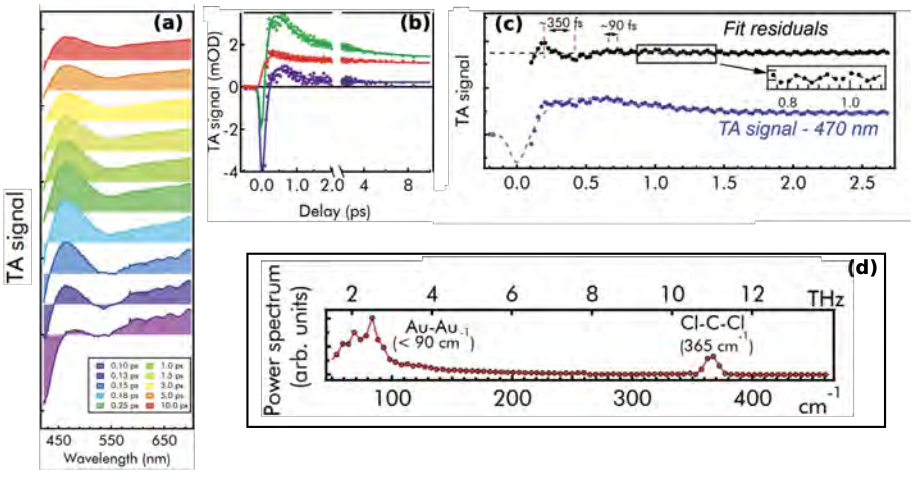

Figure 3.16: (a) Transient absorption spectra at variable delays following $400\,\mathrm{nm}$ excitation; (b) early kinetic traces at $450\,\mathrm{nm}$ (purple), $550\,\mathrm{nm}$ (green), and $650\,\mathrm{nm}$ (red); (c) TA signal at $470\,\mathrm{nm}$ (blue dots) fitted with a multi-exponential function. Fit residuals (black, vertically shifted) show coherent oscillations; (d) Fourier transform of the residuals highlighting Au–Au and Cl–C–Cl vibrational modes. Adapted from [173].

In chapter 9, we will delve into the photophysics of fibre-like superstructures self-assembled from these same $Au(I)_6$ clusters. A brief overview on how assembly impacts the properties and potential applications of NCs will be provided in the following section.

3.5 Nanocluster Superstructures

The self-assembly of atomically precise noble metal nanocluster into superstructures represents a promising strategy to harness their complex photophysical properties and expand them towards a vast number of applications. While arguably less popular than their plasmonic counterparts, NC-based superstructures are commanding increasing attention in current literature [174–182], with the appearance of emergent properties such as ultra-efficient charge migration and aggregation-induced emission. This includes both supramolecular assemblies made up entirely of NCs and hybrid superstructures combining NCs with larger nanoparticles or molecular species. Figure 3.17 summarises some examples of such assemblies.

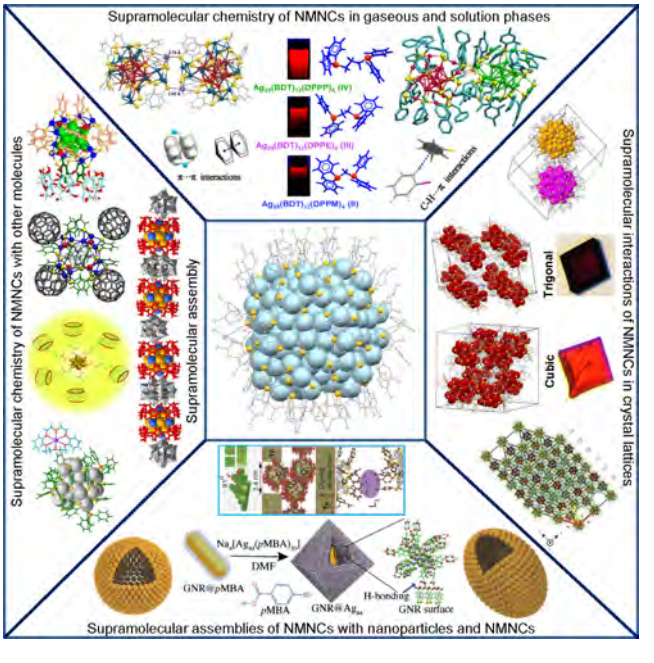

Figure 3.17: Overview of assemblies of atomically precise metal NCs. Adapted from [177].

Because of the reduced size and high sensitivity to the environment characterising metal NCs, assembly methods based on *supramolecular chemistry* are widely preferred to mechanical pathways such as emulsion- or template-based methods. In general, supramolecular chemistry involves the controlled modification of the chemical environment of the NCs (such as the pH of the solution or the ligands' functional groups), aimed at causing the clusters to coalesce or self-organise into superstructures.

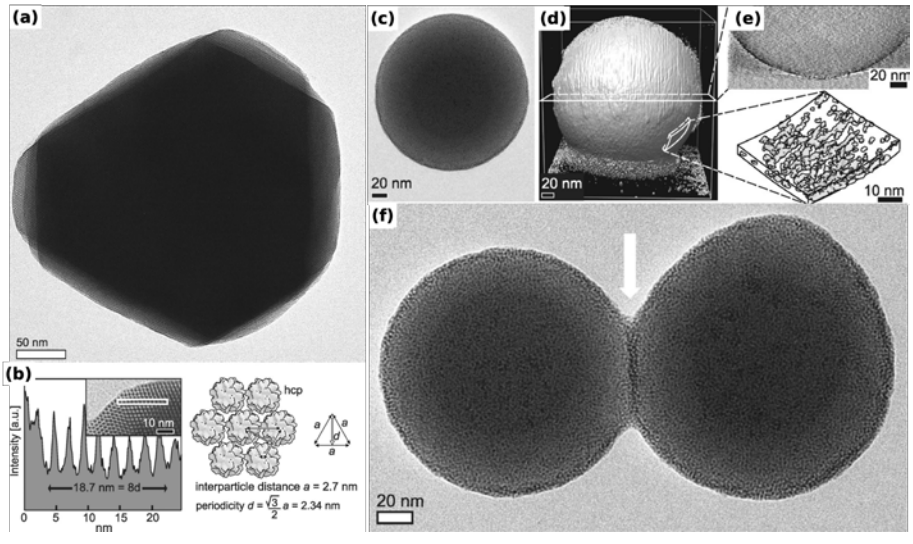

Figure 3.18: Self-assembled AuNC capsids. (a) TEM micrograph of the 2D faceted AuNC sheets (in this instance, three stacked sheets); (b) close-up of a single monolayer, highlighting the periodicity of the HCP superlattice; (c) TEM image and (d-e) electron tomographic reconstruction of a single capsid; (f) TEM micrograph of a capsid dimer. Adapted from [182].

For instance, Nonappa *et al.* [182] have reported the template-free self-assembly of $Au_{102}(pMBA)_{44}$ nanoclusters into hollow spherical shells (or *capsids*) with diameters of around $200\,\mathrm{nm}$ and an average thickness of $2.7\,\mathrm{nm}$ (essentially one NC monolayer). Their assembly strategy is based on the inter-NC hydrogen bonds made possible by the carboxylic groups of the p-mercaptobenzoic acid (pMBA) ligands under methanol dialysis: as the ligands are preferentially aligned along the equatorial plane of each NC, their bonding results in the formation of two-dimensional faceted NC sheets (panels (a-b) of Figure 3.18), with near-perfect HCP ordering guaranteed by the high monodispersity of the

NCs. Additionally, because the NC sheets possess amphiphilic character as a consequence of the partial deprotonation of ligand carboxylic groups, their exposure to a large volume of ethanol causes them to fold on themselves, forming closed sperical shells (the capsids - panels (c-e)). Once formed, the monolayer-thick shell of the capsid is stabilized by the hydrogen-bonding dimerization of the carboxylic acid groups and electrostatic attraction forces due to the presence of counter cations. Finally, the pMBA hydrogen bonds can also drive the formation of capsid multimers, such as the dimer shown in panel (f) of Figure 3.18. In this instance, the geometry of each capsid is partially distorted and a planar contact surface emerges, fusing the two. This paves the way towards higher-order hierarchical assembly, which could prove precious, for instance, for lightweight framework materials.

Despite these advances, the exploration of novel assembly strategies and superstructure geometries for AuNCs remains an active area of research. While current studies have demonstrated well-defined architectures such as sheets, capsids, and hierarchical multimers, the role of inter-cluster electronic and photophysical cross-talk within these assemblies is largely unexplored. Understanding how the spatial arrangement of NCs affects energy transfer, charge migration, and collective optical properties could unlock new functionalities and guide the rational design of next-generation nanocluster superstructures.

4

Experimental Setups and Procedures

The principle of science, the definition, almost, is the following: The test of all knowledge is experiment. Experiment is the sole judge of scientific "truth".

— Richard P. Feynman

This chapter presents the main experimental setups and procedures employed in the studies described in this Thesis. First, the synthetic routes used to obtain the different samples are outlined, followed by the techniques adopted for their structural and morphological characterization. The focus will then shift to the optical characterization, which constitutes the core of this work, with a detailed description of the various techniques and the corresponding analysis procedures.

4.1 Sample Preparation

The samples reported in this Thesis were either synthesized in-house or obtained *via* collaborations. Below, a brief description of all the relevant synthetic routes is provided. Unless specified, all chemicals were purchased commercially (usually from *Sigma-Aldrich*) and used without further purification steps.

4.1.1 Quantum Dot Superparticles

The quantum dot (QD) superparticles analysed in chapter 5 and chapter 6 were synthesized by Dr. E. Marino (University of Palermo), following the procedure detailed in [77] and briefly described hereafter. The constituent nanoparticles are CdSe/CdS core-shell QDs, with a CdSe core $3.5\,\mathrm{nm}$ in diameter and a $3.4\,\mathrm{nm}$-thick CdS shell (8 monolayers), obtained following a literature synthesis [64, 183] with small modifications outlined in [77]. The resulting QDs are quasi-type II (see chapter 2), and the CdS shell presents little to no quantum confinement.

The superparticles were synthesized through a source-sink emulsion densification protocol [77], by using a commercial droplet generator glass chip (Darwin microfluidics, T-26) connected to a multichannel pressure regulator (Elveflow, OB1MK3+). First, monodisperse droplets of QDs in toluene ($2\,\mathrm{mg/mL}$) were generated into a continuous phase consisting of a $20\,\mathrm{mM}$ solution of sodium dodecyl sulphate (SDS) in water. This "source" emulsion was then mixed with a "sink" emulsion constituted by hexadecane droplets (1%) suspended in an analogous $20\,\mathrm{mM}$ aqueous SDS solution. Once mixed, the two emulsions flow together along 11.5 m of tubing, over the course of 7 minutes. The last 10 m of tubing were wrapped around a copper rod kept at a fixed $70\,^{\circ}\mathrm{C}$. During this time, the sink emulsion removes toluene from the source emulsion, causing the formation of superparticles. The sample was collected in a scintillation vial filled with $5\,\mathrm{mL}$ of $20\,\mathrm{mM}$ SDS in water and left uncapped overnight on a hot plate set to $50\,^{\circ}\mathrm{C}$. Finally, the superparticles were washed three times by centrifugation at 100 g for 5 minutes and redispersed in $10\,\mathrm{mM}$ SDS in water.

4.1.2 Perovskite Nanocrystal Superstructures

The perovskite superstructures presented in chapter 7 were assembled in-house, in collaboration with Dr. Y. Tang and Dr. Prof. P. Shall (University of Am-

sterdam), who also provided the constituent caesium lead bromide ($CsPbBr_3$) nanocrystals.

Synthesis of Perovskite NCs

$CsPbBr_3$ nanocrystals were synthesized *via* the well-established hot injection method first proposed by Protescu et al. [88]. Caesium oleate (Cs-oleate) was first prepared by the reaction of caesium carbonate (Cs_2CO_3, $0.814\,\mathrm{g}$) with octadecene (ODE, $40\,\mathrm{mL}$) and oleic acid (OA, $2.5\,\mathrm{mL}$) at $150\,^{\circ}\mathrm{C}$ under N_2 atmosphere. Subsequently, $1.88\,\mathrm{mmol}$ of lead bromide ($PbBr_2$) and $30\,\mathrm{mL}$ of ODE were dried under N_2 at $120\,^{\circ}\mathrm{C}$, $5\,\mathrm{mL}$ each of dried OA and oleylamine (OAm) were added, and the temperature was raised to $160\,^{\circ}\mathrm{C}$ to fully dissolve the $PbBr_2$. Finally, Cs-oleate was heated to $100\,^{\circ}\mathrm{C}$ and $4\,\mathrm{mL}$ were swiftly injected into the hot $PbBr_2$ solution, followed by quenching in an ice bath after $5\,\mathrm{s}$. The obtained $CsPbBr_3$ nanocrystals were subjected to several purification cycles and redispersed in toluene.

Assembly: Slow Evaporation Method

Perovskite supercubes with an average lateral size of $3\,\mu\mathrm{m}$ were assembled *via* the slow evaporation approach described hereafter. In a typical assembly, a quartz substrate, appropriately cut and accurately washed with ethanol, was placed upright against the wall of a $5\,\mathrm{mL}$ beaker containing $2\,\mathrm{mL}$ of a $5\,\mathrm{mg/mL}$ dispersion of $CsPbBr_3$ NCs in toluene. The beaker was then placed inside a larger vessel containing $4\,\mathrm{mL}$ of isopropanol, acting as an antisolvent and slowing down the evaporation of the toluene. A lid was finally placed on top of the vessel and held slighly open, and the whole setup was left in the dark inside a fume hood until complete evaporation of the toluene was achieved (usually within 10 to 14 days). As toluene gradually evaporates, the NCs adhere to the substrate, forming regular cubic superstructures.

4.1.3 Plasmonic Gold Superparticles

The gold superparticles studied in chapter 8 were synthesized in-house in collaboration with Dr. E. Marino (University of Palermo), while the constituent nanoparticles were provided by Dr. S. Yang (University of Pennsylvania).

Synthesis of Gold Nanoparticles

Gold nanoparticles (AuNPs) with a diameter of $5.9\,\mathrm{nm}$ were synthesized following the procedure reported in [184]: a reducing solution was first prepared by adding $1\,\mathrm{mL}$ each of OAm and 1,2,3,4-tetrahydronaphtalene (tetralin) to $43.5\,\mathrm{mg}$ of borane tert-butylamine complex. A three-neck round-bottomed flask was charged with $100\,\mathrm{mg}$ of tri-hydrate chloroauric acid ($HAuCl_4{\cdot}3\,H_2O$), $10\,\mathrm{mL}$ of OAm, and $10\,\mathrm{mL}$ of tetralin. The reducing solution was then rapidly injected at room temperature under N_2 and stirring. The colour of the solution turned dark red within $5\,\mathrm{s}$, signifying the quasi-instantaneous onset of the reduction process. The dispersion was kept in a water bath and stirred for three hours. The AuNPs were subsequently precipitated with $60\,\mathrm{mL}$ of acetone, followed by centrifugation at $8000\,\mathrm{rpm}$ for $5\,\mathrm{min}$. The AuNPs were redispersed in hexane and purified twice with ethanol and centrifugation ($8000\,\mathrm{rpm}$ for $5\,\mathrm{min}$). $10\,\mathrm{mL}$ of toluene was finally used to redisperse the AuNPs, resulting in a concentration of approximately $10\,\mathrm{mg/mL}$).

Assembly via Oil-in-Water Emulsion

Crystalline gold superparticles (AuSPs) were synthesized in-house via a previously reported [185] emulsion-based assembly technique. $1\,\mathrm{ml}$ of AuNPs in toluene ($5\,\mathrm{mg/ml}$) and $4\,\mathrm{ml}$ of a $20\,\mathrm{mM}$ aqueous solution of SDS were added to a screw-cap vial and subjected to vigorous vortex mixing for $30\,\mathrm{s}$. After removing the cap, the resulting emulsion was left overnight at $30\,^{\circ}\mathrm{C}$ under gentle stirring ($400\,\mathrm{rpm}$) to achieve complete evaporation of the toluene. The obtained suspension of AuSPs was used for subsequent procedures. Due to their size, the SPs tend to precipitate within a few hours, therefore the suspension was subjected to $10\,\mathrm{s}$ vortex mixing before each use. Whenever necessary, $10\,\mu\mathrm{L}$ of AuSP suspension were drop-casted on an appropriate substrate and dried under vacuum. The substrate was then dipped three times in acetonitrile (MeCN) to remove excess SDS, and the vacuum drying process was repeated.

Ligand Exchange on Gold Superparticles

As detailed in chapter 8, the drop-casted AuSPs were subjected to a ligand exchange in order to subsitute the native oleylamine ligands with thiols of varying lengths. To do so, the substrate was submerged for $10\,\mathrm{min}$ in a $3\,\mathrm{mM}$ solution of the desired thiol in MeCN, then extracted and dipped three times in clean

MeCN to remove excess ligands. Finally, the ligand-exchanged samples were dried under vacuum and stored for characterization.

4.1.4 Gold Nanocluster Superstructures

The fibre-like gold nanocluster superstructures, or nanoribbons (NRs), presented in chapter 9 were fabricated by Dr. S. Chandra (Aalto University). Below, the synthetic procedures for both the NRs and their constituent nanoclusters are detailed.

Synthesis of Ultrasmall Gold Nanoclusters

Triazine-capped ultrasmall Au_6 nanoclusters (NCs) were synthesized according to the procedure reported in [173]. $20\,\mathrm{mg}$ of $HAuCl_4{\cdot}3\,H_2O$ were added to a vial containing $5\,\mathrm{ml}$ of methanol at room temperature. After complete dissolution was achieved, 7 mL of dicloromethane (DCM) was added. Subsequently, a solution containing $23.5\,\mathrm{mg}$ of 6-(Dibutylamino)-1,3,5-triazine-2,4-dithiol (TRZ) in $2\,\mathrm{mL}$ of DCM was added to the mixture under vigorous stirring. $1\,\mathrm{mL}$ of an aqueous solution of a reducing agent, either ascorbic acid ($45\,\mathrm{mg/mL}$) or sodium borohydride ($NaBH_4$ - $2\,\mathrm{mg/mL}$) was added to the reaction mixture, which was then stirred for 12 hours at room temperature. The solvent was removed under reduced pressure using a rotary evaporator at $30\,^{\circ}\mathrm{C}$. The residue was washed with ethanol to remove the excess ligands and the reducing agent. Finally, the product was separated by centrifugation at $5000\,\mathrm{rpm}$ for $30\,\mathrm{min}$ and dried in air. The obtained NCs were stored in a refrigerator at $4\,^{\circ}\mathrm{C}$ for further use.

H-Bond Driven Self-Assembly

The organization of $Au(I)_6$ nanoclusters into supramolecular architectures spontaneously occurs in solution phase depending on the chemical environment. In particular, introduction of formic acid to the clear dispersion of Au6 NCs in dichloromethane (DCM), triggers the self assembly of the NCs into nanoribbon (NR)-like superstructures (Au6-FA NRs), which can be isolated from the starting solution by centrifugation or sedimentation and stored for further analysis.

4.2 Structural and Morphological Characterization

Although this Thesis is primarily focused on the optical and photonic properties of superstructures, a thorough analysis of their structures and morphologies is paramount to gain deep insight into their structure-property relationships. In the following, all relevant techniques will be summarized.

4.2.1 Electron Microscopy

A significant portion of the structural and morphological characterisation of the samples presented in this Thesis was carried out by means of a number of electron microscopy techniques, including scanning electron microscopy (SEM), standard- and high-resolution transmission electron microscopy (TEM and HR-TEM), and cryogenic TEM (Cryo-TEM), which employ focused electron beams to probe materials with nanometer to sub-nanometer spatial resolution and thereby provide detailed insights into sample morphology, crystallinity, and internal structure. Such measurements were carried out thanks to a number of collaborations.

4.2.2 Dynamic Light Scattering

Dynamic Light Scattering (DLS) provides information on the hydrodynamic radius of particles in suspension by analyzing temporal intensity fluctuations of light scattered by the sample. DLS measurements reported in this Thesis were performed in collaboration with Prof. A. Emanuele (University of Palermo), by means of a custom setup constituted by a goniometer (Brookhaven BI-200SM), a CW laser unit ($532\,\mathrm{nm}$, $150\,\mathrm{mW}$), an avalanche photodiode (APD, Perkin-Elmer SPCM-AQR-14), and a 1088-channel multitau correlator (Flex-01). Each sample was appropriately diluted to limit the scattering intensity and placed in a thin quartz tube. Intensity distributions of decay times were obtained by numerically solving a Fredholm equation of the second kind [186]. Assuming that the scatterers are Brownian spherical particles of uniform density, the decay times are proportional to the radii of the scatterers, and the intensity distribution can be transformed into a mass distribution of particle sizes as follows:

$$\frac{M(R)}{M_{tot}} = \frac{\frac{I(R)}{R^3}}{\sum_R \frac{I(R)}{R^3}} \tag{4.1}$$

Where $M(R)$ is the overall mass of scattering particles of radius R. Notably, if particle sizes are not negligible with respect to the scattering vector, their scattering form factor must be taken into account.

4.2.3 Small-Angle X-ray Scattering

Small-Angle X-ray Scattering (SAXS) is a powerful technique that provides ensemble-averaged information on structural ordering over length scales up to several hundred nanometers, by measuring the elastic scattering of X-rays at small angles.

The SAXS measurements reported in chapter 7 were performed at the European Synchrotron Radiation Facility (ESRF, Beamline ID02) employing a $12.23\,\mathrm{keV}$ X-Ray beam ($100\,\mu\mathrm{m} \times 100\,\mu\mathrm{m}$) and a Eiger2-4M multi-panel detector placed at a distance of $1.3\,\mathrm{m}$ from the sample, thus guaranteeing a q-range from $0.006\,\mathrm{nm}^{-1}$ to $6\,\mathrm{nm}^{-1}$. The samples were either dropcasted on $70\,\mu\mathrm{m}$-thick glass substrates or placed in solution inside thin-walled quartz capillary tubes, and all measurements were performed in air and at ambient temperature. The sample holders were mounted on a 2D motorised stage to allow for fine movement on the sample plane. Preliminary data analysis was performed on-site *via* the provided online data reduction pipeline [187], which includes scan averaging, azimuthal integration, and masking of the central beam-stop and gaps between the detector panels.

The SAXS patterns presented in chapter 8 were obtained at the University of Pennsylvania, using a Pilatus 1M detector on a Xeuss 2.0 system (Xenocs, beam energy $8\,\mathrm{keV}$), with a sample-to-detector distance of 566 mm.

4.3 Optical Characterization

The optical properties of the superstructures were characterized by means of an array of techniques possessing various levels of temporal resolution, from the steady-state to the sub-nanosecond timescale. Additionally, as disentangling single-superstructure contributions from the ensemble-averaged signal often allows to gather precious insights into their photophysical and photonic properties, various microscopy techniques have been employed. In the following, each technique will be presented and discussed.

4.3.1 Steady-State Absorption

Ensemble UV-Vis absorption spectroscopy

Ensemble UV-Vis absorption measurements were performed *via* a fiber-optic CMOS spectrometer (Avantes Starline AvaSpec, $1\,\mathrm{nm}$ spectral resolution) coupled to a dual source deuterium/halogen lamp. The output of the lamp is guided by an optical fiber to the sample holder, where it passes through the sample (either in a quartz cuvette or dropcasted on a glass substrate). The transmitted light is then sent through a second optical fiber to the spectrometer, where its spectral distribution, $I_t(\lambda)$, is recorded. Before each measurement, two reference spectra were acquired: the incident light spectrum, $I_o(\lambda)$, obtained without the sample on the beam path, and the background spectrum, $I_b(\lambda)$, measured with the lamp shuttered. The three spectra are then combined to obtain the absorbance, or optical density, of the sample as:

$$A(\lambda) = \log_{10} \frac{I_o(\lambda) - I_b(\lambda)}{I_t(\lambda) - I_b(\lambda)} \tag{4.2}$$

Single-superstructure micro-UV-Vis

Micro-UV-Vis (μ-UV-Vis) measurements on single superstructures were performed in collaboration with Dr. S.A. Rigter and Prof. Dr. E.C. Garnett (University of Amsterdam and AMOLF Centre for Nanophotonics) on the integrating sphere microscopy setup described in [188]. Briefly, a monochromatised supercontinuum laser is tightly focused ($\sim 1\mu\mathrm{m}$ spot) on the sample, deposited on a $1\,\mathrm{mm}$ thick glass substrate and placed within a custom-built integrating sphere. Reflected and scattered light intensities are then measured as a function of the wavelength, with a $3\,\mathrm{nm}$ resolution. The recorded intensities are subsequently used to compute the absorbance according to:

$$A(\lambda) = -\log_{10}\left(1 - \frac{P_{abs}}{P_{in}}\right) \tag{4.3}$$

where P_{in} and P_{abs} indicate the incident and absorbed power, respectively.

4.3.2 Steady-State Photoluminescence (PL)

Ensemble PL and PLE

Ensemble photoluminescence (PL) and PL excitation (PLE) measurements on both solutions and dropcasted samples were carried out using a scanning

spectrofluorometer (Varian Cary Eclipse) equipped with a Xenon lamp. For PL experiments, a fixed excitation wavelength was chosen and the emission monochromator was scanned to record the emitted spectrum, whereas for PLE the emission wavelength was fixed and the excitation monochromator was scanned across the desired range. The scanning speed of the relevant monochromator, the integration time, and the number of averages were optimized for each measurement in order to maximise the signal-to-noise ratio.

Micro-PL

Micro-photoluminescence (μPL) measurements on single superstructures were performed by means of a modular setup assembled from a CW laser diode (Thorlabs), an optical microscope (Motic BA300), a monochromator (Acton SpectraPro 2300i), and a CCD camera (PI Pixis 400). The sample, drop-casted on a glass slide, is photoexcited by the focused beam of the laser diode, in a reflection wide-field geometry. An optical fiber ($1\,\mathrm{mm}$ core), positioned on the image plane of the microscope objective, collects the emission from a specific region of the sample containing only one superstructure. The collected light is subsequently dispersed by the monochromator and recorded by the CCD camera. Fluorescence images can be obtained by coupling a camera to one of the oculars of the microscope while filtering out the scattered laser light via a long-pass filter. For scale calibration, the image of a test pattern (Thorlabs) was acquired in the same experimental conditions as the measurements.

4.3.3 Absolute Quantum Yield

Absolute photoluminescence quantum yield (QY) experiments were carried out following a simplified version of the protocol reported in [189]. The spectrometer used for UV-Vis absorption measurements was coupled to an integrating sphere (LabSphere), and a CW laser diode (Thorlabs) served as the excitation source. The sample, contained in a thin quartz tube, was positioned inside the sphere and illuminated in the indirect excitation configuration. After recording the transmitted laser (L) and photoluminescence (P) spectra, the sample was replaced with a blank (an identical tube filled with pure solvent), and the reference laser spectrum (L_o) was measured. The QY was then calculated as:

$$\eta_{\%} = \frac{P}{L_o - L} \times 100 \tag{4.4}$$

4.3.4 Nanosecond-Resolved PL

Ensemble time-resolved PL

Ensemble time-resolved photoluminescence (TRPL) experiments were carried out *via* the setup schematised in Figure 4.1 and briefly described hereafter.

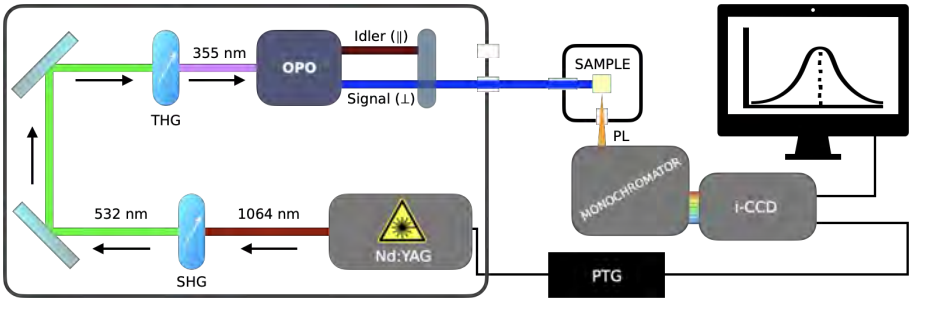

Figure 4.1: Scheme of the setup used for nanosecond-resolved PL measurements.

Excitation is provided by a tunable laser unit (Vibrant Opotek), incorporating a Q-Switched Nd:YAG laser which yields $5\,\mathrm{ns}$ pulses at $1064\,\mathrm{nm}$ with a maximum repetition rate of $10\,\mathrm{Hz}$. These pulses undergo second- and third-harmonic generation inside two successive nonlinear crystals, producing $532\,\mathrm{nm}$ and $355\,\mathrm{nm}$ beams, respectively. The third harmonic is then used to pump an optical parametric oscillator (OPO), generating two orthogonally polarised beams: the *signal* ($410 - 710\,\mathrm{nm}$) and the *idler* ($710 - 2400\,\mathrm{nm}$). A polariser is subsequently used to select one of the two beams and, if necessary, a further module is added to generate its second harmonic, guaranteeing full tunability in the range $210\,\mathrm{nm} \div 2400\,\mathrm{nm}$.
After exiting the laser unit, the pulses are steered towards the sample chamber, where photoexcitation occurs. The resulting PL emission is collected by a lens and enters a monochromator, where it is spectrally dispersed using one of three interchangeable gratings with different groove densities and blaze wavelengths, providing resolutions from about 3 nm down to 0.1 nm. The dispersed light is then detected by an intensified CCD (i-CCD, Princeton Instruments PI-Max), which employs a microchannel plate (MCP) for signal amplification. The i-CCD is synchronised with the laser unit by means of a programmable timing generator (PTG), acting as an electronic *gate*. The PTG enables the acquisition of the emission signal over a temporal window of predetermined

width (the *gate width*), starting from a controlled delay from photoexcitation (the *gate delay*). By fixing the gate width and scanning over an appropriate range of gate delays, the full decay kinetics of the emission band(s) can be reconstructed. Standard analysis procedures for kinetic traces typically involve background subtraction and least-square fitting to (multi-)exponential functions, appropriately convoluted with the instrumental response function (IRF). Additionally, by expanding the gate width to encompass the whole decay, steady-state PL spectra can be acquired. This is particularly useful for samples with poor QYs, for which the (non intensified) detector of a standard spectrofluorometer would not yield a sufficient signal-to-noise ratio.

Time-resolved PL microscopy

Time-resolved photoluminescence microscopy (μTRPL) was performed on a modular setup (PicoQuant Micro Time 100), constituted by an upright confocal PL microscope (Olympus BXFM), a $405\,\mathrm{nm}$ picosecond diode laser (PicoQuant Sepia LDH-D-C-405) with a tuneable intensity and a maximum repetition rate of $80\,\mathrm{MHz}$, and a detection unit based on a single-photon avalanche diode (SPAD, MPD PDM Series PD-100-CTB). The microscope is equipped with two interchangeable objectives ($20X/0.40$ and $100X/0.90$), guaranteeing laser spot sizes around $5\,\mu\mathrm{m}$ and $1\,\mu\mathrm{m}$, respectively. Optical micrographs were obtained by means of a monochrome CMOS camera (IDS) mounted on the ocular of the microscope. Neutral density (ND) filters are placed in front of the detector to ensure single-photon detection regime and, if necessary, appropriate band-pass filters are added to select desired portions of the PL emission profile. Under standard working conditions, the temporal resolution of the setup - determined by its instrumental response function - is around $200\,\mathrm{ps}$.

4.3.5 Transient Absorption Spectroscopy

Ultrafast Transient Absorption (TA) spectroscopy is a pump–probe technique that resolves changes in a sample's optical absorption induced by photoexcitation on sub-nanosecond timescales [190–193]. In a typical experiment, the sample is first excited by a quasi-monochromatic ultrafast optical pulse (the *pump*), which promotes a fraction of the ground-state population to electronically or vibrationally excited states. After a controlled time delay, a polychromatic ultrafast pulse (the *probe*) interrogates the sample, and its transmitted spectrum is recorded.

The transmitted probe intensity following photoexcitation, $I_p(\lambda)$, is compared with that of the unexcited sample, $I_u(\lambda)$, to determine the change in optical density. This quantity, commonly referred to as the TA signal, is defined as:

$$\Delta A(\lambda) = -\frac{1}{\ln 10} \ln\left(\frac{I_p(\lambda)}{I_u(\lambda)}\right) \simeq \frac{1}{\ln 10} \frac{I_u(\lambda) - I_p(\lambda)}{I_u(\lambda)} \tag{4.5}$$

where the second equality is valid in the - commonly verified - approximation of small absorbance variations, that is:

$$\left|I_p(\lambda) - I_u(\lambda)\right| \ll I_u(\lambda)$$

The TA signal generally arises from the combination of three contributions: *photoinduced absorption* (PA), *photoinduced bleaching* (PB), and *stimulated emission* (SE). To illustrate the origin of these components, Figure 4.2 depicts the sample as a multi-level system, with the pump resonant with the $|0\rangle \rightarrow |1\rangle$ transition.

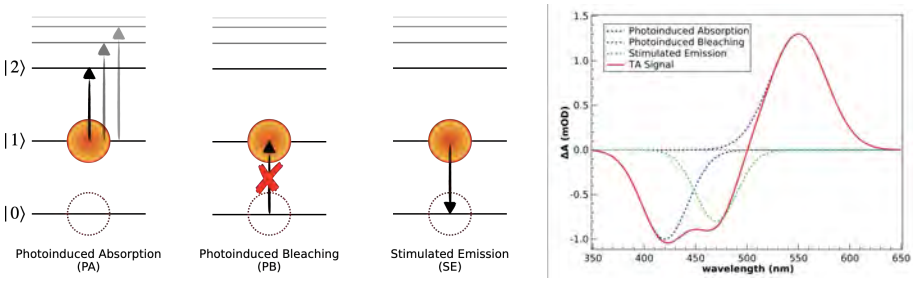

Figure 4.2: Left: schematic representation of the three main processes contributing to the TA signal. Right: exemplary TA spectrum, obtained as the sum of the three components (dotted curves).

Upon photoexcitation, a fraction of fluorophores is promoted from the ground state ($|0\rangle$) to state $|1\rangle$, enabling additional probe-induced transitions from this excited state to higher-lying states ($|1\rangle \rightarrow |2\rangle$, $|1\rangle \rightarrow |3\rangle$, . . .). These transitions, absent in the unexcited sample, produce a positive PA contribution at the corresponding wavelengths. Conversely, the depletion of the ground-state population reduces absorption at the $|0\rangle \rightarrow |1\rangle$ transition wavelength, giving rise to a negative PB signal. A further negative contribution arises from SE, whereby a probe photon resonant with the $|0\rangle \rightarrow |1\rangle$ transition induces an excited fluorophore in $|1\rangle$ to return to the ground state, emitting a second photon.

It should be noted that the SE signal typically resembles the sample's photoluminescence (PL) spectrum — though inverted in sign — since both processes originate from the same transition. However, small differences can occur for spectrally broad signals, as stimulated and spontaneous emission are governed by different Einstein coefficients with distinct wavelength dependencies. Furthermore, in an ideal two-level system, SE would be indistinguishable from PB, as both arise from the $|0\rangle \rightarrow |1\rangle$ transition. In real systems, however, the two processes are spectrally separated by a Stokes shift.

TA: setup

Most of the TA measurements reported in this Thesis were performed using the home-built setup schematised in Figure 4.3, pumped *via* the $800\,\mathrm{nm}$, $50\,\mathrm{fs}$ pulses ($\sim$ $200\,\mu\mathrm{J}$ per pulse) produced by a $5\,\mathrm{kHz}$ Ti:Sapphire regenerative amplifier (Spectra Physics, Solstice). The pulses are split by a 80%-20% beam splitter, to generate the pump and probe, respectively.

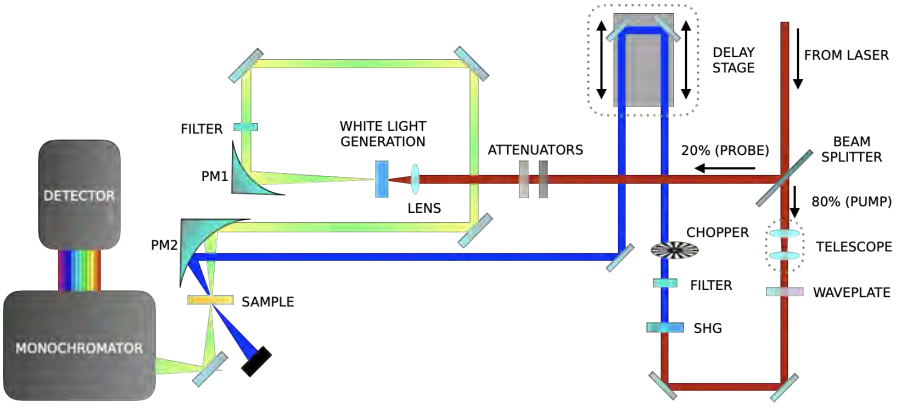

Figure 4.3: Simplified scheme of the home-built pump-probe setup employed for TA experiments

The former is obtained either by second harmonic generation ($\lambda = 400\,\mathrm{nm}$) in a $250\,\mu\mathrm{m}$ β-BBO crystal, or *via* a home-built noncollinear optical parametric amplifier (NOPA), enabling excitation in the range $490\,\mathrm{nm} \div 570\,\mathrm{nm}$ with a bandwidth up to $20\,\mathrm{nm}$, whereas the probe (spanning the range $400\,\mathrm{nm} \div 700\,\mathrm{nm}$) is generated by focusing the $800\,\mathrm{nm}$ pulses on a $1\,\mathrm{mm}$ cell containing D_2O. Both pump and probe are then focused by a parabolic mirror

($f = 150\,\mathrm{mm}$) on the sample, either dropcasted on a transparent substrate or flowing in a $0.2\,\mathrm{mm}$ flowcell driven by a peristaltic pump. Notably, the probe is focused on an area (approximately $45\,\mu\mathrm{m}$ in diameter) sensibly smaller than the pump spot ($\sim 80\,\mu\mathrm{m}$), in order to ensure that the probed portion of the sample is uniformly photoexcited by the pump. The transmitted probe is collected, dispersed by a prism-based monochromator and focused on a single-shot detector (Glaz, LineScan-I). A chopper wheel, placed along the path of the pump, blocks every other pump pulse, allowing for the alternate detection of photoexcited and unexcited spectra, whereas the pump-probe delay is controlled by a motorised delay stage. In a typical experiment, a total of 2500 photoexcited and 2500 unexcited spectra is collected at each delay, and the whole acquisition is repeated a minimum of 10 times. A waveplate on the pump arm allows to control the relative polarisation of the two beams, which was kept at the *magic angle* for all measurements. The magic angle configuration, corresponding to a relative angle of $54.7°$ between the pump and probe polarisation directions, ensures that the measured signal reflects pure population dynamics, without influences from rotational diffusion [194]. Under standard working condition, the setup guarantees a spectral resolution of $3\,\mathrm{nm}$ and a temporal resolution (instrumental response function - IRF) of around $80\,\mathrm{fs}$. For each measurement, the pump power was kept at a sufficiently low value to avoid nonlinear contributions.

Some of the TA measurements reported in chapter 8 were instead performed in collaboration with the group of Dr. Alessandra Paladini (CNR-ISM, Rome) on the setup reported in [117] and briefly described hereafter. The setup employs a laser system (Coherent) consisting of a $1\,\mathrm{kHz}$, $4\,\mathrm{mJ}$, $35\,\mathrm{fs}$ chirped pulse amplifier seeded by a Ti:Sapphire oscillator ($\lambda = 800\,\mathrm{nm}$). The probe is generated by focusing $3\,\mu\mathrm{J}$ of the laser light into a rotating CaF_2 crystal. The generated white light supercontinuum is then collimated, and subsequently focused onto the sample. The optical layout of the commercial TA spectrometer (Femto-Frame II, IB Photonics) consists of a split beam configuration in which 50% of the white light ($350 \div 800\,\mathrm{nm}$) passes through the sample, while the remainder is used as a reference to account for pulse-to-pulse fluctuations in the white light generation. The pump pulses at 370 and $550\,\mathrm{nm}$ were generated from an optical parametric amplifier (OPerA-Solo, Coherent). The pump pulse was loosely focused (circular spot diameter of $200\,\mu\mathrm{m}$) onto the sample

with an energy density from 0.1 to $1.7\,\mathrm{mJ/cm^2}$. The probe pulse was smaller ($\approx 150\,\mu\mathrm{m}$) and was delayed in time with respect to the pump by varying the length of its optical path. The IRF of the setup was measured to be $\approx 50\,\mathrm{fs}$.

TA: data correction and analysis procedures

Independently of the setup, the TA scans, performed as described above, were averaged out and underwent standard correction procedures accounting for group velocity dispersion (GVD) and cross-phase modulation (XPM) [45]. The result of this procedure is a *M*×*N* TA matrix, $TA(\lambda,t)_{M,N}$, from which both spectra at fixed delays and kinetic traces at a fixed wavelength can be extracted. In order to discriminate the processes governing the temporal behavior of the sample, the kinetic traces were typically fitted by a multiexponential model convoluted with a Gaussian IRF, that is:

$$F_{A_i,\tau_i,\Gamma}(t) = \sum_i A_i \left(e^{-t/\tau_i}_{t>0}\big|_{IRF} \right) = \sum_i A_i H_o(t) e^{-t/\tau_i} * IRF_\Gamma(t) \quad (4.6)$$

where A_i account for the weights of the various decay components, $H_o(t)$ is the well-known Heaviside function, accounting for the absence of signal at $t < 0$, and Γ indicates the width of the Gaussian IRF.
When necessary, a more refined singular value decomposition (SVD) protocol was employed. SVD consists in decomposing the original TA matrix as:

$$\mathbf{TA}(\lambda,t) = \mathbf{U}(\lambda) \times \mathbf{S} \times {}^{T}\mathbf{V}(t) \quad (4.7)$$

where $\mathbf{U}(\lambda)$ and $\mathbf{V}(t)$ are the *eigenspectra* and *eigentraces* matrices, respectively containing the spectral and kinetic information, while the diagonal *eigenvalues* matrix, $\mathbf{S}$, contains the weights associated with each eigenspectrum and its corresponding eigentrace. The aim of SVD is to single out the main processes involved in the signal, filtering out any unwanted noise. This is done by only selecting the eigenspectra and eigentraces with the largest eigenvalues, while discarding the rest. Great care must be taken when determining the number of components to retain, as weaker signals could easily be lost amongst the noise. Following SVD, the purified matrix is subjected to a global fit, that is all eigentraces are simultaneously fitted with a function $F_{A_{ij},\tau_i,\Gamma}(t)$ of the form given in (4.6), assuming Γ and all timescales τ_i as common parameters and treating only the amplitudes A_{ij} as local coefficients. Subsequently,

each time constant τ_i emerging from the fit can be linked to a spectrum, the decay-associated spectrum (DAS), defined as:

$$DAS_i(\lambda) = \sum_j A_{ij} S_{jj} U_j(\lambda) \tag{4.8}$$

where S_{jj} and U_j respectively indicate the j-th eigenvalue and its corresponding eigenspectrum. In essence, each DAS represents the spectral fingerprint of the specific process accounted for by the corresponding time constant. Therefore, the TA signal can be reconstructed as:

$$TA(\lambda, t) = \sum_i DAS_i \left(e^{-t/\tau_i}_{t>0} |_{IRF} \right) \tag{4.9}$$

4.3.6 Transient Absorption Microscopy

Transient absorption microscopy (TAM) - also called micro-pump-probe (μPP) - is a powerful technique combining traditional TA spectroscopy and optical microscopy [9, 195–203]. In general, this is achieved by tightly focusing the pump and probe beams on a desired portion of the sample, and collecting the transmitted probe by means of a microscope objective. The unique synergy of high spatial and temporal resolutions allows TAM to probe the photoinitiated dynamics of isolated superstructures at the femtosecond and picosecond timescales. Furthermore, by appropriately controlling the position and spot size of pump and probe, various acquisition configurations can be obtained, each tailored for a specific purpose. Typical configurations include:

- *Tightly focused, overlapping pump and probe*: In this configuration, the pump and probe beams overlap on a single isolated structure, similar in concept to conventional TA but with much smaller spot sizes and precise spatial control guaranteed by microscopy [9]. This enables the dynamics of single superstructures to be disentangled from ensemble-averaged responses, which are unavoidable in standard TA. Moreover, raster-scanning the overlapped beams allows mapping of ultrafast responses across multiple regions of the sample. Most of the TAM measurements reported in this Thesis were performed in this configuration.

- *Tightly focused, non-overlapping pump and probe*: In this geometry, the pump excites a given portion of the sample, while the probe is focused

on an adjacent one. This arrangement, uniquely enabled by TAM, is particularly useful to probe excitation- or energy-transfer phenomena, whereby the effects of photoexcitation propagate from the initially excited spot to the probed region [196]. Additionally, by raster-scanning the probe away from the pump spot, it is possible to directly observe the spatial propagation of the excitation. As discussed in chapter 5, we have used this approach to study excitation transfer in dimers of QD superparticles, gaining precious insight into their photonic coupling.

- *Wide-field pumping and probing*: In this configuration, both pump and probe beams are expanded to uniformly illuminate a large area of the sample, and the photoinduced change in the probe transmission (or reflection) is imaged onto a camera [203]. Rather than raster-scanning a focused probe, the TAM signal is acquired in parallel over the entire field of view, enabling the simultaneous interrogation of many structures or extended sample regions. This wide-field approach is particularly well suited for rapidly generating spatial maps of ultrafast dynamics, identifying heterogeneities, and correlating optical responses with morphology.

While, in recent years, TAM has been employed in various instances to study thin films and 2D heterostructures [9, 204–207], its application to the study of single nanocrystal superstructures is widely underexplored. Therefore, a portion of my PhD was dedicated to the construction of a custom TAM unit, employing the pump and probe beams from the TA setup described in the previous section. The transition from TA to TAM is achieved by inserting a plane mirror in front of the parabolic mirror used to focus the beams onto the sample (labeled PM2 in Figure 4.3), thereby steering both beams towards the TAM unit. This configuration offers two key advantages: First, switching between the two setups is almost trivial, requiring only the positioning or removal of a single mirror; Secondly, by steering both beams along the same path, the relative delay between pump and probe pulses (and consequently the zero-time) is preserved when switching between TAM and TA.

The working geometry of the TAM unit is reported in panel (a) of Figure 4.4.

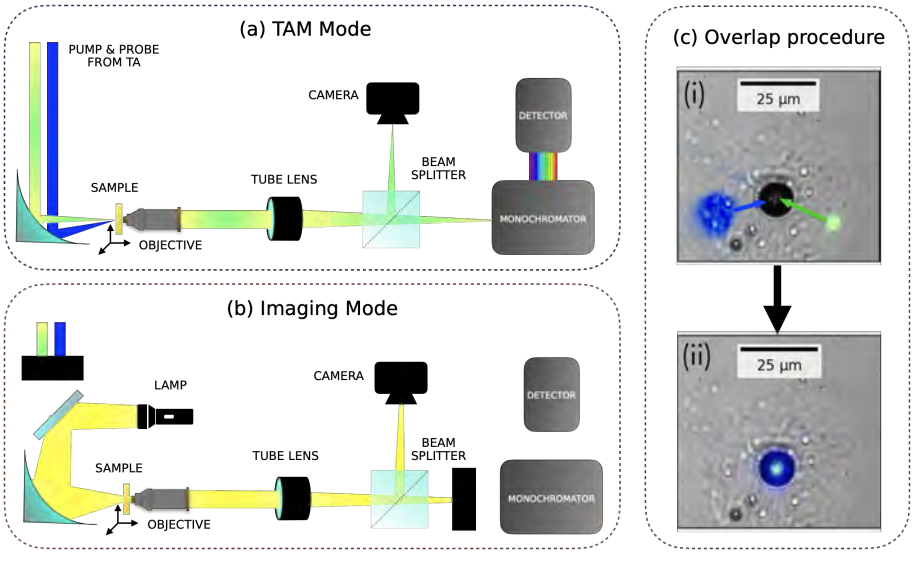

Figure 4.4: Left: Simplified scheme of the home-built TA microscopy setup in TAM (a) and imaging (b) configurations (the beampath of the pump after the sample in panel (a) is omitted for simplicity); Right: reconstructed micrograph exemplifying the overlap procedure of the pump and probe spots over a single superstructure.

A parabolic mirror ($f = 20\,\mathrm{mm}$) tightly focuses the pump and probe on the sample, and a $40X/0.65$ infinity-corrected microscope objective (Olympus Plan N) is used to collect the transmitted probe. The sample is dropcasted on a thin glass substrate (whenever possible, $70\,\mu\mathrm{m}$-thick cover glasses were used) and mounted on a sample holder fixed to a three-axis micrometric translation stage, allowing precise focusing as well as fine lateral positioning across the sample plane. To minimize the GVD and XPM effects introduced by the glass, the substrate was preferentially oriented with the sample facing the incoming beams, within the constraints imposed by the working distance of the microscope objective. The collected probe passes through a tube lens (Thorlabs, effective focal length $180\,\mathrm{mm}$), which relays the image formed by the infinity-corrected objective onto the detection plane, located at the tube lens focal distance, before reaching a beam splitter cube. Because the space between the objective and the tube lens corresponds to the infinity-corrected region of the optical path, additional elements such as filters can be conveniently inserted

there without affecting the image formation. The portion of the probe transmitted by the beam splitter (90%) is directed into a grating-based monochromator with a spectral resolution of $0.5\,\mathrm{nm}$, and subsequently detected by the same spectrograph used in the TA setup. The reflected portion (10%) is sent onto a monochromatic CCD camera (Thorlabs) positioned at the detection plane, providing a real-time micrograph of the probe spot. As schematised in panel (b) of Figure 4.4, the same camera can be used to obtain optical micrographs of the sample by shuttering the pump and probe and directing the light of a LED lamp onto the sample. Fluorescence micrographs can also be readily obtained by using a CW diode instead of the lamp and adding an appropriate long-pass filter between the objective and tube lens.

Before each experimental session, the focal planes of the parabolic mirror and microscope objective are carefully matched by minimising the size of the probe spot as seen by the CCD camera. Under typical working conditions, the probe can be focused down to a spot with a full width at half maximum (FWHM) of $2\,\mu\mathrm{m}$, determining the resolution of the setup, whereas the pump spot, whose size can be tuned as needed, is typically set at a diameter of $15\,\mu\mathrm{m}$ FWHM. Subsequently, the sample is placed on the common focal plane and imaged to select the region of interest. Finally, for a standard measurement, the pump and probe are overlapped over the desired point of the sample (for instance, a single superstructure, as exemplified in panel (c) of Figure 4.4), and the measurement is carried out as explained in the previous section. TAM data undergo the same reduction and analysis procedures discussed for TA measurements.

Importantly, the scattering properties of micrometre-sized structures, together with the numerical aperture of our objective (0.65), have important consequences on the interpretation of TAM data. To gain a better understanding of this aspect, first-principle numerical simulations were performed in collaboration with Prof. S. Lorenzo (University of Palermo). In particular, we simulated the scattering of a gaussian beam ($2\,\mu\mathrm{m}$ FWHM) with a single QD superparticle, modelled as a dielectric sphere of radius $a = 5.4\,\mu\mathrm{m}$ with an effective refractive index obtained as the weighted average of the refractive indexes of its components, namely CdSe, CdS and oleate ligands. While the theoretical details of the simulations are beyond the scope of this Thesis and are reported in full in [208], the main findings are summarised below.

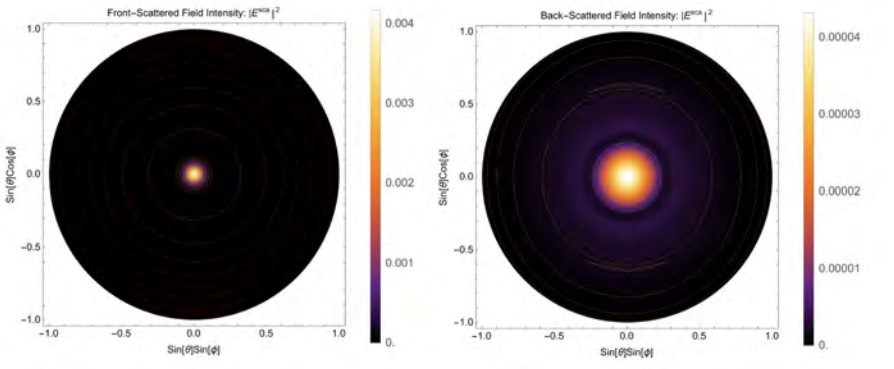

Figure 4.5: Front-Scattered (left plot) and Back-Scattered (right plot) field intensity for a $2\,\mu\mathrm{m}$ FWHM gaussian beam impinging on a dielectric sphere of radius $a = 5.4\,\mu\mathrm{m}$. Adapted from [208].

Figure 4.5 reports the simulated intensities of front- and back-scattered light at infinite distance as a function of angle. A simple comparison reveals that almost all the light is front-scattered at angles well within the $(2\vartheta \approx 80°)$ acceptance cone of our microscope objective. A rather straightforward calculation shows that, if the totality of scattered light is collected by the microscope, any TAM signal must be the consequence of a genuine photoexcitation-dependent absorbance variation. Indeed, let I_o be the incident probe intensity, and I_A, I_T, and $I_S(\Omega)$ the absorbed, transmitted, and scattered intensities, respectively. It follows that:

$$I_o(\lambda) = I_A(\lambda) + I_T(\lambda) + \int I_S(\lambda, \Omega)\, d\Omega \tag{4.10}$$

Assuming the entirety of scattered light is collected by the objective, we have:

$$I_{coll}(\lambda) = I_T(\lambda) + \int I_S(\lambda, \Omega)\, d\Omega = I_o(\lambda) - I_A(\lambda) \tag{4.11}$$

Therefore, according to (4.5), we have:

$$\Delta A(\lambda) = -\frac{1}{\ln 10} \ln\left(\frac{[I_o(\lambda) - I_A(\lambda)]_P}{[I_o(\lambda) - I_A(\lambda)]_U}\right) \tag{4.12}$$

where the indexes P and U indicate the photoexcited and unexcited systems, respectively. Because I_o does not depend on photoexcitation, any non-zero $\Delta A(\lambda)$ must be the consequence of a difference between $[I_A(\lambda)]_P$ and $[I_A(\lambda)]_U$ - that is to say - any TAM signal must stem from a photoinduced variation in the absorption profile of the system.

Part II

Results: Semiconductor-Based Superparticles

5

Quantum Dot Superparticles I: Ultrafast Modulation of Whispering Gallery Modes

So often, research needs to be somehow motivated by some societal need or application, which is fine, but there also needs to be space for just being curious, because that's where the discoveries actually come from.

— Moungi Bawendi

Microscopic dielectric structures such as quantum dot superparticles can leverage geometry and photophysics to confine light, acting as microresonators. Furthermore, photoexcitation of these structures with ultrafast light pulses opens interesting routes to reversibly manipulate the spectral pattern of photonic resonances on femto- and picosecond time scales. In this chapter, we will explore the use of femtosecond light pulses to drive reversible changes in the

resonances of quantum dot superparticle microresonators over a broad spectral range. Leveraging pump-probe microscopy, we will investigate the dynamic modulation of their photonic response, providing crucial insight into the photophysics of semiconductor superstructures and paving the way to their prospective application as ultrafast optical switches for photonics, optoelectronics, and communication technologies. Our results demonstrate that ultrafast photoexcitation can initiate ultrafast excitation transfer between neighboring superparticles, forming a dimer, and induce electronically and thermally driven changes in the refractive index of individual superparticles, dynamically modulating their resonances on distinctive time scales. The findings reported in this chapter have been published in [208].

5

5.1 Introduction

The organized assembly of nanocrystals into mesoscopic superparticles (SPs) introduces new properties stemming from interactions between constituents [209, 210]. Additionally, SPs often manifest *emergent* properties, that is behaviours or responses that cannot be seen as a mere *sum* of the properties of the constituent nanocrystals. As a prime and extremely interesting example of such emergent behaviours, circularly symmetric semiconductor superparticles can support whispering gallery modes (WGMs) [211–213], sharp optical resonances due to quasi-total internal reflection of light within a round dielectric cavity, strongly influenced by the SP's radius and refractive index. The spectral positions of the WGM resonances in a microresonator of diameter d corresponding to the transverse electric (TE) and transverse magnetic (TM) modes of the electromagnetic field can be calculated according to the Mie theory [84], as [211, 212]:

$$\lambda_{i,l} = \pi d n_s \left[\mu + \alpha_i \left(\frac{\mu}{2} \right) - \frac{p}{\sqrt{m^2+1}} + \right. \\ \left. + \frac{3\alpha_i^2 (4\mu)^{-1/3}}{10} - p \frac{m^2 - \frac{2}{3}p^2}{(m^2-1)^{3/2}} \frac{\alpha_i}{(2\mu^2)^{1/3}} \right]^{-1} \tag{5.1}$$

Where i and l are the radial and angular mode numbers of the resonance, $\mu = l + 1/2$, $m = n_s/n_e$ is the ratio between the refractive index of the sphere and that of the environment, α_i is the i-th zero of the Airy function [214], and p accounts for the two different modes ($p = m$ for TE modes and $p = 1/m$

for the TM modes). To first approximation, the resonance frequencies form a progression according to:

$$\nu_l \simeq c\frac{l}{2\pi an} \tag{5.2}$$

where c is the speed of light, a is the radius of the microresonator, and l is an integer mode index).

SPs whose light absorption and/or emission overlaps with at least some of the resonator modes, behave as active microresonators [215, 216], a novel class of systems showing great promise for applications such as fine-tunable microlasers [86, 217–219] and anticounterfeiting microlabels [220]. Although these artificial solids have the potential to result in real-world applications in photonics and optoelectronics, their fundamental physical understanding remains at an early stage. Besides, existing studies have scarcely addressed how light can induce ultrafast reversible changes in the wide-band optical response of SPs, a concept that may enable a wide range of new applications in photonics. Addressing the functional optical response of SPs requires experimental methods capable of spatial resolution comparable to the SP size (μm) and of resolving the dynamics initiated by photon absorption down to the pico- and femtosecond timescale. These are both the typical time scale of semiconductor QD relaxations [49, 221] and of relevant cross-talk and collective phenomena involving the whole SP, such as long-range excitation migration or light propagation over micrometer distances. Indeed, previous studies [222, 223] on the optical modulation of microresonators were typically limited in temporal and spectral resolution. To meet such demands for high spatial and temporal resolution, we employed ultrafast transient absorption microscopy (TAM, see chapter 4) [196, 201], a recently developed technique able to provide unique insight into the photophysics of SPs. Recently, TAM was used to address nanostructured systems such as perovskite and metal chalcogenide QD films and organic-inorganic heterostructures. However, broadband, femtosecond-resolved TAM has not yet been used to probe the photoinduced changes in optical microresonators, despite its potential to provide key insight into their optical response and functional photonic behavior.

5.2 Results and Discussion

The *building blocks* for the superstructures presented both in this chapter and in the next one, are oleate-capped CdSe/CdS core/shell QDs, $10.3\,\mathrm{nm}$ in diameter, constituted by a $3.5\,\mathrm{nm}$ core surrounded by an eight monolayer thick CdS shell, yielding a *quasi-type II* architecture. Panel (a) of Figure 5.1 reports a representative TEM image of these QDs, which are then assembled, according to a synthetic approach recently demonstrated by Marino *et al.* [77] and schematised in panel (b), into quasi-monodisperse, spherical SPs (panel (c)).

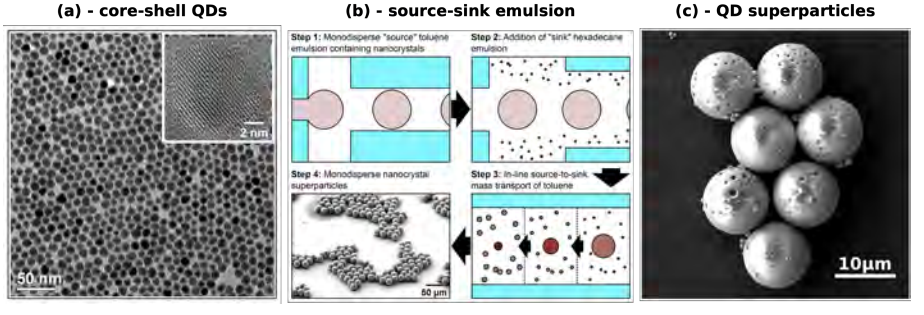

Figure 5.1: (a) TEM image of the CdSe/CdS core/shell QDs. The inset shows an HRTEM image of a single QD; (b) schematic representation of the source-sink emulsion assembly procedure (adapted from [77]); (c) SEM image of a group of QD SPs, highlighting their accurate spherical shape and very low polydispersity.

These SPs, $10.8 \pm 0.1\,\mu\mathrm{m}$ in diameter, behave as active microresonators with the QD superstructure serving as both active medium and resonator cavity [216]. In this chapter, we will explore this peculiar behaviour by using TAM to photoexcite and interrogate individual SPs, allowing to track WGM modulation effects with simultaneously high temporal, spectral, and spatial resolutions. Before delving into this study however, it is instructive to analyse the steady-state optical properties of our superstructures.

5.2.1 SPs: steady-state optical response

Figure 5.2 compares steady-state optical measurements on the QDs (panels (a) and (c)) and their SPs (panels (b), (d), and (e)). The QDs (panel (a)) strongly absorb light with wavelengths $\lambda < 520\,\mathrm{nm}$ due to their thick CdS shell (bandgap = $2.42\,\mathrm{eV}$, corresponding to a wavelength of $512\,\mathrm{nm}$), while

the much weaker absorption at $\lambda > 520\,\mathrm{nm}$ stems from the quantum confined CdSe core. The assembly of QDs into SPs significantly increases light scattering, making a traditional absorption measurement impossible. Thus, we used an integrating sphere-based micro-absorption method [188] to remove the scattering contribution from the extinction spectrum of a single SP (see chapter 4 for details). Panel (b) of Figure 5.2 displays one such measurement. The absorption cross-section of SPs shows saturation at short wavelengths ($\lambda < 520\,\mathrm{nm}$), a behavior already observed by Marino *et al.* [78]. This was previously attributed to the strong photonic coupling between QDs allowing the SP to reach an absorption cross-section σ comparable to the geometrical cross-section πa^2, in contrast to individual QDs, for which $\sigma \ll \pi a^2$.

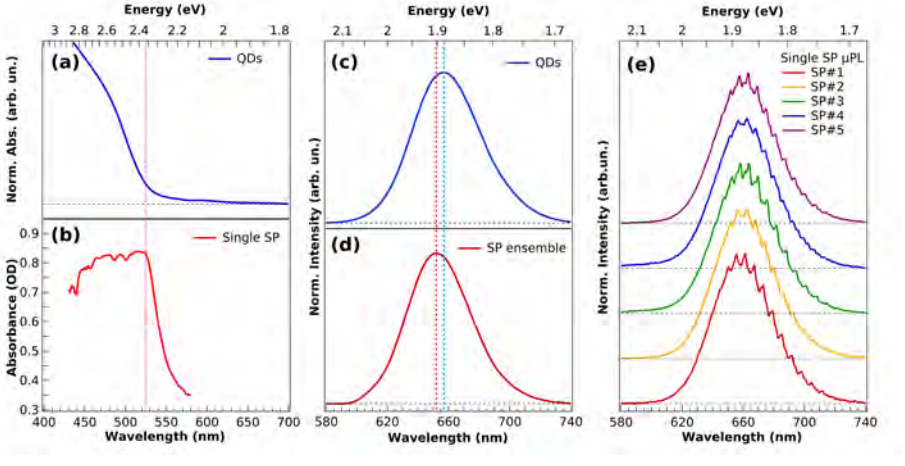

Figure 5.2: Steady-state optical response of QDs and SPs. (a) UV-Vis spectrum of well-dispersed QDs; (b) μ-UV-Vis spectrum of a single SP; (c-d) ensemble steady-state PL spectra of QDs (c) and SPs (d); (e) micro-PL spectra of five distinct SPs, vertically shifted for clarity.

Thanks to the strongly confined CdSe core, both QDs and SPs are highly photoluminescent, with comparable quantum yields of $\sim 90\%$. Ensemble measurements of well-dispersed QDs and SPs show smooth emission spectra differentiated by a 5 nm shift (panels (c-d) of Figure 5.2). Microphotoluminescence measurements (panel (e)) of individual SPs reveal their light-coupling properties. Regular, narrow peaks appear on top of the broad fluorescence envelope due to the microresonator SP selectively enhancing emission rates at its resonance frequencies [224]. The modulations appear more intense on the

red side of the envelope, likely because of increasing optical losses on the blue side [86, 225]. A direct comparison of several SPs shows that the position and relative intensities of the modulations are unique to each SP, owing to the strong dependence of WGMs on the size and shape variations among SPs. This causes the WGM features to average out in an ensemble spectrum (panel (d)). WGMs should also appear in the μ-UV-Vis spectrum in panel (b). However, these measurements mainly cover the region of high light absorption, where the quality factor of WGMs is low and the instrument's spectral resolution ($\sim 3\,\mathrm{nm}$) is insufficient.

5.2.2 TAM on single SPs

Having clarified the steady-state properties of our SPs, we proceeded to use TAM to explore their time-dependent excitation and relaxation. Contrary to traditional pump-probe spectroscopy, TAM allows isolating genuine absorption variations from scattering contributions (as discussed in chapter 4) and revealing photoinduced WGM changes by probing single SPs rather than an ensemble. Figure 5.3 summarizes the typical relaxation behavior of a single SP, as revealed by TAM measurements. The SP, deposited on a glass substrate, was excited with $0.3\,\mathrm{mJ/cm^2}$, $50\,\mathrm{fs}$ light pulses at $400\,\mathrm{nm}$ and probed in the range $440-680\,\mathrm{nm}$ at several time delays from photoexcitation. For this experiment, we employed a $14\,\mu\mathrm{m}$ FHWM pump to ensure that the SP is uniformly illuminated, and a much smaller ($< 2.5\,\mu\mathrm{m}$ FHWM) probe, aligned at the center of the SP. Differential absorption spectra at varying pump-probe delays are displayed in panel (b) as a heat map. From this map, we extract spectra at specific delays (panel (c)) and kinetic traces (panel (d)) by vertical and horizontal cuts, respectively. The inset in panel (c) shows that the TAM spectra display regular modulations over the broad signal envelope. This intriguing aspect will be thoroughly discussed after analyzing the underlying broader spectral shape. So-called state-filling effects [49] dominate the photoinduced dynamics of our SPs, leading to photoinduced bleach (PB) features appearing at the position of allowed optical transitions. Indeed, the TAM spectra display PB peaks at $\simeq 615\,\mathrm{nm}$ ($2.02\,\mathrm{eV}$), $\simeq 580\,\mathrm{nm}$ ($2.16\,\mathrm{eV}$), and $\simeq 545\,\mathrm{nm}$ ($2.28\,\mathrm{eV}$), coherently with known excitonic transitions for CdSe QDs [49], namely 1S [$1s(e) - 1s_{3/2}(h)$], 2S [$1s(e) - 2s_{3/2}(h)$], and 1P [$1p(e) - 1p_{3/2}(h)$]. The signals rise in $\simeq 3\,\mathrm{ps}$, because of the relaxation of charge carriers from highly

excited states down to the band edges driven by electron-phonon scattering. We also observe a short-lived photoinduced absorption (PA) around $540\,\mathrm{nm}$ ($2.30\,\mathrm{eV}$). The whole signal partially decays on a time scale of hundreds of picoseconds due to radiative and nonradiative depopulation of the lowest excited state.

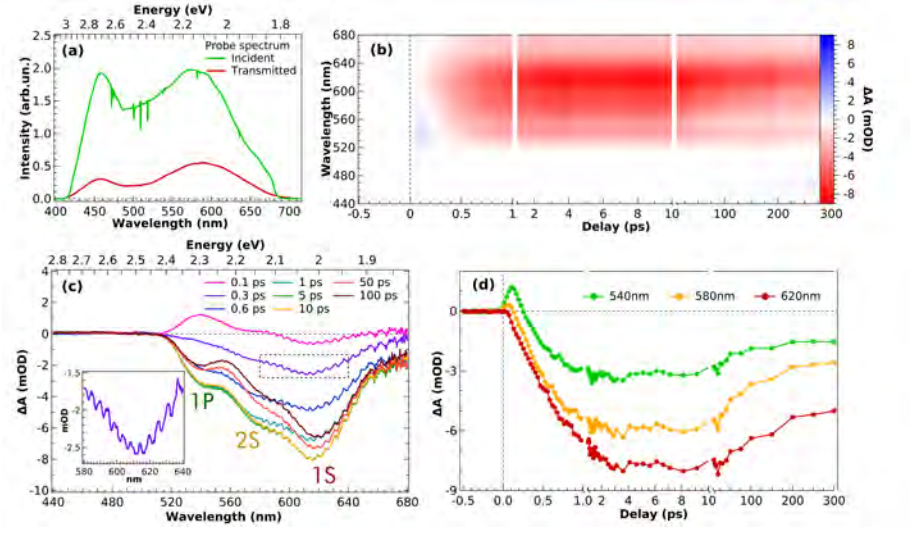

Figure 5.3: Transient Absorption Microscopy on a single SP. (a) Comparison between the spectral profiles of the incident probe light (green) and the probe light transmitted through a SP (red); (b) Two-dimensional time-wavelength plot of the pump-probe signal of a single QD superparticle; (c) TAM spectra at fixed pump-probe delays extracted from vertical cuts of panel (b). The labels 1S, 2S, and 1P indicate PB signals corresponding to known transitions of CdSe QDs, while the inset highlights the presence of modulations over the envelope of the pump-probe signal; (d) Kinetic traces extracted as horizontal cuts of panel (b) at fixed wavelengths.

Furthermore, the signal at $\lambda < 520\,\mathrm{nm}$ is zero at all delays (panel (c) of Figure 5.3), despite probe light in that spectral range still partially penetrating the SP (as shown in panel (a)). This expands on the saturation effect observed in μ-UV-Vis (panel (b) of Figure 5.2), highlighting that the saturated absorption cross section is unaffected by photoexcitation. A more thorough study of the photophysics of these SPs, together with a systematic comparison with the behaviour of the constituent QDs, will be the subject of the next chapter.
We explored the variability among three different SPs by comparing their TAM signals obtained under identical experimental conditions ($0.3\,\mathrm{mJ/cm^2}$ pump

pulses at 400 nm), as shown in Figure 5.4. While the main TAM spectral features are always present, their intensity ratios and exact spectral positions differ. For example (panel (a)), the lowest-energy 1S bleach peak at short delays is located at 614, 604, and 606 nm for the three SPs. This result emphasizes the need to study the SPs individually, as their absorption fingerprint is a unique and collective property of each SP, conditioned by minute changes in their size (1% polydispersity), shape, and refractive index. Despite these differences, the kinetic traces extracted at the PB positions are identical (panel (d)), suggesting a common relaxation pathway following photoexcitation.

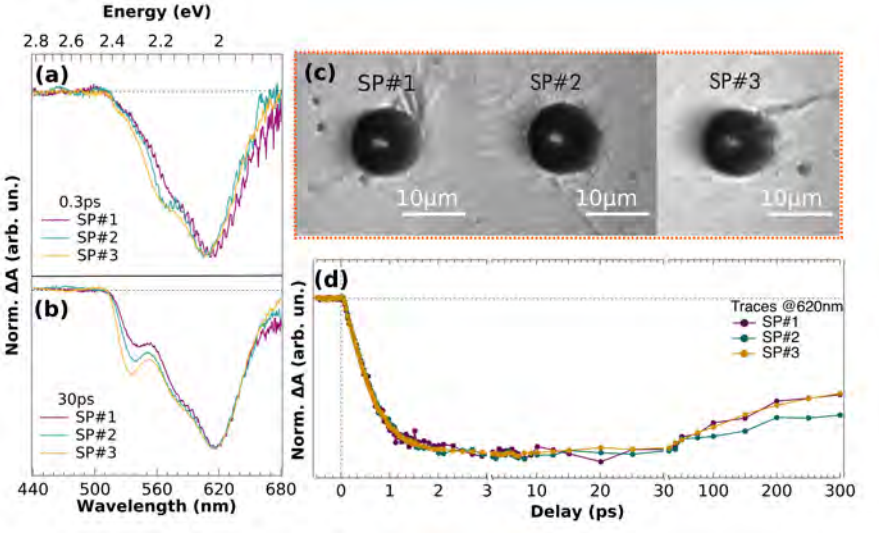

Figure 5.4: Comparing the TA response of three distinct SPs. (a-b) Normalised TAM spectra of three SPs at 0.3 ps (a) and 30 ps (b) pump-probe delays; (c) optical micrographs of the three SPs under study; (d) normalised kinetic traces of the three SPs, exctracted at $\lambda = (620 \pm 10)$ nm.

5.2.3 Ultrafast modulation of WGM resonances

We now focus on the most peculiar feature of these TAM signals: a complex modulation structure appearing over the broad signal envelope (inset of Figure 5.3(c) and panel (a) of Figure 5.5). To study the nature of the modulations, we isolate them from the signal envelope by subtracting, at each pump-probe delay, a smoothed version of the signal (panels (b-c) of Figure 5.5). The residual signals obtained for the three SPs are shown in Figure 5.5(e).

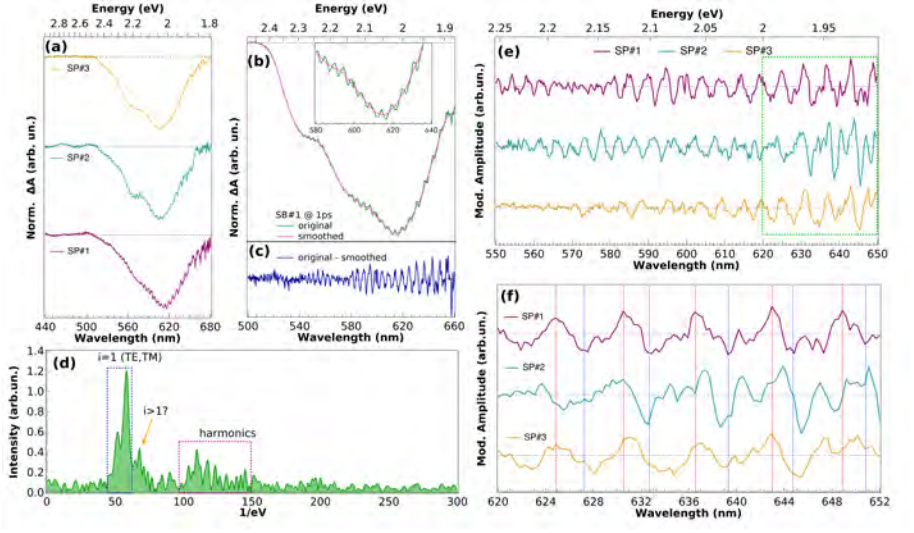

Figure 5.5: Unraveling the photonic properties of single SPs via TAM. (a) Normalized TAM spectra of SP#1, SP#2, and SP#3 (shown in panel (c) of Figure 5.4) at 0.3 ps pump-probe delay, vertically shifted in order to highlight the different relative intensities of the modulations (more visible in SP#1, less so in SP#2, almost imperceptible in SP#3); (b-c) exemplification of the analysis procedure used to extract the modulations; (d) fast Fourier transform (FFT) of the modulations shown in panel (c), plotted as a function of energy, the rectangles and arrows pinpoint the main frequency components; (e) modulations of SP#1, SP#2, and SP#3 at 1 ps delay, extracted as shown in panels (b) and (c); (f) Zoom of the extracted modulations in the range 620-652nm (green rectangle in panel (d)). The vertical lines pinpoint the positive (red) and negative (blue) lobes in the modulation of SP#1, highlighting the differences in spectral positions with respect to those of SP#2 and SP#3.

The coarse structure of these spectral modulations is a progression of negative and positive lobes in close succession. Considering the nature of our SPs as microresonators, we link these modulations with the microresonator modes, known to be extremely sensitive to the refractive index and radius of the resonator [226]. This link is more subtle than it seems: because of the differential nature of the TAM technique, any signal results from a change between the photoexcited and the nonexcited state of the system. Therefore, we conclude that these transient modulations arise from a modification of the WGM resonances, which can only be due to a photoinduced change $\Delta(an)$ of the refractive index n and/or the radius a of the SP. Thus, TAM is successful in interrogating and probing the photoinduced changes in the frequency structure

of the microresonator. To fully appreciate the spectral shape of the observed modulations, it is crucial to keep in mind that the frequency structure of the WGMs is non-trivial and not expected to appear as a simple frequency comb with a single periodicity. As reported in the literature [226], one expects to observe modes with different values of the radial index $i = \{1, 2, 3, \dots\}$, each comprising two separate progressions (TE and TM modes) with slightly different periodicity from each other and depending on the radial index. Normally the visibility of WGMs rapidly goes down with increasing radial index because of increased losses, which tends to simplify the otherwise very complex structure of the resonator. To better highlight the frequency structure of our modulations, we performed a fast Fourier transform (FFT) of the modulation amplitude as a function of energy. From the FFT (panel (d) of Figure 5.5), at least three peaks clearly emerge over the background: two of these peaks are very close to each other and are associated to the TE and TM progressions at $i = 1$, while the third is most likely the frequency comb generated by modes with higher radial index ($i = 2$ and larger).

Several observations corroborate our interpretation. First, the precise spectral positions and amplitudes of these modulations vary between SPs (panels (e-f) of Figure 5.5), consistently with the changes in WGM progression observed in the microphotoluminescence spectra (Figure 5.2(e)). Second, the modulations observed in TAM become less intense in the blue and disappear entirely below $\simeq 530\,\mathrm{nm}$, coherently with the decreasing quality factor of WGM resonances due to increasing optical losses [226, 227] (dropping from $Q > 10^3$ at $550\,\mathrm{nm}$ to $Q \simeq 32$ at $530\,\mathrm{nm}$). Third and most important, if WGMs are altered by photoexcitation, we should observe negative (bleach) and positive peaks in the differential signal, located spectrally close to the original and shifted positions of the WGMs, respectively.

Figure 5.6 shows a linear fit of the progression of negative peaks exctracted from the modulations of SP#1 (see Figure 5.5(b-c)). Consistently with our interpretations, the result matches very well with the first-approximation theoretical expression for the frequencies of WGMs of a spherical resonator (see equation (5.2)).

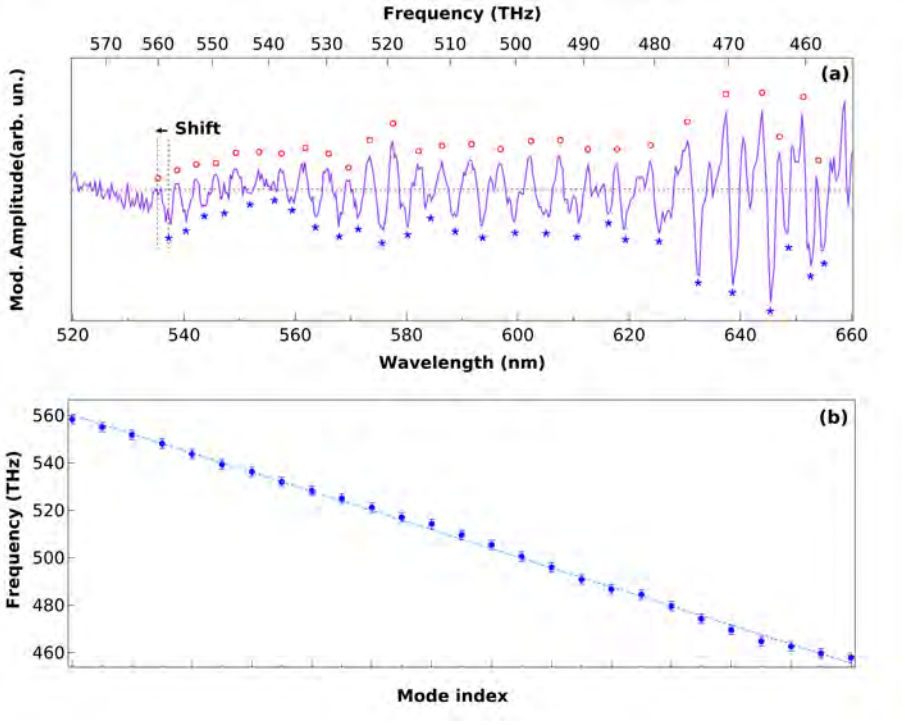

Figure 5.6: (a) Modulations extracted from the TAM signal of SP#1, as shown in panels (b-c) of Figure 5.5; the circular and star-shaped markers highlight the positions of positive and negative peaks, respectively; (b) frequency of each negative peak plotted as a function of the mode index. The dashed line indicates the linear fit on the progression

The slope of this progression represents the mode separation:

$$\Delta\nu \simeq \frac{c}{2\pi an} \tag{5.3}$$

A linear fit of the progression of negative peaks yields:

$$\Delta\nu_{neg} = (4.03 \pm 0.03)\ \text{THz} \tag{5.4}$$

From $\Delta\nu$, using the known SP radius $a = (5.4 \pm 0.2)\ \mu\text{m}$ (which can be assumed constant, as discussed below), we can then use (5.3) to estimate an effective, wavelength-averaged real part of the refractive index equal to:

$$n_{avg} = 2.19 \pm 0.02 \tag{5.5}$$

Moreover, from the average distance $\langle d\nu_l \rangle$ between a given negative peak and its nearest positive counterpart, we can calculate the photoinduced variation of $x = an$. Indeed, by differentiating (5.2), we have:

$$d\nu_l \simeq -\frac{cl\Delta x}{2\pi x^2} \tag{5.6}$$

From the data shown in Figure 5.6, we estimate:

$$\langle d\nu_l \rangle \simeq 1.8\,\mathrm{THz} \tag{5.7}$$

Comparing (5.6) and (5.7), recalling the abovementioned values for the radius and effective refractive index of the SP, and considering an intermediate value $l = 125$ for the mode index, we can calculate the relative variation $\Delta x/x$ as:

$$\frac{\Delta x}{x} = 0.0034 \pm 0.0013 \tag{5.8}$$

which corresponds to a percentage variation of $(0.34 \pm 0.13)\,\%$. It is important to bear in mind that, in principle, such variation can stem from changes in the refractive index, radius, or a combination of the two.

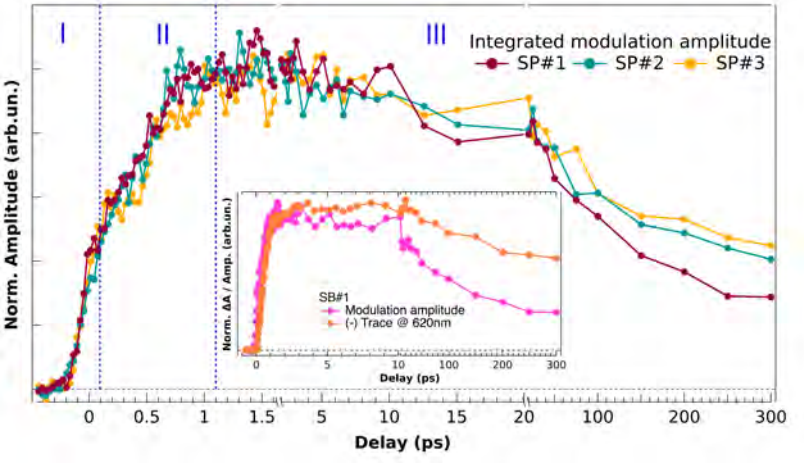

Figure 5.7: time evolution of the overall modulation amplitude for all three SPs. The vertical dashed lines separate the three phases of the dynamics, as indicated by the labels I-II-III; the inset shows a comparison between the time evolution of the modulation amplitude in SP#1 and the (upturned and normalised) kinetics of its overall signal taken at 620 nm.

To obtain further insight into the origin of these effects, we correlate the time dependence of the modulations to the known dynamics of QD relaxation [49]. The spectrally integrated absolute value of the modulation amplitude, given by:

$$M = \int_{\lambda_{in}}^{\lambda_{fin}} \left| A_m(\lambda) \right| d\lambda \tag{5.9}$$

where λ_{in} and λ_{fin} indicate the limits of the probed range, is plotted in Figure 5.7 as a function of delay. This shows that the modulations appear within the cross-correlation time of the excitation pulse (phase I), already rising to $\simeq 40\%$ of their maximum amplitude within $0.15\,\mathrm{ps}$. The modulations rise further on a time scale of $\simeq 1\,\mathrm{ps}$ (phase II), concurrently with state filling dynamics (panel (c) of Figure 5.3), and slowly decay (phase III) over hundreds of picoseconds, although faster than the overall µPP signal (see the inset of Figure 5.7). The quasi-instantaneous appearance of the modulations in phase I, that is, much faster than electron-phonon scattering [49], strongly hints at a purely electronic effect, namely the variation of the refractive index Δn_{el} caused by the impulsive redistribution of electrons upon photoexcitation. Indeed, no change in radius Δa could occur before electrons have transferred energy to the lattice. Conversely, we propose that the further rise of the modulations upon electron-phonon scattering (phase II) is thermal in origin, as the macroscopic SP temperature rise, caused by the redistribution of energy from electrons to phonons, is expected to induce an additional contribution Δn_{th} and possibly also a change of the radius Δa_{th} due to the thermal expansion of the SP.

In order to obtain the pump-induced temperature variation of the SP, we first of all need to consider the penetration depth of the pump within the superparticle. This parameter can be estimated from the tabulated absorption coefficient of CdS (the main component of our SPs) [228], yielding $\delta a \simeq 100\,\mathrm{nm}$. Therefore, we can safely assume that the whole pump energy E_p is absorbed by the SP's outermost layer (of thickness δa), causing a temperature rise ΔT according to the law:

$$E_p = 4\pi\rho a^2 \delta a C \Delta T \tag{5.10}$$

where ρ and C indicate the density and specific heat of CdS [227]. By revers-

ing this equation, we obtain:

$$\Delta T = \frac{E_p}{4\pi\rho a^2 \delta a C} \simeq 7\,\mathrm{K} \tag{5.11}$$

Such a temperature rise will contribute to further increase Δn and hence the amplitude of the modulations. Indeed, by utilizing reported data for the temperature dependence of the refractive index of CdS [229] we estimate:

$$\frac{\Delta n_{th}}{\Delta T} \simeq 4 \times 10^{-4}\,\mathrm{K}^{-1} \tag{5.12}$$

and therefore:

$$\Delta n_{th} = \frac{\Delta n_{th}}{\Delta T}\Delta T \simeq 0.003 \tag{5.13}$$

This represents a sizeable portion of the overall variation we calculate above, confirming its partial thermal origin coherently with the partial (relatively) slow rise of the modulation amplitude we observe in Figure 5.7. On the other hand, the thermally-induced radius variation Δa_{th} can be estimated from the known (linear) thermal expansion coefficient of CdS [227], that is $\alpha \simeq 4 \times 10^{-6}\,\mathrm{K}^{-1}$. From this, considering a total temperature variation $\Delta T \simeq 7\,\mathrm{K}$ and a volumetric expansion coefficient $\beta = 3\alpha$, we obtain a diameter variation of our $\simeq 10\,\mu\mathrm{m}$ SPs of about $0.3\,\mathrm{nm}$. This variation is certainly negligible when compared to the refractive index variation. Therefore, we can assume the SP radius to remain constant, and attribute the whole response to stem from a variation $\Delta n = \Delta n_{el} + \Delta n_{th}$ of the refractive index. Notably, the fact that the modulation amplitude decays faster than the overall signal in phase III is fully in line with the attribution of this decay to cooling, rather than ground state recovery.

These results confirm our attribution of the modulations observed in the TAM signal to the photoinduced modification of the WGMs of the SP microresonator. Photoexcitation acts as an all-optical switch [230] capable of modulating the microresonator on ultrafast time scales, conceptually akin to an acousto-optic modulator, or a variable impedance element in a radiofrequency device. Alternatively, we can picture the photoexcited SP as an ultrafast photonic device, encoding its unique spectral signature into the probe beam, ultimately transmitting this spectral "key" to the detector. Once scalability and other practical issues are overcome, this paradigm might lead to applications

in various fields, such as remote recognition, ultrafast telecommunication, or information processing. Notably, the TAM signal obtained by exciting an SP at $550\,\mathrm{nm}$ does not show modulations (Figure 5.8). While, at $400\,\mathrm{nm}$, the penetration depth ($\simeq 100\,\mathrm{nm}$) is comparable to the radial extent of WGMs, at $550\,\mathrm{nm}$, the whole SP is photoexcited. Because the photoexcited QDs are now distributed over the entire volume rather than in the volume probed by the WGMs, we expect both purely electronic and thermal effects to decrease substantially when exciting at $550\,\mathrm{nm}$.

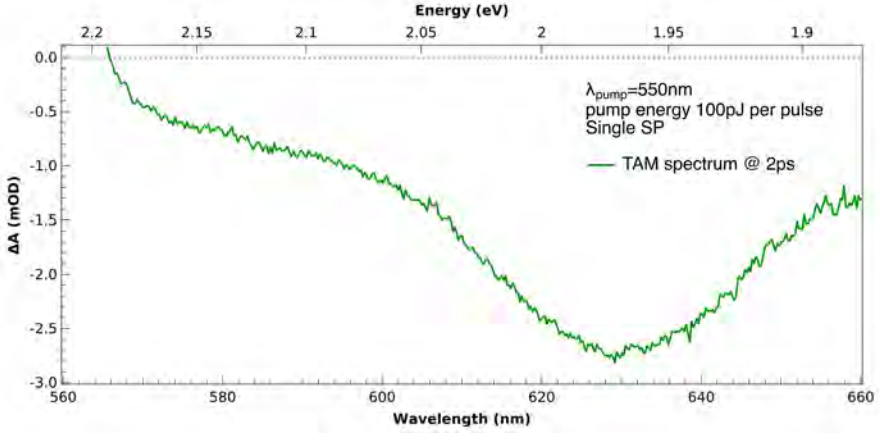

Figure 5.8: TAM spectrum of a single SP excited at 550nm, at 2ps delay, highlighting the absence of modulations.

5.2.4 Excitation transfer in SP dimers

As a final step of our experiment, we push the capabilities of TAM to explore the possibility of cross-talk between neighboring SPs. The deposition of SPs on a glass substrate causes the formation of multimers [77] following Poissonian statistics (panels (a-c) of Figure 5.9). We expect these multimers to support light propagation only through resonator modes that are common to all neighboring SPs. We explore this possibility in a SP dimer by using TAM (panels d-f). First, we focus the pump beam tightly ($3\,\mu\mathrm{m}$ FWHM, $4\,\mathrm{mJ/cm^2}$) to excite only one of the two SPs (site I in Figure 5.9d). Then, we align the probe with the center of the other SP (site II). This configuration monitors exclusively the transfer of optical excitation through the dimer from one SP to the other.

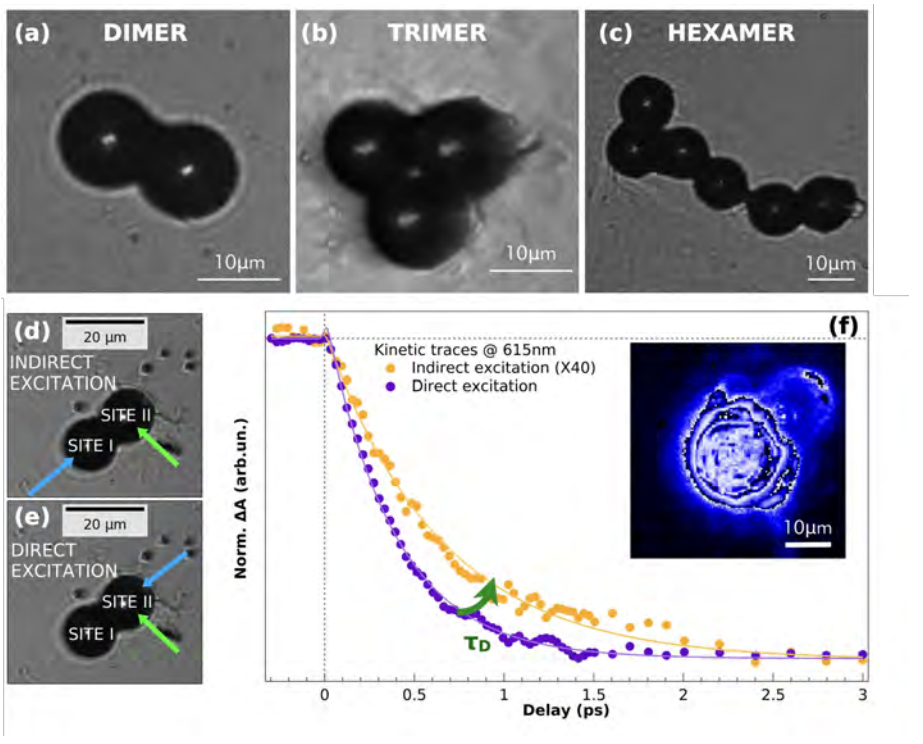

Figure 5.9: Unraveling the photonic coupling in SP dimers. (a-c) micrographs of three distinct multimers, formed by 2, 3, and 6 SPs; (d-e) Optical micrograph of a SP dimer: the SPs are labeled "site I" and "site II", while the blue and green arrows show the position of the pump and probe, respectively, in the case of indirect (d) and direct (e) pumping; (f) kinetic traces and least-square fits of the TAM signal at 615 nm in the indirect (orange curve, multiplied by 40) and direct (purple curve) pumping regimes. The inset shows a false-color micrograph of the scattered pump beam, highlighting the partial excitation transfer from site I to site II. The two kinetics are normalized to the same intensity at a delay of 3 ps, and the green arrow highlights the delay.

We perform a control experiment on the same SP dimer by exciting and probing site II (panel (e) of Figure 5.9). The results shown in panel (f) confirm the occurrence of excitation transfer: following the photoexcitation of the first SP, we observe a signal from the second SP. Interestingly, this signal is delayed with respect to that obtained in the control experiment, as indicated by the green arrow. We quantify the delay as the difference between the rise-times obtained by fitting the two traces with an exponential model convoluted with the IRF. This yields $\tau_D = 140\,\text{fs}$. Such delay is consistent with the propagation of

light in a medium with $n_{avg} = 2.19$ across a distance of about $21\,\mu m$. Importantly, this propagation length is about twice as large as the $10.8\,\mu m$ center-to-center distance between the SPs (corresponding to the distance between pump and probe spots), suggesting that light propagates via the perimeter of the SPs through WGMs. Excitation transfer is further confirmed in images of the scattered pump (inset of Figure 5.9f), showing that a small ($\approx 2.5\%$) portion of the pump is transferred from the initially excited SP to its neighbour. A further extension of these studies to more complex multimer geometries may establish the grounds to use SPs as fundamental building blocks of all-optical circuits.

5.3 Conclusions

In summary, we have shown that ultrashort optical excitation can induce fully reversible modulations of the microresonator response in individual QD superparticles. By exploiting transient absorption microscopy with simultaneously high temporal, spectral, and spatial resolution, we directly reconstruct the ultrafast evolution of the complete WGM spectral pattern, thereby gaining detailed insight into the dynamic optical response and functional photonic behavior of these systems. This approach enables a clear disentanglement of the electronic and thermal contributions underlying the photoinduced modulation of resonator modes and establishes a framework for exploiting SPs as ultrafast, light-driven and reversible photonic microswitches. Moreover, the real-time observation of ultrafast excitation transfer mediated by shared WGMs in SP dimers demonstrates the possibility of controlling light propagation at a higher hierarchical level of assembly. Although still far from technological implementation, these results lay the groundwork for the rational design of SP-based optical metamaterials, providing a clear example of how light-matter interaction is profoundly reshaped by self-assembly of colloidal nanocrystals.

5

6

Quantum Dot Superparticles II: Unravelling the Collective Exciton Dynamics

Research is to see what everybody else has seen, and to think what nobody else has thought.

— Albert Szent-Györgyi

In this chapter, we will discuss how self-assembly impacts the photocycle of core-shell CdSe/CdS quantum dots (QDs). By leveraging complementary spectroscopic techniques with different temporal resolutions, we will compare and contrast the optical response of the superparticles with that of the constituent QDs, over several time scales ranging from hundreds of femtoseconds to hundreds of nanoseconds. First, ultrafast transient absorption microscopy will provide a full picture of the state filling dynamics following photoexcitation. Subsequently, time-resolved photoluminescence microscopy will allow

to gain precious insight into the depopulation dynamics of the emissive state, uncovering in particular the role of cross-talk in quenching Auger recombination, a key factor towards efficiency-driven applications such as microlasers. The results presented in this chapter will be published in a paper currently in preparation.

6.1 Introduction

In the previous chapter, we explored the microresonator behaviour of spherical, micrometric CdSe/CdS quantum dot superparticles (SPs), unveiling the ultrafast modulation of their Whispering Gallery Mode (WGM) resonances. This chapter is, instead, focused on their photophysical properties. Indeed, as discussed in chapter 2, cross-talk between neighbouring nanocrystals within densely-packed assemblies is expected to result in a partial mixing of their discrete energy states, leading to the formation of *minibands* [66]. This has two important consequences: first, a shift in the emission and/or absorption profile is typically observed as a consequence of state mixing. Secondly, miniband formation allows excitons to delocalise over multiple adjacent QDs, with a notable impact on their kinetics. Recently, Marino *et al.* [78] explored excitonic coupling in SPs assembled from CdSe QDs, unveiling a significative drop in the biexciton binding energy with respect to that of the constituent QDs. This has been interpreted as a direct consequence of exciton delocalisation, which attenuates exciton-exciton interaction. While a similar effect can be expected for our SPs, we must bear in mind their core-shell nature: the presence of a CdS shell around each CdSe core is expected to reduce QD-QD cross-talk. Additionally, the *quasi-type II* bandgap alignment characterising our QDs implies that only electrons can delocalise over both the core and the shell, whereas holes remain localised in the former. This asymmetry could further complicate exciton dynamics, both at the single-QD and collective levels. These considerations notwithstanding, the presence of cross-talk within our SPs appears evident when comparing their emission profile with that of the constituent QDs, as discussed in the previous chapter (see in particular panels (c-d) of Figure 5.2): the superparticles exibit a photoluminescence peak blueshifted by $5\,\mathrm{nm}$ with respect to that of the isolated QDs. In order to gain further insight into this coupling, in the following we will perform a full comparison

between the photocycles of the SPs and their consituent QDs across multiple time scales.

6.2 Results and Discussion

6.2.1 TAM: state-filling and biexciton interaction in QDs and SPs

As a starting point for our investigation, we performed transient absorption microscopy (TAM) measurements on both QDs and SPs. Indeed, transient absorption spectroscopy represents a powerful tool to investigate the relaxation dynamics of QDs, as it is able to probe all optically accessible energy levels with concurrently high spectral and temporal (fs-ps) resolution. By integrating optical microscopy, TAM also provides high spatial resolution, crucial to disentangle single superstructure contributions, while also allowing to separate genuine absorption variations from scattering contributions (see detailed discussion in chapter 4).

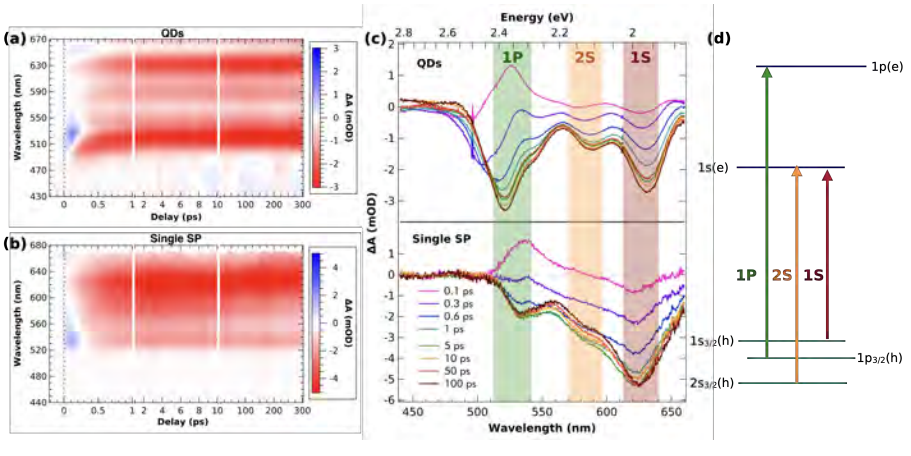

Figure 6.1: (a-b) time-wavelength plot of the TAM signal of isolated QDs (a) and a single SP (b); (c) comparison between TAM spectra at relevant pump-probe delays. The vertical bands highlight common PB signals; (d) schematic representation of the transitions responsible for the PB signals reported in panel (c).

The measurements were performed following the same protocol employed in the previous chapter (see Figure 5.3 and related discussion). The samples were pumped at 400 nm, well above the bandgap, over a 14 µm (FWHM) spot, and

probed in the range $(440 \div 660)\,\mathrm{nm}$ with a spot size of $2.5\,\mu\mathrm{m}$ (FWHM), at variable delays after photoexcitation. The constituent QDs were measured by drop casting a dilute toluene dispersion onto a thin glass substrate, analogous to that used for the SPs. Importantly, the pump fluence was kept low (approximately $0.2\,\mu\mathrm{J/cm^2}$ per pulse) in order to minimise nonlinear contributions. Moreover, to obtain a clearer view of the intrinsic spectral features, we deliberately selected a SP that did not exhibit pronounced WGM modulations. The absence of such modulations merely reflects the presence of minor surface imperfections, which are not expected to affect the collective photophysics of the SP in any meaningful way.

The TAM responses of the two samples is presented in the time-wavelength plots of Figure 6.1(a-b), while panel (c) reports spectra extracted at relevant pump-probe delays. A comparison between the two progressions reveals that for both QDs and SPs the signal is largely dominated by photoinduced bleaching (PB) features arising from the *state filling* effect, in full agreement with the results discussed previously. As the hot carriers gradually relax from the initially excited states towards the band edges, they block excitonic transitions corresponding to the states they occupy. Notably, the three PB features previously identified for SPs also appear, albeit slightly shifted, in the TAM spectra of the constituent QDs, as highlighted by the vertical bands in panel (c). As discussed in the previous chapter, the spectral positions of these features are consistent with known transitions in CdSe QDs (see panel (d) of Figure 6.1). In particular, the feature appearing at $(620 \div 630)\,\mathrm{nm}$ $((1.97 \div 2.00)\,\mathrm{eV})$ can be linked to the band-edge *1S* transition, that is, $[1s(e) - 1s_{3/2}(h)]$, while the ones at $(580 \div 590)\,\mathrm{nm}$ $((2.10 \div 2.14)\,\mathrm{eV})$ and $(520 \div 540)\,\mathrm{nm}$ $((2.29 \div 2.38)\,\mathrm{eV})$ can be linked to the *2S* $[1s(e) - 2S_{3/2}(h)]$ and *1P* $[1p(e) - 1p_{3/2}(h)]$ transitions, respectively. Additionally, both samples present a positive, short-lived photoinduced absorption (PA) feature centered at $\sim 530\,\mathrm{nm}$, indicating the presence of higher-energy states accessible from the initially photoexcited state.

Besides these similarities, we observe some notable differences between the responses of the SPs and their constituents. First, QDs do not exhibit the pronounced saturation (zero differential absorption) observed in the low wavelength region of the SP spectra. This behaviour is consistent with the interpretation that the effect originates from inter QD coupling, which allows the

absorption cross section of SPs to approach their geometrical cross section. Second, the relative intensities of the PB features differ between the two systems, indicating that interparticle interactions reshape the distribution of photoexcited carriers among the available states. Moreover, the PB features of the SP are markedly broader than those of the QDs, reflecting the energetic disorder and the complex dielectric environment characteristic of the assembled structure. Third, in the QD spectra the 1P feature undergoes a pronounced redshift within the first picosecond, shifting from $490\,\mathrm{nm}$ at a pump-probe delay of $0.3\,\mathrm{ps}$ to $520\,\mathrm{nm}$ for $t \geq 1\,\mathrm{ps}$. No analogous shift is observed for the SP, most likely because low wavelength saturation masks this dynamics. Finally, a positive signal appears in the early-time QD spectra on the red side of the band edge transition, at approximately 655 nm, whereas a comparable feature is much less evident in the SP response. This signal has been previously attributed to biexciton interactions [49, 78] and will be discussed in detail after the analysis of the overall signal kinetics.

Given the abundance of features in the TAM signals of the QDs and SPs, we performed a singular value decomposition (SVD) to get a sense of the characteristic lifetimes and spectral signatures of the main processes at play. In short (see chapter 4 for details), SVD consists in decomposing the time-wavelength transient absorption matrix into a set of *eigenspectra* and *eigentraces*, each associated with an *eigenvalue* that quantifies its relative contribution to the overall signal.

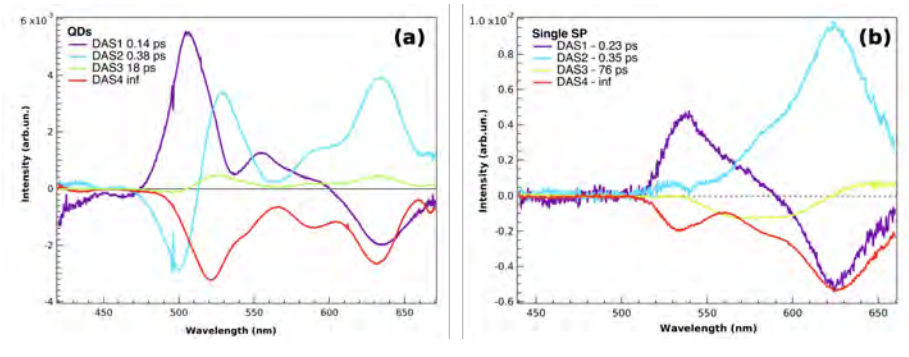

Figure 6.2: Decay-associated spectra (DAS) obtained by singular value decomposition (SVD) of the TAM signals of QDs (a) and SPs (b). The time constant associated with each DAS is reported in the legends.

By retaining only the components associated with the largest eigenvalues, the dominant physical processes can be isolated, while noise and minor contributions are effectively suppressed. In this case, for each sample we retained the three eigenspectra and eigentraces associated with the largest eigenvalues.

The eigentraces were then subjected to a global fit in order to extract their characteristic timescales. In both QDs and SPs, three distinct timescales were identified, and the corresponding *decay-associated spectra* (DAS) are reported in Figure 6.2. In addition, a fourth, effectively *infinite* timescale was included in the fitting procedure to account for long lived components that do not decay within the experimental time window of TAM: the related DAS (red curve in the plots) effectively represents the spectral profile of the TAM signal *after* all the fs-ps processes are completed.

As discussed in chapter 4, the DAS enable to identify the spectral signatures of the dynamic processes corresponding to the observed timescales. From the plots in Figure 6.2, we see that the earliest timescale ((0.14 ± 0.02) ps for the QDs and (0.23 ± 0.02) ps for the SP) are mainly related to the early-time PA feature discussed above, in agreement with its complete disappearance within a few hundred femtoseconds observed in the raw TAM data (panel (c) of Figure 6.1). The two longer timescales, associated with DAS2 and DAS3, instead reflect state filling dynamics. In particular, the first of the two, DAS2, exhibits nearly identical sub-picosecond lifetimes for the two samples ((0.38 ± 0.03) ps and (0.35 ± 0.03) ps for the QDs and SP, respectively) and is associated with the buildup of the PB signals. For the QDs, DAS2 also reveals a redshift of the 1P feature, evidenced by the derivative like lineshape on the low wavelength side of the spectrum. This feature is absent in the corresponding DAS of the SP, consistent with the lack of an observable spectral shift discussed earlier. The second state filling component, DAS3, highlights the most pronounced differences between QDs and SPs. In the case of QDs, this component exhibits a lifetime of (18.0 ± 0.8) ps and corresponds to a further, modest increase in the intensity of all PB features. In contrast, the corresponding component for the SP displays a significantly longer lifetime of (76 ± 2) ps and a markedly different spectral signature. Rather than a uniform increase of PB intensity, the SPs' DAS3 shows a partial decay of the higher energy features, namely the 2S and 1P transitions, accompanied by a small increase and a slight redshift of the 1S peak. This difference highlights the role of cross-talk in effectively reshaping

the relaxation patterns of our QDs.

As noted above, the TAM spectra, particularly those of the QDs, exhibit a short lived photoinduced absorption feature that is red shifted with respect to the 1S bleach. This feature, commonly referred to as the biexciton signal [78], arises when the exciton generated by the pump interacts with an additional exciton created upon probe absorption, leading to the formation of a biexciton. The relative spectral shift between the 1S bleach and the biexciton signal reflects the sign of the exciton-exciton interaction. In particular, a redshift indicates a net attractive interaction, corresponding to a negative biexciton binding energy.

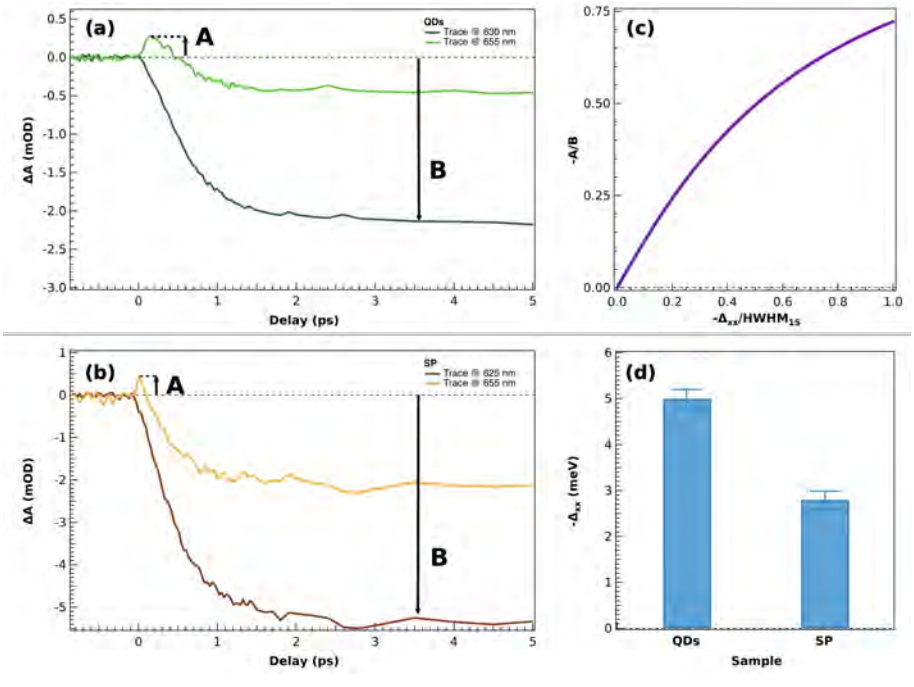

Figure 6.3: Calculating the biexciton binding energy from TAM. (a-b) kinetic traces at the 1S and biexciton peak positions for QDs (a) and SPs (b); (c) dependence of the A/B ratio upon the biexciton binding energy, normalised by the half-width at half-maximum (HWHM) of the 1S peak; (d) biexciton binding energy estimates for the QDs and their SPs.

Following the protocol proposed by Klimov [49], we can obtain a quantitative estimate of the biexciton binding energy Δ_{XX} by comparing the differential absorption signals at the 1S and biexciton spectral positions. In particular, as

shown in panels (a-b) of Figure 6.3, we evaluate the maximum intensity of the positive PA signal corresponding to the biexciton interaction (denoted as A), and the maximum (negative) intensity of the 1S bleach signal (B). Their ratio A/B can be correlated (as shown in panel (c) and discussed in detail in [49]) with the biexciton binding energy, rescaled by the half-width at half-maximum (HWHM) of the 1S bleach. This relationship does not admit a simple analytic expression, but can be obtained numerically. By multiplying the resulting normalised value by the HWHM of the 1S transition, an estimate of the absolute biexciton binding energy Δ_{XX} can be recovered. In the present analysis, we assumed the half width at half maximum of the 1S bleach of the isolated QDs as the reference value for both samples. This choice is motivated by the fact that the additional broadening observed in the SP spectra arises primarily from energetic disorder and collective effects, rather than from a modification of the intrinsic single particle linewidth, relevant for this model. The resulting binding energies are reported in panel (d) of Figure 6.3. Specifically, we obtain $\Delta_{XX} = (-5.0 \pm 0.2)\,\mathrm{meV}$ for the QDs and $\Delta_{XX} = (-2.8 \pm 0.2)\,\mathrm{meV}$ for the SPs. The reduced magnitude of the binding energy in the superstructures with respect to the isolated constituents is a clear evidence of partial exciton delocalisation, which decreases the interaction probability between the pump- and probe-generated excitons. It is instructive to compare these values with those reported by Marino *et al.* [78], who studied similar SPs composed of CdSe QDs analogous to those constituting the core of our core-shell particles. In that study, they obtain biexciton binding energies of $-7.2\,\mathrm{meV}$ and $-4.4\,\mathrm{meV}$ for the QDs and SPs, respectively. Two observations follow from this comparison. First, the absolute values of Δ_{XX} are smaller in the present case for both QDs and SPs, consistent with the quasi type II nature of our QDs, which leads to partial delocalisation of the electron over the entire nanocrystal and thus to a reduced biexciton binding energy. Second, in both systems the binding energy is reduced by approximately 40% when the QDs are assembled into SPs. This indicates that, at least for biexciton interactions, the exciton delocalisation enabled by inter particle cross talk is comparable in core only and quasi-type II core shell QDs. By contrast, one may expect type I core shell QDs to exhibit a markedly different behaviour, as the confinement of both charge carriers within the core would cause the shell to act as an effective spacer between neighbouring QDs.

6.2.2 µ-TRPL: unravelling single- and multi-exciton recombination pathways

While TAM provides a wealth of interesting information on the photoinitiated exciton dynamics in both QDs and single SPs, the fine-splitting of the band-edge in CdSe QDs implies that the emissive states cannot be directly investigated by transient absorption measurements. Therefore, aiming to probe the photoluminescence of the two samples over multiple timescales, we performed time-resolved photoluminescence microscopy (µ-TRPL), by employing a fluorescence microscope equipped with a picosecond diode at $405\,\mathrm{nm}$ (spot size $\sim 5\,\mu\mathrm{m}$) and a single-photon avalanche diode (SPAD) detector (further details are reported in chapter 4). As for the TAM experiments, both QDs and SPs were dropcasted on suitable glass substrates. Preliminary measurements on both samples revealed non-trivial, multi-exponential decays, suggesting the concurrence of multiple processes in determining the decay profile. Since the different processes typically present distinct power-dependences, we recorded the decays as a function of pump fluence, over approximately four orders of magnitude, from $0.01\,\mu\mathrm{J/cm^2}$ to $18\,\mu\mathrm{J/cm^2}$ (per pulse). The resulting curves are reported in Figure 6.4.

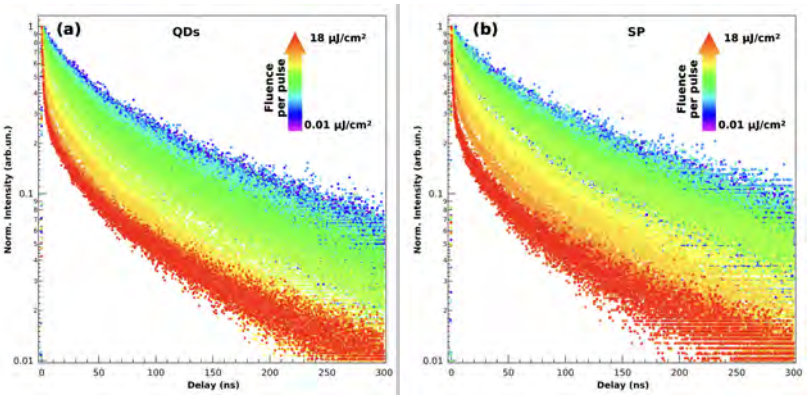

Figure 6.4: Normalised µ-TRPL decay traces as a function of pump fluence for (a) QDs and (b) a single SP.

The µ-TRPL decay traces display a clear dependence on pump fluence for both isolated QDs and their SPs. In both cases, increasing the excitation fluence results in a progressively faster decay at early delays, with a steep initial inten-

sity drop on the few nanosecond timescale emerging at higher fluences, while such a component is absent at low excitation densities. By contrast, the long lived emission component exhibits a much weaker fluence dependence, as evidenced by the fact that the decay traces become approximately parallel beyond the first $\sim 100\,\mathrm{ns}$. This regularity, together with the observation that both QDs and SPs exhibit qualitatively similar progressions, suggests the existence of a set of common, characteristic lifetimes underlying the decays, with the differences observed between the two samples and across fluences stemming from variations in the relative amplitudes of the decay components, rather than from changes in the lifetimes themselves.

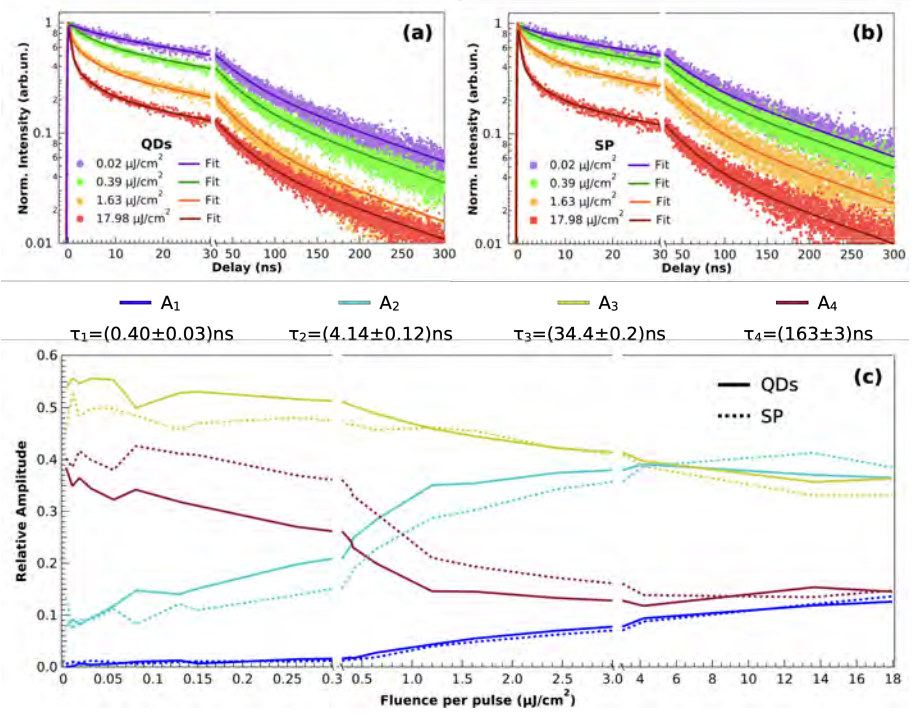

Figure 6.5: Global fitting reveals the characteristic timescales. (a-b) representative fits for (a) QDs and (b) SPs; (c) relative amplitudes of the four lifetime components, as specified by the legend.

We confirmed this assumption by performing a global fit on both datasets, from which four common lifetimes emerge: $\tau_1 = (0.40 \pm 0.03)\,\mathrm{ns}$, $\tau_2 = (4.14 \pm$

$0.12)\,\mathrm{ns}$, $\tau_3 = (34.4 \pm 0.2)\,\mathrm{ns}$, and $\tau_4 = (163 \pm 3)\,\mathrm{ns}$. Fits on representative traces for each sample are reported in panels (a-b) of Figure 6.5, while panel (c) presents the fluence-dependence of the relative amplitudes associated to each lifetime.

The four lifetimes extracted from the global fit can be attributed to distinct single- and multiexciton decay channels on the basis of extensive prior work on the photodynamics of both core-only and core–shell QDs [64, 231–240].

In particular, the two shortest components ($0.4\,\mathrm{ns}$ and $4.14\,\mathrm{ns}$) are indicative of Auger-mediated recombination of biexcitons (XX) and trions ($X^{\pm}$), respectively. This assignment is supported by their fluence dependence: at low excitation densities the biexciton-related contribution is essentially suppressed, while the second-fastest component remains limited to $\sim 10\%$. Moreover, the $0.4\,\mathrm{ns}$ lifetime is in excellent agreement with reported biexciton Auger recombination times in comparable quasi-type II core-shell QDs [235]. Notably, biexciton Auger lifetimes in CSQDs are critically dependent on shell thickness, slowing down significantly when the shell diameter increases. The attribution of the longer $4.14\,\mathrm{ns}$ decay to trion recombination, on the other hand, is substantiated by its reduced Auger rate compared to that characterising biexcitons, a difference amplified by the quasi-type II core-shell architecture of our QDs [233, 238, 239].

The two longer lifetimes, $34.4\,\mathrm{ns}$ and $163\,\mathrm{ns}$, can instead be associated with single-exciton recombination. Indeed, Hanifi *et al.* [64] showed that CdSe/CdS core–shell quantum dots with sufficiently thick shells exhibit non-monoexponential band-edge exciton recombination, reflecting the coexistence of multiple radiative channels associated with distinct recombination pathways. In this framework, the $34.4\,\mathrm{ns}$ component is consistent with the characteristic lifetime of band-edge exciton recombination in CdSe-based nanocrystals, while the emergence of the long-lived $163\,\mathrm{ns}$ emission component can be rationalised in light of the quasi–type II band alignment of the heterostructure. In particular, Hanifi *et al.* propose that shallow surface-associated states in the CdS shell (which we directly excite by pumping at $400\,\mathrm{nm}$) may temporarily trap electrons without introducing fast nonradiative losses, owing to the strong confinement of the hole within the CdSe core. Thermal re-population of emissive states following such processes can therefore contribute to delayed radiative recombination, giving rise to the observed long-lived emission tail.

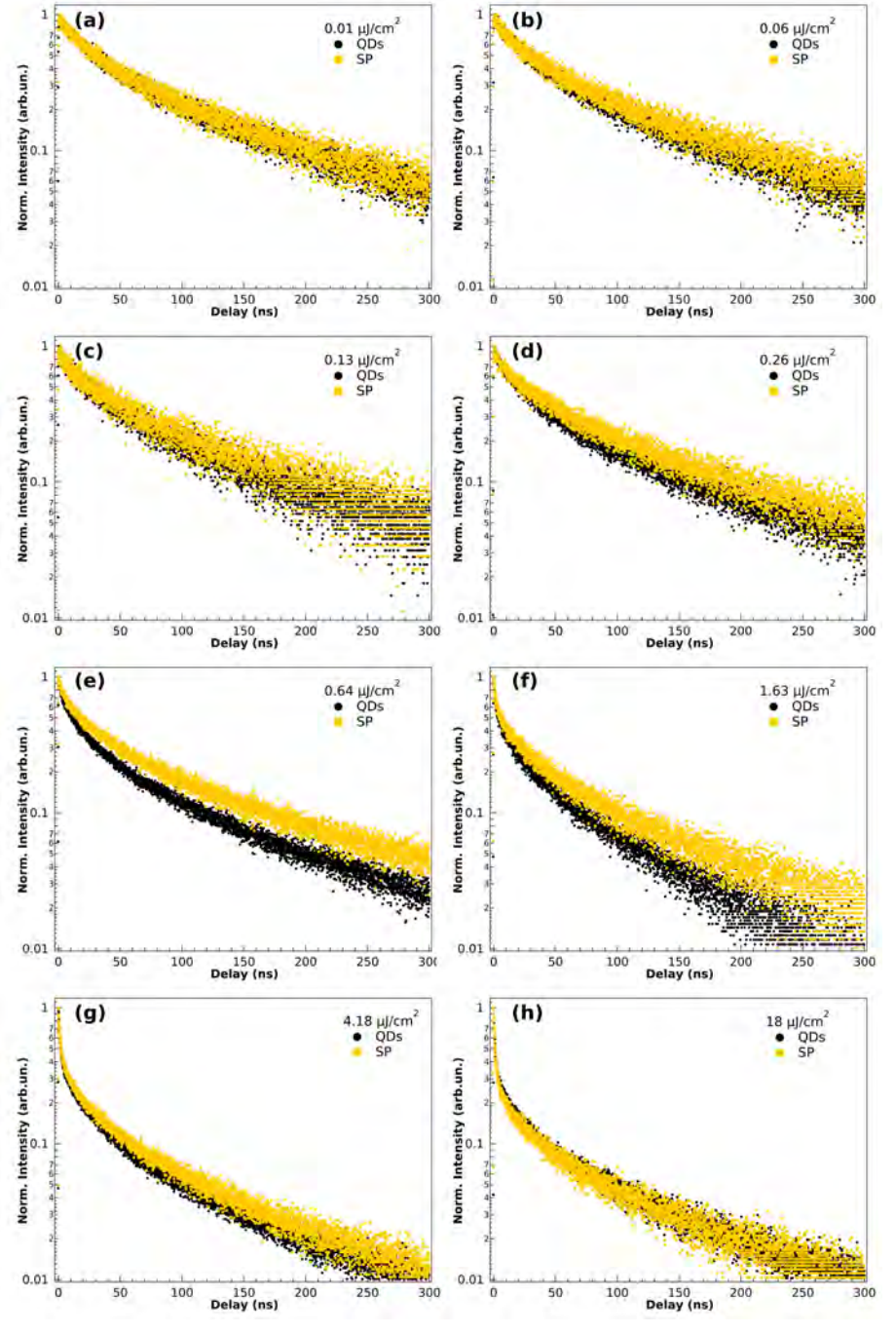

Figure 6.6: Normalised μ-TRPL spectra of QDs and a single SP at representative fluences.

The relative amplitudes of the four decay components, shown in panel (c) of Figure 6.5, display clearly distinct fluence dependences for QDs (solid lines) and SPs (dashed lines). To gain insight into the origin of these differences, Figure 6.6 compares the normalised μ-TRPL decay traces of the two systems at eight representative pump fluences. A clear and non-monotonic trend emerges from this comparison. At low fluences (panels (a–c)), the two decay traces are virtually indistinguishable. At intermediate fluences (panels (d–f)), a pronounced divergence develops, whereas at the highest fluences (panels (g–h)) the two traces converge again. Closer inspection of the intermediate regime (see, for instance, panel (e)) reveals that the discrepancy between QDs and SPs is largely confined to the first $20 \div 30\,\mathrm{ns}$, i.e. to the timescales associated with Auger-mediated recombination, while the decays become essentially parallel at longer delays.

On this basis, we propose that the observed differences originate from inter-dot cross-talk within the densely packed SPs, which partially suppresses Auger-driven decay channels. This interpretation naturally accounts for the three regimes identified above. At very low fluences, Auger processes are inefficient and the decay is dominated by single-exciton recombination. The coincidence of the QD and SP traces in this regime indicates that single-exciton transition rates are not significantly altered by cross-talk, even though such interactions do affect the transition energies, as evidenced by the PL redshift discussed in the previous chapter. At intermediate fluences (roughly $0.2 \div 2\,\mu\mathrm{J/cm^2}$ per pulse), Auger recombination becomes increasingly important, and the SPs deviate from the behaviour of isolated QDs as a consequence of the partial suppression of Auger processes induced by inter-dot interactions. Finally, at sufficiently high fluences, possibly when the average number of excitations per dot largely exceeds unity, exciton delocalisation is impaired by the presence of one or more exciton in all the neighbouring QDs, leading to a convergence of the QD and SP decay dynamics.

6.3 Conclusions

The results presented in this chapter showcase how inter-dot cross-talk within densely packed assemblies modifies the single- and multi-exciton dynamics of the constituents. On one hand, transient absorption microscopy revealed cross-talk induced modifications to early carrier relaxation, as well as a reduction of the biexciton binding energy, providing clear evidence of partial exciton delocalisation. Furthermore, μ-TRPL measurements showed that while the characteristic lifetimes of biexciton, trion, and single-exciton recombination remain unchanged after self-assembly, fast Auger-mediated decays are partially suppressed in SPs at intermediate fluences. From an application perspective, reduced Auger losses in SPs are particularly beneficial for optical gain and low-threshold lasing, as prolonged multiexciton lifetimes relax the requirements for population inversion under strong pumping. These effects could be further rationalised by a systematic study of the SPs' response as a function of core diameter, shell thickness, ligand length and chemical nature. Temperature-resolved studies would also offer precious insight, as the various recombination paths present distinct temperature dependencies. Notably, this study complements the results presented in the previous chapter, highlighting the role of quantum dot superparticles as highly efficient, collective emitters, as well as active microresonators.

7

Slow-Evaporation Assembly of Perovskite Nanocrystal Supercubes

Even though one loses out here and there, and even though one sometimes feels a kind of exhaustion, one must rally and take courage again. [...] Great things are not done by impulse, but by a series of small things brought together.

— Vincent Van Gogh

This chapter investigates the structural and optical properties of green-emitting $CsPbBr_3$ nanocrystals and their cubic superstructures (supercubes), assembled via a slow-evaporation protocol. Structural characterisation reveals that the supercubes are endowed with supracrystalline ordering over very large domain lengths, while their optical response is characterised by redshifted and broadened photoluminescence with respect to the constituent nanocrystals, as well

as accelerated decay, reflecting efficient exciton delocalization and interparticle coupling. By monitoring the assembly at intermediate stages, the kinetics of nucleation, growth, and lattice relaxation are reconstructed, highlighting the role of slow assembly in achieving large, well-ordered superstructures. Finally, the impact of varying assembly parameters on the resulting supercubes is briefly considered, providing insights for the rational design of ordered perovskite supercrystals. The results presented in this chapter will be published in a manuscript currently in preparation.

7.1 Introduction

All-inorganic caesium lead halide nanocrystals ($CsPbX_3$, where X = Cl, Br, or I) [91, 241] stand out among metal halide perovskites (MHPs) due to their facile and scalable synthesis [242], strong defect tolerance [243], high carrier mobility [244], and photoluminescence with near-unity quantum yield [88]. In striking contrast to the chalcogenide quantum dots discussed in the previous chapters, perovskite nanocrystals (NCs) typically lie in the weak quantum confinement regime (see chapter 2), where the bandgap exhibits little to no dependence on NC size [91]. Instead, their emission wavelength is primarily determined by the halide ion: $CsPbCl_3$, $CsPbBr_3$, and $CsPbI_3$ NCs emit in the blue, green, and red regions of the spectrum, respectively [88], while partial halide exchange results in mixed-composition NCs exhibiting intermediate emission profiles [245], thus enabling fine tuning of their photoluminescence across the whole visible range.

As discussed in chapter 2, the sharp cubic shape of $CsPbX_3$ NCs strongly influences the short-range interactions governing their assembly into micrometric superstructures, favouring face-to-face organisation into cubic architectures. The fabrication and study of such *supercubes* has attracted significant interest in recent years [93, 95–98, 246, 247], mainly owing to the intriguing gamut of collective behaviours they exhibit, which encompasses highly efficient electronic and excitonic coupling [99, 248], superfluorescence [94], and low-threshold lasing [102]. Despite this promising outlook and the abundance of applicative studies, the fundamental understanding of the assembly mechanism and carrier dynamics within these SCs remains a hot topic in current literature.

Here, we study green-emitting caesium lead bromide ($CsPbBr_3$) NCs, which we assemble into supercubes (SCs) according to a recently proposed slow evaporation method [249]. By combining structural and optical characterisation techniques, we delve into the collective response of the SCs. Furthermore, we gain insight into the assembly process by reconstructing its kinetics, following the growth of the superstructures from the nucleation of the NCs into small assemblies to the stabilisation of the final SCs.

7.2 Results and Discussion

7.2.1 Synthesis and characterisation of caesium lead bromide NCs

The green-emitting $CsPbBr_3$ NCs presented in this chapter were synthesised by Dr. Y. Tang (University of Amsterdam, The Netherlands), according to the well-established *hot injection* (HI) protocol developed by Protesescu *et al.* [88] and schematised in Figure 7.1.

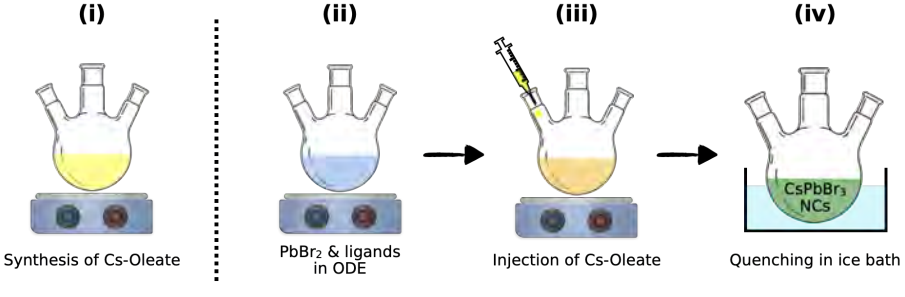

Figure 7.1: Schematic representation of the hot injection synthesis of $CsPbBr_3$ NCs.

As shown in the figure, the HI protocol involves four main steps (see chapter 4 for details):

(i) synthesis of caesium oleate (Cs-oleate);

(ii) preparation of an octadecene (ODE) precursor solution containing the ligands and a lead salt (in this case, lead bromide, $PbBr_2$);

(iii) injection of hot (hence the name) Cs-oleate into the precursor solution, triggering the nucleation and growth of the NCs;

(iv) quenching of the reaction by rapid immersion in an ice bath, typically within $\sim 5\,\mathrm{s}$ from the injection.

Notably, and in contrast with chalcogenide QDs, these NCs are stabilised by a ligand pair, typically composed of a carboxylic acid and an amine (in this case, oleic acid (OA) and oleylamine (OAm)). The two ligands adopt a spatially correlated arrangement on the NC surface, with the carboxylate and ammonium species coordinating distinct ionic surface sites. Their interplay plays a critical role in preserving the optical properties of the NCs and avoiding aggregation [250]. The immediate quenching step, occurring only a few seconds after injection, is also crucial to preserve the cubic morphology of the NCs, as a longer reaction time would lead to the formation of elongated *nanowires* (NWs) [251]. The resulting NCs were characterised by scanning transmission electron microscopy (STEM) at the *Laboratório Nacional de Nanotecnologia* (LNNano, Campinas, Brazil). Figure 7.2 summarises the results.

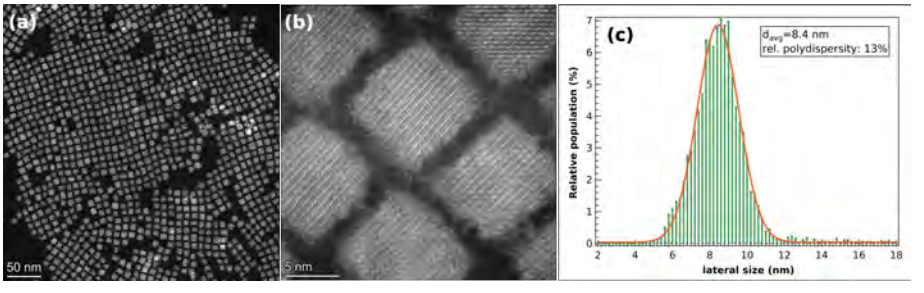

Figure 7.2: (a) STEM image of drop-casted $CsPbBr_3$ NCs; (b) high-resolution STEM micrograph of the NCs, highlighting their ordered structure; (c) lateral size distribution obtained from the STEM images.

The micrograph in panel (a) confirms the characteristic cubic morphology expected for this class of perovskite NCs, while the higher-magnification image in panel (b) highlights the ordered arrangement of the atoms within each NC. The STEM micrographs were analysed using the open-access *CellProfiler* software [252] to extract the lateral size distribution of the NCs, revealing an average size of $8.4\,\mathrm{nm}$ with a 13% relative polydispersity (calulated over a sample set of $\approx$ 2000 NCs), as shown in the histogram of panel (c). Such values are consistent with those reported in the literature for the HI synthesis of $CsPbBr_3$ NCs [88].

The NCs form a highly stable colloidal dispersion in apolar solvents such as toluene (panel (a) of Figure 7.3), exhibiting strong green photoluminescence under UV illumination (panel (b)). Steady-state UV–Vis and PL measurements (panel (c)), performed on an appropriately diluted dispersion of the NCs, elucidate their optical response: the former displays a lowest-energy absorption peak centred at $485\,\mathrm{nm}$ ($2.55\,\mathrm{eV}$), while the photoluminescence, collected under $405\,\mathrm{nm}$ excitation, exhibits a relatively narrow emission band peaking at $495\,\mathrm{nm}$ ($2.50\,\mathrm{eV}$), with a full width at half maximum (FWHM) of $18\,\mathrm{nm}$ ($90\,\mathrm{meV}$). The resulting small Stokes shift [253] of about $10\,\mathrm{nm}$ ($50\,\mathrm{meV}$) indicates that both processes originate from the same bright excitonic transition, with negligible lattice relaxation upon photoexcitation. This behaviour is a hallmark of all-inorganic $CsPbBr_3$ nanocrystals, setting them apart from conventional chalcogenide quantum dots, which typically exhibit larger Stokes shifts due to internal conversion from the absorbing (dark) exciton state to the emitting (bright) one.

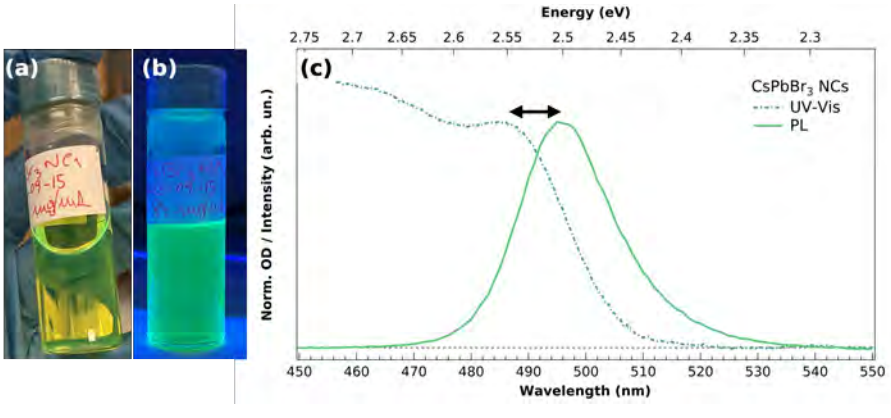

Figure 7.3: Steady-state optical response of $CsPbBr_3$ NCs. (a–b) colloidal dispersion of the NCs in toluene under natural light (a) and UV illumination (b); (c) normalised UV–Vis absorption (dashed line) and PL (continuous line) spectra. The arrow highlights the small Stokes shift.

The absolute photoluminescence quantum yield (QY), measured using the integrating sphere approach described in chapter 4, is approximately 50%, although this value is likely underestimated due to partial reabsorption of the emitted photons caused by the significant spectral overlap between absorption and emission.

7.2.2 Slow-evaporation assembly of perovskite supercubes (SCs)

The self-assembly of the $CsPbBr_3$ NCs was conducted in collaboration with Dr. Y. Tang and Prof. Dr. P. Schall (University of Amsterdam, The Netherlands), according to the *slow evaporation* protocol reported by Dibenedetto *et al.* [249] and schematised in panels (a–b) of Figure 7.4. In essence, this protocol exploits an antisolvent to control the pace at which the colloidal NC dispersion destabilizes, inducing nucleation of the NCs onto a substrate and ultimately driving the formation of ordered superstructures.

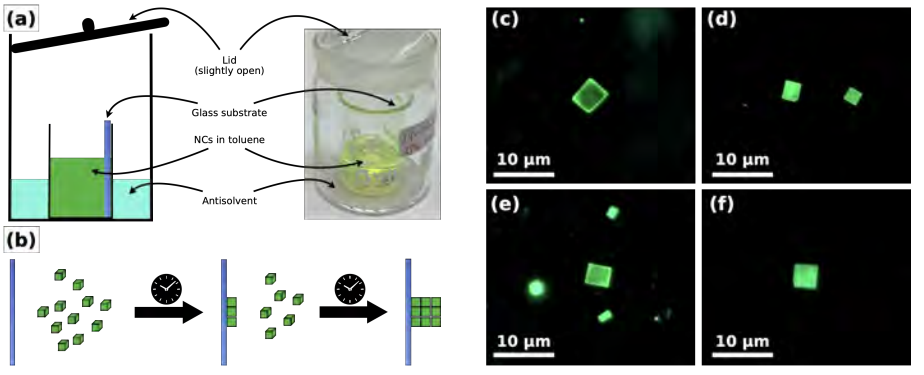

Figure 7.4: Slow-evaporation assembly of $CsPbBr_3$ NC superstructures. (a) scheme of the setup employed for the assembly; (b) representation of the gradual assembly of the NC superstructures over the substrate; (c–f) fluorescence micrographs of the resulting superstructures.

First, $2\,\mathrm{mL}$ of a $5\,\mathrm{mg/mL}$ dispersion of NCs in toluene were transferred to a small beaker, inside which a clean, appropriately cut glass substrate was placed upright against the inner wall. The choice of the substrate ultimately depends on the specific requirements of the subsequent characterisation techniques. In this case, $0.07\,\mathrm{mm}$-thick cover glasses were employed. The beaker was then positioned inside a larger vessel containing $4\,\mathrm{mL}$ of isopropanol (IpA), which served as the antisolvent. A lid was placed on top of the vessel, leaving a small opening to allow solvent evaporation. The system was kept in the dark, inside a fume hood, at room temperature until complete evaporation of toluene was achieved, typically after 10–14 days. Once dry, the substrate was then removed and stored for characterisation.

The presence of the antisolvent influences superstructure formation through two main mechanisms [249]. First, IpA vapours create a saturated atmosphere,

slowing the evaporation of toluene and enabling a more gradual destabilisation of the dispersion. This favours the growth of ordered superstructures over disordered aggregates. Second, direct interactions between IpA vapours and NCs at the air–liquid interface further decrease colloidal stability, promoting self-assembly.

Panels (c–f) of Figure 7.4 showcase fluorescence micrographs of the resulting superstructures, obtained in collaboration with the group of Dr. J. van de Groep (University of Amsterdam, The Netherlands) by means of a Witec 360 microscope equipped with a $405\,\mathrm{nm}$ laser diode. The superstructures display a very regular cubic morphology, analogous to that of their constituent NCs, with an average lateral size of 1–$5\,\mu\mathrm{m}$. Because of this morphology, these superstructures will henceforth be referred to as *supercubes* (SCs). Importantly, the micrographs reveal that the SCs retain the intense green PL emission characterising the NCs. The differences between their optical responses will be analysed after discussing the structural properties of the SCs.

7.2.3 SCs: supracrystalline structure and collective response

The ordering of the NCs within the SCs was investigated by small-angle X-ray scattering (SAXS) at the ID-02 Beamline of the *European Synchrotron Radiation Facility* (ESRF, Grenoble, France) [254] employing a $12.23\,\mathrm{keV}$ X-ray beam ($\sim 100\,\mu\mathrm{m} \times 100\,\mu\mathrm{m}$ spot) and a sample-detector distance of $1.3\,\mathrm{m}$. Each measurement was processed by subtracting the background and masking the central beam-stop and the gaps between the detector modules. The corrected 2D scattering map of the SCs, reported in panel (a) of Figure 7.5, exhibits clear rings corresponding to well-defined scattering maxima. To fully appreciate their profiles, the signal was azimuthally integrated, yielding the scattering intensity as a function of the wavevector q, shown in panel (b).

To interpret the supracrystalline structure, the experimental scattering maxima were compared with the positions expected for a simple cubic superlattice, which represents a natural starting model given the cubic shape of the NCs and their tendency to assemble via face-to-face contacts. For such a lattice, the scattering vector associated with planes indexed by Miller indices (hkl) is

$$q_{hkl} = \frac{2\pi}{d_{hkl}} = \frac{2\pi}{a}\sqrt{h^2 + k^2 + l^2}, \tag{7.1}$$

where $d_{hkl} = a/\sqrt{h^2+k^2+l^2}$ is the interplanar spacing and a is the lattice parameter (corresponding to the centre-to-centre distance between nearest-neighbour NCs).

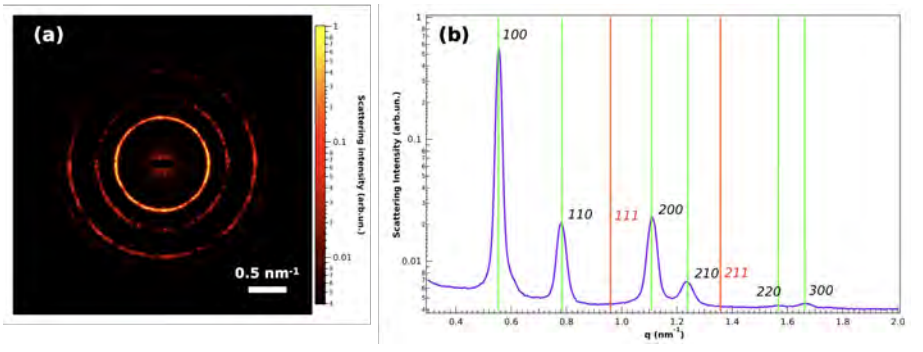

Figure 7.5: SAXS reveals the supracrystalline ordering of the $CsPbBr_3$ SCs: (a) 2D scattering intensity map of the SCs; (b) Scattering intensity as a function of the wavevector, obtained by azimuthal integration of the map in panel (a). The vertical lines represent the positions of scattering maxima expected for a simple cubic lattice with 11.3 nm (center-to-center) nearest-neighbour distances (green: observed, red: not observed), while the labels report the corresponding Miller indexes.

In particular, the lowest-wavevector peak (q_{100}) corresponds to the 100 planes and is used as a reference for all subsequent structural comparisons and calculations, due to its straightforward relationship with the lattice constant. From its position, the lattice parameter can be directly estimated as $a = 2\pi/q_{100} \approx 11.2\,\mathrm{nm}$. Using this value and the average lateral size l_{avg} of the NCs (see panel (c) of Figure 7.2), we can therefore compute the nearest-neighbour, surface-to-surface (StS) distance as:

$$d_{NN}^{StS} = a - l_{avg} = (2.9 \pm 0.3)\ \mathrm{nm} \tag{7.2}$$

The other observed scattering peaks are in excellent agreement with the positions expected for a simple cubic arrangement with this lattice parameter (pinpointed by the green lines in Figure 7.5(b)), confirming the validity of the simple cubic model. Notably, the 111 and 211 reflections, indicated by the red lines, are absent, which can be rationalized by the preferential orientation of the SCs on the substrate: the assemblies adhere with one face in contact with the surface rather than through a corner, hindering detection of these planes.

Finally, the full width at half maximum (FWHM) of the 100 peak, Δq_{100}, can be used to estimate the average crystalline domain size, ξ_{avg}, according to the *Scherrer equation* [255, 256]:

$$\xi_{avg} = \frac{2\pi K}{\Delta q_{100}} = (395 \pm 11)\ \text{nm} \tag{7.3}$$

where $K = 2\sqrt{\ln(2)/\pi} \simeq 0.94$ is the shape factor for cubic structures [257]. Notably, this estimate provides a lower bound to the true domain size, as additional effects, such as the instrumental resolution, the distribution of domain sizes, and lattice distortions, also contribute to peak broadening [256]. Thus, the crystalline domains within our SCs are remarkably large, each comprising several thousand NCs.

In order to understand how self-assembly impacts the photophysical properties of $CsPbBr_3$ NCs, we compared the steady-state and nanosecond-resolved photoluminescence of the SCs with that of their constituent NCs, as summarised in Figure 7.6.

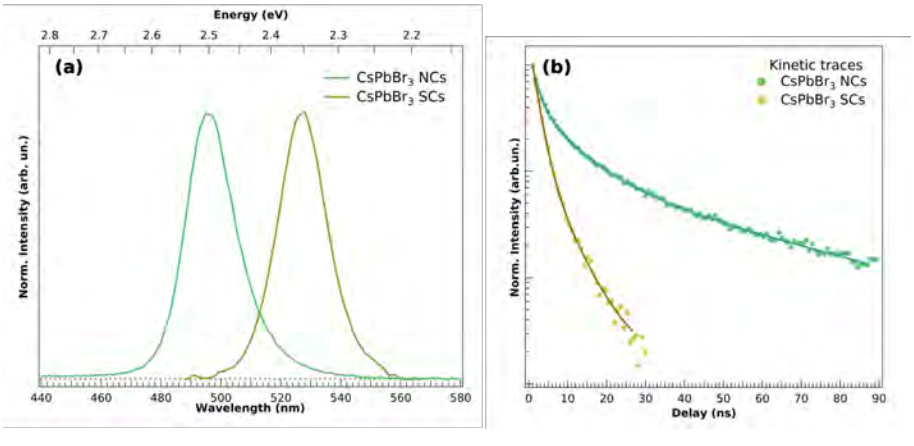

Figure 7.6: Normalised steady state PL (a) and PL decay traces (b) of $CsPbBr_3$ NCs and SCs.

The steady-state PL spectra (405 nm excitation), shown in panel (a) of Figure 7.6, reveal a pronounced redshift of 30 nm (140 meV): the PL of the SCs peaks at 525 nm (2.36 eV), whereas that of the isolated NCs is centred at 495 nm. This shift can be attributed to NC–NC interactions within the superstructures: partial delocalisation of the excitonic wavefunction over neighbouring NCs effectively lowers the bandgap, resulting in emission at longer

wavelengths. Interestingly, the FWHM of the emission slightly decreases from $90\,\mathrm{meV}$ for the NCs to $80\,\mathrm{meV}$ for the SCs. This narrowing is consistent with the notion that the self-assembly process preferentially selects NCs with more homogeneous sizes and optical properties, leading to a more uniform emissive population [258, 259].

To further elucidate this collective behaviour, nanosecond-resolved PL measurements were conducted at the University of Amsterdam, in collaboration with the group of Prof. Dr. P. Schall, using a LifeSpecII time-correlated single-photon counting (TCSPC) spectrometer equipped with a $375\,\mathrm{nm}$ picosecond laser diode. The spectrally integrated kinetic traces, reported in panel (b) of Figure 7.6, reveal that the PL of the SCs decays significantly faster than that of the NCs, providing further evidence of the highly efficient coupling within the superstructures. Multiexponential fitting quantifies this difference: the NCs exhibit three characteristic decay components (1.13 ± 0.04, 6.1 ± 0.3, and $35 \pm 2\,\mathrm{ns}$), whereas the SCs present only two (1.72 ± 0.03 and $5.6 \pm 0.6\,\mathrm{ns}$), both of which are compatible with the faster components of the NCs. The absence of the slower component in the SCs suggests that long-lived recombination pathways become strongly suppressed upon supracrystalline assembly, consistent with the emergence of efficient NC-NC coupling leading to accelerated exciton recombination.

7.2.4 SCs: disentangling the assembly kinetics

As discussed above, the formation of SCs proceeds very slowly, over the course of approximately 10–14 days. This gradual evolution provides a unique opportunity to monitor the assembly kinetics by deliberately removing the substrate from the solution after predetermined intervals. To obtain a statistically meaningful set of samples, five identical assembly procedures were initiated simultaneously. One was carried out to completion (10 days, already shown in Figure 7.5), while the remaining four were interrupted after $6\,\mathrm{h}$, $1\,\mathrm{d}$, $2.5\,\mathrm{d}$, and $5\,\mathrm{d}$, respectively. To interrupt each assembly, the relevant substrate was removed, excess liquid was gently absorbed using optical paper, and the sample was dried under vacuum.

The structural evolution of the assemblies was monitored by SAXS, and the resulting 2D patterns and azimuthally averaged scattering profiles are reported in Figure 7.7.

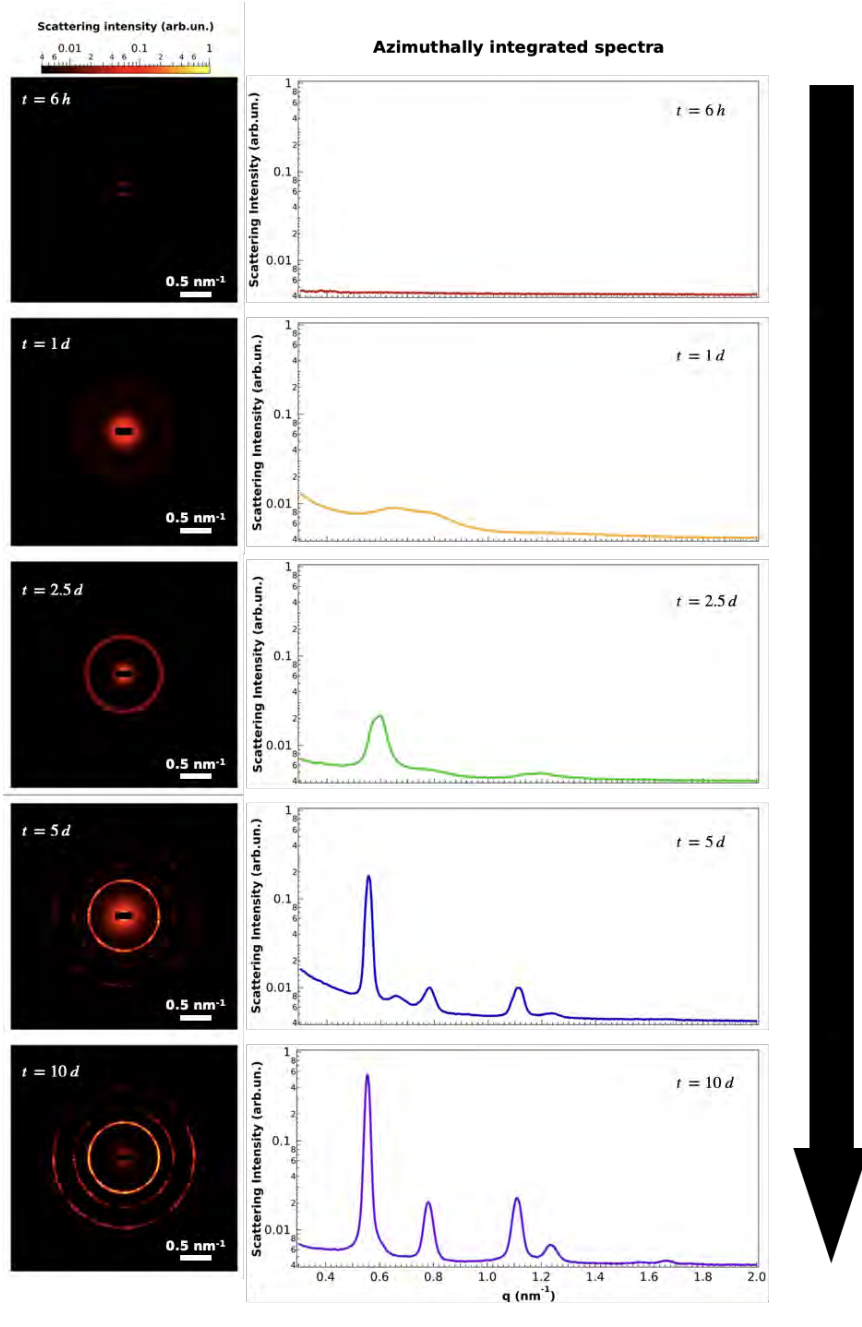

Figure 7.7: Disentangling the assembly kinetics of $CsPbBr_3$ SCs: SAXS maps (left) and azimuthally integrated spectra (right) for assembly durations of 6 h, 1 d, 2.5 d, 5 d, and 10 d (complete evaporation).

At $6\,\mathrm{h}$, the pattern shows only weak diffuse scattering, consistent with a very sparce, disordered arrangement of NCs on the substrate. After $1\,\mathrm{d}$, a broad ring becomes visible, indicating the onset of short-range positional correlations, in all probability linked to the nucleation of small NC assemblies on the substrate. A pronounced narrowing of this ring is observed at $2.5\,\mathrm{d}$, accompanied by the emergence of a weak second-order peak, signalling the progressive growth of the nuclei into small crystalline domains. By $5\,\mathrm{d}$, multiple well-resolved peaks appear at the q-positions expected for a simple cubic arrangement, revealing the consolidation of intermediate crystalline clusters of increasing size. Finally, as discussed above, after 10 days the assembly is fully accomplished, and we observe a fully developed diffraction pattern characterised by sharp peaks of high signal-to-noise ratio, testifying the presence of large supracrystalline SCs.

Interestingly, the broad diffraction maxima appearing at $t = 1\,\mathrm{d}$ and $t = 2.5\,\mathrm{d}$ are centred at higher q values with respect to the lowest-wavenumber peak $q_{100} = 0.56\,\mathrm{nm}^{-1}$ observed at $t > 5\,\mathrm{d}$, indicating (see equation (7.2)) that the average interparticle distance in the initially formed small assemblies is smaller than that characterising the final SCs. This counterintuitive evidence is suggestive of slow rearrangement processes occurring as the assembly proceeds, which allow the lattice to gradually relax toward its equilibrium configuration, leading to a slight increase in the average interparticle spacing concurrently with the emergence of long-range order. Furthermore, a weak secondary peak centred around $0.65\,\mathrm{nm}^{-1}$ appears at $t = 5\,\mathrm{d}$, but it is not visible in the final SCs ($t = 10\,\mathrm{d}$). Its disappearance in the mature samples could indicate that intermediate crystalline arrangements present during growth are eliminated as the assemblies relax toward the equilibrium simple cubic lattice.

To quantify this structural evolution, the average domain size ξ_{avg} was extracted at each time from the FWHM of the 100 peak, according to equation (7.3). The resulting growth curve, reported in Figure 7.8(a), reveals a clear, monotonic increase in ξ_{avg} from tens of nanometers at early times to several hundred nanometers in the final SCs. The sharpest increase in domain size happens between $2.5\,\mathrm{d}$ ($\xi_{avg} \simeq 90\,\mathrm{nm}$) and $5\,\mathrm{d}$ ($\xi_{avg} \simeq 300\,\mathrm{nm}$). This is expected, given the clear emergence of the simple cubic superlattice structure at $t = 5\,\mathrm{d}$.

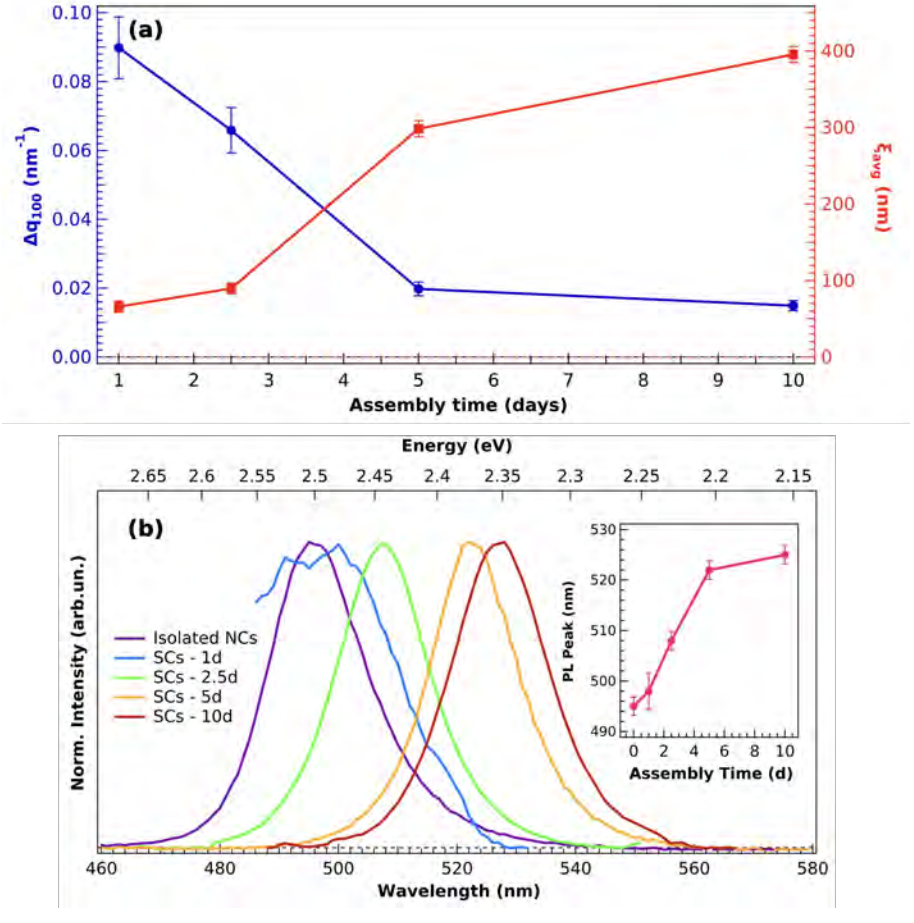

Figure 7.8: Correlating structure and optical response at increasing assembly time. (a) 100 peak width (blue) and average domain size (red) as a function of the assembly time; (b) Normalised PL spectra (excited at 405 nm) of isolated NCs and SCs at 1d, 2.5d, 5d, and 10d assembly time. The PL peak position is plotted in the inset as a function of assembly time ($t = 0$ corresponds to the isolated NCs).

Finally, we correlated the progressive growth of the SCs with the emergence of their collective optical response by comparing the PL emission of the NCs with those of the SC samples at increasing assembly times. Notably, as shown in panel (b) of Figure 7.8, the PL displays a progressive redshift from the peak position of the isolated NCs (495 nm) towards that of the mature SCs (525 nm), peaking at 498 nm, 508 nm, and 522 nm for assembly times of 1 d, 2.5 d, and

5 d, respectively (see the inset in panel (b)). This evidence complements the SAXS characterisation, showing that cross-talk effects within the SCs emerge progressively as the crystalline domains grow.

7.3 Conclusions

In this chapter, we delved into the structural and optical properties of all-inorganic $CsPbBr_3$ perovskite NCs and their supracrystalline cubic superstructures (SCs). We employed a slow-evaporation protocol in the presence of an antisolvent, to trigger the self assembly of the NCs into micrometre-sized SCs that preserve their cubic morphology as well as their intense emission. The highlight of this study is represented by small-angle X-ray scattering, which revealed that the SCs possess simple cubic supracrystalline order, with inter-particle distances of a few nanometres and domain sizes of several hundred nm. The optical properties of the SCs differ from those of the constituent NCs, showing a redshifted emission along with a faster photoluminescence decay. These changes reflect partial exciton delocalisation and efficient inter-NC coupling, signaling a transition from isolated quantum emitters toward a collectively interacting ensemble. Monitoring the assembly at intermediate stages *via* SAXS allowed to unravel the gradual growth of the SCs from small nuclei into large, well-defined superstructures. These findings enrich our mechanistic understanding of the assembly pathways of this prosperous class of NCs, paving the way towards the rational design of highly ordered perovskite superlattices with an array of desirable optical properties. In the broader context of this Thesis, these systems provide a clear example of how the morphology of the constituent nanocrystals governs the geometry of the resulting superstructures, while simultaneously illustrating a template-free assembly approach in which slow kinetics are essential for forming large, highly regular assemblies.

Part III

Results: Metallic Superstructures

8

Distance-Dependent Coupling in Crystalline Plasmonic Gold Superparticles

It has long been an axiom of mine that the little things are infinitely the most important.

— Arthur Conan Doyle

The assembly of plasmonic nanoparticles into superstructures expands the tunability of their plasmonic response by enabling cross-talk between neighbouring nanoparticles. This chapter delves into the role played by interparticle distances within the assembly in determining the collective plasmonic behavior of the superparticle. More in detail, we assembled gold nanoparticles into face-centered cubic crystals through slow emulsion densification, controlling the distance between nearest neighbours via ligand exchange. We used transient absorption microscopy to investigate the influence of the inter-nanoparticle

distance on the ultrafast photodynamics of carriers at the single superparticle level, uncovering a blueshift of the plasmonic resonance and an increase in the electron-phonon scattering timescale, as the interparticle distance progressively decreases. By combining advanced optical techniques and first-principle numerical simulation, we managed to link the observed trends to the fundamental characteristics of the superstructures, demonstrating the sensitivity of their collective response upon the inter-nanoparticle distance, and paving the way to finely tailorable plasmonic superstructures. The results presented in this chapter have been published in [260].

8.1 Introduction

Metal nanoparticles (NPs) show a characteristic resonant behavior arising from the collective oscillations of conduction electrons, known as localized surface plasmon resonance (LSPR) [261, 262]. LSPR results in an enhancement of the optical cross-section of the NPs, creating intense electromagnetic fields near their surface and resulting in resonant features appearing in their optical extinction spectra. As discussed in chapter 3, the spectral profile of LSPR strongly depends upon a number of factors, such as the shape and size of the NP, its composition, and the surrounding medium, thereby promoting plasmonic NPs as highly tailorable nanomaterials for numerous applications [121, 130, 263, 264].

Given the extensive tunability of individual NP plasmon modes, assembling NPs into well-defined mesoscopic superstructures (SPs) is a promising strategy to provide additional control over their collective optical behavior. Indeed, SPs assembled from metallic nanoparticles of varying shape and size exhibit plasmon coupling phenomena [144, 145, 265], wherein near-field interactions between adjacent particles lead to collective resonances that differ from those of isolated NPs. Plasmon coupling provides many opportunities to tailor the response of such systems, promoting them for multiple applications ranging from ultra-efficient surface-enhanced Raman spectroscopy (SERS) [266], plasmonic photocatalysis [267], and nonlinear plasmonics [268].

Despite their technological promise, plasmon coupling effects remain insufficiently understood. In particular, while coupling effects in assemblies of a few NPs (so-called oligomers or metamolecules) have been extensively stud-

ied [135, 136, 138], analogous results for 3D, densely packed SPs are lacking. Moreover, the influence of the structural features of the SPs, specifically the interparticle distances within the assemblies, on their collective plasmonic behavior is underexplored in the current literature. Such influence can be investigated by following the ultrafast relaxation dynamics of the hot electrons produced by photoexcitation of the SPs. Improving our understanding and control of these features may enable the rational design of SPs with predetermined plasmonic characteristics, advancing their integration into real-world technologies. While the tuning of interparticle distance in SPs has been reported [151], systematic studies that simultaneously address structural and photophysical properties of single SPs with high spatial and temporal resolution are still scarce, both because of the difficulty of tightly controlling the supercrystalline order of the SPs, and for the lack of appropriate methods capable of probing relaxations of individual SPs.

We address this knowledge gap by using gold superparticles (AuSPs) as a model system to study plasmon coupling effects. We synthesize AuSPs by an emulsion-templated assembly of gold nanoparticles (AuNPs), resulting in spherical assemblies with a face-centered cubic structure. Once the crystalline SPs are formed, we perform a ligand exchange to change the distance between nanoparticle constituents. Using state-of-the-art techniques, ranging from the structural characterization to ultrafast optical measurements, we investigate the fundamental photophysics of AuSPs, benchmarking it against that of the isolated building blocks. Our study reveals a clear dependence of both the LSPR spectral position and hot electron relaxation dynamics on the interparticle spacing. Contrary to expectations, we find that the plasmonic peak blueshifts when the particles are closer and that the cooling kinetics slow down significantly when the mutual distance between the particles within the superstructure is decreased. We correlate our experimental observations with the intrinsic properties of the SPs through detailed simulations, providing a direct and quantitative link between the experimentally observed trends and the fundamental electromagnetic behavior of the SPs and shedding light on their unusual response. This approach clarifies the role of interparticle spacing in dictating the optical and plasmonic characteristics of the SPs and provides insights that could pave the way for their systematic engineering towards many applications.

8.2 Results and Discussion

8.2.1 Assembly and characterisation of AuSPs

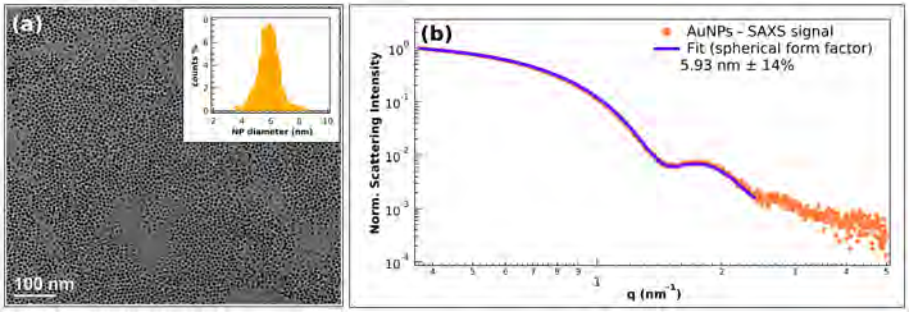

Figure 8.1: (a) TEM image of dropcasted AuNPs, the inset shows their size distribution; (b) Normalized SAXS spectrum of 5.9 nm AuNPs, fitted by a spherical form factor convoluted with a Gaussian distribution to account for polydispersity.

The *building blocks* of the superparticles are oleylamine-capped gold nanoparticles (AuNPs – Figure 8.1), synthesized following the literature procedure reported in chapter 4. Transmission electron microscopy (TEM) images (panel (a)) indicate that the AuNPs have an average diameter of $5.9\,\mathrm{nm}$ with a polydispersity of 14%, as shown in the inset. These dimensions are consistent with their small-angle X-ray scattering pattern, fit with a spherical form factor (panel (b) of Figure 8.1).

We use an emulsion-based approach to assemble these AuNPs into AuSPs, as schematised in panel (a) of Figure 8.2 and detailed in chapter 4. Briefly, the dispersion of AuNPs in toluene is added to an aqueous solution of sodium dodecyl sulfate (SDS) in a glass vial (i). The vial is then capped and vortexed (ii). The resulting emulsion (iii) is left overnight, uncapped, under gentle stirring and heating (iv). Following the complete evaporation of toluene, an aqueous suspension of AuSPs (v) is finally obtained. Dynamic light scattering (DLS) measurements reveal an average diameter of $160\,\mathrm{nm}$ with a 25% polydispersity (inset of panel (b)), suggesting the successful assembly of AuNPs into AuSPs. Panel (b) of Figure 8.2 shows a representative TEM micrograph of a single AuSP, characterized by a spherical shape and compact morphology with the near-absence of electron transmission through the center indicating

the high packing density of the $\sim 10^4$ AuNPs constituting each SP.

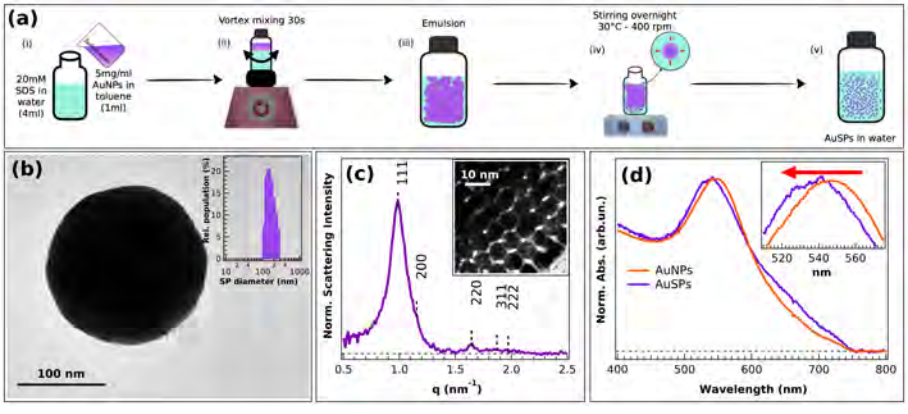

Figure 8.2: (a) schematic representation of the emulsion-based assembly of AuNPs into AuSPs; (b) TEM micrograph of a single AuSP, the inset reports their size distribution as obtained via DLS; (c) SAXS pattern of AuSPs, the vertical dashed lines indicate the positions of the reflections expected for a FCC superlattice, as indicated by the Miller indexes, while the inset shows a zoom near the edge of an AuSP obtained via TEM, highlighting the hexagonal packing of AuNPs; (d) steady-state UV-Vis spectra of AuNPs and AuSPs, where the red arrow highlights the blueshift of the LSPR peak.

We characterize the arrangement of the AuNPs within the AuSPs by Small-Angle X-ray Scattering (Figure 8.2 - panel (c)), revealing Face-Centered Cubic (FCC) symmetry. As the penetration depth of X-rays within our SPs is about 400-600 nm, i.e. significatively larger than the average SP diameter, we conclude that such supra-crystalline structure is consistent throughout the whole volume of each SP. This ordering can also be appreciated by focusing TEM on the edge of the AuSP, where electron transmission is sufficient to distinguish the hexagonal symmetry of the assembled AuNPs (inset of panel (c)). From the 111 reflection wavevector, it is possible to calculate the surface-to-surface (StS) nearest-neighbor distance between NPs as:

$$d_{NN}^{StS} = \frac{\pi\sqrt{6}}{q_{111}} - 2a_{NP}$$

where a_{NP} represents the radius of the AuNPs and q_{111} is the wavenumber of the 111 reflection, yielding $d_{NN}^{StS} = (1.90 \pm 0.03)$ nm.

Interestingly, the assembly of AuNPs affects their optical extinction properties, as shown in panel (d) of Figure 8.2. A direct comparison between well-dispersed AuNPs and AuSPs reveals that the latter present a slight (15 nm) blueshift of the LSPR peak with respect to the former. While numerous studies have shown cross-talk between plasmonic NPs to result in a redshift of the LSPR [136, 269, 270], the unusual behavior of our SPs can be explained in light of their structure and geometry. Indeed, such behavior is attracting significant attention in the current literature, having been observed in a number of similar systems [271–274]. In particular, Jenkins et al. [275] have proved that, in large ordered arrays of AuNPs with comparable interparticle distances, long-range plasmon coupling gives rise to a blueshift of the LSPR, whereas much narrower spacing or smaller aggregates would result in the much more commonly observed redshift. Therefore, we propose that the collective plasmonic response of our SPs is dominated by long-range interactions.

Notably, analogous assembly attempts on two batches of larger AuNPs (respectively 7.9 nm and 9.2 nm in diameter) yielded poorer results, as summarized in Figure 8.3. This could be explained by their higher polydispersity (>17, as measured via SAXS) as well as by the steric repulsion of the ligands being insufficient for the stabilization of larger AuNPs into regular SPs.

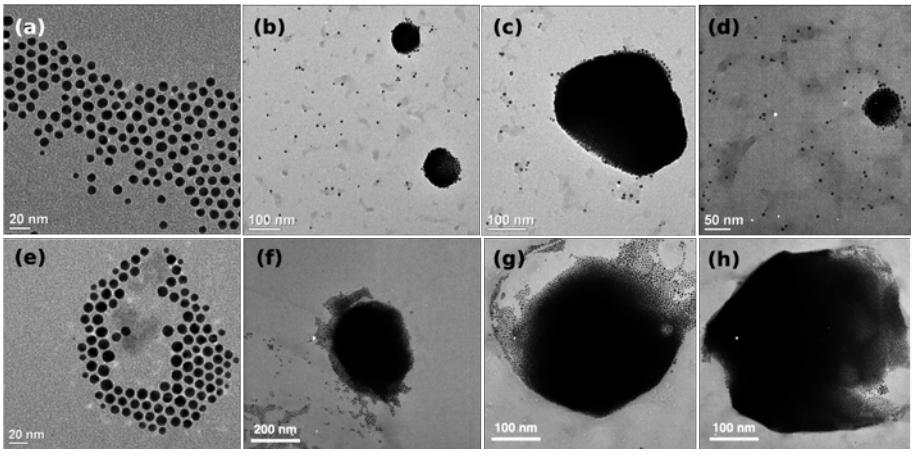

Figure 8.3: TEM micrographs of (a) 7.9 nm AuNPs, (b-d) SPs obtained from 7.9 nm AuSPs, (e) 9.2 nm AuNPs, (f-h) SPs obtained from 9.2 nm AuNPs.

8.2.2 Ligand Exchange on AuSPs

As a next step, we design a controlled way to investigate inter-AuNP coupling by varying their distance through ligand exchange, as schematized in Figure 8.4. To do so, we first drop-cast AuSPs onto a glass substrate. After drying and washing away the excess surfactant, we dip the substrate in a 2 mM solution of different alkanethiols in acetonitrile. Specifically, we employed 1-Hexanethiol (Panel (a)), 1-Octanethiol (Panel (b)), and 1-Dodecanethiol (Panel (c)). After washing away the excess thiol, we investigate the integrity of the AuSPs. TEM confirms that the AuSPs maintain their structural integrity as shown in panel (d) (1-hexanethiol, AuSPs-6CSH), panel (e) (1-octanethiol, AuSPs-8CSH), and panel (f) (1-dodecanethiol, AuSPs-12CSH) of Figure 8.4. The ligand-exchanged AuSPs show no visible cracks, that instead have been observed in larger systems after ligand-exchange [216].

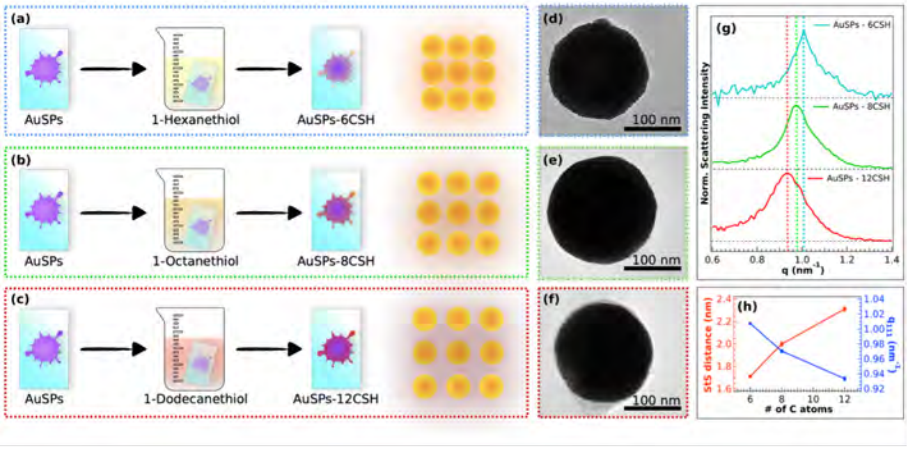

Figure 8.4: Tuning NP-NP distance via ligand exchange. (a-c) schematic representation of the ligand exchange procedure; (d-f) TEM micrographs of AuSPs-6CSH (d), AuSPs-8CSH (e), and AuSPs-12CSH (f); (g) detail of the 111 SAXS reflection at varying ligand length, the vertical dashed lines highlight the gradual shift; (h) wavenumber of the 111 reflection and corresponding surface-to-surface (StS) nearest-neighbor distances at varying ligand lengths (where not visible, the error bars fall within the size of the marker).

Most importantly, the success of the ligand exchange procedure is confirmed by SAXS, which shows that the 111 reflection shifts towards larger wavevector values as a function of decreasing length of the alkanethiol (panel (g) of Fig-

ure 8.4). This shift corresponds to a decrease in StS nearest-neighbor distance from $(2.31 \pm 0.02)\mathrm{nm}$ (1-dodecanethiol) to $(2.00 \pm 0.02)\mathrm{nm}$ (1-octanethiol) and $(1.71 \pm 0.01)\mathrm{nm}$ (1-hexanethiol), as shown in panel (h) of Figure 8.4. Notably, the StS distance in SPs with the native oleylamine ligands does not fall within this trend, which is expected given their different chemical nature. These results confirm that the alkanethiol ligands successfully diffuse within the whole volume of the AuSP, replacing the native oleate ones and yielding a more compact structure in a controlled fashion. While the supercrystalline order is overall preserved by ligand exchange, it is worth noting that shorter ligands result in a more uniform spacing within the SP, while longer ones exhibit higher conformational disorder, as demonstrated by the width of the 111 reflection peak increasing with the ligand length.

8.2.3 Ultrafast plasmon dynamics

Having confirmed ligand exchange as a reliable means of finely controlling the inter-AuNP distance within AuSPs, and having already shown that the cross-talk between NPs modifies the plasmon resonance when going from isolated NPs to SPs (see panel (d) of Figure 8.2), we investigate how varying this distance impacts the plasmonic behaviour and the photo-induced dynamical relaxations in these systems. We do so by leveraging the capabilities of ultrafast transient absorption microscopy (TAM). Indeed, traditional transient absorption (TA) spectroscopy plays an important role in garnering insight into the photo-initiated dynamics of non-luminescent systems, such as plasmonic NPs and their superstructures, down to the sub-picosecond timescale. As discussed in chapter 4, TAM augments the capabilities of TA by adding the high spatial resolution provided by optical microscopy. Coupling this spatial resolution with the sparse coverage of the AuSPs on the glass substrate, TAM allows the investigation of individual AuSPs.

Figure 8.5 summarizes our findings. Panels a-c show the TAM signal from individual AuSPs ligand-exchanged with 1-hexanethiol (AuSPs-6CSH – panel (a)), 1-octanethiol (AuSPs-8CSH – panel (b)), and 1-dodecanethiol (AuSPs-12CSH – panel (c)), respectively, obtained by pumping at $400\,\mathrm{nm}$ ($15\,\mu\mathrm{m}$ FWHM spot size, $5\,\mathrm{mJ/cm^2}$ fluence) and probing in the range $450 \div 660\,\mathrm{nm}$ at variable time delays from photoexcitation. The main feature of these spectra is a negative peak appearing at the plasmon resonance wavelength, a conse-

quence of the photoinduced bleaching (PB) of the LSPR transition. On either side of this PB signal, we observe positive features due to photoinduced absorption (PA), as well-known from the literature [276, 277]. The LSPR bleach signals of all three samples appear to decay in magnitude and blueshift by $\sim 10\,\mathrm{nm}$ over the first $\sim 5\,\mathrm{ps}$. This is a direct consequence of the initially photoexcited hot electron gas thermalizing with the lattice via electron-phonon scattering.

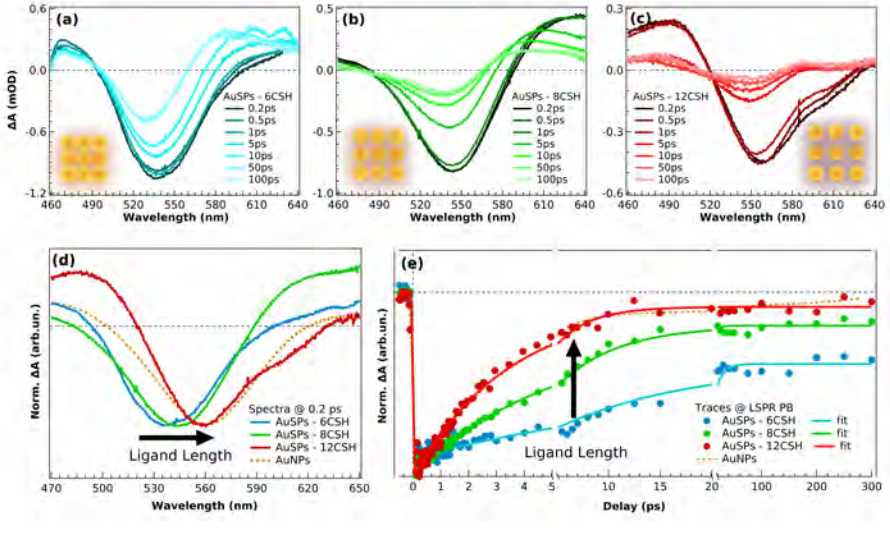

Figure 8.5: (a-c) Transient absorption microscopy (TAM) spectra at varying pump-probe delays of (a) AuSPs-6CSH, (b) AuSPs-8CSH and (c) AuSPs-12CSH, pumped by 400nm pulses at 5 mJ cm-2 fluence; (d) Normalized TAM spectra of AuSPs as a function of ligand and dropcasted AuNPs at 0.2 ps pump-probe delays; the arrow shows the redshift of the plasmon bleach peak at increasing interparticle distance; (e) normalized kinetic traces and associated fits at the plasmon bleach position of AuSPs as a function of ligands length, and of drop casted AuNPs; the arrow indicates the faster decay observed when increasing the interparticle distance.

Importantly, TAM reveals clear differences between the SP samples: normalized TAM spectra at a fixed $0.2\,\mathrm{ps}$ pump-probe delay shown in panel (d) of Figure 8.5 display a progressive redshift of the LSPR bleach as the ligand length increases, ranging from $537\,\mathrm{nm}$ for AuSPs-6CSH to $545\,\mathrm{nm}$ for AuSPs-8CSH and $560\,\mathrm{nm}$ for AuSPs-12CSH. The observation of such a strong dependence of the plasmonic resonance peak position on the ligand length, in addition to the spectral shift already observed between the LSPR of AuNPs and AuSPs

(panel (d) of Figure 8.2), confirms that the cross-talk between NPs within our SPs is governed by long-range interactions, which are expected to result in a blue-shift of the LSPR when decreasing the interparticle spacing [275, 278].

Kinetic traces for the three samples, extracted at the LSPR bleach wavelength and normalized, are reported in panel (e) of Figure 8.5. As known from the literature [117], after photoexcitation the coherent plasmon quickly dephases (within 10 fs) and the resulting hot electron gas thermalizes via electron-electron scattering. As both processes occur within 50 fs, they are below the temporal resolution of our TAM measurements. However, we observe a decay of the signal with timescales in the picosecond range. This decay can be ascribed to electron-phonon scattering, that is, the physical process by which the hot electrons transfer energy to the lattice. Least-square fitting of these traces with a model taking into account exponential decays convoluted with the IRF of our setup reveals that the electron-phonon scattering time constant strongly increases when the ligand length decreases, ranging from $(13 \pm 1\mathrm{ps}$ in AuSPs-6CSH and $(5.78 \pm 0.16)\mathrm{ps}$ in AuSPs-8CSH, down to $(3.31 \pm 0.14)\mathrm{ps}$ for AuSPs-12CSH. Finally, we observe a further, minor decay of the signal over hundreds of picoseconds, which can be attributed to energy dissipation towards the environment mediated by phonon-phonon scattering. Therefore, our results show that the relaxation dynamics of charge carriers in the superstructure are sensitive to the cross-talk between individual AuNPs, which is expected to depend on their mutual distance. Notably, performing TAM on the constituent AuNPs (dashed traces in panels (d-e) of Figure 8.5) yields very similar results to those observed for the SPs with the largest interparticle distance (AuSPs-12CSH), suggesting that $2.3\,\mathrm{nm}$ represents a threshold distance below which inter-NP cross-talk switches on.

Using TAM instead of more conventional TA spectroscopy is crucial to this investigation. We prove this statement by comparing our results with those of a traditional TA experiment, performed in collaboration with the group of Dr. Alessandra Paladini (CNR-IFM, Rome). In particular, in Figure 8.6 we report the TA spectra (panel (a)) and kinetic traces (panel (b)) of the same three AuSP samples, excited with $370\,\mathrm{nm}$ pulses at $0.7\,\mathrm{mJ/cm^2}$. No clear trend emerges here at varying ligand length. Instead, the spectra are essentially identical to one another, with slight shifts that appear uncorrelated with the ligand.

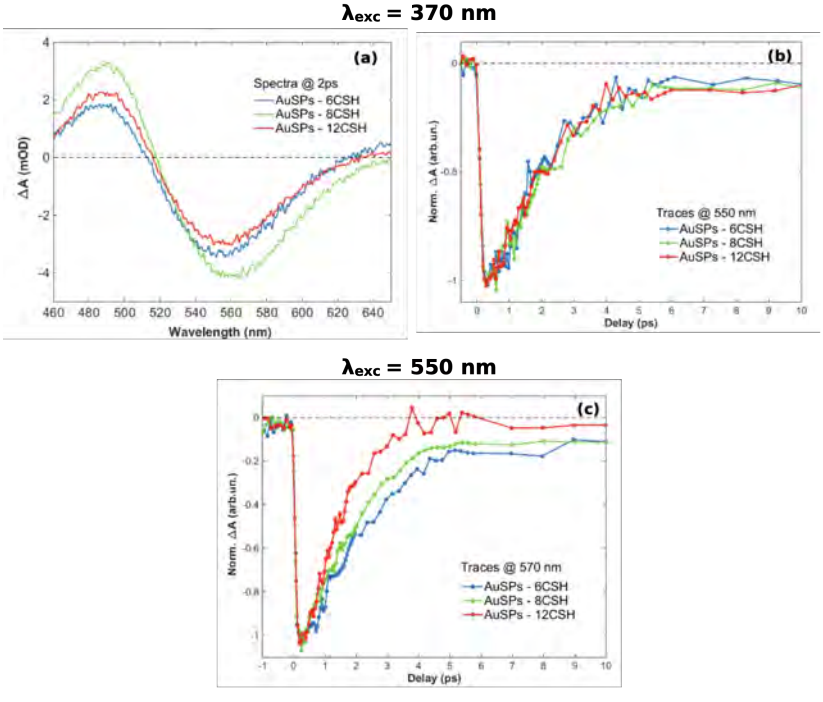

Figure 8.6: (a) TA spectra and (b) kinetic traces at the LSPR bleach wavelength for AuSPs-6CSH, AuSPs-8CSH, and AuSPs-12CSH excited at 370 nm; (c) normalized TA kinetic traces at the LSPR bleach position of AuSPs-6CSH, AuSPs-8CSH, and AuSPs-12CSH excited at 550 nm

This evidence also stands true for the LSPR kinetic traces displayed in panel (b), which present the same quasi-instantaneous rise and subsequent decay over a few picoseconds already observed in TAM. However, they appear essentially identical for all three samples. Because of the lack of spatial resolution, TA is most likely affected by aggregates present on the substrate being indiscriminately excited together with the target SPs, thus losing the true signal of the SPs under that of the surrounding aggregates. In contrast, the spatial resolution of TAM allows to selectively probe the SPs, revealing their true dynamical response (Figure 8.5). Furthermore, as discussed in chapter 4, TAM is also capable of isolating genuine absorption variations from scattering contributions. Interestingly, TA experiments performed with 550 nm excitation (resonant with the LSPR, panel (c) of Figure 8.6) reproduces the TAM-observed trend in bleach kinetics (panel (e) of Figure 8.5), due to the superior sensi-

tivity obtained by pumping at the LSPR, as further clarified by the numerical simulations discussed below.

8.2.4 Near-field enhancement simulations

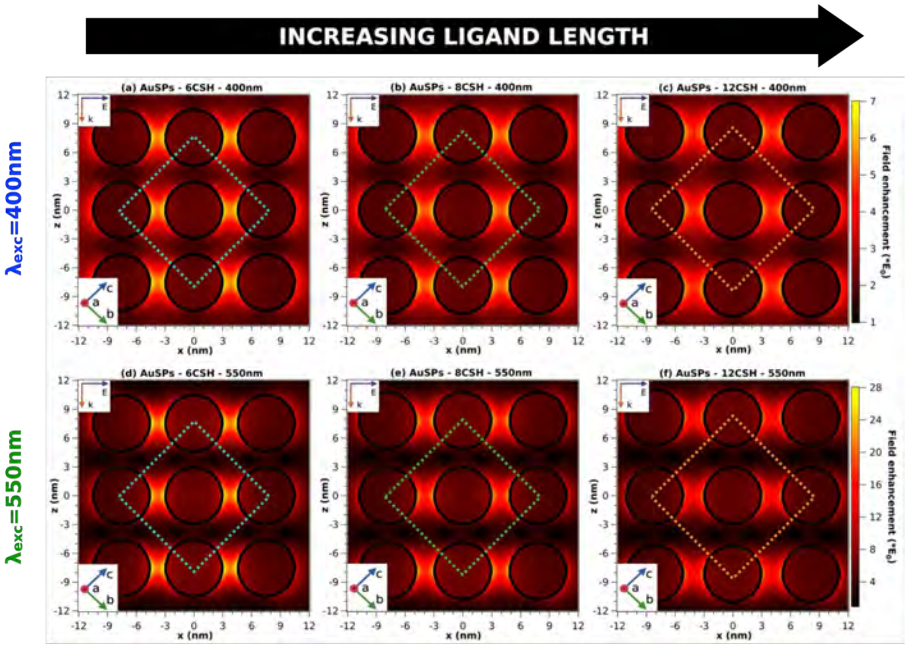

Figure 8.7: Boundary element-based simulation of the near-field enhancement in AuSPs with varying ligand length at 400nm (a-c) and 500nm (d-f) excitation wavelength. The insets show the polarization and propagation direction of the excitation plane wave and the orientation of the principal axes of the FCC lattice, while the dashed squares highlight the unit cell.

Summarizing, the TAM results in Figure 8.5 clearly indicate progressive changes of the electron-phonon relaxation timescales as a function of NP distances within the SP. Therefore, varying the interparticle distance impacts the photoinitiated dynamics of carriers within our AuSPs, further promoting ligand exchange as a versatile strategy towards the fine-tuning of the optical properties of plasmonic superstructures. It is worth noting that the observed trend – i.e. electron-phonon scattering slowing down when the ligand length decreases – is counterintuitive, as the increase in cross-talk between neighboring NPs determined by the decrease in their mutual distance could be expected to promote electron-phonon scattering, thereby lowering its timescale. This ap-

parently baffling evidence can be explained considering the fundamental electromagnetic properties of these superstructures.

With this in mind, we employed the open-source MNPBEM package [279, 280] to simulate the near-field enhancement for a unit cell of the FCC lattice that composes our AuSPs. MNPBEM uses a Boundary-Elements Method (BEM) to calculate the charge and current densities on the surface of metal NPs subject to an external electric field and the consequent field enhancement.

Here, we simulated a small portion of an SP as an array of nine AuNPs in a 3X3 configuration with $y = 0$ as the common equatorial plane, their radii and center-to-center distances set to the values experimentally obtained from SAXS. The NP array is submerged in a dielectric medium with the refractive index of thiols ($n \simeq 1.45$). The x-axis of the simulation is taken parallel to the 111 axis of the FCC lattice. The excitation source is a monochromatic plane wave propagating along the $-z$ direction and linearly polarized along x.

The color plots in Figure 8.7 report the simulated field enhancement (in units of the incident field amplitude E_o), assuming excitation with a wavelength of either $400\,\mathrm{nm}$ (the pump wavelength used for our TAM measurements) or $550\,\mathrm{nm}$ (resonant with the LSPR). We observe the maximum enhancement of the electric field near the surface of each NP, due to the individual plasmon oscillations amplifying the incident field in their proximity. It is crucial to remember that the field enhancement is sensitive to the complex refractive index mismatch between the metallic NP and its surrounding medium, as well as to the size and shape of the former. For example, chemically distinct ligands can alter field enhancement due to their differing refractive indices. Furthermore, we observe hot spots between adjacent NPs, a hallmark of near-field plasmon coupling driven by mutual LSPR interactions. These hot spots appear exclusively along the x-axis, consistent with the polarization direction of the incident field.

At a given excitation wavelength, the peak field enhancement observed at the surface of individual AuNPs clearly decreases in magnitude as the ligand length increases, as shown by the horizontal cuts of the 2D map reported in Figure 8.8. This yields a quantitative confirmation of the critical role played by the ligand length in determining our system's plasmonic response, putting into perspective the significant fine-tuning opportunity represented by ligand exchange.

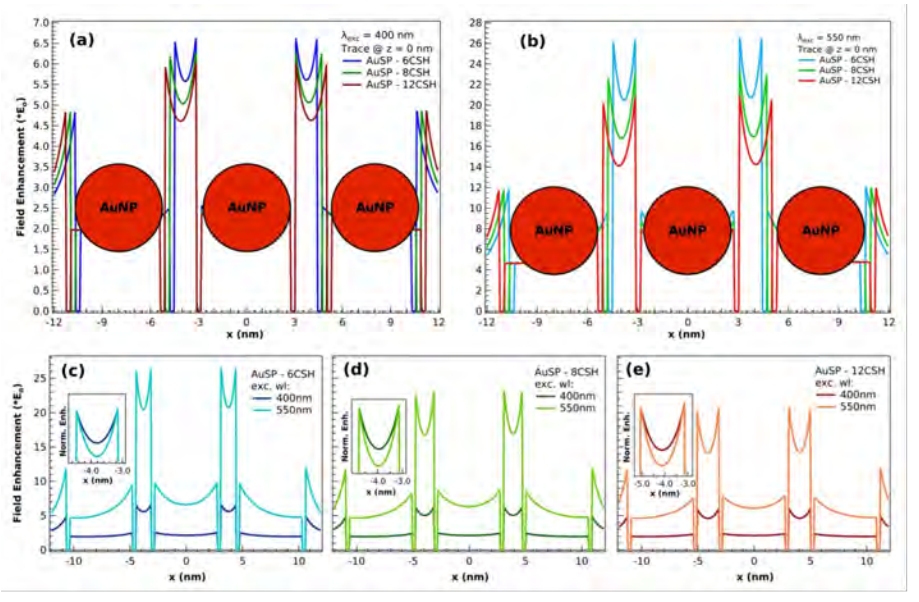

Figure 8.8: field enhancement traces obtained by horizontal cuts at z=0 of the plots in Figure 8.7. (a-b): field enhancement at varying ligand length under (a) 400 nm and (b) 550 nm plane wave excitation, the red circles pinpoint the position of each AuNP; (d-e): comparison between 400 nm and 550 nm excitation for (c) AuSPs-6CSH, (d) AuSPs-8CSH, and (e) AuSPs-12CSH. The insets report a detail of the normalized traces in order to highlight the different shapes of the hot spots.

8

Notably, resonant LSPR excitation at $550\,\mathrm{nm}$ yields not only a stronger field enhancement at fixed interparticle distance, but also a much more pronounced dependence of the enhancement upon the ligand length, compared with exciting at $400\,\mathrm{nm}$. To appreciate this trend, we expanded the range of interparticle distances beyond the experimentally observed ones, performing analogous simulations with Surface-to-Surface distances ranging from $1.25\,\mathrm{nm}$ to $3.2\,\mathrm{nm}$ at $0.15\,\mathrm{nm}$ intervals.

The results, shown in Figure 8.9, reveal that, at $550\,\mathrm{nm}$ excitation, increasing the inter-NP distance from $1.25\,\mathrm{nm}$ to $3.2\,\mathrm{nm}$ results in the maximum field enhancement decreasing from $37.2E_o$ to $17.2E_0$ (less than half its initial value), while at $400\,\mathrm{nm}$ excitation the maximum field enhancement goes from $7.65E_o$ to $5.58E_o$ (therefore only decreasing by about 28%) for the same distance increase.

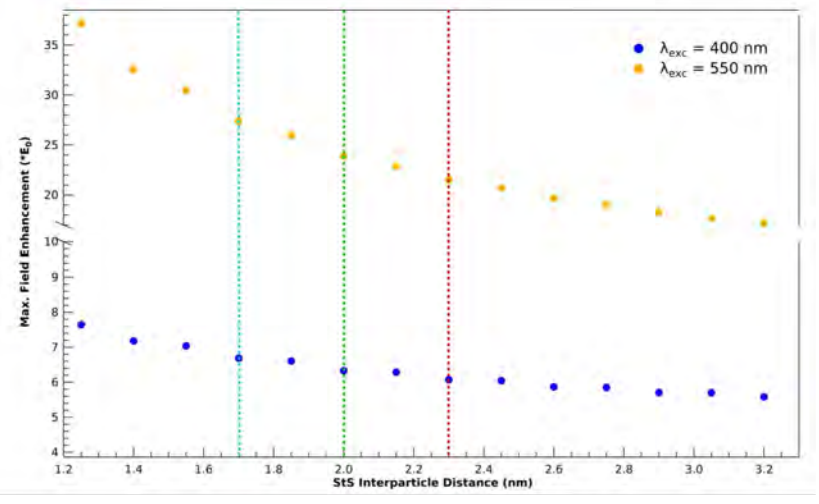

Figure 8.9: Maximum field enhancement as a function of the surface-to-surface (StS) interparticle distance at 400 nm and 550 nm excitation. The light blue, green, and red vertical lines pinpoint the StS distances corresponding to AuSPs-6CSH, AuSPs-8CSH, and AuSPs-12CSH, respectively.

Combining the results of simulation with our experimental findings, the presence of hot spots and their dependence upon ligand length sheds light on the trends observed via TAM, particularly on the increase in electron-phonon scattering time at lower interparticle distance. Indeed, the more pronounced near-field enhancement at shorter ligand lengths will result in a larger population of hot electrons after photoexcitation, which will transfer energy to the gold lattice over a longer timescale determining the slowing down of electron-phonon scattering we observe in our TAM measurements. We believe that even smaller interparticle distances would eventually produce an opposite trend, as stronger interactions would promote inelastic scattering, resulting in a more efficient damping which would speed up the decay as the NP distance decreases. Therefore, the synergy between TAM experiments and numerical simulations provides unparalleled insight into the ultrafast dynamics of our SPs, correlating their unusual behavior with their fundamental characteristics.
This analysis helps reinterpret the TA data shown in Figure 8.6. The absence of a clear trend when exciting at 400 nm likely stems from the relatively weak dependence of field enhancement on interparticle spacing at that wavelength, which prevents clear separation of AuSP signals from those of disordered ag-

gregates. In contrast, a distinct trend becomes evident at $550\,\mathrm{nm}$, where coupling is stronger and more distance sensitive. This supports our initial assumptions and further highlights how the spatial resolution of TAM enables selective probing of individual SPs within heterogenous samples.

8.3 Conclusions

We reported the synthesis of spherical, supra-crystalline AuSPs composed of AuNPs arranged in an FCC super-lattice with a variable inter-NP spacing tunable by ligand exchange. We gained deep insight into the fundamental physics governing the plasmonic response of this system down to the sub-picosecond time scale by combining advanced optical characterization and first-principles simulations. Our study highlights the role of interparticle distance in determining the magnitude and spatial distribution of the hot spots of field enhancement and elucidating how such hot spots condition the photoinitiated electron-phonon scattering processes within our SPs.

Besides providing interesting insight on the understanding of the collective plasmonic behavior of AuSPs, our findings may provide the foundation for the bottom-up engineering of a palette of metallic SPs with fine-tunable LSPR characteristics, which could facilitate applications in both plasmon-enhanced technology and nanophotonics. Indeed, by carefully selecting both the starting NPs and the ligands, it would in principle be possible to obtain AuSPs with complex functionalities, such as ultra-efficient SERS detection of specific molecular species, site-selective theranostic capabilities, or highly precise live monitoring of environmental changes.

Within the broader framework of this Thesis, this study further illustrates how minute variations in superstructure geometry - here, interparticle distances differing by mere fractions of a nanometre — can markedly influence the collective behavior of the assembly. It thus provides a clear working example of ligand exchange as a versatile strategy for the rational design of finely tuned superstructures, while also showcasing TAM as a uniquely powerful tool for probing the fundamental optical response of individual, non-luminescent superstructures.

9

Self-Assembly of Gold Nanoclusters into Hierarchical Fibrillar Superstructures

Satis longa vita et in maximarum rerum consummationem large data est, si tota bene collocaretur.

— Lucius Anneus Seneca

Atomically precise metal nanoclusters (NCs), consisting of up to a few hundred metal atoms, exhibit unique optical and electronic properties due to their "molecule-like" discrete energy levels. Compared to the plasmonic NPs that make up the superparticles covered in the previous chapter, NCs offer superior monodispersity (by virtue of their atomically precise structure) as well as efficient photoluminescence emission enabled by transitions between the discretised energy levels introduced by quantum confinement. In this chapter, we analyse how ultrasmall $Au(I)_6$ NCs can form crystalline superstruc-

tures under precise aggregation conditions controlled by protonation and site-specific hydrogen bonding. In particular, we demonstrate the emergence of self-assembled fibre-like superstructures, which further assemble to form nanoribbons. The collective optical response of these superstructures stands out from that of the constituent NCs: in particular, we observe strong photoluminescence emission characterised by a non-trivial power-law decay which we attribute to carrier diffusion across the 1D architecture of the fibrillar superstructure. This work highlights the potential of ultrasmall NCs as versatile building blocks for tunable, responsive optoelectronic materials, demonstrating the emergence of novel, collective properties and providing new insights into the mechanisms of self-assembly, thus opening opportunities for designing advanced functional nanomaterials. The results presented in this chapter are included in a manuscript at the submission stage.

9.1 Introduction

Within the extensive spectrum of nanomaterials suitable as building blocks for functional superstructures, atomically precise noble metal nanoclusters (NCs), consisting of up to a few hundred metal atoms protected by organic ligands, constitute a promising class of systems [281]. The widespread interest towards NCs is justified by their role in "bridging the gap" between small molecules and larger plasmonic nanoparticles both in terms of size and optical properties [282, 283]. Among NCs, gold nanoclusters (GNCs) are particularly promising due to their high biocompatibility and impressive stability [284]. GNCs also exhibit intriguing optical properties, that are highly different from larger metal nanoparticles, including photoluminescence stemming from the molecule-like transitions between their discrete energy levels [285]. However, their optical response is generally complex, owing to the interaction between the gold core and the ligands promoting phenomena such as ligand-to-metal charge transfer (LMCT) [173, 286]. One of the key features driving interest in GNC-based self-assemblies is their tunable electronic and optical properties [287, 288]. Self-assembly processes driven by non-covalent interactions like hydrogen bonding, van der Waals forces, and electrostatic interaction, enables the formation of highly ordered nanostructures from zero dimensional GNCs [289]. Consequently, the chemistry and structure of surface ligands over

the GNCs are pivotal in dictating the mode and strength of intercluster interactions. For instance, ligands with aromatic groups can promote $\pi - \pi$ stacking, facilitating the formation of ordered structures [290]. Yao et al. reported the self-assembly of $Au_{25}(SR)_{18}$ NCs into micrometer-sized rod-like supercrystals, in which the type and concentration of tetraalkylammonium ions have determined the geometrical properties of the obtained superstructures [291]. In addition, solvent polarity, concentration, and temperature can significantly affect the self-assembly process. The solubility of GNCs and the strength of intermolecular interactions are solvent-dependent, often requiring fine control to achieve the desired assemblies [292, 293]. Moreover, external stimuli such as metal ions, pH, light, and magnetic/electric fields can also be utilized to steer the self-assembly process [284]. For example, pH-responsive ligands can trigger reversible assembly and disassembly of GNCs, enabling dynamic control over the material properties [294]. Hence, the size and arrangement of the NCs within the assemblies along with the factors influencing this process of autonomous organization, such as solvent and external stimuli, contribute to the distinct optical and electronic properties of the resulting superstructures. By manipulating these parameters, it is possible to tailor their architecture and thus finely engineer their function in view of sensing, imaging, and optoelectronic applications [295, 296]. However, ultrasmall GNCs (possessing less than ten gold atoms and therefore lacking the well-defined Au(0) core characterising larger clusters) have been rarely used as building blocks of more complex superstructures, and the consequences of cross-talk between neighbouring GNCs within the assemblies remains virtually unexplored. Recently, Chandra *et al.* [173] reported the synthesis of ultrasmall $Au(I)_6$ NCs, capped by 6-(dibutylamino)-1,3,5-triazine-2,4-dithiol (TRZ) and displaying unique optoelectronic properties and quantum coherence effects.

Here, we demonstrate the controlled assembly of these NCs into fibrous superstructures through accurately controlled, chemically induced mechanisms like protonation and solvation. We show that hydrogen bonding facilitates and coordinates the assembly process, which is also guided by aurophilic interactions. Appropriately varying the chemical environment yields diverse hierarchical superstructures, ultimately culminating in a three-dimensional network of nanofibers, where chains of ligand-coordinated NCs are further aligned in ribbon-like ordered domains. We delve into the optical properties of these su-

perstructures, uncovering collective behaviors such as diffusion-driven carrier migration, which go beyond those of individual Au6 NCs, further expanding their applicability.

9.2 Results and Discussion

9.2.1 Self-assembly of Au nanoribbons

The synthesis of ultrasmall $Au(I)_6$ NCs and their assembly into nanoribbon-like superstructures were performed by Dr. S. Chandra (Aalto University, Finland), who also performed the structural characterisation presented below. As a starting point, 6-(dibutylamino)-1,3,5-triazine-2,4-dithiol (TRZ) stabilized ultrasmall $Au(I)_6$ NCs were synthesized according to a previously reported method [173]. As shown in panel (a) of Figure 9.1, a single cluster consists of a core of six gold atoms that is covalently bound to three TRZ ligands via di-thiolate bonds.

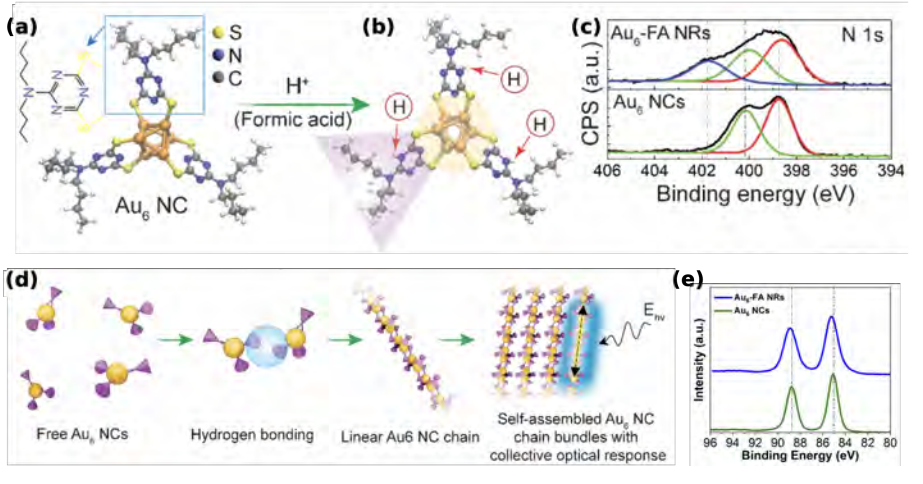

Figure 9.1: Supramolecular organisation of $Au(I)_6$ NCs. Top row: schematic representations of (a) the chemical structure of the NCs and (b) the protonation of the amino group in the TRZ ligand; (c) N 1s XPS spectra highlighting the change in the binding energy due to the protonation of the amino groups. Bottom row: (d) schematics of the self-assembly process; (e) Au 4f XPS spectra highlighting the onset of aurophylic interactions.

The organization of individual nanoclusters into supramolecular architectures can be triggered in solution phase by appropriately controlling the chemical environment of the NCs. In particular, we have observed (see panels (b-e) of Figure 9.1) that, after introduction of formic acid (FA) to the clear dispersion of $Au(I)_6$ NCs in dichloromethane (DCM), the isolated NCs form self-assembled nanoribbon (NR)-like superstructures (Au-FA NRs), which can be isolated from the starting solution by centrifugation or sedimentation and then subjected to further analysis. A significant positive shift in the N 1s binding energy for Au-FA NRs, as revealed by X-ray photoelectron spectroscopy (XPS - panel (c)), confirms the protonation of the amino group in the ligand. The protonated amino groups form H-bonds between the NCs, which results in self-assembled superstructures, where the particles are strongly interacting with each other. The whole process is schematically represented in panel (d). Finally, Au 4f XPS spectra (panel (e)) show small positive shifts of the peaks following self-assembly, indicating the onset of strong aurophilic Au(I)-Au(I) interactions in between the aligned NCs within the NRs.

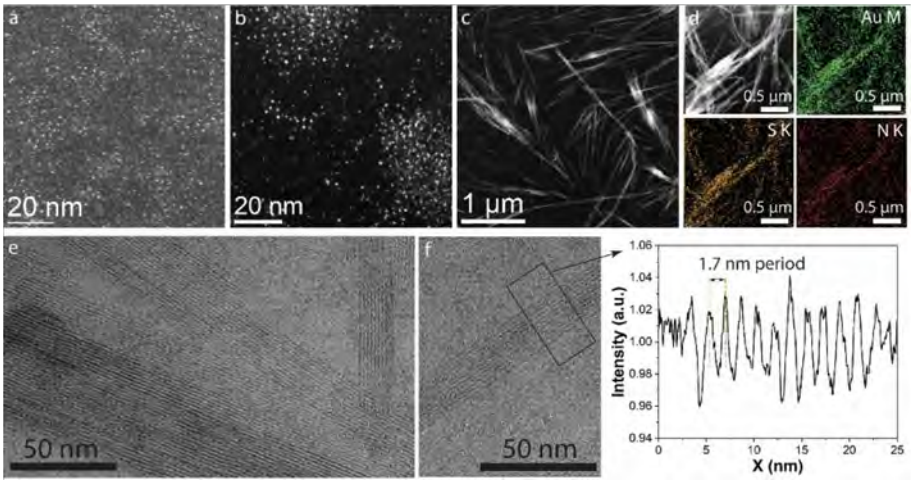

Figure 9.2: Structural characterisation of $Au(I)_6$ superstructures. (a) scanning transmission electron microscopy (STEM) images of isolated $Au(I)_6$ NCs synthesized using DCM (a) and $CHCl_3$ (b) as the solvent. (c) STEM image, (d) corresponding energy-dispersive X-ray (EDX) mapping and (e) Cryo-TEM image of Au-FA nanoribbons (NRs). (f) Line profile from the indicated box in the Cryo-TEM image, highlighting the periodicity within the NRs.

The morphology of the NRs has been characterized using transmission electron

microscopy (TEM - Figure 9.2). While the isolated $Au(I)_6$ NCs are $\sim 1\,\mathrm{nm}$ in diameter (panels (a-b)), Au-FA NRs are typically several micrometres in length and $20 - 30\,\mathrm{nm}$ in width (panel (c)). The composition of the NRs was verified using energy-dispersive X-ray mapping (EDX - panel (d)), which confirmed that they are composed solely of Au, S, C, and N. These are the same components found in the NCs, as anticipated. Further details on their structure can be revealed by cryogenic transmission electron microscopy (Cryo-TEM). The NC assemblies are highly sensitive to the electron beam, and therefore their real structures have been evaluated by fast exposure ($8\,\mathrm{s}$) in Cryo-TEM microscopic analysis. The Cryo-TEM images of Au6-FA NRs (panel (e)) demonstrate that the NCs align according to a well-defined structure. In particular, they form 1D linear chains, which in turn align in bundles, forming the NRs. The ordered alignment of the NC chains within the NR is confirmed by the $\simeq 1.7\,\mathrm{nm}$ periodicity observed in the transverse direction (see panel (f)).

To evaluate how different chemical environments impact the geometry and degree of ordering of the resulting superstructures, analogous assembly processes were carried out, substituting formic acid with acetic acid, acetic acid and D-sorbitol, and ethanol. The details of such mechanistic study are beyond the scope of this thesis, and are reported in full in the abovementioned manuscript. In the following, we will focus on the optical properties of Au-FA NRs, from the steady-state down to the sub-nanosecond timescale. In particular, we will compare and contrast the response of the superstructures with that of the constituent NCs, in order to understand how self-assembly impacts the photocycle of the NCs.

9.2.2 Au Nanoribbons: collective optical response

Figure 9.3 summarises the steady-state optical response (UV-Vis absorption - panel (a), and photoluminescence - panel (b)) of Au-FA NRs and their constituent NCs. The optical absorption spectrum of the isolated NCs shows a strong peak, centred at $290\,\mathrm{nm}$ with a weaker shoulder peaking at $440\,\mathrm{nm}$. After self-assembly, the absorption profile substantially changes, exhibiting spectral shifts in Au-FA NRs, where the two peaks are centred at $340\,\mathrm{nm}$ and $400\,\mathrm{nm}$ respectively. The self-assembly also causes a modification of the amplitude ratio between the two peaks, suggesting strong NC-NC ground-state electronic crosstalk within the NRs. Considering the modifications of the ab-

sorption profiles, it can be expected that self-assembly would also result in a modification of the photoluminescence (PL) spectrum. This is indeed the case, as the two samples show rather different emission profiles (panel (b) of Figure 9.3).

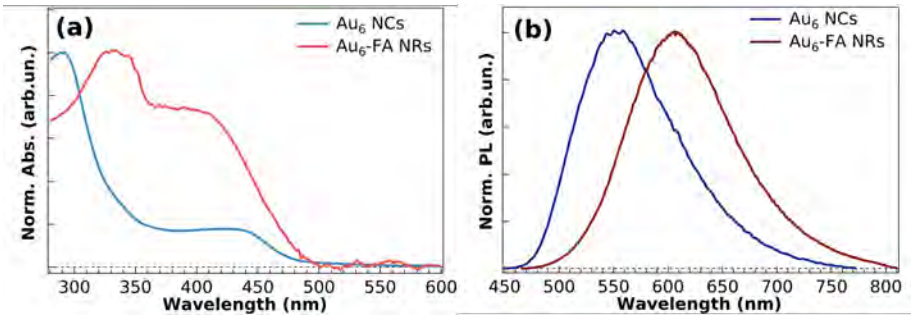

Figure 9.3: Normalised UV-Vis (a) and photoluminescence (PL) (b) spectra of $Au(I)_6$ NCs (blue traces) and Au-FA NRs (red traces).

In particular, the self-assembled Au-FA NRs display a significantly red-shifted PL spectrum (centered around $610\,\mathrm{nm}$) with respect to that of isolated NCs (peaking at $550\,\mathrm{nm}$). The variations in the emission profiles are again indicative of strong cross-talk between the individual NCs composing the superstructure, whereby the superposition of single-NC orbitals results in a variation of the energy level positions and of the energy gap between the emitting excited state manifold and the ground state.

Nanosecond (ns) and femtosecond (fs) time-resolved optical measurements on both $Au(I)_6$ NCs and Au-FA NRs allow to clarify the population and depopulation dynamics of the relevant electronic states. Nanosecond-resolved PL measurements have been performed at $410\,\mathrm{nm}$ excitation for both isolated NCs and NRs. Normalized spectra at representative delays are reported in panels (a-b) of Figure 9.4. A comparison between their spectral evolution reveals that, while the PL peak at $550\,\mathrm{nm}$ of the isolated NCs exhibits no spectral shift with time, a significant redshift ($\simeq 20\,\mathrm{nm}$) can be observed in the spectrum of the NRs as the delay from photoexcitation increases. This is probably a consequence of the greater polydispersity associated with the self-assembly of NCs into NRs of varying lengths and spatial configurations. The decay traces, extracted at the respective peak wavelengths (panel (c)), show non-exponential

kinetics spanning multiple time scales in the ns-µs range. Such a nontrivial decay is consistent with the strong spin-orbit coupling and fast inter-system crossing expected for nanosystems comprised of heavy atoms [297] and reflects a complex relaxation dynamic across a manifold of closely lying emitting states with mixed singlet and triplet character [173].

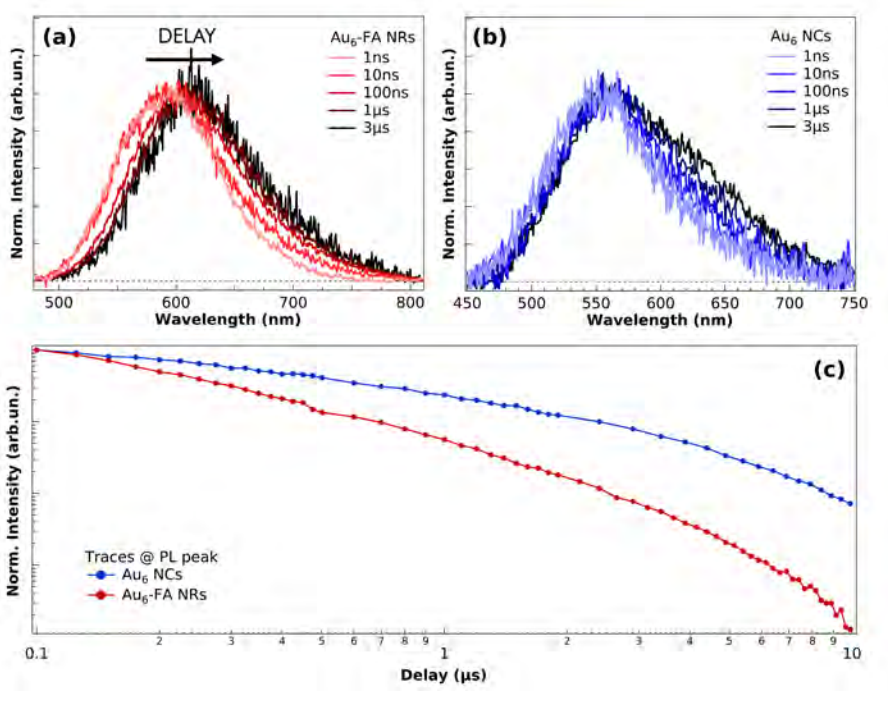

Figure 9.4: Nanosecond-resolved PL measurements. Top row: PL spectra at relevant delays from photoexcitation of (a) $Au(I)_6$ NCs and (b) Au-FA NRs; (c) normalised kinetic traces (log-log scale) of the two samples, extracted at the respective PL peak positions.

9

To unravel such a complex photocycle, we performed ultrafast transient absorption (TA) measurements, photoexciting the sample via $\simeq 90\,\mathrm{fs}$ laser pulses at $400\,\mathrm{nm}$ and probing in the range $420 - 700\,\mathrm{nm}$. Subsequently, differential absorption spectra have been extracted at relevant pump-probe delays as shown in Figure 9.5, where each spectrum has been vertically shifted to aid legibility. Interestingly, and in contrast with the steady-state and nanosecond-resolved measurements, the TA signal of Au-FA NRs exhibits a profoundly different shape with respect to that of the isolated NCs. Indeed, the former shows a neg-

ative, short-lived photoinduced bleach (PB) signal centred at $440\,\mathrm{nm}$, consistent with the depopulation of the lowest energy absorption transition observed in steady state (panel (a) of Figure 9.3), a photoinduced absorption (PA, positive contribution) around $500\,\mathrm{nm}$ and a clear downward dip centred at $600\,\mathrm{nm}$, which can be attributed to a stimulated emission (SE) contribution [45]. On the other hand, the TA spectra of the constituent NCs are dominated by a broad PA signal (hence their positivity over most of the spectral range), combined with a PB at $420\,\mathrm{nm}$ (barely visible at the left edge of the spectra). Furthermore, we observe a negative dip around $550\,\mathrm{nm}$ (more evident at early times), strongly suggestive of an SE contribution superimposed to the positive PA. Such a marked difference is indicative of the role of the NC-NC crosstalk in shaping the whole energy spectrum (not only the emissive state) of the NRs.

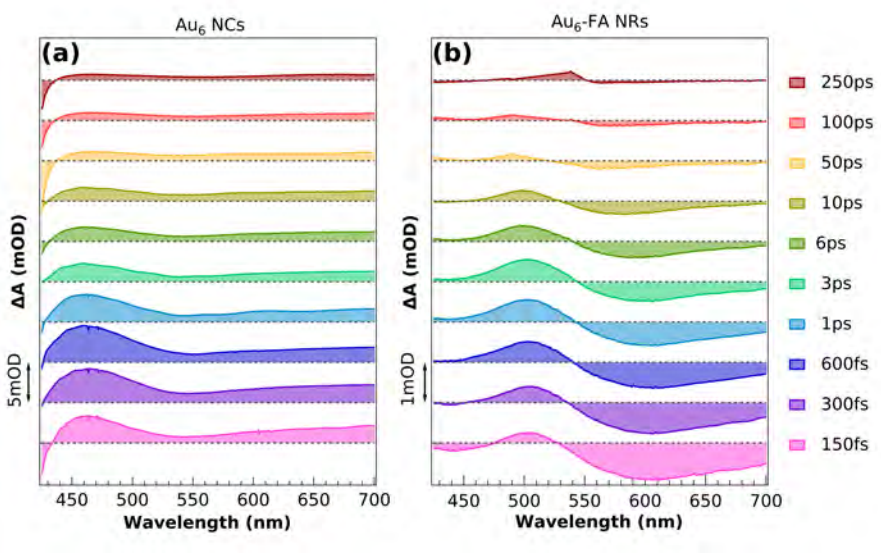

Figure 9.5: Transient Absorption (TA) spectra of $Au(I)_6$ NCs (a) and Au-FA NRs (b) at specific pump-probe delays, obtained by photoexciting at $400\,\mathrm{nm}$ and probing in the range $420 - 700\,\mathrm{nm}$. The spectra are vertically shifted to aid legibility.

To understand the relationship between the TA spectra of each sample and the respective PL emission, we have compared a representative TA spectrum (taken at $600\,\mathrm{fs}$ pump-probe delay) with the steady-state PL, appropriately rescaled and upturned to be superimposed to the SE signal in TA (for the NCs,

a vertical shift was also needed to account for the fact that the SE is superimposed to the broad PA and the overall signal is therefore positive). Indeed, we expect (see chapter 4) the SE feature to spectrally match the PL, save for small spectral differences due to the distinct dependencies of the A and B Einstein coefficients upon the wavelength, since both processes originate from the same transition. The comparisons, shown in panels (a-b) of Figure 9.6, confirm that the observed SE matches very well, in both cases, the peak position and spectral shape of the long-lived PL emission.

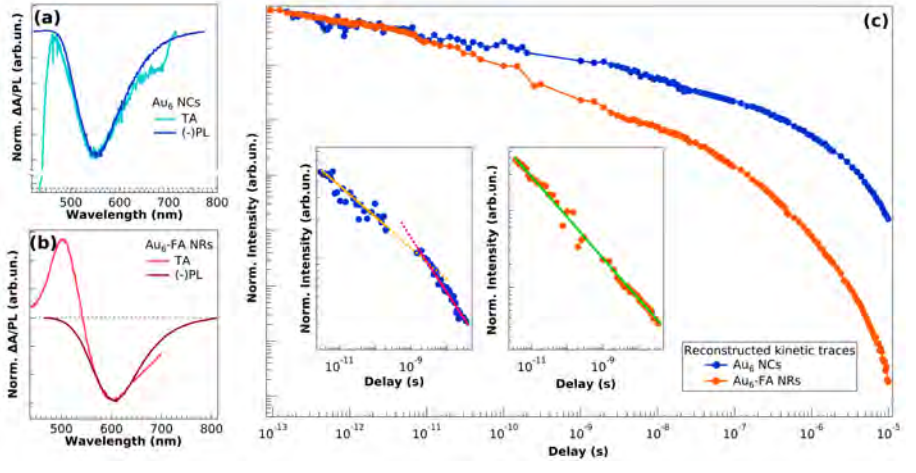

Figure 9.6: Reconstructing the photoluminescence of NCs and NRs over multiple time scales. (a-b) comparison between the TA signal and (upturned, rescaled, and vertically shifted) PL of (a) the isolated NCs and (b) the Au-FA NRs; (c) reconstructed kinetic traces of the two samples, spanning the range $10^{-13} \div 10^{-5}$ s. Each one was obtained by joining the (upturned and rescaled) TA trace, taken at the SE position, with the corresponding PL trace. The inset shows a zoom of the decay kinetics between 10^{-11} s and 10^{-8} s, highlighting the fact that, while the kinetics of the isolated NCs shows two distinct slopes within this time frame (yellow and magenta lines), the Au-FA NRs appear to follow a single power-law decay (green line) with a slope of -0.5.

On these grounds, one can use the TA signal at the spectral position of the SE peak (550 nm for the isolated NCs and 600 nm for the NRs) as a probe of the PL dynamics in the sub-nanosecond scale. The resulting decay trace extracted around the peak wavelength of the SE can finally be upturned, rescaled, and finally combined with the corresponding ns-µs PL kinetic trace, thus creating the *reconstructed* traces reported in panel (c) of Figure 9.6. This type of re-

construction of the excited-state relaxation dynamics spanning an impressive $10^{-13} \div 10^{-5}$ s time range is unprecedented, both for $Au(I)_6$ NCs and Au-FA NRs, and provides insightful information on the different excited-state properties of these nanosystems.

In fact, a comparison between the two traces in Figure 9.6(c) reveals that, while at short delays ($10^{-13} \div 10^{-11}$ s) the two samples exhibit a similar decay, at intermediate delays the kinetics differ significantly from one another. Indeed, between 10^{-11} s and 10^{-8} s, the isolated NCs exhibit at least two distinct decay trends, whereas the relaxation of the Au-FA NRs is described by a single power law decay, as clearly shown in the inset of Fig. 6g. Finally, at even longer times ($10^{-8} \div 10^{-5}$ s), both samples display an analogous multiexponential decay. A power law decay, inherently slower than classical exponential kinetics, is typically associated to the radiative recombination of charge carriers temporary trapped on defects, as reported in the literature [298, 299]. Here, this behavior is only observed for the superstructures, in contrast with the multiexponential decay characterizing the isolated NCs. Therefore, one can surmise that in the superstructures a spontaneous charge separation takes place after photoexcitation, followed by migration of the carriers, trapping within defects and finally radiative recombination. It is fundamental to notice that this is only made possible by the strong crosstalk between constituent NCs, which creates the delocalized electronic states across the NRs that in turn allow the migration of charge carriers. Upon fitting the decay with a power-law model, that is:

$$I(t) = A \cdot t^{-k} \tag{9.1}$$

the value of k was found to be approximately equal to 0.5. This value is suggestive of diffusion-driven decay, as it is well known that random diffusion processes evolve as the square root of time. Indeed, Russo *et al.* [300] have reported an analogous decay kinetics for single-walled carbon nanotubes (SWCNTs) on similar time scales as the one we report. The authors ascribe such a kinetics to pair recombination processes happening whilst the charge carriers diffuse along the CNT. In spite of the many important differences between CNTs and the AuNC superstructures reported here, it is worth noting that, because both samples are characterized by a 1D geometry, an analogous one dimensional diffusion model can be employed to justify the power law decay.

9.3 Conclusions

In summary, this work showcases the remarkable ability of ultrasmall gold nanoclusters to form highly ordered superstructures under appriopriate environmental conditions. Our investigation reveals that aggregation leads to the controlled self-assembly of Au6 NCs into extended nanoribbons, spanning several hundred micrometers, constituted by bundles of one-dimentional nanocluster fibres coordinated by hydrogen bonds. The NC-NC cross-talk within the NRs underpins their collective photophysics, leading to the emergence of novel optical properties. Our reconstruction of their photoinitiated relaxation kinetics over a wide temporal range, made possible by combining ultrafast TA and time-resolved photoluminescence spectroscopies, reveals an intriguing power-law decay kinetics, suggestive of diffusion-driven decays of the charge carriers along the one-dimensional chains formed by self-assembly. Together, these findings consolidate the role of ultrasmall AuNCs as promising building blocks for tunable self-assembled superstructures with a gamut of potential functionalities and emerging photophysical properties.

Part IV

Concluding Remarks

Conclusions and Outlook

The sun was already high in the horizon when the Duke woke up the next morning. He went over to the battlements to consider, be it ever so little, the historical situation. A layer of mud still covered the earth, but he could already see, blossoming here and there, some little blue flowers.

— Raymond Queneau

The overarching aim of this thesis was to investigate the fundamental photophysics and photonics of superstructures self-assembled from colloidal building blocks, specifically pinpointing how interparticle cross-talk and emergent properties reshape their behaviour. Rather than focusing on a single material platform or a specific assembly route, this study was designed as a systematic exploration of the *artificial solid* concept. By combining diverse classes of constituents, assembly strategies, and geometries, we have mapped a landscape where functionality is dictated as much by the organization of matter as it is by its physico-chemical nature.

To achieve this breadth, we utilized a varied palette of building blocks, including chalcogenide quantum dots, perovskite nanocrystals, plasmonic metal nanoparticles, and atomically precise noble-metal nanoclusters. Their organisation into mesoscopic architectures was undertaken by means of distinct assembly strategies, dictated both by the nature of the building block and by the desired superstructure geometry: emulsion-templated assembly for spherical architectures, slow-evaporation for highly ordered cubic supracrystals, and supramolecular chemistry-based assembly for fibre-like structures. This multipronged approach offered a unique platform to probe the interplay between structural confinement and light-matter interactions.

Central to the success of this study was the use of advanced optical techniques, chief among which was transient absorption microscopy (TAM). By

combining ultrafast temporal resolution with micrometric spatial resolution, TAM allowed us to interrogate individual superstructures, bypassing the inhomogeneous broadening and structural polydispersity inherent in ensemble measurements, while also enabling us to observe relevant photoinitiated dynamics, unraveling at the femto- and picosecond timescales.

This multifaceted approach allowed us to uncover unique physical phenomena specific to each material class. Chalcogenide QD superparticles allowed us to delve into the world of active microresonators (chapter 5), where the interplay between spherical geometry and effective dielectric index supports whispering gallery mode resonances that can couple to light absorption and emission features and be reversibly modulated on sub-picosecond timescales via electronic and thermal refractive index changes. In the same systems, we explored collective single- and multi-exciton dynamics (chapter 6), uncovering the role of cross-talk in reshaping the relaxation pathways of QDs and mitigating Auger-driven recombination. In the realm of lead halide perovskites (chapter 7), slow-evaporation assembly allowed us to obtain supercubes with long-range supracrystalline order, correlating their formation with the gradual transition from *isolated* to *collective* optical behaviour. Transitioning to metallic systems, we demonstrated how the precise control of interparticle spacing in gold superlattices (chapter 8) allows for the tuning of field enhancement *hot-spots*, in turn affecting the generation and subsequent relaxation of hot electrons. Finally, the supramolecular assembly of gold nanoclusters produced extended fibre-like superstructures (chapter 9), showcasing a unique photocycle dominated by one-dimensional diffusion of charge carriers along the assembled chains.

Beyond these individual insights, our studies traced an underlying *fil-rouge* that connects these diverse systems: the transition from "isolated" to "collective" physics is a universal consequence of mesoscopic organization. Regardless of whether the building block is a semiconductor or a metal, the act of three-dimensional assembly creates an environment where interparticle cross-talk rewires the light-matter interaction properties of the system, modifying its response and unlocking properties that are fundamentally absent in the individual precursors.

Thus, the findings presented here concur in establishing a foundation for the rational, bottom-up design of multifunctional materials, while also shedding

light onto the immense vastness of the mesoscopic design space. Exploring how collective effects can be tuned both by careful selection of the building blocks and through structural parameters such as packing density, symmetry, and ligand-mediated spacing, pushes nanoscience toward a regime of *programmable matter*, where the response of a material can be engineered by design, rather than discovered by chance.

Looking forward, the most compelling frontier lies in the realization of hybrid superstructures. While this thesis largely dealt with chemically homogeneous assemblies, the *artificial solid* concept can, in principle, be pushed even further by intertwining multiple nanoparticle species into heterogeneous assemblies. Besides benefiting from the cross-talk and collective effects we explored, such hybrid superstructures can present unique behaviours arising from the synergy between fundamentally different building blocks, potentially bypassing the inherent trade-offs of individual materials. For instance, placing plasmonic "antennas" within a quantum dot superlattice could allow to leverage the plasmonic near-field to actively control excitonic processes in the QD phase, to drive non-linear responses, or to steer energy transport across macroscopic distances. Furthermore, our observations of sub-picosecond modulations hint at a future where these materials are not static, but dynamically responsive. The ability to utilize external stimuli, such as ultrashort optical pulses, to reconfigure collective modes in real-time could transform these superstructures from passive components into active, switchable photonic elements.

Ultimately, the transition of these materials into practical technologies will require two parallel developments. First, the move toward high-throughput, robust fabrication is essential to ensure that the fine control over interparticle cross-talk we observed can be reliably translated to device-level applications. Second, the development of *operando* characterization techniques, extending the ultrafast insights we gained through TAM to systems under actual working conditions, will be vital to understand how these collective interactions evolve during device operation. While challenges remain in bridging these gaps, the fundamental photophysical principles explored in this thesis provide a roadmap for navigating the complex interactions that define the physics of artificial solids.

References

[1] D. Liu, R. Aleisa, Z. Cai, Y. Li, and Y. Yin, "Self-assembly of superstructures at all scales", Matter **4**, 927 (2021).

[2] R. B. Gennis, *Biomembranes : Molecular Structure and Function* (Springer New York, 1989), p. 533.

[3] N. W. Ashcroft and N. D. Mermin, *Solid state physics* (Harcourt Brace, 1976), p. 826.

[4] B. Scalvini, V. Sheikhhassani, and A. Mashaghi, "Topological principles of protein folding", Physical Chemistry Chemical Physics **23**, 21316 (2021).

[5] C. Kittel and P. McEuen, *Introduction to solid state physics* (Wiley, 2018).

[6] D. Vollath, *Nanoparticles - Nanocomposites Nanomaterials : an Introduction for Beginners* (Wiley, 2013), p. 322.

[7] C. L. Bassani, G. van Anders, U. Banin, D. Baranov, Q. Chen, M. Dijkstra, M. S. Dimitriyev, E. Efrati, J. Faraudo, O. Gang, N. Gaston, R. Golestanian, G. I. Guerrero-Garcia, M. Gruenwald, A. Haji-Akbari, M. Ibáñez, M. Karg, T. Kraus, B. Lee, R. C. Van Lehn, R. J. Macfarlane, B. M. Mognetti, A. Nikoubashman, S. Osat, O. V. Prezhdo, G. M. Rotskoff, L. Saiz, A. C. Shi, S. Skrabalak, I. I. Smalyukh, M. Tagliazucchi, D. V. Talapin, A. V. Tkachenko, S. Tretiak, D. Vaknin, A. Widmer-Cooper, G. C. Wong, X. Ye, S. Zhou, E. Rabani, M. Engel, and A. Travesset, "Nanocrystal Assemblies: Current Advances and Open Problems", ACS Nano **18**, 14791 (2024).

[8] T. V. Sekh, I. Cherniukh, E. Kobiyama, T. J. Sheehan, A. Manoli, C. Zhu, M. Athanasiou, M. Sergides, O. Ortikova, M. D. Rossell, F. Bertolotti, A. Guagliardi, N. Masciocchi, R. Erni, A. Othonos, G. Itskos, W. A. Tisdale, T. Stöferle, G. Rainò, M. I. Bodnarchuk, and M. V. Kovalenko, "All-Perovskite Multicomponent Nanocrystal Superlattices", ACS Nano **18**, 8423 (2024).

[9] Z. Guo, J. S. Manser, Y. Wan, P. V. Kamat, and L. Huang, "Spatial and temporal imaging of long-range charge transport in perovskite thin films by ultrafast microscopy", Nature Communications **6**, 7471 (2015).

[10] H. Mizuno, S. Nasu, K. Kitamura, T. Aoki-Matsumoto, A. Fujita, Y. Fujita, and I. Hiromitsu, "Enhanced photoluminescence by excitation energy transfer in thin films consisting of fluorescent conjugated polymer and porphyrin", Thin Solid Films **653**, 136 (2018).

[11] H. Inan, M. Poyraz, F. Inci, M. A. Lifson, M. Baday, B. T. Cunningham, and U. Demirci, "Photonic crystals: Emerging biosensors and their promise for point-of-care applications", Chemical Society Reviews **46**, 366 (2017).

[12] I. M. Ross, "The foundation of the silicon age", Bell Labs Technical Journal **2**, 3 (2002).

[13] R. S. Knox, "Introduction to Exciton Physics", in *Collective excitations in solids* (Springer US, Boston, MA, 1983), pp. 183–245.

[14] A. Rockett, "Semiconductor Alloys", in *The materials science of semiconductors* (Springer US, Boston, MA, 2008), pp. 237–287.

[15] C. Cohen-Tannoudji, B. Diu, F. Laloë, S. R. Hemley, N. Ostrowsky, and D. B. Ostrowsky, *Quantum mechanics* (Wiley, 1977), p. 1524.

[16] T. Kippeny, L. A. Swafford, and S. J. Rosenthal, "Semiconductor Nanocrystals: A Powerful Visual Aid for Introducing the Particle in a Box", Journal of Chemical Education **79**, 1094 (2002).

[17] Y. Masumoto and T. Takagahara, eds., *Semiconductor Quantum Dots* (Springer Berlin Heidelberg, Berlin, Heidelberg, 2002).

[18] L. Van Hove, "The Occurrence of Singularities in the Elastic Frequency Distribution of a Crystal", Physical Review **89**, 1189 (1953).

[19] H. SHULL and G. G. HALL, "Atomic Units", Nature **184**, 1559 (1959).

[20] A. L. Rogach, *Semiconductor nanocrystal quantum dots : synthesis, assembly, spectroscopy and applications* (Springer, 2010), p. 372.

[21] A. Ekimov and A. Onushchenko, "Quantum size effect in three-dimensional microscopic semiconductor crystals", JETP Letters **118**, S15 (1981).

[22] Z. Alfassi, D. Bahnemann, and A. Henglein, "Photochemistry of colloidal metal sulfides. 3. Photoelectron emission from cadmium sulfide and cadmium sulfide-zinc sulfide cocolloids", The Journal of Physical Chemistry **86**, 4656 (1982).

[23] A. Ekimov, A. Efros, and A. Onushchenko, "Quantum size effect in semiconductor microcrystals", Solid State Communications **56**, 921 (1985).

[24] L. E. Brus, "Electron–electron and electron-hole interactions in small semiconductor crystallites: The size dependence of the lowest excited electronic state", The Journal of Chemical Physics **80**, 4403 (1984).

[25] A. Efros and A. Efros, "Interband light absorption in semiconductor spheres", Soviet physics. Semiconductors **16**, 772 (1982).

[26] C. B. Murray, D. J. Norris, and M. G. Bawendi, "Synthesis and characterization of nearly monodisperse CdE (E = sulfur, selenium, tellurium) semiconductor nanocrystallites", Journal of the American Chemical Society **115**, 8706 (1993).

[27] Nobelprize.org, *Press release: the nobel prize in chemistry 2023*, (Oct. 4, 2023) https://www.nobelprize.org/prizes/chemistry/2023/press-release/.

[28] C. d. M. Donegá, "Synthesis and properties of colloidal heteronanocrystals", Chem. Soc. Rev. **40**, 1512 (2011).

[29] F. Montanarella, "A Self-Assembly Tale Collective structural and optical phenomena in supraparticles of nanocrystals", PhD thesis (Universiteit Utrecht, Utrecht, Jan. 2019).

[30] I. V. Martynenko, A. P. Litvin, F. Purcell-Milton, A. V. Baranov, A. V. Fedorov, and Y. K. Gun'ko, "Application of semiconductor quantum dots in bioimaging and biosensing", Journal of Materials Chemistry B **5**, 6701 (2017).

[31] M. Zhang, H. Dai, Y. Zhao, and X. Chen, "Miniaturization of Multicolor Quantum Dots Lasing Based on 2D Constrained Resonator", Advanced Optical Materials **12**, 10.1002/adom.202400017 (2024).

[32] R. Zhu, Z. Luo, H. Chen, Y. Dong, and S.-T. Wu, "Realizing Rec 2020 color gamut with quantum dot displays", Optics Express **23**, 23680 (2015).

[33] M. A. Kastner, "Artificial Atoms", Physics Today **46**, 24 (1993).

[34] R. C. Ashoori, "Electrons in artificial atoms", Nature **379**, 413 (1996).

[35] U. Banin, Y. Cao, D. Katz, and O. Millo, "Identification of atomic-like electronic states in indium arsenide nanocrystal quantum dots", Nature **400**, 542 (1999).

[36] C. Kittel, *Quantum theory of solids* (Wiley, 1963), p. 435.

[37] J. M. Luttinger and W. Kohn, "Motion of Electrons and Holes in Perturbed Periodic Fields", Physical Review **97**, 869 (1955).

[38] E. O. Kane, "Band structure of indium antimonide", Journal of Physics and Chemistry of Solids **1**, 249 (1957).

[39] C. R. Pidgeon and R. N. Brown, "Interband Magneto-Absorption and Faraday Rotation in InSb", Physical Review **146**, 575 (1966).

[40] F. Masia, W. Langbein, I. Moreels, Z. Hens, and P. Borri, "Exciton dephasing in lead sulfide quantum dots by X-point phonons", Physical Review B **83**, 201309 (2011).

[41] D. A. Wheeler and J. Z. Zhang, "Exciton dynamics in semiconductor nanocrystals", Advanced Materials **25**, 2878 (2013).

[42] P. Kambhampati, "Unraveling the Structure and Dynamics of Excitons in Semiconductor Quantum Dots", Accounts of Chemical Research **44**, 1 (2011).

[43] P. T. Landsberg, *Recombination in Semiconductors* (Cambridge University Press, Jan. 1992).

[44] K. J. Standley and R. A. Vaughan, "The Phonon Bottleneck", in *Electron spin relaxation phenomena in solids* (Springer US, Boston, MA, 1969), pp. 62–74.

[45] A. Sciortino and F. Messina, "Ultrafast Optical Spectroscopies", in *Spectroscopy for materials characterization* (Wiley, July 2021), pp. 65–95.

[46] P. Dahan, V. Fleurov, P. Thurian, R. Heitz, A. Hoffmann, and I. Broser, "Properties of the intermediately bound α-, β-, and γ-excitons in ZnO:Cu", Journal of Physics: Condensed Matter **10**, 2007 (1998).

[47] J. K. Cooper, A. M. Franco, S. Gul, C. Corrado, and J. Z. Zhang, "Characterization of Primary Amine Capped CdSe, ZnSe, and ZnS Quantum Dots by FT-IR: Determination of Surface Bonding Interaction and Identification of Selective Desorption", Langmuir **27**, 8486 (2011).

[48] S.-H. Chi, L. Mazeina, S. M. Prokes, J. D. Caldwell, G. Beadie, S. R. Flom, and J. S. Shirk, "Below Bandgap Excitation of SnO2 Nanowires: The Relaxation of Trap States", in Cleo:2011 - laser applications to photonic applications (2011), JWA71.

[49] V. I. Klimov, "Spectral and Dynamical Properties of Multiexcitons in Semiconductor Nanocrystals", Annual Review of Physical Chemistry **58**, 635 (2007).

[50] M. A. Lampert, "Mobile and Immobile Effective-Mass-Particle Complexes in Nonmetallic Solids", Physical Review Letters **1**, 450 (1958).

[51] M. Bayer, O. Stern, P. Hawrylak, S. Fafard, and A. Forchel, "Hidden symmetries in the energy levels of excitonic 'artificial atoms'", Nature **405**, 923 (2000).

[52] S. S. Li, ed., *Semiconductor Physical Electronics* (Springer New York, New York, NY, 2006).

[53] A. I. Ekimov, I. A. Kudryavtsev, A. L. Efros, T. V. Yazeva, F. Hache, M. C. Schanne-Klein, A. V. Rodina, D. Ricard, and C. Flytzanis, "Absorption and intensity-dependent photoluminescence measurements on CdSe quantum dots: assignment of the first electronic transitions", Journal of the Optical Society of America B **10**, 100 (1993).

[54] D. J. Norris, A. Sacra, C. B. Murray, and M. G. Bawendi, "Measurement of the size dependent hole spectrum in CdSe quantum dots", Physical Review Letters **72**, 2612 (1994).

[55] M. Nirmal, D. J. Norris, M. Kuno, M. G. Bawendi, A. L. Efros, and M. Rosen, "Observation of the "Dark Exciton" in CdSe Quantum Dots", Physical Review Letters **75**, 3728 (1995).

[56] D. J. Norris, A. L. Efros, M. Rosen, and M. G. Bawendi, "Size dependence of exciton fine structure in CdSe quantum dots", Physical Review B **53**, 16347 (1996).

[57] S. Adachi, "Wurtzite Cadmium Selenide (w-CdSe)", in *Optical constants of crystalline and amorphous semiconductors* (Springer US, Boston, MA, 1999), pp. 517–529.

[58] P. Handler, "Properties of Compounds: Physics and Chemistry of II-VI Compounds", Science **159**, 185 (1968).

[59] A. L. Efros, M. Rosen, M. Kuno, M. Nirmal, D. J. Norris, and M. Bawendi, "Band-edge exciton in quantum dots of semiconductors with a degenerate valence band: Dark and bright exciton states", Physical Review B **54**, 4843 (1996).

[60] P. C. Sercel and A. L. Efros, "Band-Edge Exciton in CdSe and Other II-VI and III-V Compound Semiconductor Nanocrystals - Revisited", Nano Letters **18**, 4061 (2018).

[61] E. K. Vishnu, E. M. Thomas, L. Prasad, and K. G. Thomas, "Trap States in Semiconductor Quantum Dots: Friends or Foes", The Journal of Physical Chemistry C **128**, 4373 (2024).

[62] X. Tong and Z. M. Wang, eds., *Core/Shell Quantum Dots*, Vol. 28 (Springer International Publishing, Cham, 2020).

[63] A. Sahu and D. Kumar, "Core-shell quantum dots: A review on classification, materials, application, and theoretical modeling", Journal of Alloys and Compounds **924**, 10.1016/j.jallcom.2022.166508 (2022).

[64] D. A. Hanifi, N. D. Bronstein, B. A. Koscher, Z. Nett, J. K. Swabeck, K. Takano, A. M. Schwartzberg, L. Maserati, K. Vandewal, Y. van de Burgt, A. Salleo, and A. P. Alivisatos, "Redefining near-unity luminescence in quantum dots with photothermal threshold quantum yield", Science **363**, 1199 (2019).

[65] O. L. Lazarenkova and A. A. Balandin, "Miniband formation in a quantum dot crystal", Journal of Applied Physics **89**, 5509 (2001).

[66] C. R. Kagan and C. B. Murray, "Charge transport in strongly coupled quantum dot solids", Nature Nanotechnology **10**, 1013 (2015).

[67] P. Guyot-Sionnest, "Electrical Transport in Colloidal Quantum Dot Films", The Journal of Physical Chemistry Letters **3**, 1169 (2012).

[68] E. Marino, "Assembling nanocrystal superstructures", PhD thesis (Universiteit van Amsterdam, Amsterdam, Mar. 2019).

[69] D. V. Talapin and C. B. Murray, "PbSe Nanocrystal Solids for n- and p-Channel Thin Film Field-Effect Transistors", Science **310**, 86 (2005).

[70] E. A. Gaulding, B. T. Diroll, E. D. Goodwin, Z. J. Vrtis, C. R. Kagan, and C. B. Murray, "Deposition of wafer-scale single-component and binary nanocrystal superlattice thin films via dip-coating", Advanced Materials **27**, 2846 (2015).

[71] J. H. Choi, A. T. Fafarman, S. J. Oh, D. K. Ko, D. K. Kim, B. T. Diroll, S. Muramoto, J. G. Gillen, C. B. Murray, and C. R. Kagan, "Bandlike transport in strongly coupled and doped quantum dot solids: A route to high-performance thin-film electronics", Nano Letters **12**, 2631 (2012).

[72] J. S. Lee, M. V. Kovalenko, J. Huang, D. S. Chung, and D. V. Talapin, "Band-like transport, high electron mobility and high photoconductivity in all-inorganic nanocrystal arrays", Nature Nanotechnology **6**, 348 (2011).

[73] M. I. Bodnarchuk, M. V. Kovalenko, S. Pichler, G. Fritz-Popovski, G. Hesser, and W. Heiss, "Large-area ordered superlattices from magnetic wüstite/cobalt ferrite core/shell nanocrystals by doctor blade casting", ACS Nano **4**, 423 (2010).

[74] E. Marino, E. Marino, A. W. Keller, D. An, S. Van Dongen, S. Van Dongen, T. E. Kodger, K. E. MacArthur, M. Heggen, C. R. Kagan, C. R. Kagan, C. R. Kagan, C. B. Murray, C. B. Murray, and P. Schall, "Favoring the Growth of High-Quality, Three-Dimensional Supercrystals of Nanocrystals", Journal of Physical Chemistry C **124**, 11256 (2020).

[75] S. Wintzheimer, T. Granath, M. Oppmann, T. Kister, T. Thai, T. Kraus, N. Vogel, and K. Mandel, "Supraparticles: Functionality from Uniform Structural Motifs", ACS Nano **12**, 5093 (2018).

[76] L.-Y. Chu, A. S. Utada, R. K. Shah, J.-W. Kim, and D. A. Weitz, "Controllable Monodisperse Multiple Emulsions", Angewandte Chemie International Edition **46**, 8970 (2007).

[77] E. Marino, S. W. van Dongen, S. J. Neuhaus, W. Li, A. W. Keller, C. R. Kagan, T. E. Kodger, and C. B. Murray, "Monodisperse Nanocrystal Superparticles through a Source–Sink Emulsion System", Chemistry of Materials **34**, 2779 (2022).

[78] E. Marino, A. Sciortino, A. Berkhout, K. E. MacArthur, M. Heggen, T. Gregorkiewicz, T. E. Kodger, A. Capretti, C. B. Murray, A. F. Koenderink, F. Messina, and P. Schall, "Simultaneous Photonic and Excitonic Coupling in Spherical Quantum Dot Supercrystals", ACS Nano **14**, 13806 (2020).

[79] X. Lan, M. Chen, M. H. Hudson, V. Kamysbayev, Y. Wang, P. Guyot-Sionnest, and D. V. Talapin, "Quantum dot solids showing state-resolved band-like transport", Nature Materials **19**, 323 (2020).

[80] R. W. Crisp, J. N. Schrauben, M. C. Beard, J. M. Luther, and J. C. Johnson, "Coherent Exciton Delocalization in Strongly Coupled Quantum Dot Arrays", Nano Letters **13**, 4862 (2013).

[81] X. Tian, H. Chang, H. Dong, C. Zhang, and L. Zhang, "Fluorescence Resonance Energy Transfer Properties and Auger Recombination Suppression in Supraparticles Self-Assembled from Colloidal Quantum Dots", Inorganics **11**, 218 (2023).

[82] J. Liu, L. Guillemeney, B. Abécassis, and L. Coolen, "Long Range Energy Transfer in Self-Assembled Stacks of Semiconducting Nanoplatelets", Nano Letters **20**, 3465 (2020).

[83] F. Montanarella, M. Biondi, S. O. M. Hinterding, D. Vanmaekelbergh, and F. T. Rabouw, "Reversible Charge-Carrier Trapping Slows Förster Energy Transfer in CdSe/CdS Quantum-Dot Solids", Nano Letters **18**, 5867 (2018).

[84] G. Mie, "Beiträge zur Optik trüber Medien, speziell kolloidaler Metallösungen", Annalen der Physik **330**, 377 (1908).

[85] M. R. Foreman, J. D. Swaim, and F. Vollmer, "Whispering gallery mode sensors", Advances in Optics and Photonics **7**, 168 (2015).

[86] S. J. Neuhaus, E. Marino, C. B. Murray, and C. R. Kagan, "Frequency Stabilization and Optically Tunable Lasing in Colloidal Quantum Dot Superparticles", Nano Letters **23**, 645 (2023).

[87] M. A. Green, A. Ho-Baillie, and H. J. Snaith, "The emergence of perovskite solar cells", Nature Photonics **8**, 506 (2014).

[88] L. Protesescu, S. Yakunin, M. I. Bodnarchuk, F. Krieg, R. Caputo, C. H. Hendon, R. X. Yang, A. Walsh, and M. V. Kovalenko, "Nanocrystals of Cesium Lead Halide Perovskites (CsPbX ₃ , X = Cl, Br, and I): Novel Optoelectronic Materials Showing Bright Emission with Wide Color Gamut", Nano Letters **15**, 3692 (2015).

[89] D. Aldakov and P. Reiss, "Safer-by-Design Fluorescent Nanocrystals: Metal Halide Perovskites vs Semiconductor Quantum Dots", Journal of Physical Chemistry C **123**, 12527 (2019).

[90] Y. Cai, P. Zhang, W. Bai, L. Lu, L. Wang, X. Chen, and R. J. Xie, "Synthesizing Bright CsPbBr3Perovskite Nanocrystals with High Purification Yields and Their Composites with in Situ-Polymerized Styrene for Light-Emitting Diode Applications", ACS Sustainable Chemistry and Engineering **10**, 7385 (2022).

[91] A. Dey, J. Ye, A. De, E. Debroye, S. K. Ha, E. Bladt, A. S. Kshirsagar, Z. Wang, J. Yin, Y. Wang, L. N. Quan, F. Yan, M. Gao, X. Li, J. Shamsi, T. Debnath, M. Cao, M. A. Scheel, S. Kumar, J. A. Steele, M. Gerhard, L. Chouhan, K. Xu, X. G. Wu, Y. Li, Y. Zhang, A. Dutta, C. Han, I. Vincon, A. L. Rogach, A. Nag, A. Samanta, B. A. Korgel, C. J. Shih, D. R. Gamelin, D. H. Son, H. Zeng, H. Zhong, H. Sun, H. V. Demir, I. G. Scheblykin, I. Mora-Seró, J. K. Stolarczyk, J. Z. Zhang, J. Feldmann, J. Hofkens, J. M. Luther, J. Pérez-Prieto, L. Li, L. Manna, M. I. Bodnarchuk, M. V. Kovalenko, M. B. Roeffaers, N. Pradhan, O. F. Mohammed, O. M. Bakr, P. Yang, P. Müller-Buschbaum, P. V. Kamat, Q. Bao, Q. Zhang, R. Krahne, R. E. Galian, S. D. Stranks, S. Bals, V. Biju, W. A. Tisdale, Y. Yan, R. L. Hoye, and L. Polavarapu, "State of the Art and Prospects for Halide Perovskite Nanocrystals", ACS Nano **15**, 10775 (2021).

[92] C. Yin, L. Chen, N. Song, Y. Lv, F. Hu, C. Sun, W. W. Yu, C. Zhang, X. Wang, Y. Zhang, and M. Xiao, "Bright-Exciton Fine-Structure Splittings in Single Perovskite Nanocrystals", Physical Review Letters **119**, 026401 (2017).

[93] Y. Tang, L. Gomez, A. Lesage, E. Marino, T. E. Kodger, J. M. Meijer, P. Kolpakov, J. Meng, K. Zheng, T. Gregorkiewicz, and P. Schall, "Highly Stable Perovskite Supercrystals via Oil-in-Oil Templating", Nano Letters **20**, 5997 (2020).

[94] G. Rainò, M. A. Becker, M. I. Bodnarchuk, R. F. Mahrt, M. V. Kovalenko, and T. Stöferle, "Superfluorescence from lead halide perovskite quantum dot superlattices", Nature **563**, 671 (2018).

[95] J. S. van der Burgt, J. J. Geuchies, B. van der Meer, H. Vanrompay, D. Zanaga, Y. Zhang, W. Albrecht, A. V. Petukhov, L. Filion, S. Bals, I. Swart, and D. Vanmaekelbergh, "Cuboidal Supraparticles Self-Assembled from Cubic CsPbBr3 Perovskite Nanocrystals", The Journal of Physical Chemistry C **122**, 15706 (2018).

[96] Z. Dang, B. Dhanabalan, A. Castelli, R. Dhall, K. C. Bustillo, D. Marchelli, D. Spirito, U. Petralanda, J. Shamsi, L. Manna, R. Krahne, and M. P. Arciniegas, "Temperature-Driven Transformation of CsPbBr3 Nanoplatelets into Mosaic Nanotiles in Solution through Self-Assembly", Nano Letters **20**, 1808 (2020).

[97] I. Cherniukh, G. Rainò, T. Stöferle, M. Burian, A. Travesset, D. Naumenko, H. Amenitsch, R. Erni, R. F. Mahrt, M. I. Bodnarchuk, and M. V. Kovalenko, "Perovskite-type superlattices from lead halide perovskite nanocubes", Nature **593**, 535 (2021).

[98] N. Soetan, W. R. Erwin, A. M. Tonigan, D. G. Walker, and R. Bardhan, "Solvent-Assisted Self-Assembly of CsPbBr3 Perovskite Nanocrystals into One-Dimensional Superlattice", The Journal of Physical Chemistry C **121**, 18186 (2017).

[99] Y. Tang, D. Poonia, M. van der Laan, D. Timmerman, S. Kinge, L. D. Siebbeles, and P. Schall, "Electronic Coupling of Highly Ordered Perovskite Nanocrystals in Supercrystals", ACS Applied Energy Materials **5**, 5415 (2022).

[100] M. Yang, P. Moroz, E. Miller, D. Porotnikov, J. Cassidy, C. Ellison, X. Medvedeva, A. Klinkova, and M. Zamkov, "Energy Transport in CsPbBr3 Perovskite Nanocrystal Solids", ACS Photonics **7**, 154 (2020).

[101] W. Shcherbakov-Wu, S. Saris, T. J. Sheehan, N. N. Wong, E. R. Powers, F. Krieg, M. V. Kovalenko, A. P. Willard, and W. A. Tisdale, *Persistent enhancement of exciton diffusivity in CsPbBr 3 nanocrystal solids*, tech. rep. (2024), p. 2630.

[102] C. Zhou, J. M. Pina, T. Zhu, D. H. Parmar, H. Chang, J. Yu, F. Yuan, G. Bappi, Y. Hou, X. Zheng, J. Abed, H. Chen, J. Zhang, Y. Gao, B. Chen, Y. K. Wang, H. Chen, T. Zhang, S. Hoogland, M. I. Saidaminov, L. Sun, O. M. Bakr, H. Dong, L. Zhang, and E. H. Sargent, "Quantum Dot Self-Assembly Enables Low-Threshold Lasing", Advanced Science **8**, 10.1002/advs.202101125 (2021).

[103] Z. Liu, J. Yang, J. Du, Z. Hu, T. Shi, Z. Zhang, Y. Liu, X. Tang, Y. Leng, and R. Li, "Robust Subwavelength Single-Mode Perovskite Nanocuboid Laser", ACS Nano **12**, 5923 (2018).

[104] L. Zhang and E. Wang, "Metal nanoclusters: New fluorescent probes for sensors and bioimaging", Nano Today **9**, 132 (2014).

[105] K. Kolwas and A. Derkachova, "Impact of the Interband Transitions in Gold and Silver on the Dynamics of Propagating and Localized Surface Plasmons", Nanomaterials **10**, 1411 (2020).

[106] D. Höing, "Time-resolved studies of electron-phonon coupling in gold nanoparticles and nanoparticle assemblies", PhD thesis (2023).

[107] H. Raether, *Surface plasmons on smooth and rough surfaces and on gratings* (Springer-Verlag, 1988), p. 136.

[108] S. A. Maier, *Plasmonics: Fundamentals and Applications* (Springer US, New York, NY, 2007).

[109] M. Pelton, J. Aizpurua, and G. Bryant, "Metal-nanoparticle plasmonics", Laser & Photonics Reviews **2**, 136 (2008).

[110] J. L. Montaño-Priede and U. Pal, "Estimating Near Electric Field of Polyhedral Gold Nanoparticles for Plasmon-Enhanced Spectroscopies", The Journal of Physical Chemistry C **123**, 11833 (2019).

[111] M. A. Garcia, "Surface plasmons in metallic nanoparticles: fundamentals and applications", Journal of Physics D: Applied Physics **44**, 283001 (2011).

[112] Y. Shin, C. Lee, M.-S. Yang, S. Jeong, D. Kim, and T. Kang, "Two-dimensional Hyper-branched Gold Nanoparticles Synthesized on a Two-dimensional Oil/Water Interface", Scientific Reports **4**, 6119 (2014).

[113] T. Ambreen and M.-H. Kim, "Influence of particle size on the effective thermal conductivity of nanofluids: A critical review", Applied Energy **264**, 114684 (2020).

[114] A. J. Haes, S. Zou, G. C. Schatz, and R. P. Van Duyne, "A Nanoscale Optical Biosensor: The Long Range Distance Dependence of the Localized Surface Plasmon Resonance of Noble Metal Nanoparticles", The Journal of Physical Chemistry B **108**, 109 (2004).

[115] P. K. Kuiri, "Control of Ultraviolet Surface Plasmon Absorption of Al Nanoparticles by Changing Particle Size, Shape, Interaction, and Medium Dielectric Constant", Plasmonics **15**, 933 (2020).

[116] S. V. Boriskina, T. A. Cooper, L. Zeng, G. Ni, J. K. Tong, Y. Tsurimaki, Y. Huang, L. Meroueh, G. Mahan, and G. Chen, "Losses in plasmonics: from mitigating energy dissipation to embracing loss-enabled functionalities", Advances in Optics and Photonics **9**, 775 (2017).

[117] D. Catone, L. Di Mario, F. Martelli, P. O'Keeffe, A. Paladini, J. Stefano Pelli Cresi, A. K. Sivan, L. Tian, F. Toschi, and S. Turchini, "Ultrafast optical spectroscopy of semiconducting and plasmonic nanostructures and their hybrids", Nanotechnology **32**, 025703 (2020).

[118] V. E. Alexopoulou and A. P. Markopoulos, "A Critical Assessment Regarding Two-Temperature Models: An Investigation of the Different Forms of Two-Temperature Models, the Various Ultrashort Pulsed Laser Models and Computational Methods", Archives of Computational Methods in Engineering **31**, 93 (2024).

[119] J. Li, J. Wu, X. Zhang, Y. Liu, D. Zhou, H. Sun, H. Zhang, and B. Yang, "Controllable Synthesis of Stable Urchin-like Gold Nanoparticles Using Hydroquinone to Tune the Reactivity of Gold Chloride", The Journal of Physical Chemistry C **115**, 3630 (2011).

[120] M. Petersen, Z. Yu, and X. Lu, "Application of Raman Spectroscopic Methods in Food Safety: A Review", Biosensors **11**, 187 (2021).

[121] A. Sciortino, A. Panniello, G. Minervini, N. Mauro, G. Giammona, G. Buscarino, M. Cannas, M. Striccoli, and F. Messina, "Enhancing carbon dots fluorescence via plasmonic resonance energy transfer", Materials Research Bulletin **149**, 111746 (2022).

[122] A. B. Taylor and P. Zijlstra, "Single-Molecule Plasmon Sensing: Current Status and Future Prospects", ACS Sensors **2**, 1103 (2017).

[123] W. Zhang, M. Caldarola, X. Lu, and M. Orrit, "Plasmonic Enhancement of Two-Photon-Excited Luminescence of Single Quantum Dots by Individual Gold Nanorods", ACS Photonics **5**, 2960 (2018).

[124] Y. Fu, J. Zhang, and J. R. Lakowicz, "Plasmon-Enhanced Fluorescence from Single Fluorophores End-Linked to Gold Nanorods", Journal of the American Chemical Society **132**, 5540 (2010).

[125] J. Zhao, Y. Cheng, H. Shen, Y. Y. Hui, T. Wen, H.-C. Chang, Q. Gong, and G. Lu, "Light Emission from Plasmonic Nanostructures Enhanced with Fluorescent Nanodiamonds", Scientific Reports **8**, 3605 (2018).

[126] E. Garcia, C. Arnold, J.-P. Hermier, and M. D'Amico, "Gold plasmonic enhanced luminescence of silica encapsulated semiconductor heteronanoplatelets", Nanoscale Advances **3**, 4572 (2021).

[127] R. Collison, J. B. Pérez-Sánchez, M. Du, J. Trevino, J. Yuen-Zhou, S. O'Brien, and V. M. Menon, "Purcell Effect of Plasmonic Surface Lattice Resonances and Its Influence on Energy Transfer", ACS Photonics **8**, 2211 (2021).

[128] A. B. Yankovich, B. Munkhbat, D. G. Baranov, J. Cuadra, E. Olsén, H. Lourenço-Martins, L. H. G. Tizei, M. Kociak, E. Olsson, and T. Shegai, "Visualizing Spatial Variations of Plasmon–Exciton Polaritons at the Nanoscale Using Electron Microscopy", Nano Letters **19**, 8171 (2019).

[129] C. Gao, F. Lyu, and Y. Yin, "Encapsulated Metal Nanoparticles for Catalysis", Chemical Reviews **121**, 834 (2021).

[130] V. Chandrakala, V. Aruna, and G. Angajala, "Review on metal nanoparticles as nanocarriers: current challenges and perspectives in drug delivery systems", Emergent Materials **5**, 1593 (2022).

[131] S. Yu, G. Xia, N. Yang, L. Yuan, J. Li, Q. Wang, D. Li, L. Ding, Z. Fan, and J. Li, "Noble Metal Nanoparticle-Based Photothermal Therapy: Development and Application in Effective Cancer Therapy", International Journal of Molecular Sciences **25**, 5632 (2024).

[132] D. Liu and C. Xue, "Plasmonic Coupling Architectures for Enhanced Photocatalysis", Advanced Materials **33**, 10.1002/adma.202005738 (2021).

[133] E. W. Visser, M. Horáček, and P. Zijlstra, "Plasmon Rulers as a Probe for Real-Time Microsecond Conformational Dynamics of Single Molecules", Nano Letters **18**, 7927 (2018).

[134] C. A. Tajon, D. Seo, J. Asmussen, N. Shah, Y. W. Jun, and C. S. Craik, "Sensitive and selective plasmon ruler nanosensors for monitoring the apoptotic drug response in Leukemia", ACS Nano **8**, 9199 (2014).

[135] J. A. Fan, C. Wu, K. Bao, J. Bao, R. Bardhan, N. J. Halas, V. N. Manoharan, P. Nordlander, G. Shvets, and F. Capasso, "Self-Assembled Plasmonic Nanoparticle Clusters", Science **328**, 1135 (2010).

[136] N. J. Greybush, I. Liberal, L. Malassis, J. M. Kikkawa, N. Engheta, C. B. Murray, and C. R. Kagan, "Plasmon Resonances in Self-Assembled Two-Dimensional Au Nanocrystal Metamolecules", ACS Nano **11**, 2917 (2017).

[137] H. Zhou, S. Su, W. Qiu, Z. Zhao, Z. Lin, P. Qiu, and Q. Kan, "Multiple Fano Resonances with Tunable Electromagnetic Properties in Graphene Plasmonic Metamolecules", Nanomaterials **10**, 236 (2020).

[138] N. J. Greybush, V. Pacheco-Peña, N. Engheta, C. B. Murray, and C. R. Kagan, "Plasmonic Optical and Chiroptical Response of Self-Assembled Au Nanorod Equilateral Trimers", ACS Nano, acsnano.8b07619 (2019).

[139] B. Luk'Yanchuk, N. I. Zheludev, S. A. Maier, N. J. Halas, P. Nordlander, H. Giessen, and C. T. Chong, "The Fano resonance in plasmonic nanostructures and metamaterials", Nature Materials **9**, 707 (2010).

[140] Y. Y. Cai, A. Fallah, S. Yang, Y. C. Choi, J. Xu, A. Stein, J. M. Kikkawa, C. B. Murray, N. Engheta, and C. R. Kagan, "Open and Close-Packed, Shape-Engineered Polygonal Nanoparticle Metamolecules with Tailorable Fano Resonances", Advanced Materials **35**, 10.1002/adma.202301323 (2023).

[141] M. I. Tribelsky and B. S. Luk'yanchuk, "Anomalous Light Scattering by Small Particles", Physical Review Letters **97**, 263902 (2006).

[142] A. Christ, S. G. Tikhodeev, N. A. Gippius, J. Kuhl, and H. Giessen, "Waveguide-Plasmon Polaritons: Strong Coupling of Photonic and Electronic Resonances in a Metallic Photonic Crystal Slab", Physical Review Letters **91**, 183901 (2003).

[143] D. Liu, F. Zhou, C. Li, T. Zhang, H. Zhang, W. Cai, and Y. Li, "Black Gold: Plasmonic Colloidosomes with Broadband Absorption Self-Assembled from Monodispersed Gold Nanospheres by Using a Reverse Emulsion System", Angewandte Chemie **127**, 9732 (2015).

[144] N. Kwon, H. Oh, R. Kim, A. Sinha, J. Kim, J. Shin, J. W. M. Chon, and B. Lim, "Direct Chemical Synthesis of Plasmonic Black Colloidal Gold Superparticles with Broadband Absorption Properties", Nano Letters **18**, 5927 (2018).

[145] D. García-Lojo, S. Núñez-Sánchez, S. Gómez-Graña, M. Grzelczak, I. Pastoriza-Santos, J. Pérez-Juste, and L. M. Liz-Marzán, "Plasmonic Supercrystals", Accounts of Chemical Research **52**, 1855 (2019).

[146] C. Hanske, E. H. Hill, D. Vila-Liarte, G. González-Rubio, C. Matricardi, A. Mihi, and L. M. Liz-Marzán, "Solvent-Assisted Self-Assembly of Gold Nanorods into Hierarchically Organized Plasmonic Mesostructures", ACS Applied Materials and Interfaces **11**, 11763 (2019).

[147] S. Kim, C. Y. Zheng, G. C. Schatz, K. Aydin, K. H. Kim, and C. A. Mirkin, "Mie-resonant three-dimensional metacrystals", Nano Letters **20**, 8096 (2020).

[148] X. Li, X. Chen, J. Liu, X. Zhao, J. Liu, Z. Cheng, and T. S. Deng, "Superparticles of gold nanorods with controllable bandwidth and spectral shape for lipophilic SERS", Nanoscale **15**, 12270 (2023).

[149] K. J. Si, Y. Chen, Q. Shi, and W. Cheng, "Nanoparticle Superlattices: The Roles of Soft Ligands", Advanced Science **5**, 10.1002/advs.201700179 (2018).

[150] F. Schulz, O. Pavelka, F. Lehmkühler, F. Westermeier, Y. Okamura, N. S. Mueller, S. Reich, and H. Lange, "Structural order in plasmonic superlattices", Nature Communications **11**, 10.1038/s41467-020-17632-4 (2020).

[151] Y. Wan, N. Goubet, P.-A. Albouy, N. Schaeffer, and M.-P. Pileni, "Hierarchy in Au Nanocrystal Ordering in a Supracrystal: II. Control of Interparticle Distances", Langmuir **29**, 13576 (2013).

[152] M. Chen, X. Chen, R. Li, H. Yang, N. Hao, Q. Liu, M. Peng, L. Wang, and Y. Hu, "Simultaneous in situ extraction and self-assembly of plasmonic colloidal gold superparticles for sers detection of organochlorine pesticides in water", Analytical Chemistry **93**, 4657 (2021).

[153] R. Antoine, M. Broyer, and P. Dugourd, "Metal nanoclusters: from fundamental aspects to electronic properties and optical applications", Science and Technology of Advanced Materials **24**, 10.1080/14686996.2023.2222546 (2023).

[154] M. Zhou, C. Zeng, Q. Li, T. Higaki, and R. Jin, "Gold nanoclusters: Bridging gold complexes and plasmonic nanoparticles in photophysical properties", Nanomaterials **9**, 10.3390/nano9070933 (2019).

[155] L. He, T. Dong, D. e. Jiang, and Q. Zhang, "Recent progress in atomically precise metal nanoclusters: From bio-related properties to biological applications", Coordination Chemistry Reviews **535**, 10.1016/j.ccr.2025.216633 (2025).

[156] P. D. Jadzinsky, G. Calero, C. J. Ackerson, D. A. Bushnell, and R. D. Kornberg, "Structure of a Thiol Monolayer-Protected Gold Nanoparticle at 1.1 Å Resolution", Science **318**, 430 (2007).

[157] S. Chen, S. Wang, J. Zhong, Y. Song, J. Zhang, H. Sheng, Y. Pei, and M. Zhu, "The Structure and Optical Properties of the [Au ₁₈ (SR) ₁₄] Nanocluster", Angewandte Chemie International Edition **54**, 3145 (2015).

[158] T. C. Jones, L. Sumner, G. Ramakrishna, M. b. Hatshan, A. Abuhagr, S. Chakraborty, and A. Dass, "Bulky t -Butyl Thiolated Gold Nanomolecular Series: Synthesis, Characterization, Optical Properties, and Electrocatalysis", The Journal of Physical Chemistry C **122**, 17726 (2018).

[159] S. Tian, Y.-Z. Li, M.-B. Li, J. Yuan, J. Yang, Z. Wu, and R. Jin, "Structural isomerism in gold nanoparticles revealed by X-ray crystallography", Nature Communications **6**, 8667 (2015).

[160] H. Dong, L. Liao, S. Zhuang, C. Yao, J. Chen, S. Tian, M. Zhu, X. Liu, L. Li, and Z. Wu, "A novel double-helical-kernel evolution pattern of gold nanoclusters: alternate single-stranded growth at both ends", Nanoscale **9**, 3742 (2017).

[161] C. Zeng, C. Liu, Y. Chen, N. L. Rosi, and R. Jin, "Atomic Structure of Self-Assembled Monolayer of Thiolates on a Tetragonal Au92 Nanocrystal", Journal of the American Chemical Society **138**, 8710 (2016).

[162] N. Xia and Z. Wu, "Controlling ultrasmall gold nanoparticles with atomic precision", Chemical Science **12**, 2368 (2021).

[163] M. Walter, J. Akola, O. Lopez-Acevedo, P. D. Jadzinsky, G. Calero, C. J. Ackerson, R. L. Whetten, H. Grö Nbeck ‡ ‡, and H. Hä Kkinen † §, *A unified view of ligand-protected gold clusters as superatom complexes*, tech. rep. (2008).

[164] X. Kang, H. Chong, and M. Zhu, "Au25(SR)18: The captain of the great nanocluster ship", Nanoscale **10**, 10758 (2018).

[165] M. Zhu, C. M. Aikens, F. J. Hollander, G. C. Schatz, and R. Jin, "Correlating the crystal structure of A thiol-protected Au25 cluster and optical properties", Journal of the American Chemical Society **130**, 5883 (2008).

[166] K. L. M. Weerawardene and C. M. Aikens, "Theoretical Insights into the Origin of Photoluminescence of Au25(SR)18- Nanoparticles", Journal of the American Chemical Society **138**, 11202 (2016).

[167] J.-Y. Zhao, R. Cui, Z.-L. Zhang, M. Zhang, Z.-X. Xie, and D.-W. Pang, "Cytotoxicity of nucleus-targeting fluorescent gold nanoclusters", Nanoscale **6**, 13126 (2014).

[168] M. S. Devadas, J. Kim, E. Sinn, D. Lee, T. Goodson, and G. Ramakrishna, " Unique Ultrafast Visible Luminescence in Monolayer-Protected Au 25 Clusters ", The Journal of Physical Chemistry C **114**, 22417 (2010).

[169] T. D. Green and K. L. Knappenberger, "Relaxation dynamics of Au25L18 nanoclusters studied by femtosecond time-resolved near infrared transient absorption spectroscopy", Nanoscale **4**, 4111 (2012).

[170] S. H. Yau, O. Varnavski, and T. Goodson, "An Ultrafast Look at Au Nanoclusters", Accounts of Chemical Research **46**, 1506 (2013).

[171] Z. Wu and R. Jin, "On the ligand's role in the fluorescence of gold nanoclusters", Nano Letters **10**, 2568 (2010).

[172] M. Jin and H. Ito, "Solid-state luminescence of Au(I) complexes with external stimuli-responsive properties", Journal of Photochemistry and Photobiology C: Photochemistry Reviews **51**, 10.1016/j.jphotochemrev.2021.100478 (2022).

[173] S. Chandra, A. Sciortino, S. Das, F. Ahmed, A. Jana, J. Roy, D. Li, V. Liljeström, H. Jiang, L.-S. Johansson, X. Chen, Nonappa, M. Cannas, T. Pradeep, B. Peng, R. H. A. Ras, Z. Sun, O. Ikkala, and F. Messina, "Gold Au(I)6Clusters with Ligand-Derived Atomic Steric Locking: Multifunctional Optoelectrical Properties and Quantum Coherence", Advanced Optical Materials **11**, 10.1002/adom.202202649 (2023).

[174] K. R. Krishnadas, A. Baksi, A. Ghosh, G. Natarajan, and T. Pradeep, "Structure-conserving spontaneous transformations between nanoparticles", Nature Communications **7**, 10.1038/ncomms13447 (2016).

[175] P. Chakraborty, A. Nag, K. S. Sugi, T. Ahuja, B. Varghese, and T. Pradeep, "Crystallization of a Supramolecular Coassembly of an Atomically Precise Nanoparticle with a Crown Ether", ACS Materials Letters **1**, 534 (2019).

[176] A. Nag, P. Chakraborty, G. Paramasivam, M. Bodiuzzaman, G. Natarajan, and T. Pradeep, "Isomerism in Supramolecular Adducts of Atomically Precise Nanoparticles", Journal of the American Chemical Society **140**, 13590 (2018).

[177] A. Nag and T. Pradeep, "Assembling Atomically Precise Noble Metal Nanoclusters Using Supramolecular Interactions", ACS Nanoscience Au **2**, 160 (2022).

[178] X. Kang, S. Wang, and M. Zhu, "Observation of a new type of aggregation-induced emission in nanoclusters", Chemical Science **9**, 3062 (2018).

[179] M. A. Moussawi, N. Leclerc-Laronze, S. Floquet, P. A. Abramov, M. N. Sokolov, S. Cordier, A. Ponchel, E. Monflier, H. Bricout, D. Landy, M. Haouas, J. Marrot, and E. Cadot, "Polyoxometalate, Cationic Cluster, and γ-Cyclodextrin: From Primary Interactions to Supramolecular Hybrid Materials", Journal of the American Chemical Society **139**, 12793 (2017).

[180] B. Yoon, W. D. Luedtke, R. N. Barnett, J. Gao, A. Desireddy, B. E. Conn, T. Bigioni, and U. Landman, "Hydrogen-bonded structure and mechanical chiral response of a silver nanoparticle superlattice", Nature Materials **13**, 807 (2014).

[181] M. Jash, A. Jana, A. K. Poonia, E. Khatun, P. Chakraborty, A. Nagar, T. Ahuja, K. V. Adarsh, and T. Pradeep, "Phosphine-Protected Atomically Precise Silver-Gold Alloy Nanoclusters and Their Luminescent Superstructures", Chemistry of Materials **35**, 313 (2023).

[182] Nonappa, T. Lahtinen, J. S. Haataja, T.-R. Tero, H. Häkkinen, and O. Ikkala, "Template-Free Supracolloidal Self-Assembly of Atomically Precise Gold Nanoclusters: From 2D Colloidal Crystals to Spherical Capsids", Angewandte Chemie **128**, 16269 (2016).

[183] L. Carbone, C. Nobile, M. De Giorgi, F. D. Sala, G. Morello, P. Pompa, M. Hytch, E. Snoeck, A. Fiore, I. R. Franchini, M. Nadasan, A. F. Silvestre, L. Chiodo, S. Kudera, R. Cingolani, R. Krahne, and L. Manna, "Synthesis and Micrometer-Scale Assembly of Colloidal CdSe/CdS Nanorods Prepared by a Seeded Growth Approach", Nano Letters **7**, 2942 (2007).

[184] A. T. Fafarman, W.-k. Koh, B. T. Diroll, D. K. Kim, D.-K. Ko, S. J. Oh, X. Ye, V. Doan-Nguyen, M. R. Crump, D. C. Reifsnyder, C. B. Murray, and C. R. Kagan, "Thiocyanate-Capped Nanocrystal Colloids: Vibrational Reporter of Surface Chemistry and Solution-Based Route to Enhanced Coupling in Nanocrystal Solids", Journal of the American Chemical Society **133**, 15753 (2011).

[185] E. Marino, R. A. LaCour, T. C. Moore, S. W. van Dongen, A. W. Keller, D. An, S. Yang, D. J. Rosen, G. Gouget, E. H. R. Tsai, C. R. Kagan, T. E. Kodger, S. C. Glotzer, and C. B. Murray, "Crystallization of binary nanocrystal superlattices and the relevance of short-range attraction", Nature Synthesis **3**, 111 (2023).

[186] T. G. Braginskaya, P. D. Dobitchin, M. A. Ivanova, V. V. Klyubin, A. V. Lomakin, V. A. Noskin, G. E. Shmelev, and S. P. Tolpina, "Analysis of the Polydispersity by Photon Correlation Spectroscopy. Regularization Procedure", Physica Scripta **28**, 73 (1983).

[187] T. Narayanan, M. Sztucki, T. Zinn, J. Kieffer, A. Homs-Puron, J. Gorini, P. Van Vaerenbergh, and P. Boesecke, "Performance of the time-resolved ultra-small-angle X-ray scattering beamline with the Extremely Brilliant Source", Journal of Applied Crystallography **55**, 98 (2022).

[188] S. A. Mann, B. Sciacca, Y. Zhang, J. Wang, E. Kontoleta, H. Liu, and E. C. Garnett, "Integrating Sphere Microscopy for Direct Absorption Measurements of Single Nanostructures", ACS Nano **11**, 1412 (2017).

[189] J. C. de Mello, H. F. Wittmann, and R. H. Friend, "An improved experimental determination of external photoluminescence quantum efficiency", Advanced Materials **9**, 230 (1997).

[190] C. Ruckebusch, M. Sliwa, P. Pernot, A. de Juan, and R. Tauler, "Comprehensive data analysis of femtosecond transient absorption spectra: A review", Journal of Photochemistry and Photobiology C: Photochemistry Reviews **13**, 1 (2012).

[191] Y. D. Glinka, "Ultrafast transient absorption spectroscopy of 2D semiconductors: a review", Journal of Physics: Condensed Matter **37**, 463002 (2025).

[192] N. Li, Y. Ma, and W. Sun, "Exploring the Dynamics of Charge Transfer in Photocatalysis: Applications of Femtosecond Transient Absorption Spectroscopy", Molecules **29**, 3995 (2024).

[193] S. Mukamel, "Multidimensional Femtosecond Correlation Spectroscopies of Electronic and Vibrational Excitations", Annual Review of Physical Chemistry **51**, 691 (2000).

[194] J. R. Lakowicz, *Principles of fluorescence spectroscopy* (Springer, 2006), p. 954.

[195] B. A. Nechay, U. Siegner, M. Achermann, H. Bielefeldt, and U. Keller, "Femtosecond pump-probe near-field optical microscopy", Review of Scientific Instruments **70**, 2758 (1999).

[196] Y. Zhu and J.-X. Cheng, "Transient absorption microscopy: Technological innovations and applications in materials science and life science", The Journal of Chemical Physics **152**, 10.1063/1.5129123 (2020).

[197] W. Min, C. W. Freudiger, S. Lu, and X. S. Xie, "Coherent nonlinear optical imaging: Beyond fluorescence microscopy", Annual Review of Physical Chemistry **62**, 507 (2011).

[198] E. S. Massaro, A. H. Hill, and E. M. Grumstrup, "Super-Resolution Structured Pump-Probe Microscopy", ACS Photonics **3**, 501 (2016).

[199] K. Karki, M. Namboodiri, T. Z. Khan, and A. Materny, "Pump-probe scanning near field optical microscopy: Sub-wavelength resolution chemical imaging and ultrafast local dynamics", Applied Physics Letters **100**, 10.1063/1.3701724 (2012).

[200] E. M. Grumstrup, M. M. Gabriel, E. E. Cating, E. M. Van Goethem, and J. M. Papanikolas, "Pump-probe microscopy: Visualization and spectroscopy of ultrafast dynamics at the nanoscale", Chemical Physics **458**, 30 (2015).

[201] T. Zhu, J. M. Snaider, L. Yuan, and L. Huang, "Ultrafast Dynamic Microscopy of Carrier and Exciton Transport", Annual Review of Physical Chemistry **70**, 219 (2019).

[202] M. C. Fischer, J. W. Wilson, F. E. Robles, and W. S. Warren, "Invited Review Article: Pump-probe microscopy", Review of Scientific Instruments **87**, 10.1063/1.4943211 (2016).

[203] K. S. Wilson, T. S. Volek, N. Gross, S. Link, C. R. Baiz, and S. T. Roberts, "Transient Absorption Microscopy Using Widefield Lock-in Camera Imaging", The Journal of Physical Chemistry C **128**, 11723 (2024).

[204] C. Schnedermann, J. M. Lim, T. Wende, A. S. Duarte, L. Ni, Q. Gu, A. Sadhanala, A. Rao, and P. Kukura, "Sub-10 fs Time-Resolved Vibronic Optical Microscopy", The Journal of Physical Chemistry Letters **7**, 4854 (2016).

[205] S. Li, F. Hu, Y. Bi, H. Yang, B. Lv, C. Zhang, J. Zhang, M. Xiao, and X. Wang, "Micrometer-Scale Carrier Transport in the Solid Film of Giant CdSe/CdS Nanocrystals Imaged by Transient Absorption Microscopy", Nano Letters **23**, 9887 (2023).

[206] L. Yuan, T.-F. Chung, A. Kuc, Y. Wan, Y. Xu, Y. P. Chen, T. Heine, and L. Huang, "Photocarrier generation from interlayer charge-transfer transitions in WS2-graphene heterostructures", Science Advances **4**, 10.1126/sciadv.1700324 (2018).

[207] D. Davydova, A. de la Cadena, D. Akimov, and B. Dietzek, "Transient absorption microscopy: advances in chemical imaging of photoinduced dynamics", Laser & Photonics Reviews **10**, 62 (2016).

[208] P. Castronovo, M. Reale, S. A. Rigter, C. R. Kagan, C. B. Murray, S. Lorenzo, E. C. Garnett, P. Schall, E. Marino, A. Sciortino, and F. Messina, "Ultrafast Switching of Whispering Gallery Modes in Quantum Dot Superparticles", Nano Letters **25**, 5828 (2025).

[209] M. A. Boles, M. Engel, and D. V. Talapin, "Self-assembly of colloidal nanocrystals: From intricate structures to functional materials", Chemical Reviews **116**, 11220 (2016).

[210] C. B. Murray, C. R. Kagan, and M. G. Bawendi, "Synthesis and Characterization of Monodisperse Nanocrystals and Close-Packed Nanocrystal Assemblies", Annual Review of Materials Science **30**, 545 (2000).

[211] C. C. Lam, P. T. Leung, and K. Young, "Explicit asymptotic formulas for the positions, widths, and strengths of resonances in Mie scattering", Journal of the Optical Society of America B **9**, 1585 (1992).

[212] A. B. Matsko and V. S. Ilchenko, "Optical resonators with whispering-gallery modes - Part I: Basics", IEEE Journal on Selected Topics in Quantum Electronics **12**, 3 (2006).

[213] L. Cai, J. Pan, Y. Zhao, J. Wang, and S. Xiao, "Whispering Gallery Mode Optical Microresonators: Structures and Sensing Applications", physica status solidi (a) **217**, 10.1002/pssa.201900825 (2020).

[214] D. E. Aspnes, *Electric-Field Effects on Optical Absorption near Thresholds in Solids**, tech. rep. (1966), p. 15.

[215] D. Vanmaekelbergh, L. K. van Vugt, H. E. Bakker, F. T. Rabouw, B. de Nijs, R. J. A. van Dijk-Moes, M. A. van Huis, P. J. Baesjou, and A. van Blaaderen, "Shape-Dependent Multiexciton Emission and Whispering Gallery Modes in Supraparticles of CdSe/Multishell Quantum Dots", ACS Nano **9**, 3942 (2015).

[216] E. Marino, H. Bharti, J. Xu, C. R. Kagan, and C. B. Murray, "Nanocrystal Superparticles with Whispering-Gallery Modes Tunable through Chemical and Optical Triggers", Nano Letters **22**, 4765 (2022).

[217] B. le Feber, F. Prins, E. De Leo, F. T. Rabouw, and D. J. Norris, "Colloidal-Quantum-Dot Ring Lasers with Active Color Control", Nano Letters **18**, 1028 (2018).

[218] C. Zhang, H. Dong, C. Zhang, Y. Fan, J. Yao, and Y. S. Zhao, "Photonic skins based on flexible organic microlaser arrays", Science Advances **7**, 10.1126/sciadv.abh3530 (2021).

[219] M. Reale, P. Castronovo, M. Cannas, E. Marino, A. Sciortino, and F. Messina, "Excitation-Wavelength-Tunable Lasing in Individual Quantum Dot Superparticles", Advanced Optical Materials **13**, 10.1002/adom.202500838 (2025).

[220] M. Reale, E. Marino, E. Maçôas, F. Ciccarello, M. Cannas, C. M. Cruz, A. G. Campaña, A. Sciortino, and F. Messina, "Carbon-Based Photonic Microlabels Based on Fluorescent Nanographene-Polystyrene Com-

posites", Advanced Functional Materials **34**, 10.1002/adfm.202402079 (2024).

[221] Z. Li, J. Wei, F. Wang, Y. Tang, A. Li, Y. Guo, P. Huang, S. Brovelli, H. Shen, and H. Li, "Carrier Dynamics in Alloyed Chalcogenide Quantum Dots and Their Light-Emitting Devices", Advanced Energy Materials **11**, 10.1002/aenm.202101693 (2021).

[222] W. Yoshiki and T. Tanabe, "All-optical switching using Kerr effect in a silica toroid microcavity", Optics Express **22**, 24332 (2014).

[223] J. S. Pelc, K. Rivoire, S. Vo, C. Santori, D. A. Fattal, and R. G. Beausoleil, "Picosecond all-optical switching in hydrogenated amorphous silicon microring resonators", Optics Express **22**, 3797 (2014).

[224] C. Sauvan, J. P. Hugonin, I. S. Maksymov, and P. Lalanne, "Theory of the Spontaneous Optical Emission of Nanosize Photonic and Plasmon Resonators", Physical Review Letters **110**, 237401 (2013).

[225] F. Montanarella, D. Urbonas, L. Chadwick, P. G. Moerman, P. J. Baesjou, R. F. Mahrt, A. van Blaaderen, T. Stöferle, and D. Vanmaekelbergh, "Lasing Supraparticles Self-Assembled from Nanocrystals", ACS Nano **12**, 12788 (2018).

[226] A. Chiasera, Y. Dumeige, P. Féron, M. Ferrari, Y. Jestin, G. Nunzi Conti, S. Pelli, S. Soria, and G. Righini, "Spherical whispering-gallery-mode microresonators", Laser & Photonics Reviews **4**, 457 (2010).

[227] D. R. Lide, *CRC Handbook of Chemistry and Physics*, 79th ed. (CRC-Press, BocaRaton, 1998).

[228] J. Enríquez, "Influence of the thickness on structural, optical and electrical properties of chemical bath deposited CdS thin films", Solar Energy Materials and Solar Cells **76**, 313 (2003).

[229] M. P. Lisitsa, L. F. Gudymenko, V. N. Malinko, and S. F. Terekhova, "Dispersion of the Refractive Indices and Birefringence of CdS_xSe_{1-x} Single Crystals", physica status solidi (b) **31**, 389 (1969).

[230] J. M. Gérard, D. Barrier, J. Y. Marzin, R. Kuszelewicz, L. Manin, E. Costard, V. Thierry-Mieg, and T. Rivera, "Quantum boxes as active probes for photonic microstructures: The pillar microcavity case", Applied Physics Letters **69**, 449 (1996).

[231] C. De Mello Donegá, M. Bode, and A. Meijerink, "Size- and temperature-dependence of exciton lifetimes in CdSe quantum dots", Physical Review B - Condensed Matter and Materials Physics **74**, 10.1103/PhysRevB.74.085320 (2006).

[232] L. Dong, A. Sugunan, J. Hu, S. Zhou, S. Li, S. Popov, M. S. Toprak, A. T. Friberg, and M. Muhammed, *Photoluminescence from quasi-type-II spherical CdSe-CdS core-shell quantum dots*, tech. rep. (2012).

[233] T. Ihara, R. Sato, T. Teranishi, and Y. Kanemitsu, "Delocalized and localized charged excitons in single CdSe/CdS dot-in-rods revealed by polarized photoluminescence blinking", Physical Review B - Condensed Matter and Materials Physics **90**, 10.1103/PhysRevB.90.035309 (2014).

[234] O. Chen, J. Zhao, V. P. Chauhan, J. Cui, C. Wong, D. K. Harris, H. Wei, H. S. Han, D. Fukumura, R. K. Jain, and M. G. Bawendi, "Compact high-quality CdSe-CdS core-shell nanocrystals with narrow emission linewidths and suppressed blinking", Nature Materials **12**, 445 (2013).

[235] D. Kong, Y. Jia, Y. Ren, Z. Xie, K. Wu, and T. Lian, "Shell-Thickness-Dependent Biexciton Lifetime in Type i and Quasi-Type II CdSe@CdS Core/Shell Quantum Dots", Journal of Physical Chemistry C **122**, 14091 (2018).

[236] Y. He, S. Hu, T. Han, X. Chen, Y. Yu, T. Li, W. Zhu, and G. Ouyang, "Suppression of the Auger Recombination Process in CdSe/CdS Core/Shell Nanocrystals", ACS Omega **4**, 9198 (2019).

[237] J. P. Philbin and E. Rabani, "Auger Recombination Lifetime Scaling for Type i and Quasi-Type II Core/Shell Quantum Dots", Journal of Physical Chemistry Letters **11**, 5132 (2020).

[238] Y. S. Park, W. K. Bae, J. M. Pietryga, and V. I. Klimov, "Auger recombination of biexcitons and negative and positive trions in individual quantum dots", ACS Nano **8**, 7288 (2014).

[239] P. P. Jha and P. Guyot-Sionnest, "Trion decay in colloidal quantum dots", ACS Nano **3**, 1011 (2009).

[240] J. M. Pietryga, Y. S. Park, J. Lim, A. F. Fidler, W. K. Bae, S. Brovelli, and V. I. Klimov, "Spectroscopic and device aspects of nanocrystal quantum dots", Chemical Reviews **116**, 10513 (2016).

[241] M. V. Kovalenko, L. Protesescu, and M. I. Bodnarchuk, "Properties and potential optoelectronic applications of lead halide perovskite nanocrystals", Science **358**, 745 (2017).

[242] C. K. Ng, W. Yin, H. Li, and J. J. Jasieniak, "Scalable synthesis of colloidal CsPbBr3 perovskite nanocrystals with high reaction yields through solvent and ligand engineering", Nanoscale **12**, 4859 (2020).

[243] H. Huang, M. I. Bodnarchuk, S. V. Kershaw, M. V. Kovalenko, and A. L. Rogach, "Lead Halide Perovskite Nanocrystals in the Research Spotlight: Stability and Defect Tolerance", ACS Energy Letters **2**, 2071 (2017).

[244] W. J. Mir, A. Warankar, A. Acharya, S. Das, P. Mandal, and A. Nag, "Colloidal thallium halide nanocrystals with reasonable luminescence, carrier mobility and diffusion length", Chemical Science **8**, 4602 (2017).

[245] Y. Wu, P. Wang, Z. Guan, J. Liu, Z. Wang, Z. Zheng, S. Jin, Y. Dai, M.-H. Whangbo, and B. Huang, "Enhancing the Photocatalytic Hydrogen Evolution Activity of Mixed-Halide Perovskite $CH_3NH_3PbBr_{3-x}I_x$ Achieved by Bandgap Funneling of Charge Carriers", ACS Catalysis **8**, 10349 (2018).

[246] D. Vila-Liarte, M. W. Feil, A. Manzi, J. L. Garcia-Pomar, H. Huang, M. Döblinger, L. M. Liz-Marzán, J. Feldmann, L. Polavarapu, and A. Mihi, "Templated-Assembly of CsPbBr3 Perovskite Nanocrystals into 2D Photonic Supercrystals with Amplified Spontaneous Emission", Angewandte Chemie - International Edition **59**, 17750 (2020).

[247] Y. Tong, E. P. Yao, A. Manzi, E. Bladt, K. Wang, M. Döblinger, S. Bals, P. Müller-Buschbaum, A. S. Urban, L. Polavarapu, and J. Feldmann, "Spontaneous Self-Assembly of Perovskite Nanocrystals into Electronically Coupled Supercrystals: Toward Filling the Green Gap", Advanced Materials **30**, 10.1002/adma.201801117 (2018).

[248] S. Levy, O. Be'er, S. Shaek, A. Gorlach, E. Scharf, Y. Ossia, R. Liran, K. Cohen, R. Strassberg, I. Kaminer, U. Banin, and Y. Bekenstein, "Collective Interactions of Quantum-Confined Excitons in Halide Perovskite Nanocrystal Superlattices", ACS Nano **19**, 963 (2025).

[249] C. N. Dibenedetto, D. Conelli, D. Altamura, F. Scattarella, E. Altamura, H. Mateos, F. Olivieri, A. Panniello, G. Minervini, E. Fanizza, A. Milella, R. Tommasi, N. Depalo, R. Comparelli, C. Ingrosso, M. L. Curri, C. Giannini, G. P. Suranna, R. Grisorio, and M. Striccoli, "Beyond Nano Building Blocks: The Influence of Mn(II) Doping on 3D Self-Assembled Perovskite Supercrystals", Small Structures, 10.1002/sstr.202500373 (2025).

[250] J. De Roo, M. Ibáñez, P. Geiregat, G. Nedelcu, W. Walravens, J. Maes, J. C. Martins, I. Van Driessche, M. V. Kovalenko, and Z. Hens, "Highly Dynamic Ligand Binding and Light Absorption Coefficient of Cesium Lead Bromide Perovskite Nanocrystals", ACS Nano **10**, 2071 (2016).

[251] D. Zhang, S. W. Eaton, Y. Yu, L. Dou, and P. Yang, "Solution-Phase Synthesis of Cesium Lead Halide Perovskite Nanowires", Journal of the American Chemical Society **137**, 9230 (2015).

[252] D. R. Stirling, M. J. Swain-Bowden, A. M. Lucas, A. E. Carpenter, B. A. Cimini, and A. Goodman, "CellProfiler 4: improvements in speed, utility and usability", BMC Bioinformatics **22**, 10.1186/s12859-021-04344-9 (2021).

[253] S. Agnello, "Radiation–Matter Interaction Principles", in *Spectroscopy for materials characterization* (Wiley, July 2021), pp. 1–34.

[254] P. Castronovo, R. Rubino, P. Schall, F. Messina, and A. Sciortino, *Unraveling the 3d architecture of perovskite supercubes: insights into structure-property relationships* (Experimental session: MA-6665 - Beamline ID02 - European Synchrotron Radiation Facility (ESRF), 2025).

[255] P. Scherrer, "Bestimmung der größe und der inneren struktur von kolloidteilchen mittels röntgenstrahlen", Nachrichten von der Gesellschaft der Wissenschaften zu Göttingen, Mathematisch-Physikalische Klasse **1918**, 98 (1918).

[256] P. Scardi, M. Leoni, and R. Delhez, "Line broadening analysis using integral breadth methods: a critical review", Journal of Applied Crystallography **37**, 381 (2004).

[257] J. I. Langford and A. J. C. Wilson, "Scherrer after sixty years: A survey and some new results in the determination of crystallite size", Journal of Applied Crystallography **11**, 102 (1978).

[258] R. P. Mirin, K. L. Silverman, D. H. Christensen, and A. Roshko, "Narrow photoluminescence linewidths from ensembles of self-assembled InGaAs quantum dots", Journal of Vacuum Science & Technology B: Microelectronics and Nanometer Structures Processing, Measurement, and Phenomena **18**, 1510 (2000).

[259] D. Yan, Q. Shan, Y. Dong, L. Han, X. Wu, Y. Peng, and H. Zeng, "Perovskite nanocrystal superlattices: self-assembly, collective behavior, and applications", Chemical Communications **59**, 5365 (2023).

[260] P. Castronovo, C. Gonzalez, G. Ammirati, S. Yang, D. Catone, A. Paladini, P. O'Keeffe, C. R. Kagan, C. B. Murray, A. Emanuele, E. Marino, F. Messina, and A. Sciortino, "Interparticle Distance Controls Ultrafast Photodynamics in Crystalline Gold Superstructures", Advanced Optical Materials, 10.1002/adom.202502501 (2025).

[261] K. L. Kelly, E. Coronado, L. L. Zhao, and G. C. Schatz, "The Optical Properties of Metal Nanoparticles: The Influence of Size, Shape, and Dielectric Environment", The Journal of Physical Chemistry B **107**, 668 (2003).

[262] L. Wang, M. Hasanzadeh Kafshgari, and M. Meunier, "Optical Properties and Applications of Plasmonic-Metal Nanoparticles", Advanced Functional Materials **30**, 10.1002/adfm.202005400 (2020).

[263] M. Reale, S. Chandra, G. Buscarino, A. Emanuele, M. Cannas, O. Ikkala, A. Sciortino, and F. Messina, "Photoinduced charge separation in functional carbon–silver nanohybrids", Physical Chemistry Chemical Physics **24**, 12974 (2022).

[264] K. Kant, R. Beeram, Y. Cao, P. S. S. dos Santos, L. González-Cabaleiro, D. García-Lojo, H. Guo, Y. Joung, S. Kothadiya, M. Lafuente, Y. X. Leong, Y. Liu, Y. Liu, S. S. B. Moram, S. Mahasivam, S. Maniappan, D. Quesada-González, D. Raj, P. Weerathunge, X. Xia, Q. Yu, S. Abalde-Cela, R. A. Alvarez-Puebla, R. Bardhan, V. Bansal, J. Choo, L. C. C. Coelho, J. M. M. M. de Almeida, S. Gómez-Graña, M. Grzelczak, P. Herves, J. Kumar, T. Lohmueller, A. Merkoçi, J. L. Montaño-Priede, X. Y. Ling, R. Mallada, J. Pérez-Juste, M. P. Pina, S. Singamaneni, V. R. Soma, M. Sun, L. Tian, J. Wang, L. Polavarapu, and I. P. Santos, "Plasmonic nanoparticle sensors: current progress, challenges, and future prospects", Nanoscale Horizons **9**, 2085 (2024).

[265] K. Bian, H. Schunk, D. Ye, A. Hwang, T. S. Luk, R. Li, Z. Wang, and H. Fan, "Formation of self-assembled gold nanoparticle supercrystals with facet-dependent surface plasmonic coupling", Nature Communications **9**, 2365 (2018).

[266] H. Wang, L. Yao, X. Mao, K. Wang, L. Zhu, and J. Zhu, "Gold nanoparticle superlattice monolayer with tunable interparticle gap for surface-enhanced Raman spectroscopy", Nanoscale **11**, 13917 (2019).

[267] M. Herran, S. Juergensen, M. Kessens, D. Hoeing, A. Köppen, A. Sousa-Castillo, W. J. Parak, H. Lange, S. Reich, F. Schulz, and E. Cortés, "Plasmonic bimetallic two-dimensional supercrystals for H2 generation", Nature Catalysis **6**, 1205 (2023).

[268] J. Wang, L. Zhang, and M. Qiu, "Nonlinear plasmonics: second-harmonic generation and multiphoton photoluminescence", PhotoniX **4**, 32 (2023).

[269] T. Chen, M. Pourmand, A. Feizpour, B. Cushman, and B. M. Reinhard, "Tailoring Plasmon Coupling in Self-Assembled One-Dimensional Au Nanoparticle Chains through Simultaneous Control of Size and Gap Separation", The Journal of Physical Chemistry Letters **4**, 2147 (2013).

[270] P. K. Jain and M. A. El-Sayed, "Plasmonic coupling in noble metal nanostructures", Chemical Physics Letters **487**, 153 (2010).

[271] Y. Chen, J. Zheng, L. Zhang, S. Li, Y. Chen, K. K. Chui, W. Zhang, L. Shao, and J. Wang, "Inversion of the Chiroptical Responses of Chiral Gold Nanoparticles with a Gold Film", ACS Nano **18**, 383 (2024).

[272] S. K. Gahlaut, O. Avalos-Ovando, R. M. Kim, R. Hussein, S. Juergensen, S. Reich, A. O. Govorov, K. T. Nam, and I. Bald, "Amplification of Photochemical Chiroptical Activity of Chiral Gold Nanocubes", Small, 10.1002/smll.202505093 (2025).

[273] N. Kowalska, F. Bandalewicz, J. Kowalski, S. Gómez-Graña, M. Bagiński, I. Pastoriza-Santos, M. Grzelczak, J. Matraszek, J. Pérez-Juste, and W. Lewandowski, "Hydrophobic Gold Nanoparticles with Intrinsic Chirality for the Efficient Fabrication of Chiral Plasmonic Nanocomposites", ACS Applied Materials & Interfaces **14**, 50013 (2022).

[274] C. Zhang, D. Li, G. Zhang, X. Wang, L. Mao, Q. Gan, T. Ding, and H. Xu, "Switching plasmonic nanogaps between classical and quantum regimes with supramolecular interactions", Science Advances **8**, 10.1126/sciadv.abj9752 (2022).

[275] J. A. Jenkins, Y. Zhou, S. Thota, X. Tian, X. Zhao, S. Zou, and J. Zhao, "Blue-Shifted Narrow Localized Surface Plasmon Resonance from Dipole Coupling in Gold Nanoparticle Random Arrays", The Journal of Physical Chemistry C **118**, 26276 (2014).

[276] C. Voisin, D. Christofilos, P. A. Loukakos, N. Del Fatti, F. Vallée, J. Lermé, M. Gaudry, E. Cottancin, M. Pellarin, and M. Broyer, "Ultrafast electron-electron scattering and energy exchanges in noble-metal nanoparticles", Physical Review B **69**, 195416 (2004).

[277] T. Stoll, P. Maioli, A. Crut, N. Del Fatti, and F. Vallée, "Advances in femto-nano-optics: ultrafast nonlinearity of metal nanoparticles", The European Physical Journal B **87**, 260 (2014).

[278] M. Hasegawa, K. Watanabe, H. Namigata, T. A. Welling, K. Suga, and D. Nagao, "Surface lattice resonance in three-dimensional plasmonic arrays fabricated via self-assembly of silica-coated gold nanoparticles", Journal of Colloid and Interface Science **633**, 226 (2023).

[279] F. J. García de Abajo and A. Howie, "Retarded field calculation of electron energy loss in inhomogeneous dielectrics", Physical Review B **65**, 115418 (2002).

[280] J. Waxenegger, A. Trügler, and U. Hohenester, "Plasmonics simulations with the MNPBEM toolbox: Consideration of substrates and layer structures", Computer Physics Communications **193**, 138 (2015).

[281] R. Jin, C. Zeng, M. Zhou, and Y. Chen, "Atomically Precise Colloidal Metal Nanoclusters and Nanoparticles: Fundamentals and Opportunities", Chemical Reviews **116**, 10346 (2016).

[282] I. Chakraborty and T. Pradeep, "Atomically Precise Clusters of Noble Metals: Emerging Link between Atoms and Nanoparticles", Chemical Reviews **117**, 8208 (2017).

[283] X. Kang and M. Zhu, "Tailoring the photoluminescence of atomically precise nanoclusters", Chemical Society Reviews **48**, 2422 (2019).

[284] S. Chandra, Nonappa, G. Beaune, A. Som, S. Zhou, J. Lahtinen, H. Jiang, J. V. I. Timonen, O. Ikkala, and R. H. A. Ras, "Highly Luminescent Gold Nanocluster Frameworks", Advanced Optical Materials **7**, 10.1002/adom.201900620 (2019).

[285] S. Maity, S. Kolay, S. Chakraborty, A. Devi, Rashi, and A. Patra, "A comprehensive review of atomically precise metal nanoclusters with emergent photophysical properties towards diverse applications", Chemical Society Reviews **54**, 1785 (2025).

[286] S. Chandra, A. Sciortino, S. Shandilya, L. Fang, X. Chen, Nonappa, H. Jiang, L.-S. Johansson, M. Cannas, J. Ruokolainen, R. H. A. Ras, F. Messina, B. Peng, and O. Ikkala, "Core-Selective Silver-Doping of Gold Nanoclusters by Surface-Bound Sulphates on Colloidal Templates: From Synthetic Mechanism to Relaxation Dynamics", Advanced Optical Materials **11**, 10.1002/adom.202201901 (2023).

[287] L. Shi, L. Zhu, J. Guo, L. Zhang, Y. Shi, Y. Zhang, K. Hou, Y. Zheng, Y. Zhu, J. Lv, S. Liu, and Z. Tang, "Self-Assembly of Chiral Gold Clusters into Crystalline Nanocubes of Exceptional Optical Activity", Angewandte Chemie International Edition **56**, 15397 (2017).

[288] J. V. Rival, P. Mymoona, K. M. Lakshmi, Nonappa, T. Pradeep, and E. S. Shibu, "Self-Assembly of Precision Noble Metal Nanoclusters: Hierarchical Structural Complexity, Colloidal Superstructures, and Applications", Small **17**, 10.1002/smll.202005718 (2021).

[289] N. Nonappa, "Precision nanoengineering for functional self-assemblies across length scales", Chemical Communications **59**, 13800 (2023).

[290] Z. Wu, Y. Du, J. Liu, Q. Yao, T. Chen, Y. Cao, H. Zhang, and J. Xie, "Aurophilic Interactions in the Self-Assembly of Gold Nanoclusters into Nanoribbons with Enhanced Luminescence", Angewandte Chemie **131**, 8223 (2019).

[291] Q. Yao, L. Liu, S. Malola, M. Ge, H. Xu, Z. Wu, T. Chen, Y. Cao, M. F. Matus, A. Pihlajamäki, Y. Han, H. Häkkinen, and J. Xie, "Supercrystal engineering of atomically precise gold nanoparticles promoted by surface dynamics", Nature Chemistry **15**, 230 (2023).

[292] P. Yuan, R. Zhang, E. Selenius, P. Ruan, Y. Yao, Y. Zhou, S. Malola, H. Häkkinen, B. K. Teo, Y. Cao, and N. Zheng, "Solvent-mediated assembly of atom-precise gold–silver nanoclusters to semiconducting one-dimensional materials", Nature Communications **11**, 10.1038/s41467-020-16062-6 (2020).

[293] H. O. S. Yadav, "Three-body interaction of gold nanoparticles: the role of solvent density and ligand shell orientation", Physical Chemistry Chemical Physics **26**, 11558 (2024).

[294] J. V. Rival, Nonappa, and E. S. Shibu, "Light-Triggered Reversible Supracolloidal Self-Assembly of Precision Gold Nanoclusters", ACS Applied Materials & Interfaces **12**, 14569 (2020).

[295] V. Sethumadhavan and Nonappa, "Atomically precise noble metal nanoclusters for engineering self-assembled two-dimensional materials", Dalton Transactions **54**, 11770 (2025).

[296] H. Li, X. Kang, and M. Zhu, "Nanocluster-based aggregates: Assembled forms, driving forces, and structure-related properties", Coordination Chemistry Reviews **539**, 10.1016/j.ccr.2025.216738 (2025).

[297] D. Beljonne, Z. Shuai, G. Pourtois, and J. L. Bredas, "SpinOrbit Coupling and Intersystem Crossing in Conjugated Polymers: A Configuration Interaction Description", The Journal of Physical Chemistry A **105**, 3899 (2001).

[298] D. J. Huntley, “An explanation of the power-law decay of luminescence”, Journal of Physics: Condensed Matter **18**, 1359 (2006).

[299] M. K. Sahai, A. K. Bakshi, and D. Datta, “Revisit to power law decay of luminescence”, Journal of Luminescence **195**, 240 (2018).

[300] R. M. Russo, E. J. Mele, C. L. Kane, I. V. Rubtsov, M. J. Therien, and D. E. Luzzi, “One-dimensional diffusion-limited relaxation of photoexcitations in suspensions of single-walled carbon nanotubes”, Physical Review B **74**, 041405 (2006).

List of Activities

Cover feature

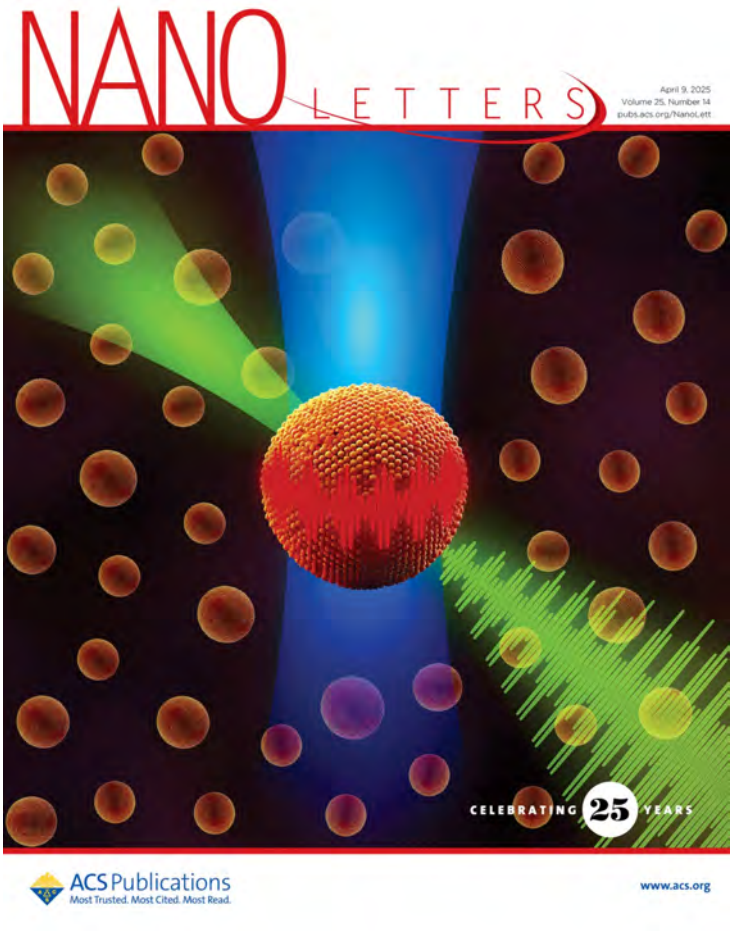

Published papers

- **P. Castronovo**, M. Reale, S.A. Rigter, C.R. Kagan, C.B. Murray, S. Lorenzo, E.C. Garnett, P. Schall, E. Marino, A. Sciortino, F. Messina. "Ultrafast Switching of Whispering Gallery Modes in Quantum Dot Superparticles", *Nano Letters*, 25, 14, 5828-5835 (2025) - DOI: 10.1021/acs.nanolett.5c00643 - **selected for main cover feature**;
- L.G. Barbata, M. Mazaj, R. Ettlinger, G. Ficarra, **P. Castronovo**, A. Sciortino, F. Messina, R.E. Morris, G. Buscarino. "Luminescent sensing of Hg^{2+} ions using MOF-808 combined with Au25@BSA nanoclusters", *Materials Research Bulletin*, 188, 113397 (2025) - DOI: 10.1016/j.materresbull.2025.113397;
- M. Reale, **P. Castronovo**, M. Cannas, E. Marino, A. Sciortino, F. Messina. "Excitation-Wavelength-Tunable Lasing in Individual Quantum Dot Superparticles", *Advanced Optical Materials*, 13, 2500838 (2025) - DOI: 10.1002/adom.202500838;
- **P. Castronovo**, C. Gonzales, G. Ammirati, S. Yang, D. Catone, A. Paladini, P. O'Keeffe, C. R. Kagan, C. B. Murray, A. Emanuele, E. Marino, F. Messina, A. Sciortino. "Interparticle Distance Controls Ultrafast Photodynamics in Crystalline Gold Superstructures", *Advanced Optical Materials*, e02501 (2025) - DOI: 10.1002/adom.202502501;
- N. Hosseiniyan, **P. Castronovo**, G. Beaune, E. Abdelrady, X. Chen, A. Zhyvolozhnyi, H. Siddiqui, J. Farhana, H. Jiang, M. Makki, M. Cannas, A. Sciortino, I. Skovorodkin, A. Samoylenko, J.V.I. Timonen, S. Vaino, F. Messina, S. Chandra. "Synergistic effects in matrix-embedded alloy nanoclusters: Advanced Type-I photosensitizers for theranostics". *ACS Applied Materials and Interfaces*, ASAP (2026) - DOI: 10.1021/acsami.5c22942.

Submitted and in-preparation papers

- V. Liljeström*, **P. Castronovo***, D. Agrawal, S. Das, N. Hosseiniyan, H. Jiang, M. Cannas, A. Sciortino, Z. Sun, F. Messina, S. Chandra. "Controlled self-assembly of atomically precise ultrasmall Au6 nanoclusters

into hierarchical fibrillar superstructures". *Submitted* (2025);
** co-first authors*

- **P. Castronovo**, R. Rubino, Y. Tang, R. Szostak, P. Schall, F. Messina, A. Sciortino. "Real-Time Observation of the Formation of Ordered Perovskite Supercrystals". *In preparation* (2026);

- **P. Castronovo**, M. Reale, E. Marino, A. Sciortino, F. Messina. "Collective Exciton Dynamics and Auger Shielding in Core-Shell Quantum Dot Superparticles". *In preparation* (2026);

Oral communications

- **P. Castronovo**, A. Sciortino, F. Messina. "There's plenty of room in the blink of an eye: ultrafast phenomena and their observation" - *Italian Conference of Physics Students 2023* (CISF23) - Palermo (Italy), April 12th 2023 - April 16th, 2023;

- **P. Castronovo**, M. Reale, Y. Tang, P. Schall, E. Marino, A. Sciortino, F. Messina. "(Self-)Assembly of Nanomaterials: a Pathway to the Tailoring of their (Photo)-Physical Properties" - *German-Italian Physics Exchange 2023* (GIPE23) - Bari (Italy), October 5th, 2023 - October 9th, 2023;

- **P. Castronovo**, M. Reale, C.R. Kagan, C.B. Murray, E. Marino, A. Sciortino, F. Messina. "Ultrafast Photodynamics of Quantum Dot Superparticles Unraveled by Transient Absorption Microscopy" - *EMRS Spring 2024* - Strasbourg (France), May 27th, 2024 - May 31st, 2024;

- **P. Castronovo**, M. Reale, C.R. Kagan, C.B. Murray, E. Marino, A. Sciortino, F. Messina. "Pump-Probe Microscopy Unravels the Ultrafast Photodynamics of Quantum Dot Superparticles for Future Applications in Micro-Photonics" - **Invited talk** - *MetaFUN 2024* - Palermo (Italy), July 23rd, 2024 - July 26th, 2024;

- **P. Castronovo**, Y. Tang, V. De Michele, P. Schall, A. Boukenter, M. Cannas, A. Sciortino, F. Messina. "Enabling Collective Behaviour of

Metal Halide Perovskite Nanocubes via Hierarchical Assembly into Superstructures" - *13th Young Researcher Meeting* - Palermo (Italy), September 24th, 2024 - September 27th, 2024.

- **P. Castronovo**, G. Ammirati, C. Gonzales, S. Yang, D. Catone, A. Paladini, P. O'Keeffe, C.B. Murray, E. Marino, F. Messina, A. Sciortino. "Unraveling the collective plasmonic behaviour of gold nanocrystal superparticles via ultrafast pump-probe microscopy" - *8th International Conference on Multifunctional, Hybrid and Nanomaterials* - Montpellier (France), March 3rd, 2025 - March 6th, 2025;

- **P. Castronovo**, M. Reale, C.R. Kagan, C.B. Murray, E. Marino, A. Sciortino, F. Messina. "Emergent Properties of Mesoscopic Self-Assembled Superstructures" - *International Scientific Highlights 2025* (Insight25) - Online event, April 27th, 2025.

- **P. Castronovo**, G. Ammirati, D. Catone, A. Paladini, P. O'Keeffe, E. Marino, F. Messina, A. Sciortino. "Unraveling the collective excitonic behaviour of gold nanocrystal superparticles via ultrafast pump-probe microscopy" - *The 5th International Online Conference on Nanomaterials* - Online event, September 22nd, 2025 - September 24th, 2025, **Best Oral Presentation Award winner**;

- **P. Castronovo**, C. Gonzales, G. Ammirati, S. Yang, D. Catone, A. Paladini, P. O'Keeffe, C. R. Kagan, C. B. Murray, A. Emanuele, E. Marino, F. Messina, A. Sciortino. "Pump-Probe Microscopy Unravels Distance-Dependent Collective Plasmonic Behaviour in Gold Nanoparticle Supercrystals" - *The 4th International Online Conference on Materials* - Online event, November 3rd, 2025 - November 5th, 2025, **Best Oral Presentation Award winner**.

Poster contributions

- **P. Castronovo**, M. Reale, E. Marino, A. Sciortino, F. Messina. "Ultrafast Transient Absorption Microscopy on Semiconductor Quantum Dot Supercrystals" - *Mecareact 2023*, Paris (France), June 18th, 2023 - June 23rd, 2023.

- **P. Castronovo**, C. Gonzales, G. Ammirati, S. Yang, D. Catone, A. Paladini, P. O'Keeffe, C. R. Kagan, C. B. Murray, A. Emanuele, E. Marino, F. Messina, A. Sciortino. "Distance-Dependent Collective Plasmonic Behaviour in Gold Nanoparticle Supercrystals" - *AFuN 2025*, Palermo (Italy), September 29th, 2025 - October 2nd, 2025;

Research periods abroad

- Van der Waals - Zeeman Institute, Institute of Physics, University of Amsterdam (The Netherlands) - September 1st, 2023 - November 14th, 2023 - Supervisor: Prof.Dr. Peter Schall;
- Laboratoire Hubert Curien, Jean Monnet University, Saint Etienne (France) - January 15th, 2024 - April 15th, 2024 - Supervisor: Dr. Vincenzo de Michele.

Research visits

- *Low temperature PL measurements on QD Superparticles under strong magnetic fields* - Department of Materials Science - Bicocca University, Milan (Italy), July 8th, 2024 - July 10th, 2024;
- *Unraveling the 3D Architecture of Perovskite Supercubes: Insights into Structure-Property Relationships* - Experiment Session at the European Synchrotron Radiation Facility (ESRF) - Beamline ID02 - Grenoble (France), July 19th, 2025 - July 21st, 2025 - Session DOI: 10.15151/ESRF-ES-2170333667

Acknowledgements

Mentri si mittiva 'n vucca la prima forchittata, Montalbano pinsò che, tutto sommato, meglio d'accussì non sarebbi potuta annare.

(As he put the first forkful in his mouth, Montalbano thought that, when all was said and done, things could not have gone any better.)

— Andrea Camilleri

This Thesis represents (or attempts to represent) three years of research, professional and personal growth, and life in general. Three years that have literally flown by (didn't I graduate last week?) and yet have totally transformed me, both as a person and, I hope, as a young researcher. For this reason, I feel the need to acknowledge all those who have guided, accompanied, supported, and put up with me, both within and outside the lab.

First and foremost, I would like to express my deepest gratitude to my amazing supervisors, Prof. Fabrizio Messina and Dr. Alice Sciortino. Fabrizio and Alice, it's really hard to condense in just a few words what your support and guidance have meant for me. Ever since my B.Sc. project, you have been true mentors, teachers, and inspiration, always patiently giving me space to explore and "bang my head" around, while never failing to make me feel supported and cared about. Fabrizio, thank you for never letting your endless tasks and responsibilities stop you from being an enthusiastic, good-humoured labmate, always curious and supportive. Thank you for being a veritable role model of what a mentor, teacher, and leader should be. Alice, thank you for your fairness, firmness, and level-headedness. Thank you for bringing me back on track when I felt disoriented and discomforted, and for teaching me the importance of being on-task and having a good work-life balance.

During my PhD, I've been fortunate enough to work closely with, and learn loads from, two scientists who have supported, challenged, and encouraged

me more than they probably realise: Dr. Emanuele Marino and Dr. Marco Reale. Emanuele, thank you for being a constant source of precious advice, constructive criticism, and forward-looking perspective, for challenging my overly romantic view of research, and always encouraging me to push my limits and boundaries. Marco, your unmatched selflessness and work ethic have truly compelled me to become a better researcher. Thank you for your constant kindness and availability, and for our many interesting conversations about science, fountain pens, and countless other topics.

With Fabrizio, Alice, and Marco, I have been fortunate enough to witness the birth, expansion, and official establishment of the *Photo*^{2}*N* Group, more affectionately known as the *Hippo Team*: a close-knit, supportive, and stimulating environment that I have been honoured and proud to be part of. I am truly grateful to the other current members of the team—Giuseppe, Riccardo, Caterina, and Gianluca—for the daily interactions, shared struggles, and many, many moments of laughter that made life in the lab lighter and more enjoyable. I also warmly thank past members Laureline and Ashim for their contributions and for the time we spent working together. Finally, I am grateful to all the visitors from all over the world who crossed paths with the group over the years, each of whom left something behind, scientifically and personally.

Photo^2*N* is part of the broader *LaBAM* group, within which I had the opportunity to interact with many inspiring colleagues at different stages of their career (as well as taking part in engaging table-tennis tournaments). I am particularly grateful to Prof. Marco Cannas for his constant support and encouragement. I would also like to thank the other senior members of the group—Prof. Franco Gelardi, Prof. Simonpietro Agnello, Dr. Gianpiero Buscarino, Dr. Antonino Madonia, Dr. Simone Barbarossa, and Dr. Salvatore Ferruggia Bonura—for our many insightful discussions and their willingness to share their experience. I am really grateful to my other junior colleagues—Emanuele S., Francesca, Ludovico, Giammarco, and Saranya—for all the laughs, coffee breaks, and unwavering mutual support in the lab. I am also grateful to Dr. Salvatore Lorenzo and Dr. Antonio Emanuele for their precious collaboration, and to Giacomo Tricomi and Gianluca Napoli for their technical support, patience, and for our pleasant, non-scientific conversations.

My PhD journey has been enriched by my research stays in Amsterdam and Saint-Etienne. I would therefore like to thank all those who have made my

months abroad scientifically poignant and humanly enjoyable.

I warmly thank Prof. Dr. Peter Schall for welcoming me in Amsterdam and for all our insightful conversations. I thank Dr. Yingying Tang for supervising my lab activities and providing a wealth of useful suggestions. I am grateful to Marco and Ina for making me feel at home in the office, and for our many, enjoyable coffee breaks. I thank Susan for our pleasant conversations and the amazing experiments we performed together. I am also grateful to the groups of Dr. J. van de Groep and Prof. Dr. E. Garnett for generously providing their laboratory facilities. Outside the lab, I've been fortunate enough to find an amazing Dutch-Italian-British family. I warmly thank Tommaso, Sarah, Eleonora, Daniela, Valentina, Hannah, and Massimiliano, for our dinners, laughs, and weekend trips. With you, the weeks in Amsterdam flew by!

I am grateful to Dr. Vincenzo de Michele, for being a true mentor and friend, making my stay in Saint-Etienne amazing both inside and out of the lab, from our exciting experiments to the equally exciting board game evenings. I thank the senior members of the Laboratoire Hubert Curien for welcoming me in their lab, and all the juniors for our pleasant lunches and coffee breaks. I am also grateful to Darlene for making me feel at home.

Approaching the final step of my student life (at least formally), I look back on many years of learning, certain that I wouldn't be here were it not for the many fantastic teachers I encountered over the years. I thank them all for instilling in me their passion and curiosity. Amongst them, I would like to especially acknowledge Dr. Marina Guccione, for her endless care and support.

During all these years, I have also been blessed with many precious colleagues and friends who have been confidants, advisors (scientific and not), and true teachers. Simona, Santi, Alice, Dario, Sabrina, Nico, Margherita, Andrea, Vittoria, Giulia, and many others: I thank you from the bottom of my heart, I wouldn't have achieved any of this without you by my side. These last years have also been shaped by the big, beautiful family that is the Italian Association of Physics Students (AISF), which I have had the honour to serve as Secretary (2023-2024) and Treasurer (2024-2025). I consider AISF an integral part of my journey as a young researcher, as well as real-world practice of what being part of, and undertaking responsibilities in, a scientific community is all about. AISF has also gifted me countless precious friends and future colleagues, among which I'd like to specifically thank my apulian fam-

ily—Giorgia, Arianna, Davide, Chiara, Francesco, and Gabriele—for their unwavering presence and closeness, despite the physical distance. I am also grateful to Alessandro, Stefania, and all the members of the two Executive Committees with whom I have worked. I hope to meet all of you as fellow scientists in the years to come.

Last, but decidedly not least, I express my deepest thanks to my parents and my whole family. You have taught me the immense power of selflessness, sacrifice, and dedication. Day in, day out, you have encouraged me to overcome my fears and resistances, and to become a better person. None of this would have been possible, and nothing of what's to come will be, without your unwavering support and trust. You understand, more than anyone, why this thesis is dedicated to Nonno Biagio and Nonno Pietro, and you know what they would have said, and thought, in this occasion.

As a final note, I confess that I am acutely aware of my many failures and shortcomings, as well as of the many things that could have gone better in the lab (any reference to lasers breaking down is purely fictional…). Nonetheless, I consider these an unavoidable and precious part of any PhD journey, from which one learns resilience and ingenuity in the face of adversity. I am grateful for these experiences just as I am for all the positive ones—and I should be! After all, as the old saying goes, *all psalms end in glory*.

Grazie a tutti,

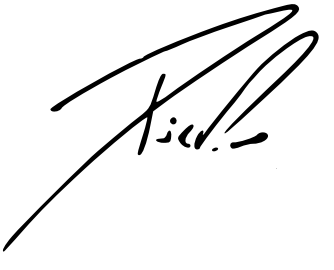

Palermo, February 2026